DOE/ER-0046/7 ~~FRW~~ JLS 5-7-82

Damage Analysis and Fundamental Studies

Quarterly Progress Report
July-Sept 1981

November 1981

U.S. Department of Energy
Assistant Secretary for Energy Technology
Office of Fusion Energy
Washington, DC 20545

NOTICE

This report was prepared as an account of work sponsored by the United States Government. Neither the United States nor the U.S. Department of Energy (DOE), nor any of its employes, nor any of its contractors, subcontractors or their employes, makes any warranty, expressed or implied, or assumes any legal liability or responsibility for any third party's use or the results of such use of any information, apparatus, product or process disclosed in this report, or represents that its use by such third party would not infringe privately owned rights.

Printed in the United States of America
Available from
National Technical Information Service
U.S. Department of Commerce
5285 Port Royal Road
Springfield, VA 22161

NTIS price codes
Printed copy: A12
Microfiche copy: A01

DOE/ER-0046/7
UC-20;20c

Damage Analysis and Fundamental Studies

Quarterly Progress Report
July-Sept 1981

November 1981

U.S. Department of Energy
Assistant Secretary for Energy Technology
Office of Fusion Energy
Washington, DC 20545

FOREWORD

This report is the fifteenth in a series of Quarterly Technical Progress Reports on Damage Analysis and Fundamental Studies (DAFS), which is one element of the Fusion Reactor Materials Program, conducted in support of the Magnetic Fusion Energy Program of the U. S. Department of Energy (DOE). The first eight reports in this series were numbered DOE/ET-0065/1 through 8. Other elements of the Materials Program are:

- Alloy Development for Irradiation Performance (ADIP)
- Plasma-Materials Interaction (PMI)
- Special Purpose Materials (SPM).

The DAFS program element is a national effort composed of contributions from a number of National Laboratories and other government laboratories, universities, and industrial laboratories. It was organized by the Materials and Radiation Effects Branch, Office of Fusion Energy, DOE, and a Task Group on Damage Analysis and Fundamental Studies, which operates under the auspices of that Branch. The purpose of this series of reports is to provide a working technical record of that effort for the use of the program participants, the fusion energy program in general, and the DOE.

This report is organized along topical lines in parallel to a Program Plan of the same title so that activities and accomplishments may be followed readily, relative to that Program Plan. Thus, the work of a given laboratory may appear throughout the report. The Table of Contents is annotated for the convenience of the reader.

This report has been compiled and edited under the guidance of the Chairman of the Task Group on Damage Analysis and Fundamental Studies, D. G. Doran, Hanford Engineering Development Laboratory (HEDL). His efforts, those of the supporting staff of HEDL, and the many persons who made technical contributions are gratefully acknowledged. M. M. Cohen, Materials and Radiation Effects Branch, is the DOE counterpart to the Task Group Chairman and has responsibility for the DAFS Program within DOE.

T. C. Reuther, Acting Chief
Materials and Radiation Effects Branch
Office of Fusion Energy

CONTENTS

Page

Foreword iii

Figures xii

Tables xviii

CHAPTER 1: IRRADIATION TEST FACILITIES

1. RTNS-II Irradiations and Operations (LLNL) 3

Irradiations were performed on three primary experiments involving Nb, Ti, V, Cu, and mica, and on three secondary ("piggyback") experiments. No major unscheduled outages occurred. A 50 em target was operated at 5000 rpm and high vacuum for 250 hours with no problems encountered.

CHAPTER 2: DOSIMETRY AND DAMAGE PARAMETERS

1. Fission Reactor Dosimetry (ANL) 8

Fluence and damage maps are presented for the EBR-II-X287 experiment. Dosimeters have been provided for several new experiments in HFIR.

2. Characterization of Spallation Neutron Sources (ANL) 17

The Radiation Effects Facility (REF) of the Intense Pulsed Neutron Source (IPNS) became operational in July 1981. Fluence and damage parameters are given for the vertical thimble (VT2) and rabbit irradiation tubes.

3. Heliun Production in ORR MFE 4A Nickel (RIES) 24

A series of analyses has been performed on om of the nickel dosimetry wires removed from the ORR MFE-4A experiment.

CONTENTS (Cont'd)

Page

4. Heliun Generation Cross Sections for 14.8 MeV Neutrons (RIES) 28

The total heliwn generation cross sections have been measured for V, Fe, Ni, Cu, Zr, Nb, Mo, Au and the separated isotopes of Fe, Ni, Cu, and Mo irradiated in RTNS-II. The results are presented along with the previous cross-section measurements made as part of two RTNS-I experiments.

5. Helium Generation Cross Sections for Be(d,n) Neutrons (RIES) 34

Helium analyses have been completed for the Fe, Ni, and Cu isotopes irradiated in the Be(d,n) neutron field, and average integral cross sections huve been determined for all of the Be(d,n)-irradiated materials analyzed to date.

6. Measurements of the $^{27}Al(n,2n)^{26}Al$ Cross Section (ANL) 39

A new technique, AMS (accelerator mass spectrometry), was used to measure the (n,2n) cross section in aluminum. The experimentally measured cross section was found to be approximately one half the theoretically calculated cross section presently being used in neutron damage calculations.

7. Nuclear Data Applications in Radiation Damage Studies (HEDL) 50

Vanadium was added to the nuclear cross section library associated with the transmutation code REAC.

The damage energy cross sections and helium production from ENDF/B-V for 25 materials were processed with the NJOY code.

CONTENTS (Cont'd)

8. Reflection of Low Energy Helium Atoms From Tungsten Surfaces (ORNL) 53

The computer program MARLOWE (Version 11.5) has been used to simulate the reflection of 8 eV to 1.5 keV heliwn atoms from monocrystalline, polycrystalline, and amorphous tungsten targets. Comparisons of calculated and measured ion ranges indicate that the electronic stopping cross section of low energy heliwn atoms in tungsten is significantly greater than the traditional LSS value. The reflection coefficients calculated for the <001> surface are in fair agreement with experiment.

9. Radiation Damage Studies (U. of Wisconsin) 66

Range and damage calculations with the new Monte Carlo computer program HERAD shows improved agreement with recent range and damage experimental data. The effect of voids developed during irradiation is included. A parameter study indicates that the electronic stopping cross section of low energy He in Ni is significantly lower than the traditional LSS value.

CHAPTER 3: FUNDAMENTAL MECHANICAL BEHAVIOR

1. Environmental Effects on Fracture of Fusion Reactor Materials (PNL) 81

The known stress corrosion and corrosion fatigue fracture processes in austenitic and ferritic steels are reviewed with an emphasis on aqueous and liquid metal environments. Possible effects of irradiation are discussed and precautions are given for the use of austenitic and ferritic stainless steels in fusion reactor environments. Finally, an approach to modeling the environmental effect on the local fracture toughness at the tip of a crack is given.

CONTENTS (Cont'd)

CHAPTER 4: CORRELATION METHODOLOGY

1. Fusion Swelling Predictions From a Model-Based Fission-Fusion-Fission Interpolation (UCSB) 97

The helium/dpa (He/dpa) ratio in stainless steel under fusion conditions will be about 30 times greater than in EBR-II and about 7 times less than in HFIR. A rate theory model that explicitly considers some potential He/dpa ratio effects has been calibrated using data from both EBR-11 and HFIR. Application of the model to fusion conditions indicates that simple extrapolations of swelling data from either EBR-11 or HFIR may not be valid.

2. Helium Bubble Formation and Swelling in Metals (U. of Wisconsin, HEOL) 114

The effect of continuous production of helim on swelling is analyzed using an improved equation of state for gaseous helim that incorporates both a gas-kinetic as well as a static pressure for densely packed helim. At high temperatures, bubbles grow by thermal vacancy emission at dislocations and their absorption at cavities. For high He/dpa ratios, bubbles remain overpressurized, and swelling is less than if equilibrium is assmed. At low temperatures, swelling or void growth driven by a modest bias is always larger than bubble swelling, and helim has no effect on the swelling rate.

3. The Radiation-Induced Evolution of AISI 316 (DO-Heat) in HFIR and EBR-II (HEDL) 127

Examination of a HFIR-irradiated specimen at 42 dpa shows that the dislocation and phase evolution are consistent with that of comparable EBR-II irradiated material but that the void densities are higher. Microchemical analyses show that evolution is in progress

Page

at 42 dpa and it is expected that the swelling rate will increase at higher fluence.

4. Miqration and Trapping of Heliun by Cavities and Dislocations in Dual Ion Irradiated Stainless Steels (W-R&D) 142

The results of dual ion experiments suggest that approximately 99 percent of the helim is in visible cavities near the peak swelling temperature. Numerical calculations of helim partitioning based on cavity and dislocation sink strengths for vacancies are shown to over-estimate the number of gas atoms associated with dislocations, and to reduce the maximum possible equilibrium bubble size by a factor of two.

5. Bubble Growth Kinetics Associated With Irradiated and Postirradiation Annealed Metals (U. of Virginia) 155

During in-situ observations of the irradiation of chemical vapor deposited Ni films with He ions, it was found that the growth rate of bubbles on the grain boundary increased up to 4.5 times that of bubbles growing in the grain interior. Neighboring bubbles on a grain boundary were dynamically seen shrinking and growing in volume exchange patterns when the He-irradiated Ni was annealed. The annealing of He irradiated 316 stainless steel specimens showed that bubbles grew in underpressurized states as well as in overpressurized states; the overpressurized bubbles were found to grow more rapidly than underpressurized bubbles.

6. Single- and Dual-Ion Irradiations of Ferritic Alloys and Type 316 Stainless Steel (ANL) 167

Ferritic alloys were single- and dual-ion irradiated to isolate the effects of nickel additions and helium; 316 SS was irradiated for studies of helim injection schedule and prior thermomechanical treatment. Specimens have not yet been analyzed.

CONTENTS (Cont'd)

Page

7. Further Examination of Swelling of "Pure" AISI 316 Irradiated in DRR (HEDL), 172

Examination of additional specimens of Fe-17Cr-16.7Ni-2.5Mo corroborate the previously reported result that cold working of this "pure" 316 alloy has no influence on suppressing void formation.

Density change and aging studies indicate that swelling exists in the form of unresolvable voids in specimens of this alloy preinjected with 40 appm heliwn.

8. The Effect of Applied Stress on Precipitate Stability in Irradiated AISI 316 (MIT, HEDL) 180

A particular state of applied stress may either stabilize, destabilize, or have no effect on a particular phase, depending on the transformation strain.

Shear stresses can alter precipitation as effectively as hydrostatic stresses. It appears, however, that the acceleration of swelling of AISI 316 by applied stress at high temperature is accomplished by the hydrostatic and not the deviatoric components.

9. Measurement and Calculation of Solid Transmutants Formed in AISI 316 (HEDL) 198

A reassessment of the calculation of two transmutation products produced in HFIR irradiations of AISI 316 has shown that the inclusion of all competing reactions leads to changes in the predicted concentrations. The peak vanadium level is reduced somewhat from what was reported earlier, but not enough to dismiss it as a potential determinant of alloy behavior. The

Page

copper level has been increased substantially, but not enough to influence the swelling of AISI 316.

10. A Model for the Evolution of Network Dislocation Density in Irradiated Metals (U. of Wisconsin, HEDL) 210

A model has been developed to explain the relative insensitivity of network dislocation density in irmdiated metals at high fluence to starting microstructure, temperature, stress and displacement rate. The model also explains how the rate of approach to saturation can be sensitive to flux and temperature while the saturation level itself is not dependent on temperature.

11. The Microstructural Origins of Yield Strength Changes in AISI 316 During Fission or Fusion Irradiation (HEDL) 220

The changes in yield strength of AISI 316 irradiated in fast reactors have been successfully modeled in tens of concurrent changes in microstructural components. Extrapolation to anticipated fusion behavior based on microstructural cmparisons leads to the conclusion that the primary influence of transmutational differences in non-pulsed environments is to alter the tmnsient behavior and not the saturation level of yield strength.

12. Canpositional Dependence of Radiation-Induced Change in Dimensional and Physical Properties of Fe-Cr-Ni Austenitic Alloys (U. of Wisconsin, HEDL) 234

Nickel segregates to void embryos in these alloys, increasing the nickel level at their surfaces, and leading to changes in their interstitia2 capture efficiency. This leads to changes in the void nucleation rate and the duration of the transient regime of swelling.

FIGURES

Page

CHAPTER 2

1. Fission Reactor Dosimetry (ANL)

FIGURE 1. Adjusted Flux Spectrum for EBR-II-X287 Experiment. 13

FIGURE 2. Calculated Fluence Gradients are Compared to Measurements at Twelve Locations Within the EBR-II-X287 Experiment. 13

2. Characterization of Spallation Neutron Sources (ANL)

FIGURE 1. Measured Energy Spectrun for Position VT2. 19

FIGURE 2. Measured Energy Spectrum for the Rabbit. 19

FIGURE 3. Vertical Flux Gradients in the Verticle Thimble 2 of IPNS-REF. 21

FIGURE 4. Horizontal Flux Gradients Measured in the Center of the IPNS-REF Rabbit Tube. 21

6. Measurement of the $^{27}Al(n,2n)^{26}Al$ Cross Section (ANL)

FIGURE 1. Systematic Layout of the Argonne FN Tandem Accelerator and Experimental Systems Used in the Accelerator Mass Spectrometry (AMS) Measurements. 43

FIGURE 2. A Comparison of the Theoretical Cross Section for the $^{27}Al(n,2n)^{26}Al$ Reaction Presently Used in Damage Calculations. 46

8. Reflection of Low Energy Helium Atoms From Tungsten Surfaces (ORNL)

FIGURE 1. Particle Reflection Coefficients Calculated for "He Ions Normally Incident on Various Tungsten Surfaces, Compared with Experiments. 57

FIGURE 2. Ranges Calculated for ^{4}He Ions Normally Incident on Various Tungsten Surfaces, Compared with Experiments. 59

FIGURES (Cont'd)

Page

FIGURE 3. The Calculated Effect of the Angle of Incidence on the Reflection of ^4He Ions From Tungsten Surfaces. 60

9. Radiation Damage Studies (U. of Wisconsin)

FIGURE 1. The Projected Range for 5, 15, 30, and 60 keV Sb-Si. 69

FIGURE 2. The Damage Distribution for 14 MeV Cu on Void-Free Nickel Target. 71

FIGURE 3. The Damage Energy for 14 MeV Cu Ions Incident on Nickel Target Containing Voids. 73

FIGURE 4. The Swelling and the Damage Profiles for 20 keV He Ions on Ni; With Different Electronic Stopping Used in HERAD. 74

CHAPTER 4

1. Fusion Swelling Predictions From a Model-Based Fission-Fusion-Fission Interpolation (UCSB)

FIGURE 1. Schematic Plot of Cavity Growth Rate (r). 102

FIGURE 2. Comparison of Observed and Predicted Void Densities (N_V). 103

FIGURE 3. Temperature Dependence of Dislocation Density and Sub-Grain Size. 103

FIGURE 4. Comparison Between Observed and Predicted Fluence Dependence of Swelling in EBR-2 and HFIR at Two Temperatures. 106

FIGURE 5. Canparison Between Observed and Predicted Temperature Dependence of Swelling in HFIR. 107

FIGURE 6. Predicted Fluence Dependence of Swelling Under Fusion Conditions. 109

FIGURE 7. Temperature Dependence of Swelling Parameters Under Fusion Conditions as Normalized to Fast Reactor Predictions. 110

FIGURES (Cont'd)

Page

2. Helium Bubble Formation and Swelling in Metals (U. of Wisconsin, HEDL)

FIGURE 1. Void Number Densities in Stainless Steels. 118

FIGURE 2. Compressibility Factor for Gaseous Heliun. 119

FIGURE 3. Swelling for He/dpa Ratios of 70 (a,b,c) and 1 (d) After 100 appm He is Produced. 122

FIGURE 4. Swelling for He/dpa Ratio of 70 After 1000 appm He is Produced. 122

FIGURE 5. Swelling for He/dpa Ratio of 70 After 10,000 appm He is Produced. 123

3. The Radiation-Induced Evolution of AISI 316 (DO-Heat) in HFIR and EBR-II (HEDL)

FIGURE 1. Near-Precipitate Composition Profiles Measured for $M_{23}C_6$ in 20% Cold-Worked DO-Heat Specimen Irradiated at 620°C to 75 dpa in EBR-II. 131

FIGURE 2. Near-Precipitate Composition Profiles Measured for Laves in 20% Cold-Worked 00-Heat Specimen Irradiated at 620°C to 75 dpa in EBR-II. 131

FIGURE 3. Near-Precipitate Composition Profiles Measured for Another Laves Precipitate in 20% Cold-Worked DO-Heat Specimen Irradiated at 620°C to 75 dpa in EBR-II. 132

FIGURE 4. Tvoical Void Microstructures Observed in 20% Cold-Worked DO-Heat Specimen Irradiated at 550°C (Nominal) to 42 dpa in HFIR. 133

FIGURE 5. Near-Precipitate Composition Profiles Measured for Laves in the HFIR Irradiated Specimen Shown in Figure 4. 135

FIGURE 6. Nickel and Silicon Levels Measured at Various Points in the Matrix of the HFIR Irradiated Specimen. 136

FIGURE 7. Comparison of Annealed and Cold-Worked DO-Heat in HFIR With That of Cold-Worked DO-Heat in EBR-II. 138

FIGURES (Cont'd)

FIGURE 8. Comparison of Composite Swelling Curve for 20% Cold-Worked DO-Heat With Predictions Based on HFIR Data Only and Rate Theory Principles. 138

4. Migration and Trapping of Helium by Cavities and Dislocations in Dual Ion Irradiated Stainless Steels (W-R&D)

FIGURE la. Experimental Cavity Size Distribution for 304 SS Following Dual Ion Bombardment at 600°C to 6 dpa and 782 appn Heliun. 148

FIGURE lb. Maximum Equilibriun Bubble Diameter for the Distribution Shown in Figure la for Various Choices of Van der Waals Constant. 148

FIGURE lc. Effect of Surface Energy (mJ/m^2) and Helium Concentration on the Calculated Maximun Equilibrium Bubble Diameter for the Distribution in Figure la. 148

FIGURE 2. Fraction of Implanted Heliun Atoms Numerically Partitioned to Dislocations ($1 - Q^{-1}$) as a Function of the Measured Dislocation Density for Dual Ion Bombarded 316 SS in the Solution Annealed, 20% Cold-Rolled or Aged (800°C) Condition. 150

FIGURE 3. Cavity Size Distribution for 304 SS Dual Ion Bombarded to 1.1 dpa and 117 appm He at 700°C Followed by Bombardment Without Heliun to 3.3 dpa at 500°C. 151

FIGURE 4. Comparison of Calculated Maximun Equilibrium Bubble Sizes Calculated From Dual Ion Data Assuning all Helium Partitioned to Cavities ($Q^{-1} = 1$) or a Portion to Dislocations ($Q^{-1} < 1$). 152

5. Bubble Growth Kinetics Associated With Irradiated and Postirradiation Annealed Metals (U. of Virginia)

FIGURE 1. Bubble Radius Versus Irradiation Time for Grain Boundary Bubbles in Nickel Under Continuous Observation. 161

FIGURE 2. Swelling and Ratio of Implanted Helium to Helium in Equilibriun Bubbles Versus Annealing Time for Type 316 Stainless Steel as Calculated From Data of Braski et al. 162

FIGURES (Cont'd)

Page

7. Further Examination of Swelling of "Pure" AISI 316 Irradiated in ORR (HEDL)

FIGURE 1. Void Microstructure in Annealed and 20% Cold-Worked Fe-17Cr-16.7Ni-2.5Mo Irradiated in ORR at 550°C to 3 to 5 dpa. 175

FIGURE 2. Effect of Foil Thickness of Number Density of Visible Voids. 177

9. Measurements and Calculations of Solid Transmutants Formed in AISI 316 (HEDL)

FIGURE 1. Predicted Vanadiun Concentration in AISI 316 as a Function of Exposure for Various Reactors. 200

FIGURE 2. Comparison of Predictions of Vanadium Concentration Produced in AISI 316 During Irradiation in the PTP Position of HFIR with and Without Burnout of Vanadiun. 201

FIGURE 3. Predicted Changes in Manganese Concentration in AISI 316 in Various Reactors. 203

FIGURE 4. Predicted Time Histories of ^{58}Ni, ^{60}Ni, and ^{61}Ni in Pure Nickel Irradiated in the PTP Position of HFIR. 204

FIGURE 5. Predicted Time History of ^{59}Ni in Pure Nickel Irradiated in the PTP Position of HFIR. 205

FIGURE 6. Predicted Time Histories of ^{62}Ni, ^{63}Ni, ^{64}Ni, and ^{65}Cu in Pure Nickel Irradiated in the PTP Position of HFIR. 206

FIGURE 7. Dependence on Copper Content and Temperature of Density Change of Annealed AISI 316 Irradiated in EBR-II. 207

FIGURE 8. Void Formation in Copper-Modified AISI 316 Alloys in the Annealed Condition. 208

10. A Model for the Evolution of Network Dislocation Densitv in Irradiated Metals (U. of Wisconsin, HEDL)

FIGURE 1. Schematic Representation of Correlated Movement of Dislocation Pairs (Dipoles). 212

FIGURES (Cont'd)

Page

FIGURE 2. Predictions of the Evolution of Dislocation Density in AISI 316 at 500°C for Starting Densities of 7 x 10^{11} cm/cm^3 and 4 x 10^8 cm/cm^3, Chosen to Represent Cold-Worked and Annealed Conditions. 217

FIGURE 3. Calculation of Dislocation Climb Velocity V at 500°C for Several Values of Bias Difference Between Dislocations in Different Configurations. 218

11. The Microstructural Origins of Yield Strength Changes in AISI 316 During Fission or Fusion Irradiation (HEDL)

FIGURE 1. Yield Strength of 20% Cold-Worked AISI 316 After Irradiation in EBR-II. 223

FIGURE 2. Yield Strength of Irradiated AISI 316 at Temperatures of 427, 538, and 650°C. 224

FIGURE 3. Yield Strength of Unirradiated AISI 316. 227

FIGURE 4. Comparison of Microstructurally-Based Predictions With Yield Stress Measurements of AISI 316. 228

12. Compositional Dependence of Radiation-Induced Chanses in Dimensional and Physical Properties of Fe-Cr-Ni Austenitic Allovs (U. of Wisconsin, HEDL)

FIGURE 1. Compositional Dependence of Lattice Parameter Measured for Fe-Ni-Cr Alloys at Room Temperature. 237

FIGURE 2. Compositional Dependence of Shear Modulus Measured for Fe-Ni-Cr Alloys at Room Temperature. 237

FIGURE 3. Calculated Effect of Lattice Parameter Mismatch on the Void Nucleation Rate at 500°C for Shell Thicknesses of 10% and 20% of the Void Radius. 239

FIGURE 4. Calculated Effect of Shear Modulus Difference on the Void Nucleation Rate at 500°C for Shell Thicknesses of 10% and 20% of the Void Radius. 239

FIGURE 5. Influence of Nickel Content on Swelling Behavior on Fe-15Cr-XNi Alloys at 675°C When Bombarded with 5 MeV N_i + Ions. 241

FIGURE 6. Compositional Dependence of Excess Free Energy at 1472°K in Fe-Cr-Ni Alloys. 241

TABLES

Page

CHAPTER 2

1. Fission Reactor Dosimetry (ANL)

TABLE 1. Status of Reactor Experiments 9

TABLE 2. Activation Rates for EBR-II-X287 Experiment 10

TABLE 3. Neutron Fluences for EBR-II-X287 12

TABLE 4. Damage Parameters for EBR-II-X287, Capsules D and B 14

TABLE 5. Damage Parameters for EBR-II-X287, Capsules F and C 15

2. Characterization of Spallation Neutron Sources (ANL)

TABLE 1. Integral Flux Values for IPNS-REF 20

TABLE 2. Damage Parameters for IPNS (REF) 22

3. Helium Production in ORR MFE-4A Nickel (RIES)

TABLE 1. Measured Helium Concentrations for ORR MFE-4A Nickel Dosimetry Wire 26

4. Helium Generation Cross Sections for 14.8 MeV Neutrons (RIES)

TABLE 1. Heliun Generation Cross Sections for ∿14.8 MeV Neutrons 30

5. Heliun Generation Cross Sections for Be(d,n) Neutrons (RIES)

TABLE 1. Integral Helium Generation Cross Sections for the ∿0-32 MeV Be(d,n) Neutron Spectrum Produced by 30 MeV Deuteons 36

6. Measurements of the $^{27}Al(n,2n)^{26}Al$ Cross Section (ANL)

TABLE 1. Preliminary Results From the RTNS Foils for the $^{27}Al(n,2n)^{26}Al$ Reaction 47

TABLES (Cont'd)

Page

TABLE 2. Preliminary Results from the U. of C. at Davis Foils [Be(d,n) Neutrons] for the ^{27}Al (n,2n) ^{26}Al Reaction 47

8. Reflection of Low Energy Heliun Atoms From Tungsten Surfaces (ORNL)

TABLE 1. Effects of Thermal Displacements on Mean 'He Penetration Depths in W <001> Crystals 61

TABLE 2. Effects of Thermal Displacements on Mean 'He Penetration Depths in W <011> Crystals 61

9. Radiation Damage Studies (U. of Wisconsin)

TABLE 1. Comparison Between HERAD Results and the Experimental Results of Combasson et al. for Eu, Gd, Tb, and Oy Ions in Silicon 70

CHAPTER 4

1. Fusion Swelling Predictions From a Model-Based Fission-Fusion-Fission Interpolation (UCSB)

TABLE 1. Rate Theory Parameters 105

4. Migration and Trapping of Heliun bv Cavities and Dislocations in Dual Ion Irradiated Stainless Steels (W-R&D)

TABLE 1. Effect of Fluence on the Fraction of Implanted Heliun (Q^{-1}) Nunerically Partitioned to Cavities for 304 SS Dual Ion Bombarded at 600°C and 2 x 10^{-4} dpa/s 149

5. Bubble Growth Kinetics Associated With Irradiated and Postirradiation Annealed Metals (U. of Virginia)

TABLE 1. Microstructural Parameters for Helium Irradiated Nickel 158

TABLE 2. Microstructural Parameters for Heliun Irradiated Type 316 Stainless Steel 160

TABLE 3. Ratio of Implanted Helium to Heliun in Equilibriun Bubbles for Type 316 Stainless Steel 161

TABLES (Cont'd)

Page

6. Sinqle- and Dual-Ion Irradiations of Ferritic Alloys and Type 316 Stainless Steel (ANL)

TABLE 1. Irradiation Conditions for Ferritic Alloys 171

7. Further Examination of Swelling of "Pure" AISI 316 Irradiated in ORR (HEDL)

TABLE 1. Void Formation in Fe-17Cr-16.7Ni-2.5Mo Specimens 174

8. The Effect of Applied Stress on Precipitate Stability in Irradiated 316 SS (MIT, HEDL)

TABLE 1. Summary of Crystallographic Data of Precipitate Phases in 316 Stainless Steels 193

CHAPTER 1

IRRADIATION TEST FACILITIES

RTNS-II IRRADIATIONS AND OPERATIONS

C. M. Logan and D. W. Heikkinen (Lawrence Livermore National Laboratory)

1.0 Objective

The objectives of this work are operation of OFE's RTNS-II (a 14-MeV neutron source facility), machine development, and support of the experimental program that utilizes this facility. Experimenter services include dosimetry handling, scheduling, coordination, and reporting. RTNS-II is dedicated to materials research for the fusion, power program. Its primary use is to aid in the development of models of high-energy neutron effects. Such models are needed in interpreting and projecting to the fusion environment engineering data obtained in other neutron spectra.

2.0 Summary

Irradiations were performed on a total of six different experiments. No major unscheduled outages occurred. Approximately two weeks of scheduled outage was used for 50-cm target testing.

3.0 Program

Title: RTNS-II Operations (WZJ-16)
Principal Investigator: C. M. Logan
Affiliation: Lawrence Livermore National Laboratory

4.0 Relevant DAFS Program Plan Task/Subtask

TASK II.A.2,3,4.
TASK II.B.3,4.
TASK II.C.1,2,6,11,18.

5.0 Accomplishments and Status

5.1 Irradiations - C. M. Logan, D. W. Heikkinen and M. W. Guinan (LLNL)

An irradiation of Nb, Ti, and V samples to a total fluence of 2.0 x 10^{18} n/cm^2 was completed for R. Bradley (PNL). An irradiation of Cu for resistivity measurements was done for S. Zinkle (Univ. of Wisconsin). The peak fluence was 2.3 x 10^{17} n/cm^2. An irradiation of Mica samples for J. Fowler (LANL) was begun. The fluence requirement is 10^{18} n/cm^2. "Piggy-back" experiments were done for Logan-Heikkinen (LLNL) on thermocouple wires, L. Coleman (LLNL) on laser glasses, and R. Jalbert (LANL) for tritium detector development.

5.2 RTNS-II Status - C. M. Logan and D. W. Heikkinen (LLNL)

There were no major unscheduled outages during this quarter. Approximately two weeks of outage were scheduled for mechanical and electrical testing of the 50-cm target system. This was done to prepare for installation of a 50-cm target on the operating RTNS-II neutron source. The 50-cm target has operated at 5000 rpm and high vacuum for ∿ 250 hrs with no problems encountered.

6.0 Future Work

Irradiations are scheduled for W. Barmore (LLNL), J. Fowler (LANL), D. Kaletta (Karlsruhe), M. Guinan (LLNL), D. Nethaway (LLNL) and H. Vonach (Vienna).

7.0 Publications

RTNS-II Facility and Experiments, C. M. Logan and D. W. Heikkinen, (UCRL 86699) to be presented at the International Conference on Neutron Irradiation Effects, Argonne National Laboratory, Nov. 9-12, 1981.

Irradiations at RTNS-II, D. W. Heikkinen and C. M. Logan, (UCRL 86747) to be presented at the Fast, Thermal, and Fusion Reactor Experiments Conference, Salt Lake City, April 12-15, 1982.

Electroforming Copper Targets for RTNS-II, W. K. Kelley, J. W. Dini and C. M. Logan, (UCRL 84922) presented at American Electroplates Society SUR/FIN '81, Boston, June 28–July 2, 1981.

CHAPTER 2

DOSIMETRY AND DAMAGE PARAMETERS

FISSION REACTOR DOSIMETRY

L. R. Greenwood (Argonne National Laboratory)

1.0 Objective

To establish the best practicable dosimetry for fission reactors and to provide routine dosimetry and damage analysis for OFE experiments.

2.0 Summary

Analysis has been completed for the EBRII-X287 experiment. Fluence and damage maps are presented. Dosimeters have been provided for several new experiments in HFIR.

3.0 Program

Title: Dosimetry and Damage Analysis
Principal Investigator: L. R. Greenwood
Affiliation: Argonne National Laboratory

4.0 Relevant DAFS Program Plan Task/Subtask

Task II.A.l Fission Reactor Dosimetry

5.0 Accomplishments and Status

The status of all fission reactor dosimetry is given in Table 1.

5.1 Dosimetry for the EBRII-X287 Irradiation

The EBRII-X287 experiment was irradiated in Row 7 from January 1977 to November 1978 for a total exposure of 30,496 MWD. Most of the exposure was in position 7A4 during runs 87A-95H (25,000 MWD). The experiment was then moved

to position 7E3 for runs 96A-97G (5000 MWD). The average operating power was 62.5 MW.

TABLE 1

STATUS OF REACTOR EXPERIMENTS

Facility/Experiment		Status and Comments
ORR	- MFE1	Completed 12/79
	- MFE2	Completed 6/81
	- MFE4A	Completed 8/81
	- MFE4B,C	Irradiation in Progress
	- TBC07	Completed 7/80
	- TRIO	Planning in Progress
HFIR	- CTR 32	Samples Received 5/81
	- CTR 30, 31	Irradiation in Progress
	- CTR 34, 35	Samples Provided 9/81
	- T1,T2	Irradiation in Progress
	- T3	Samples Provided 9/81
	- RB1, 2, 3	Samples Provided 9/81
Omega West	- Spectral Analysis	Completed 10/80
	- HEDL1	Completed 5/81
EBR II	- X287	Completed 9/81

Twelve dosimetry capsules were irradiated, three each in subassemblies 8, C, D, and F. Ten reactions were measured from each dosimetry capsule which contained Fe, Ni, Co, Cu, Nb, Sc, Ti, ^{235}U, and ^{238}U. The activation results are reported in Table 2.

Burnup corrections were required for the $^{235}U(n,f)$ reaction. The corrections varied from 5-7% depending on the flux at each location. Corrections were also required for the ^{238}U and ^{237}Np fission reactions due to the production and subsequent fission of ^{239}Pu in the samples. In this case, it can be shown that the correction for each fission product has the form:

TABLE 2

ACTIVATION RATES FOR EBRII-X287 EXPERIMENT

Values normalized to 62.5 MW. Accuracy ±2% except ^{238}U (±10%) and ^{237}Np (5%).

	σφ (atom/atom-s)					
	D (R = 30 cm)			B (R = 31.6 cm)		
Reaction Z,cm:	-17.1	-0.44	+16.2	-11.4	+5.1	t15.3
$^{59}Co(n,\gamma)^{60}Co$ (x 10^{-11})	18.22	4.87	6.80	-	5.39	-
$^{45}Sc(n,\gamma)^{46}Sc$ (x 10^{-11})	3.24	2.67	2.77	2.86	-	2.69
$^{54}Fe(n,p)^{54}Mn$ (x 10^{-11})	1.13	2.38	1.77	1.73	-	1.54
$^{58}Ni(n,p)^{58}Co$ (x 10^{-11})	1.48	3.26	2.33	2.49	-	-
$^{60}Ni(n,p)^{60}Co$ (x 10^{-13})	2.65	5.90	4.19	4.43	-	-
$^{46}Ti(n,p)^{46}Sc$ (x 10^{-12})	1.33	2.88	2.24	2.16	-	1.73
$^{63}Cu(n,\alpha)^{60}Co$ (x 10^{-14})	6.81	14.42	9.83	10.15	-	10.66
$^{235}U(n,f)$ (x 10^{-9})	2.65	2.46	2.14	2.35	2.41	2.15
$^{238}U(n,f)$ (x 10^{-11})	6.96	11.52	8.38	8.72	10.23	7.42
$^{237}Np(n,f)$ (x 10^{-10})	5.68	8.58	6.38	7.07	7.60	5.45

	F (R = 33.6 cm)			C (R = 34.0 cm)		
Z,cm:	-17.1	-0.44	+16.2	-11.4	+5.1	+15.3
$^{59}Co(n,\gamma)^{60}Co$ (x 10^{-11})	21.22	7.38	10.68	-	-	11.08
$^{45}Sc(n,\gamma)^{46}Sc$ (x 10^{-11})	3.33	2.80	2.91	2.98	2.95	2.84
$^{54}Fe(n,p)^{54}Mn$ (x 10^{-11})	0.88	1.92	1.23	1.39	1.47	1.14
$^{58}Ni(n,p)^{58}Co$ (x 10^{-11})	1.30	2.90	1.96	1.89	2.22	1.75
$^{60}Ni(n,p)^{60}Co$ (x 10^{-13})	2.03	4.38	3.10	3.01	3.58	3.45
$^{46}Ti(n,p)^{46}Sc$ (x 10^{-12})	1.14	2.58	1.67	1.63	1.75	1.39
$^{63}Cu(n,\alpha)^{60}Co$ (x 10^{-14})	5.11	10.54	7.48	7.30	7.52	6.60
$^{235}U(n,f)$ (x 10^{-9})	2.62	2.42	1.93	2.48	2.43	2.23
$^{238}U(n,f)$ (x 10^{-11})	6.16	9.47	6.36	7.25	-	6.32
$^{237}Np(n,f)$ (x 10^{-10})	4.72	7.68	5.05	6.09	6.15	4.83

$$(\sigma\phi)_1 = (\sigma\phi)_0 \, (1 - k_i \, R_i) \qquad (1)$$

where $(\sigma\phi)_0$ is the uncorrected activation rate, $(\sigma\phi)_1$ is the true reaction rate, R_i is the ratio of fission yields for product i from Pu divided by U, and k is a constant for any given location dependent on the production and fission rates for Pu. Fortunately, three fission products were measured for each reaction, namely ^{106}Ru, ^{137}Cs, and ^{144}Ce. A computer program was then written to vary the parameter k in equation (1) for each case until the three fission products gave values of $(\sigma\phi)_1$ with the smallest standard deviation. The corrections varied smoothly with the flux level and ranged from 0.71 to 0.79 for $^{238}U(n,f)$ and from 0.85 to 0.97 for $^{237}Np(n,f)$. The absolute accuracy of the corrected activation rates is estimated to be ±10% for ^{238}U and ±5% for ^{237}Np. No other corrections were required for the remaining reactions.

The STAYSL computer code was used to adjust the calculated[1] neutron spectrum at each location. Reasonable fits were obtained using an input spectrum at a radius of 31.0 cm for capsules B and D and one of 33.7 cm for capsules C and F. In each case, these values are within 1 cm of the center of each capsule. Calculations were also available for positions within 1 cm of the vertical height (Z) of each capsule. In all cases, the measurements agreed rather well with the calculated spectra, especially considering the steep flux gradients across the assembly.

The final integral fluence values are listed in Table 3. A typical adjusted flux spectrum is shown in Figure 1. Fluence gradients are shown in Figure 2.

Damage calculations were performed using our recently revised ENDF/B-V cross section file. DPA and helium production rates are given for each dosimetry capsule position in Tables 4 and 5. The DPA for 316 SS ranges from 15 to 27 with a corresponding helium production between 3 and 8 appm.

TABLE 3

NEUTRON FLUENCES FOR EBRII-X287

Fluence x 10^{22} n/cm^2. Percent errors are listed in parentheses.

		Total Fluence			
		D	B	F	C
Z,cm	R,cm:	30.0	31.6	33.6	34.0
-17.1		5.47 (10)	-	5.00 (10)	-
-11.4		-	6.05 (15)	-	5.72 (10)
-0.4		6.73 (8)	-	6.16 (9)	-
+5.1		-	6.76 (15)	-	5.86 (9)
+15.3		-	5.02 (14)	-	4.68 (10)
+16.2		5.14 (9)	-	4.36 (9)	-
		Fluence >0.11 MeV			
-17.1		4.16 (14)	-	3.66 (15)	-
-11.4		-	4.95 (12)	-	4.50 (13)
-0.4		5.75 (11)	-	5.08 (12)	-
+5.1		-	5.13 (12)	-	4.69 (13)
+15.3		-	3.93 (13)	-	3.51 (14)
+16.2		4.04 (12)	-	3.25 (13)	-
		Fluence >1.0 MeV			
-17.1		0.82 (13)	-	0.69 (13)	-
-11.4		-	1.08 (12)	-	0.90 (12)
-0.4		1.38 (12)	-	1.15 (12)	-
+5.1		-	1.20 (12)	-	0.97 (13)
+15.3		-	0.86 (12)	-	0.72 (13)
+16.2		0.96 (12)	-	0.74 (12)	-

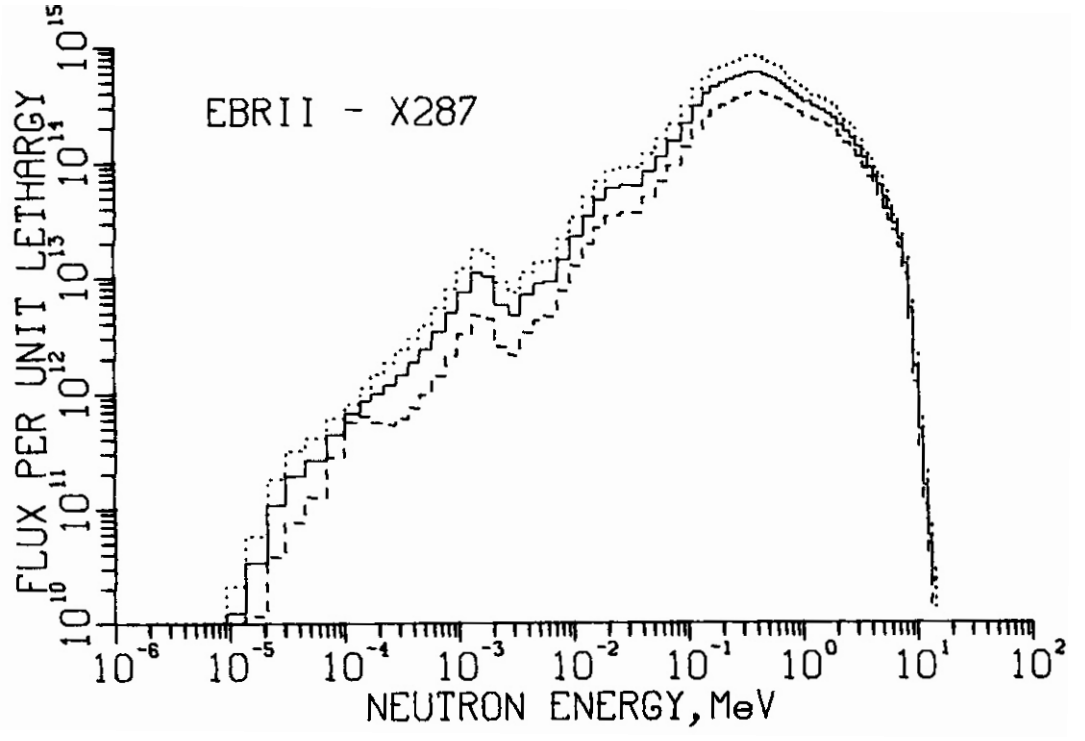

FIGURE 1. Adjusted Flux Spectrum for EBRII-X287 Experiment. Capsule D is Shown at Midplane. This is the Highest Flux Observed at (R,Z) Coordinates of (30.0, -0.4) cm. The Dotted and Dashed Lines Represent One Standard Deviation.

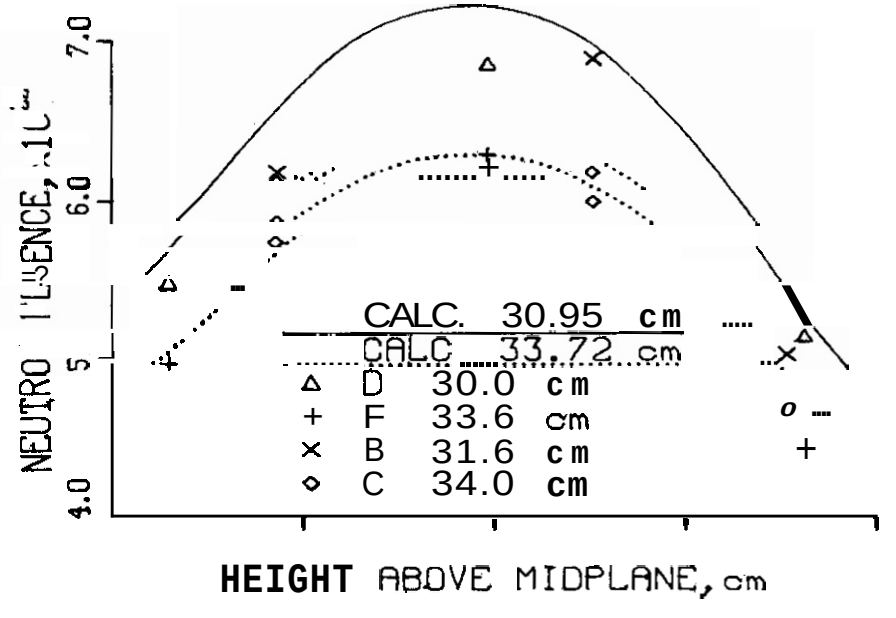

FIGURE 2. Calculated Fluence Gradients (Solid and Dotted Lines) Are Compared to Measurements at Twelve Locations Within the EBRII-X287 Experiment. As Can Be Seen, All Measurements Agree Absolutely Within the Estimated Error of ±10%.

TABLE 4

DAMAGE PARAMETERS FOR EBRII-X287

OPA (±10%); He in appm (±15%)

	Capsule 0 (R = 30.0 cm)					
Z:	-17.1 cm		-0.4 cm		+16.2 cm	
Element	DPA	He	DPA	He	DPA	He
Al	41.1	3.12	58.9	6.33	41.5	4.16
Ti	17.7	4.81	26.7	9.02	19.0	6.37
V	23.4	0.066	34.1	0.13	24.3	0.082
Cr	19.7	0.77	29.4	1.62	20.9	1.13
Mn	21.4	0.60	31.3	1.21	22.3	0.82
Fe	17.7	1.42	26.6	3.03	18.7	2.06
co	19.4	0.66	28.5	1.35	20.1	0.93
Ni	20.4	25.71	29.8	55.86	21.1	39.58
Cu	18.3	1.20	27.0	2.49	19.1	1.64
Zr	22.0	0.12	32.2	0.26	22.6	0.17
Nb	20.0	0.29	29.6	0.61	20.7	0.42
Mo	14.7	-	21.1	-	15.1	-
Ta	4.8	-	7.3	-	5.1	-
316 SS	18.3	3.70	27.4	7.99	19.3	5.60
	Capsule 8 (R = 31.6 cm)					
2:	-11.4 cm		+5.1 cm		+15.3 cm	
Al	49.8	4.66	53.2	4.53	39.5	4.67
Ti	22.0	6.90	24.7	7.44	17.8	5.77
V	28.6	0.097	31.0	0.095	22.9	0.095
Cr	24.5	1.21	26.5	1.22	19.6	1.15
Mn	26.2	0.91	28.5	0.88	21.0	0.90
Fe	22.0	2.18	23.7	2.16	17.6	2.16
co	23.8	1.03	25.8	1.01	19.0	1.00
Ni	24.9	40.83	26.9	41.91	20.0	37.65
Cu	22.5	1.82	24.3	1.76	18.0	1.81
Zr	27.0	0.19	28.8	0.18	21.4	0.18
Nb	24.7	0.45	26.2	0.44	19.6	0.44
Mo	17.8	-	19.4	-	14.3	-
Ta	6.0	-	6.5	-	4.8	-
316 SS	22.7	5.82	24.5	5.92	18.2	5.48

TABLE 5

DAMAGE PARAMETERS FOR EBRII-X287

DPA (±10%); He in appm (±15%)

	Capsule F (R = 33.6 cm)					
Z:	-17.1 cm		-0.4 cm		+16.2 cm	
Element	DPA	He	DPA	He	OPA	He
Al	35.8	2.30	51.4	4.50	33.4	3.10
Ti	15.4	3.95	23.0	7.45	15.3	4.80
V	20.4	0.051	29.7	0.091	19.5	0.064
Cr	15.7	0.61	25.6	1.24	16.6	0.84
Mn	18.6	0.45	27.2	0.87	17.8	0.60
Fe	15.3	1.10	23.0	2.22	14.9	1.53
co	16.9	0.51	24.8	0.99	16.2	0.68
Ni	17.8	20.25	25.9	43.74	16.9	29.12
cu	15.9	0.90	23.5	1.79	15.2	1.22
Zr	19.1	0.10	28.0	0.19	18.1	0.13
Nb	17.4	0.22	25.7	0.46	16.5	0.32
Mo	12.8	-	18.5	-	12.1	-
Ta	4.2	-	6.3	-	4.1	-
316 SS	15.6	2.90	23.7	6.14	15.4	4.13

	Capsule C (R = 34.0 cm)					
Z:	-11.4 cm		+5.1 cm		+15.3 cm	
Al	44.6	3.26	46.6	3.52	35.0	3.09
Ti	19.3	5.55	20.2	5.98	15.4	4.59
V	25.4	0.07	26.6	0.075	20.2	0.065
Cr	21.6	0.89	22.7	0.96	17.1	0.80
Mn	23.2	0.63	24.3	0.69	18.4	0.60
Fe	19.3	1.54	20.3	1.70	15.3	1.45
co	21.1	0.72	22.1	0.78	16.7	0.67
Ni	22.2	30.03	23.3	32.82	17.6	27.14
cu	20.0	1.26	20.9	1.41	15.8	1.22
Zr	24.0	0.13	25.1	0.15	18.8	0.13
Nb	21.9	0.32	23.0	0.35	17.2	0.30
Mo	15.9	-	16.6	-	12.6	-
Ta	5.3	-	5.5	-	4.2	-
316 SS	20.0	4.24	21.0	4.64	15.8	3.87

6.0 References

1. F. C. Franklin, E. R. Ebersole, and R. R. Heinrich, "Analysis of EBRII Low-Power Dosimetry Run 78C," ANL-77-76 (1977).

7.0 Future Work

Dosimetry samples have been prepared for several new irradiations in HFIR including T3, RB1, RB2, RB3, CTR34, and CTR35.

8.0 Publications

Papers entitled "Neutron Flux and Spectral Measurements for Materials Studies" and "Displacement Damage Calculations with ENDF/B-V" are being prepared for presentation at the Advisory Group Meeting on Nuclear Data for Radiation Damage Assessment and Reactor Safety Aspects in Vienna, Austria, on October 12-16, 1981.

CHARACTERIZATION OF SPALLATION NEUTRON SOURCES

L. R. Greenwood and R. J. Popek (Argonne National Laboratory)

1.0 Objective

To characterize the neutron flux, spectrum, and damage parameters for spallation neutron sources.

2.0 Sumnary

The Radiation Effects Facility (REF) of the Intense Pulsed Neutron Source (IPNS) became operational in July 1981. Dosimetry experiments were irradiated to characterize the vertical thimble (VT2) and rabbit irradiation tubes.

3.0 Program

Title: Dosimetry and Damage Analysis
Principal Investigator: L. R. Greenwood
Affiliation: Argonne National Laboratory

4.0 Relevant OAFS Program Plan Task/Subtask

Task II.A.2 High-Energy Neutron Dosimetry

5.0 Accomplishments and Status

The Radiation Effects Facility of the IPNS at ANL became operational in July of 1981.[1,2] This facility consists of a ^{238}U target surrounded by a lead reflector. The beam of 495 ± 3 MeV protons presently has a current of 4 μA; however, we expect to increase the current to 8 μA shortly. The expected plant factor for the facility is 85-90%; however, time must be shared with the neutron scattering target, and actual running time for the REF will be limited by the available funding.

There are three primary irradiation positions. Two vertical thimbles (VT1 and VT2) are located on either side of the target. Experiments can be instrumented in these positions and cooled with liquid helium. A rabbit tube runs horizontally beneath the target, although samples are loaded manually at present. Each position has an irradiation volume of several liters; however, flux and spectral gradients must be considered both perpendicular and parallel to the target. There are also two smaller, horizontal irradiation tubes located on the sides of the separate neutron scattering target. We plan to measure the flux spectra at these positions in September 1981.

Dosimetry experiments were conducted on July 16-17, 1981 during the first experiments conducted in the new facility. The total exposure over 25.5 hours was 1.5 x 10^{18} protons for a time-averaged beam current of 2.7 μA (peak current ~4 μA). Complete spectral sets for dosimetry were located at the maximum flux locations in VT2 and the rabbit positions. Seventeen different materials were irradiated resulting in 41 activation reaction-rate measurements. Nickel wires were used to measure the vertical and horizontal flux gradients at each location.

The neutron flux spectra were unfolded for the VT2 and rabbit positions using the STAYSL computer code.(3) Thirty-six reactions were used and the input spectrum was taken from neutronics calculations using the HETC and VIM computer codes.(1) The integral flux values are listed in Table 1. The maximum flux for 8 μA beam current should be 1.4 x 10^{12} n/cm^2-s (1 x 10^{12} above 0.1 MeV). The flux above 44 MeV could not be measured with our current knowledge of cross sections. However, calculations indicate that this flux is less than 1‰ of the total. Secondary proton fluxes were also measured using the ^{51}V and ^{65}Cu(p,n) reactions. Our best estimate is that the proton flux between 20-40 MeV is less than 0.2% of the neutron flux.

The adjusted flux spectra are shown in Figures 1 and 2. The dotted and dashed lines show the standard deviation for each flux group; however, correlation effects are very strong, thereby reducing the error in broad-group fluxes or damage parameters.

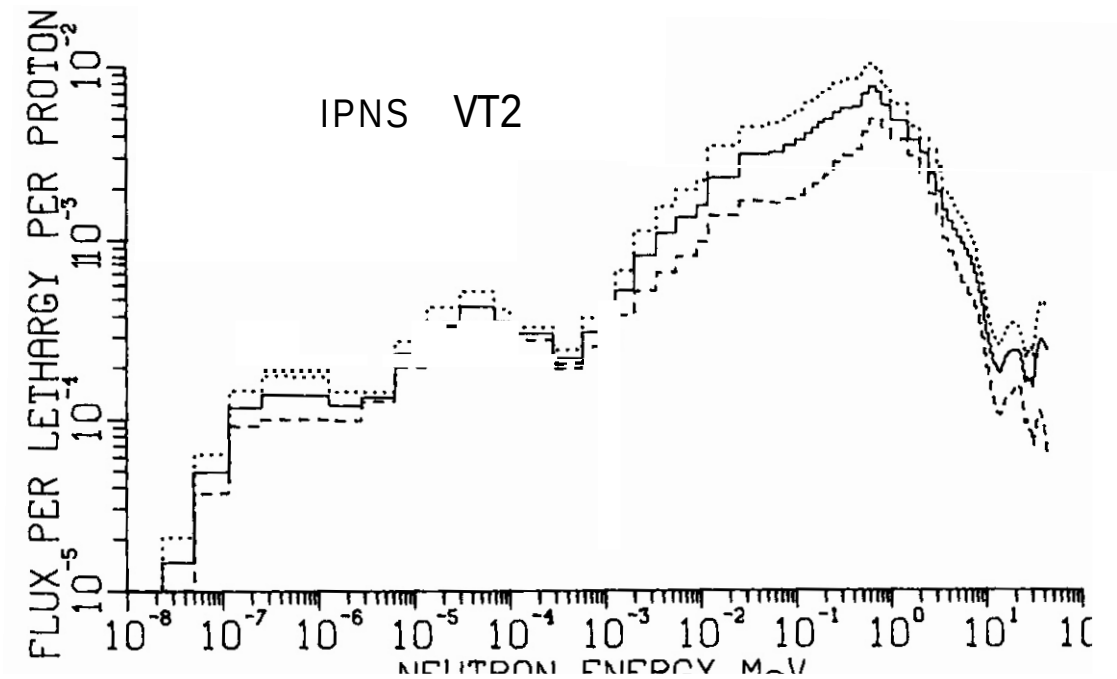

FIGURE 1. Measured Energy Spectrum for Position VT2. The Dotted and Dashed Lines Represent One Standard Deviation; However, the Fluxes Are Highly Correlated (See Table 2).

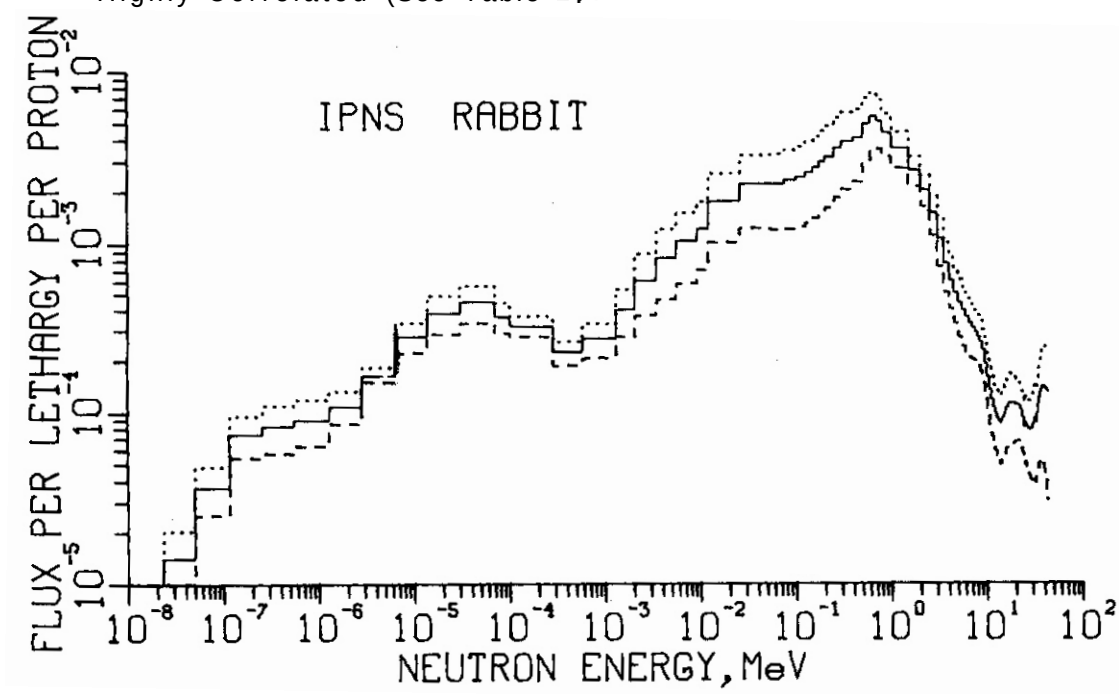

FIGURE 2. Measured Energy Spectrum for the Rabbit. The Dotted and Dashed Lines Represent One Standard Deviation; However, the Fluxes Are Highly Correlated (See Table 2).

TABLE 1

INTEGRAL FLUX VALUES FOR IPNS-REF

(Normalized to maximum flux locations at center of each irradiation tube assuming 8 μA proton current.)

	Neutron Flux (n/cm^2-s)		
Energy Range	VT2 ($\times 10^{11}$)	Rabbit ($\times 10^{11}$)	Error, %
Total	15.6	12.2	14
>0.1 MeV	9.92	7.30	17
Thermal	0.13	0.10	21
0.55 eV - 100 keV	5.60	4.73	24
0.1 - 1 MeV	6.79	5.15	25
1-5	2.64	1.92	12
5-10	0.29	0.13	21
10-15	0.048	0.026	19
15-20	0.036	0.019	23
20-30	0.043	0.022	15
30-40	0.036	0.019	32
40-44	0.013	0.008	63
>44	~0.11[a]	~0.08[a]	

[a]Estimated from HETC calculations.

Horizontal and vertical flux gradients were measured in the VT2 and rabbit positions using the $^{58}Ni(n,p)^{58}Co$ reaction. Nickel wires were strung along each position and then segmented into 1" pieces for analysis. The estimated fast flux gradients are shown in Figures 3 and 4. In position VT2, wires were placed on either side of and in the center of the irradiation tube (~1.75" diameter). As can be seen, significant gradients exist across the tube as well as along the vertical length of the tube. As with any other accelerator-based neutron source, adequate dosimetry should thus be included with all materials irradiations to obtain accurate neutron exposure parameters.

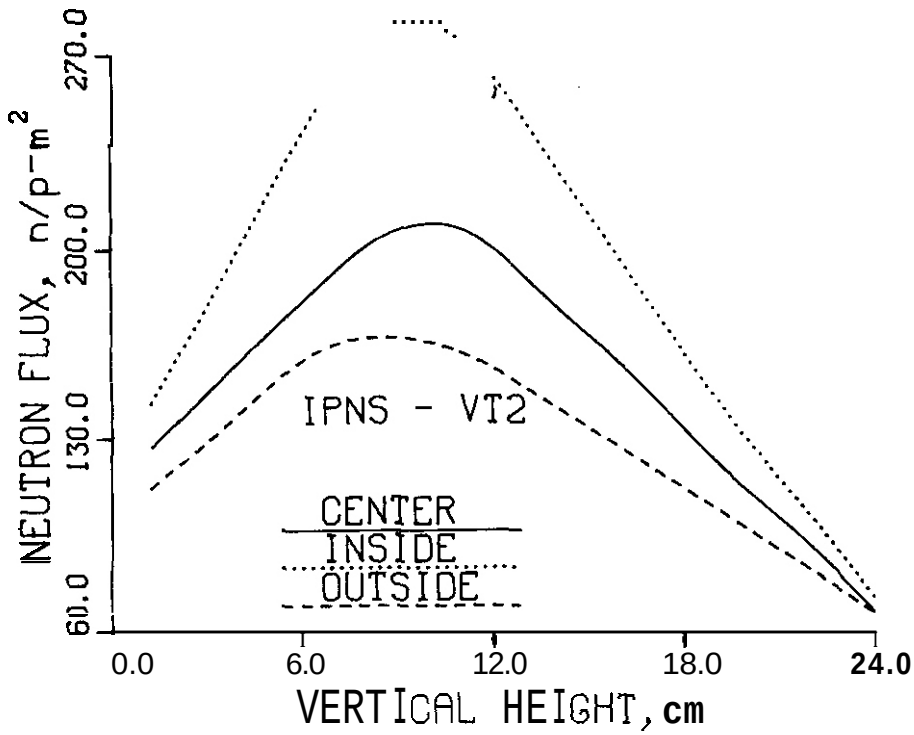

FIGURE 3. Vertical Flux Gradients in the Verticle Thimble 2 of IPNS-KEF. The Solid Line Was at the Center of the Tube; The Dotted Line Was on the Inside Radius, 2 cm Closer to the Target; The Dashed Line Was on the Outside Radius, 2 cm Farther from the Target.

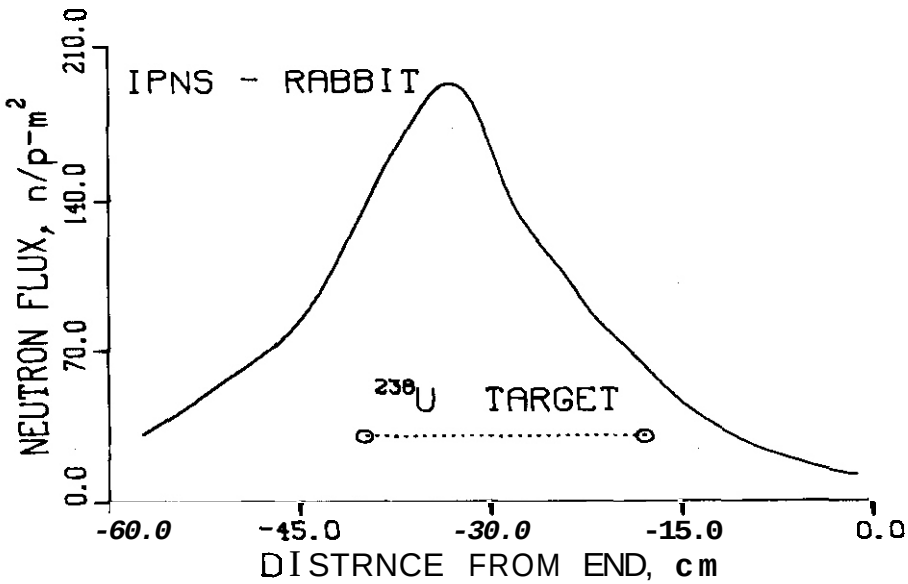

FIGURE 4. Horizontal Flux Gradients Measured in the Center of the IPNS-REF Rabbit Tube, Parallel to the ^{238}U Target. Distances Are Relative to the End of the Rabbit Hole. The Target Location is Shown. The Beam is Incident from the Left.

Damage rates have been calculated for IPNS using our recently revised (ENDF/B-V) displacement damage cross sections. Spectral-averaged damage rates are listed in Table 2 along with expected displacements per week. Helium-to-dpa ratios are about 1-2 for iron, higher than produced in reactors (0.1-0.3), but lower than high-energy neutron sources (e.g., 10-15 for RTNS-II or FMIT). Although the damage rates at IPNS are rather low for fusion studies, the REF is presently the only instrumented, cryogenic irradiation facility in the country.

TABLE 2

DAMAGE PARAMETERS FOR IPNS (REF)

Calculations are for the center of VT2. Weekly rate normalized to 8 μA beam current (Fluence = 9.4 x 10^{17}).

Element	Spectral-Averaged Cross Sections[a]		Rate/Week	
	DPA, keV-b	He, mb	DPA (x 10^{-4})	He, appm (x 10^{-4})
Al	48.2	0.88	4.5	8.3
Ti	39.0	0.34	3.7	3.2
V	45.3	0.093	4.3	0.88
Cr	39.0	0.37	3.7	3.5
Fe	35.5	0.30	3.3	2.8
Ni	39.5	2.21	3.7	20.9
Cu	35.9	0.27	3.4	2.5
Nb	37.3	0.065	3.5	0.61
Au	21.2	0.004	2.7	0.04

[a]Cross sections are averages for total flux. For averages above 0.1 MeV, multiply by 1.57.

6.0 References

1. R. C. Birtcher, M. A. Kirk, T. H. Blewitt, T. L. Scott, L. R. Greenwood, and R. J. Popek, "Neutron Irradiation Facilities at the Intense Pulsed Neutron Source," Proceedings of International Conference on Neutron Irradiation Effects, November 1981, Argonne National Laboratory, to be published in Journal of Nuclear Materials.

2. M. A. Kirk, R. C. Birtcher, T. H. Blewitt, L. R. Greenwood, R. J. Popek, and R. R. Heinrich, "Measurements of Neutron Spectra and Fluxes at Spallation-Neutron Sources and Their Application to Radiation Effects Research," J. Nucl. Mater. 96, 37 (1981).

3. F. G. Perey, "Least-Squares Dosimetry Unfolding: The Program STAYSL," ORNL-TM-6062 (1977); modified by L. R. Greenwood, ANL (1979).

7.0 Future Work

Further dosimetry experiments are planned at IPNS in September 1981 to characterize the neutron scattering target horizontal irradiation tubes. The spectrum may be somewhat softer in these tubes due to the use of carbon and organic moderators rather than the lead moderator used in the REF.

8.0 Publications

A paper entitled "Neutron Source Characterization and Radiation Damage Calculations for Materials Studies," will be presented at the International Conference on Neutron Irradiation Effects at Argonne National Laboratory, November 9-12, 1981; proceedings to be published in Journal of Nuclear Materials.

HELIUM PRODUCTION IN ORR MFE-4A NICKEL

J. G. Bradley, D. W. Kneff, and Harry Farrar IV (Rockwell International, Energy Systems Group)

1.0 Objective

The objective of this work is to develop and apply helium accumulation neutron dosimetry to the measurement of neutron fluences and energy spectra in mixed-spectrum fission reactors utilized for fusion materials testing.

2.0 Summary

A series of helium analyses has been performed on one of the nickel dosimetry wires removed from the ORR MFE-4A experiment. The results show a slightly nonlinear thermal neutron fluence gradient along the wire, consistent with Argonne National Laboratory's radiometric dosimetry results,

3.0 Program

Title: Helium Generation in Fusion Reactor Materials
Principal Investigators: D. W. Kneff and Harry Farrar IV
Affiliation: Rockwell International, Energy Systems Group

4.0 Relevant DAFS Program Plan Task/Subtask

Subtask II.A.1.1 Flux-Spectral Definition in a Tailored Fission Reactor

5.0 Accomplishments and Status

A series of helium analyses has been performed on one of the nickel dosimetry wires irradiated in the Oak Ridge Research Reactor (ORR) experiment MFE-4A. This wire is part of a set of nickel wires incorporated in the center of the experimental assembly by Oak Ridge National Laboratory (ORNL) to monitor

helium production, and is one of four nickel wires originally sent from ORNL to Argonne National Laboratory (ANL) after the irradiation for radiometric counting. These wires were irradiated for an equivalent 183.2 days at 30 MW reactor power, between June 1980 and January 1981. The subject wire was segmented at ANL for their radiometric analysis, and the 8 counted segments were subsequently sent to Rockwell International for helium analysis. The helium was produced in the irradiation by the two-stage reaction $^{58}Ni(n,\gamma)^{59}Ni(n,\alpha)^{56}Fe$ with thermal neutrons, a reaction used to simulate helium generation in fusion reactor materials under service conditions. The helium analyses were performed in cooperation with ORNL and ANL.

Each of the 8 ANL-counted wire segments was further subdivided at Rockwell into two or more pieces, and a total of 18 helium analyses were performed by high-sensitivity gas mass spectrometry. Table 1 presents the results, along with the sample location information supplied by ANL. The absolute 1σ uncertainty in each helium measurement is ±1%. The top of the original nickel wire was 1.6 cm above the ORR core midplane, and 9.2 cm above the axial center of the MFE-4A test region.

The helium concentration results in Table 1 indicate that the ORR thermal neutron flux was highest at the upper end of the dosimetry wire (near core midplane), and had a slightly nonlinear gradient along the length of the wire. This *suggests* some perturbation of the thermal neutron flux, possibly by the MFE-4A test assembly. A similar perturbation was observed in ANL's radiometric measurements of the thermal flux gradient.[1] The total helium concentration variation along the 12.7-cm wire length was about 16%, relative to the upper end.

The complete retention of helium in nickel at the elevated temperatures used for this experiment (~600°C) is not certain at this time, and thus adds some additional uncertainty to the results presented above. The question of helium retention will be examined by measuring the helium generation in samples of stainless steel tubing also incorporated in this experiment. If the helium

TABLE 1

MEASURED HELIUM CONCENTRATIONS FOR ORR MFE-4A NICKEL DOSIMETRY WIRE*

ANL Segment Identification	Average Oistance From Wire Top (cm)	^{4}He Concentration (appm)**	
		Measured	Average
4	0.41	122.8, 119.3	121.1
7	2.92	111.5, 112.3	111.9
8	4.00	109.3, 109.8	109.6
9	5.10	106.8, 106.7	106.8
10	5.37, 7.33	109.8, 107.4†	-
	6.35	111.1, 110.5	110.8
11	7.67	108.7; 107.7	108.2
13	10.09	108.6, 108.7	108.7
15	12.51	102.0, 101.3	101.7

*Wire also counted radiometrically at ANL.
**Atomic parts per million (10^{-6} atom fraction).
+End segments of a 2-cm-long piece whose relative orientation was not known.

concentrations in the stainless steel, which will be almost entirely due to the two-stage nickel reaction, agree with the results from pure nickel, it will be assumed that both materials retained essentially all of their helium. The nickel content of the stainless steel samples will be established at ANL by radiometrically determining the ^{58}Ni(n,p)^{58}Co and ^{60}Ni(n,p)^{60}Co reaction rates relative to those in the pure nickel.

The helium data in Table 1 have been communicated to T. A. Gabriel (ORNL) for comparison with calculations. This helium information is important because a knowledge of the helium/dpa ratio from these dosimeters is one of the factors considered in ORNL's planning for future phases of this irradiation.

6.0 References

1. L. R. Greenwood, personal communication.

7.0 Future Work

Irradiated stainless steel tubing samples will be obtained from ANL and analyzed for helium to compare with the nickel wire results. Further nickel wire helium correlations will also be made with ANL's radiometric results.

8.0 Publications

A final draft has been written of a paper entitled "The Production Rate of Helium During Irradiation of Nickel in Thermal Spectrum Fission Reactors," by F. W. Wiffen, E. J. Allen (ORNL), Harry Farrar IV (Rockwell International), E. E. Bloom, T. A. Gabriel, H. T. Kerr, and F. G. Perey (ORNL). This paper is now ready for submission to the Journal of Nuclear Materials.

HELIUM GENERATION CROSS SECTIONS FOR 14.8-MeV NEUTRONS

B. M. Oliver, D. W. Kneff, M. M. Nakata, and Harry Farrar IV (Rockwell International, Energy Systems Group)

1.0 Objective

The objectives of this work are to measure helium generation rates of materials for Magnetic Fusion Reactor applications in the ~14.8-MeV T(d,n) neutron environment, to characterize the T(d,n) neutron field of the Rotating Target Neutron Source-II (RTNS-II), and to develop helium accumulation neutron dosimeters for this test environment.

2.0 Summary

The total helium generation cross sections have been measured for V, Fe, Ni, Cu, Zr, Nb, Mo, Au and the separated isotopes of Fe, Ni, Cu, and Mo irradiated in the ~14.8-MeV T(d,n) neutron spectrum of RTNS-II. The results are presented along with the previous cross section measurements made as part of two RTNS-I experiments.

3.0 Program

Title: Helium Generation in Fusion Reactor Materials
Principal Investigators: D. W. Kneff and Harry Farrar IV
Affiliation: Rockwell International, Energy Systems Group

4.0 Relevant DAFS Program Plan Task/Subtask

Subtask II.A.2.2 Flux-Spectral Definition in RTNS-II
Subtask II.A.4.2 T(d,n) Helium Gas Production Data

5.0 Accomplishments and Status

Total helium generation cross sections have now been measured for V, Fe, Ni, Cu, Zr, Nb, Mo, Au, and the separated isotopes of Fe, Ni, Cu, and Mo, irradiated in the ~14.8-MeV T(d,n) neutron spectrum of RTNS-II. The irradiation, a joint experiment with Argonne National Laboratory (ANL) and Lawrence Livermore National Laboratory (LLNL), has been described previously in some detail.[1] The cross sections were determined by analyzing multiple samples of each material by high-sensitivity gas mass spectrometry for generated helium, and combining the helium results with the neutron fluence at each sample position in the irradiation volume. The position-dependent neutron fluence was determined by constructing a neutron fluence map of the irradiation volume from a combination of radiometric and helium accumulation neutron dosimetry. The source characterization work was supported by the Office of Fusion Energy of the U.S. Department of Energy (DOE) and the cross section measurements were supported by the DOE's Office of Basic Energy Sciences.

The cross section results are given in Table 1, where they are compared with previous cross section measurements made as part of two RTNS-I experiments. The neutron fluence map derived for the RTNS-II irradiation is based primarily on the average profile constructed from the segmented radiometric dosimetry foils. Correlations with the helium accumulation dosimetry indicated that the radial fluence profile is generally uniform as a function of polar angle about the RTNS-II neutron source axis, although the irradiation assembly was offset from this axis by 1.1 mm. Some further adjustments may be made in the map to account for small variations in the fluence profile. These are expected to have a negligible effect on the reported cross section results, however, as the multiple samples analyzed for each material were distributed throughout the irradiation volume. The estimated relative fluence uncertainties in the present map are ±5%, and the absolute fluence uncertainties are 57%. The absolute values were normalized to the niobium radiometric foil results, for which the $^{93}Nb(n,2n)^{92m}Nb$ cross section was assumed to be 463 ± 19 mb.[2] Absolute 1σ uncertainties for most of the ^{4}He measurements were 52%. The fluence mapping results will be reported in more detail in a later report.

TABLE 1

HELIUM GENERATION CROSS SECTIONS FOR ~14.8-MeV NEUTRONS

Material	Measured Cross Section (mb)			Adopted Value (mb)
	RTNS-I Run 1	RTNS-I Run 2	RTNS-II	
C (diamond)	900 ± 70[a]			900 ± 70[a]
Al	143 ± 7	145 ± 10		144 ± 7
Ti	38 ± 3	37 ± 3		37 ± 3
V	18 ± 2	18.7 ± 1.4	18.5 ± 1.3	18.6 ± 1.3
Cr	-	34 ± 4		34 ± 4
Fe	48 ± 3	48 ± 3	49 ± 3	48 ± 3
^{54}Fe	-	88 ± 6	94 ± 7	91 ± 7
^{56}Fe	-	45 ± 4	47 ± 3	46 ± 3
^{57}Fe	-	-	33 ± 2	33 ± 2
^{58}Fe	-	20 ± 2	20 ± 2	20 ± 2
Ni	98 ± 6	100 ± 7	101 ± 7	100 ± 7
^{58}Ni	-	116 ± 7	126 ± 9	121 ± 8
^{60}Ni	-	79 ± 6	80 ± 6	80 ± 6
^{61}Ni	-	53 ± 4	49 ± 4	51 ± 4
^{62}Ni	-	18 ± 6	22 ± 2	22 ± 2
^{64}Ni	-	61 ± 4[b]	9 ± 1	9 ± 1
cu	51 ± 3	51 ± 3	51 ± 4	51 ± 3
^{63}Cu	-	67 ± 5	64 ± 5	65 ± 5
^{65}Cu	-	17 ± 2	17 ± 1	17 ± 1
Zr	10 ± 2[a]	10.2 ± 0.8	10.1 ± 0.7	10.1 ± 0.7
Nb	17 ± 5		14 ± 1	14 ± 1

(continued on next page)

TABLE 1 (Continued)

HELIUM GENERATION CROSS SECTIONS FOR ~14.8-MeV NEUTRONS

Material	Measured Cross Section (mb)			Adopted Value (mb)
	RTNS-I Run 1	RTNS-I Run 2	RTNS-II	
Mo	15 ± 2	15 ± 2	14 ± 1	14 ± 1
^{92}Mo	-	31 ± 2	31 ± 2	31 ± 2
^{94}Mo	-	22 ± 2	22 ± 2	22 ± 2
^{95}Mo	-	17 ± 2	17 ± 1	17 ± 1
^{96}Mo	-	11 ± 1	12 ± 1	12 ± 1
^{97}Mo	-	10 ± 1	10 ± 1	10 ± 1
^{98}Mo	-	23 ± 2[b]	22 ± 2[b]	(b)
^{100}Mo	-	3.8 ± 0.5	3.8 ± 0.3	3.8 ± 0.3
Au	-	0.72 ± 0.09	0.50 ± 0.04	0.50 ± 0.04
316 SS	57 ± 4			57 ± 4

(a) Unetched samples. Corrections for a-recoil effects have *not* been made; this is reflected in increased cross section uncertainties.
(b) See text.

The cross section determinations from the three irradiations listed in Table 1 are independent except for the fluence normalization to the ^{93}Nb(n,2n) cross section. The cross sections for the isotopes were determined in each case by first evaluating the cross sections for the actual isotopic enrichments used (generally >95%), and then solving a matrix of equations for each material to correct for the small concentrations of each of the other isotopes in the material. For all separated isotopes used, the assumed isotopic compositions and impurity concentrations were those provided by the vendor (Oak Ridge National Laboratory).

We believe that there is some basis for questioning the values obtained for ^{64}Ni (RTNS-I) and for ^{98}Mo. The ^{64}Ni cross section measured in the RTNS-I Run 2 experiment is inconsistent with the RTNS-II results, and does not follow

the general trend of decreasing cross section with higher isotopic mass. Since two different lots of ^{64}Ni isotopic metal were used for these experiments, the material irradiated in RTNS-I appears suspect, and the Table 1 adopted cross section for ^{64}Ni is based solely on the RTNS-II results.

As noted in a previous report describing RTNS-I results,[3] the ^{98}Mo isotopic metal exhibited different properties than the other separated molybdenum isotopes during analysis. Chemical analyses to date on this lot of material, used for both the RTNS-I and RTNS-II experiments, do not, however, indicate significant impurity concentrations. The unexpectedly high cross section value appears to explain the difference between the measured natural molybdenum cross section (14 ± 1 mb) and that derived from a weighted average of the measured isotopic cross sections (18 ± 1 mb). A reduced value of -7 mb for ^{98}Mo would give a calculated natural molybdenum cross section in agreement with the measurement. A new lot of separated ^{98}Mo will be obtained for a future irradiation.

In general, excellent agreement was obtained between the cross section results from the three different experiments. A further comparison shows that the natural Fe, Ni, and Cu cross sections derived from weighted averages of the measured isotopic cross sections (48 ± 3, 105 ± 6, and 50 ± 3 mb, respectively) are also in good agreement with the measured pure element cross sections. This provides further confidence in the data. Analyses will now be extended to other materials irradiated in RTNS-II.

6.0 References

1. D. W. Kneff, B. M. Oliver, M. M. Nakata, and H. Farrar IV, "Characterization of the RTNS-II Neutron Field," in Damage Analysis and Fundamental Studies, Quarterly Progress Report July-September 1980, DOE/ER-0046/3, U.S. Department of Energy, 25 (1980).

2. D. R. Nethaway, "The $^{93}Nb(n,2n)^{92m}Nb$ Cross Section," J. Inorg. Nucl. Chem., 40, 1285 (1978).

3. B. M. Oliver, D. W. Kneff, M. M. Nakata, and H. Farrar IV, "Helium Generation Cross Sections for Fast Neutrons," in Damage Analysis and Fundamental Studies, Quarterly Progress Report January-March 1981, DOE/ER-0046/5, U.S. Department of Energy, 19 (1981).

7.0 Future Work

The helium analyses of selected RTNS-irradiated pure elements and separated isotopes will continue. The highest-priority elements for analysis during the next quarter include Cr, Co, Sn, and the separated isotopes of Cr.

8.0 Publications

A paper entitled "Experimental Helium Generation Cross Sections for Fast Neutrons," by D. W. Kneff, B. M. Oliver, M. M. Nakata, and Harry Farrar IV, was presented at the Second Topical Meeting on Fusion Reactor Materials, Seattle, Washington, on August 11, 1981, and has been submitted for publication in the symposium proceedings in the Journal of Nuclear Materials.

HELIUM GENERATION CROSS SECTIONS FOR Be(d,n) NEUTRONS

D. W. Kneff, B. M. Oliver, M. M. Nakata, and Harry Farrar IV (Rockwell International, Energy Systems Group)

1.0 Objective

The objectives of this work are to measure helium generation rates of materials for Magnetic Fusion Reactor applications in the Be(d,n) neutron environment, to characterize this neutron environment, and to develop helium accumulation neutron dosimeters for routine neutron fluence and energy spectrum measurements in Be(d,n) and Li(d,n) neutron fields.

2.0 Summary

Helium analyses have been completed for the Fe, Ni, and Cu isotopes irradiated in the Be(d,n) neutron field. Average integral cross sections have been determined for all of the Be(d,n)-irradiated materials analyzed to date.

3.0 Program

Title: Helium Generation in Fusion Reactor Materials
Principal Investigators: D. W. Kneff and Harry Farrar IV
Affiliation: Rockwell International, Energy Systems Group

4.0 Relevant DAFS Program Plan Task/Subtask

Subtask II.A.2.1 Flux-Spectral Definition in the Be(d,n) Field
Subtask II.A.4.3 Be(d,n) Helium Gas Production Data

5.0 Accomplishments and Status

The Be(d,n) irradiation was performed as a joint Rockwell International-Argonne National Laboratory (ANL)-Lawrence Livermore National Laboratory (LLNL) experiment, to characterize the Be(d,n) neutron field for 30-MeV

deuterons, to develop energy-sensitive helium accumulation neutron dosimeters, and to provide experimental information on helium production in Be(d,n) and, by implication, Li(d,n) neutron environments. Details of the irradiation and the neutron source characterization have been described previously.[1]

Several pure elements and separated isotopes irradiated in this experiment have now been analyzed for generated helium, including, during the last quarter, the separated isotopes of Fe, Ni, and Cu. Integral total helium generation cross sections have now been determined for these materials.

The cross section results were derived by combining the helium generation measurement for each sample with the integral neutron fluence calculated for that sample position. The neutron fluence distribution as a function of sample position was calculated by L. R. Greenwood at ANL,[1] using the least-squares spectral analysis code STAY'SL. Since the neutron spectrum shape changes with sample position within the irradiation capsule, the integral helium generation cross sections are also position-dependent. For the present report, however, the cross section data for each material have been averaged over several different sample irradiation locations for that material. More detailed consideration will be given to energy spectrum variations in future reports, when the helium results are used as integral tests for theoretical cross section evaluations.

The cross section results are presented in Table 1, where they are given in two forms: average spectrum-integrated total helium production cross sections evaluated for the total Be(d,n) neutron fluence, and average spectrum-integrated cross sections evaluated for the neutron fluence above 5 MeV. The cross sections calculated for the total neutron yield provide an estimate of helium generation in the measured materials for any similar Be(d,n) or Li(d,n) spectrum, given a knowledge of the total neutron fluence. The cross section values for neutrons above the 5-MeV cutoff provide a rough estimate of the average differential total helium generation cross sections for high-energy neutrons. This follows from the typically ~6 MeV effective threshold for

TABLE 1

INTEGRAL HELIUM GENERATION CROSS SECTIONS FOR THE -0-32-MeV Be(d,n) NEUTRON SPECTRUM PRODUCED BY 30-MeV DEUTERONS

Material	Average Cross Section (mb) Total Fluence[a]	Average Cross Section (mb) Fluence >5 MeV[a]	Material	Average Cross Section (mb) Total Fluence[a]	Average Cross Section (mb) Fluence >5 MeV[a]
Al	60	121	cu	18	41
V	8	16	^{63}Cu	22	55
Fe	19	41		8	15
^{54}Fe	34	76	Zr	4	9
^{56}Fe	18	43	Mb	6	14
^{57}Fe	-	-	^{92}Mo	12	26
^{58}Fe	8	21	^{94}Mo	8	20
Ni	40	98	^{95}Mo	9	16
^{58}Ni	51	127	^{96}Mo	5	9
^{60}Ni	32	73	^{97}Mo	5	10
^{61}Ni	23	47	^{98}Mo	9[b]	20[b]
^{62}Ni	15	36	^{100}Mo	2	4
^{64}Ni	-[b]	-[b]	Au	0.5	1.2

[a] The cross section uncertainty for a given Be(d,n) irradiation position is ~±35% for the total fluence and ~±18% for the fluence above 5 MeV, reflecting the changing neutron spectrum and thus cross section with source angle.

[b] See text.

helium production in most of these materials, and their slowly increasing helium generation cross sections at high energies.[2] This is coupled with the decreasing neutron yield above 13 MeV for the Be(d,n) neutron spectrum produced by 30-MeV deuterons.[1]

The uncertainties in the tabulated cross sections for a given Be(d,n) irradiation position are ~±35% for the total fluence and ~±18% for the fluence above 5 MeV. They reflect the absolute fluence uncertainties (~±15%), the

changing cross sections with source angle (~0-42°) due to the changing neutron spectrum, and the single irradiation positions for the isotopes. The variations are larger for the total fluence because of the changing ratio of low-energy to high-energy neutrons as a function of source angle. This is reflected in the apparent differences in the ratios of molybdenum isotope cross sections for the two fluence ranges; these differences are attributed to position effects. The absolute lo uncertainties in the helium measurements, by comparison, were generally $\leq \pm 2\%$, and therefore were not a contributing factor.

The isotopic cross sections were unfolded from the measurements made with the available isotopic enrichments by matrix analysis, as described for our 14.8-MeV T(d,n) cross section results in another section of this quarterly report.[3] The ^{98}Mo results are questionable, both because of the unexpectedly high cross section values and the observed properties of this material during analysis.[4] The measured ^{64}Ni cross section results were omitted from Table 1, because both the Be(d,n) and T(d,n) results indicate problems with this lot of material.[3]

It must be emphasized that the results in Table 1 are preliminary in that they are position- and therefore spectrum-averaged cross sections, and the isotopic cross sections exhibit some position dependence. More detailed analyses will be presented later. However, they do provide data for planning and design purposes. For example, the Be(d,n) cross sections determined for fluences >5 MeV are similar to those for T(d,n) neutrons,[3] as expected from the fluence range used in the determination. This indicates that helium generation in a Be(d,n) neutron environment is comparable to that for T(d,n) neutrons.

6.0 References

1. D. W. Kneff, H. Farrar IV, L. R. Greenwood, and M. W. Guinan, "Characterization of the Be(d,n) Neutron Field by Passive Dosimetry Techniques," in Proc. Symp. on Neutron Cross-Sections from 10 to 50 MeV, M. R. Bhat

and S. Pearlstein, eds., BNL-NCS-51245, Brookhaven National Laboratory, N.Y. (1980), p. 113.

2. D. W. Kneff, H. Farrar IV, F. M. Mann, and R. E. Schenter, "Experimental and Theoretical Determination of Helium Production in Copper and Aluminum by 14.8-MeV Neutrons," Nucl. Techno1., 49, 498 (1980).

3. B. M. Oliver, D. W. Kneff, M. M. Nakata, and H. Farrar IV, "Helium Generation Cross Sections for 14.8-MeV Neutrons," in Damage Analysis and Fundamental Studies, Quarterly Progress Report July-September 1981 (this volume).

4. B. M. Oliver, D. W. Kneff, M. M. Nakata, and H. Farrar IV, "Helium Generation Cross Sections for Fast Neutrons," in Damage Analysis and Fundamental Studies, Quarterly Progress Report January-March 1981, DOE/ER-0046/5, U.S. Department of Energy, 19 (1981).

7.0 Future Work

The helium analysis of materials irradiated in the Be(d,n) neutron field will continue, with present emphasis on Cr, Co, Nb, and Sn. Correlations will be made between the total integral helium generation results reported above and helium production cross section evaluations, in a joint effort with ANL and the Hanford Engineering Development Laboratory (HEDL).

8.0 Publications

A paper entitled "Experimental Helium Generation Cross Sections for Fast Neutrons," by D. W. Kneff, B. M. Oliver, M. M. Nakata, and Harry Farrar IV, was presented at the Second Topical Meeting on Fusion Reactor Materials, Seattle, Washington, on August 11, 1981, and has been submitted for publication in the symposium proceedings in the Journal of Nuclear Materials.

MEASUREMENT OF THE $^{27}Al(n,2n)^{26}Al$ CROSS SECTION

R. K. Smither and L. R. Greenwood (Argonne National Laboratory)

1.0 Objective

To develop new cross sections and techniques for dosimetry and damage calculations.

2.0 Sumnary

A new technique, AMS[1] (accelerator mass spectrometry), was used to measure the (n,2n) cross section in aluminum. The experimentally measured cross section was found to be approximately one half the theoretically calculated cross section[2] presently being used in neutron damage calculations. This result agrees with a more standard radioactivity experiment performed at the same time. The AMS work was done in collaboration with W. Kutschera, W. Henning, and J. Yutema of the Argonne National Laboratory, Physics Department.

3.0 Program

Title: Dosimetry and Damage Analysis
Principal Investigator: L. R. Greenwood
Affiliation: Argonne National Laboratory

4.0 Relevant DAFS Program Plan Task/Subtask

Task II.A.5 Technique Development for Dosimetry Applications

Task II.B.1.2 Acquisition of Nuclear Data for the Calculation of Defect Production Cross Sections

5.0 Accomplishments and Status

5.1 Introduction

The $^{27}Al(n,2n)^{26}Al$ reaction produces most of the displacement damage cross section for neutrons with energies above 15 MeV. The only other important reactions are elastic and inelastic neutron scattering which are lower by a factor of 2-3. The total cross section for (n,2n) in aluminum has never been measured. The present damage calculations use a theoretically derived cross section for this reaction. Since this type of calculation can be in error by an unknown factor, it is important to obtain an experimental check; otherwise large errors must be assigned to any damage calculation for energetic neutrons.

The (n,2n) cross section for the formation of ^{26}Al in the 0^+ isomeric state of 0.228 MeV has been measured by Mani et al.[3] in the neutron energy range of 16 to 20 MeV, by measuring the 6-decay of the isomeric state to the ground state of ^{26}Mg. This state decays to ^{26}Mg 100% of the time with a $T_{1/2}$ = 6.35 sec. This short half life makes the experiment difficult but doable. The very-long half life of the ^{26}Al ground state, $T_{1/2} = 7.3 \times 10^5$ years,[4,5] makes a similar type of experiment to measure the (n,2n) cross section for the production of the ground state and gama cascades that lead to the ground state very difficult if not impossible. Accelerator running time and/or counting time would have to be extended by a factor of 4×10^{12} to get similar counting statistics for the ^{26}Al ground state production as were obtained for the isomeric state work. The measured values for the (n,2n) cross section for the production of ^{26}Al in the isomeric state correspond to about 36% of the theoretical total (n,2n) cross section above 18 MeV and decreases to less than 3% at E_n = 16 MeV. This leaves considerable uncertainty in the total (n,2n) cross section.

Recently, a new method, AMS (accelerator mass spectrometry), for measuring the relative abundance of low concentration of long lived radioactive isotopes or rare stable isotopes has been developed at the Argonne National Laboratory[1] (and at other laboratories). The new method uses the Argonne Tandem Van de Graaff accelerator and the considerable associated experimental equipment normally used in nuclear physics experiments as a very special mass spectrometer.

In most cases, the system can detect concentrations of rare isotopes as low as one part in 10^{12} atoms. In special cases, the sensitivity can reach one part in 10^{14} atoms. This new method (AMS) was used to measure the concentration of ^{26}Al in two sets of aluminum dosimetry foils that had been exposed to well-documented doses of high energy neutrons. The measured ratio of $^{26}Al/^{27}Al$ in these foils was used to calculate the cross section for the $^{27}Al(n,2n)^{26}Al$ reaction that leads to the formation of the ^{26}Al ground state as a function of neutron energy.

Just prior to the accelerator experiments (AMS), a radioactivity type cross section measurement was performed on the Al dosimetry foil that had received the highest neutron dose of all the samples available from previous dosimetry measurements. Based on the theoretical value of the (n,2n) cross section[2] [$\sigma_{g.s.} = \sigma_{total}$ (theory) - $\sigma_{isomeric\ state}$ (exp)], the concentration of ^{26}Al in this sample was 6 parts in 10^8 atoms. Although this concentration of ^{26}Al was 20 times higher than any of the samples used in the accelerator experiments, the counting rate in the radioactive experiment was the order of 1 count per hour.

5.2 The Radioactive Measurement of the $^{27}Al(n,2n)^{26}Al$ Cross Section

The ground state of ^{26}Al decays to ^{26}Mg and emits a 1808 keV gama ray 99.36% of the time. By measuring this decay rate and combining it with the known half life of the ground state of ^{26}Al, one can calculate the concentration of ^{26}Al in the foil. Two long counting runs were made on successive weekends with counting times of 4500 min (75 hr) and 4150 min (69 hr) and total detected counts for the 1808 keV peak in the Ge(Li) detector of 119 counts and 140 counts, respectively. After corrections for detector efficiency, solid angle, absorption, summing, etc., these counting rates when averaged translate into a value of $\lambda N = 5.49 \pm 0.5$ dpm. Using the measured half life of $^{26}Al(g.s.)$ of $T_{1/2} = 7.3 \times 10^5$ yr[4,5] and thus a A of 3.01×10^{-14} (s^{-1}) with a quoted error of ±5%, the number of ^{26}Al atoms in the sample is calculated to be $N = (1.029 \pm 0.12) \times 10^{20}$ and the ratio of $^{26}Al/^{27}Al$ is $(2.96 \pm 0.36) \times 10^{-8}$. The calculated value for this ratio of $^{26}Al/^{27}Al$, based on the theoretical

values for the total (n,2n) cross section minus the measured values for the (n,2n) cross section for the production of the 0^+ isomeric state in ^{26}Al, is 6.2 x 10^{-8}. This suggests that the theoretical value for the (n,2n) cross section for the production of the ground state of ^{26}Al is a factor of 2 too high and that the total (n,2n) cross sections presently being used in damage calculations are 30-40% too high for neutron energies above 16 MeV and a factor of 2 too high in the 14-16 MeV region.

5.3 The Accelerator Mass Spectrometry Measurement of the $^{27}Al(n,2n)^{26}Al$ Correction

The accelerator mass spectrometry (AMS)[1] method for measuring abundances of rare isotopes uses the Argonne Tandem accelerator and much of the auxiliary equipment associated with it, including a large magnetic spectrometer and a special detector in the focal plane of the magnetic spectrometer. The experimental arrangement is shown in Figure 1. The material to be measured is put into the ion source at the left as a pellet or foil about 1/4" to 1/2" in diameter. The sample is bombarded with a 12 keV Cs ion beam and the negative ions produced are accelerated to 120-150 keV and analyzed by the 40° injection magnet. In this experiment, one selects either mass *26* or mass 27 and accelerates this beam in the Tandem accelerator. The negative ion beam is changed to a positive ion beam in the terminal of the Tandem by passing it through a carbon foil. This allows further acceleration with a larger charge on the ions, and at the same time dissociates the molecular ion beams that were present in the ion source beam and had the right mass to pass through the 40" injection magnet ($^{12}C^{14}N$ = mass 26). The accelerated beam is then refocused by the magnetic quadrupole and analyzed in the 90" analyzing magnet to select only one mass with one charge state. We used the 8^+ charge state for both the ^{26}Al beam and the ^{27}Al beam. The ion beam is bent once more by the 30" switching magnet that deflects it down the appropriate beam line to the scattering chamber, where it is focused by the magnetic quadrupole into a special faraday cup to measure the electrical beam current of the ^{27}Al ion beam or on to a scattering foil (29 μg of carbon) for the ^{26}Al ion beam. The ^{26}Al ion beam is further stripped

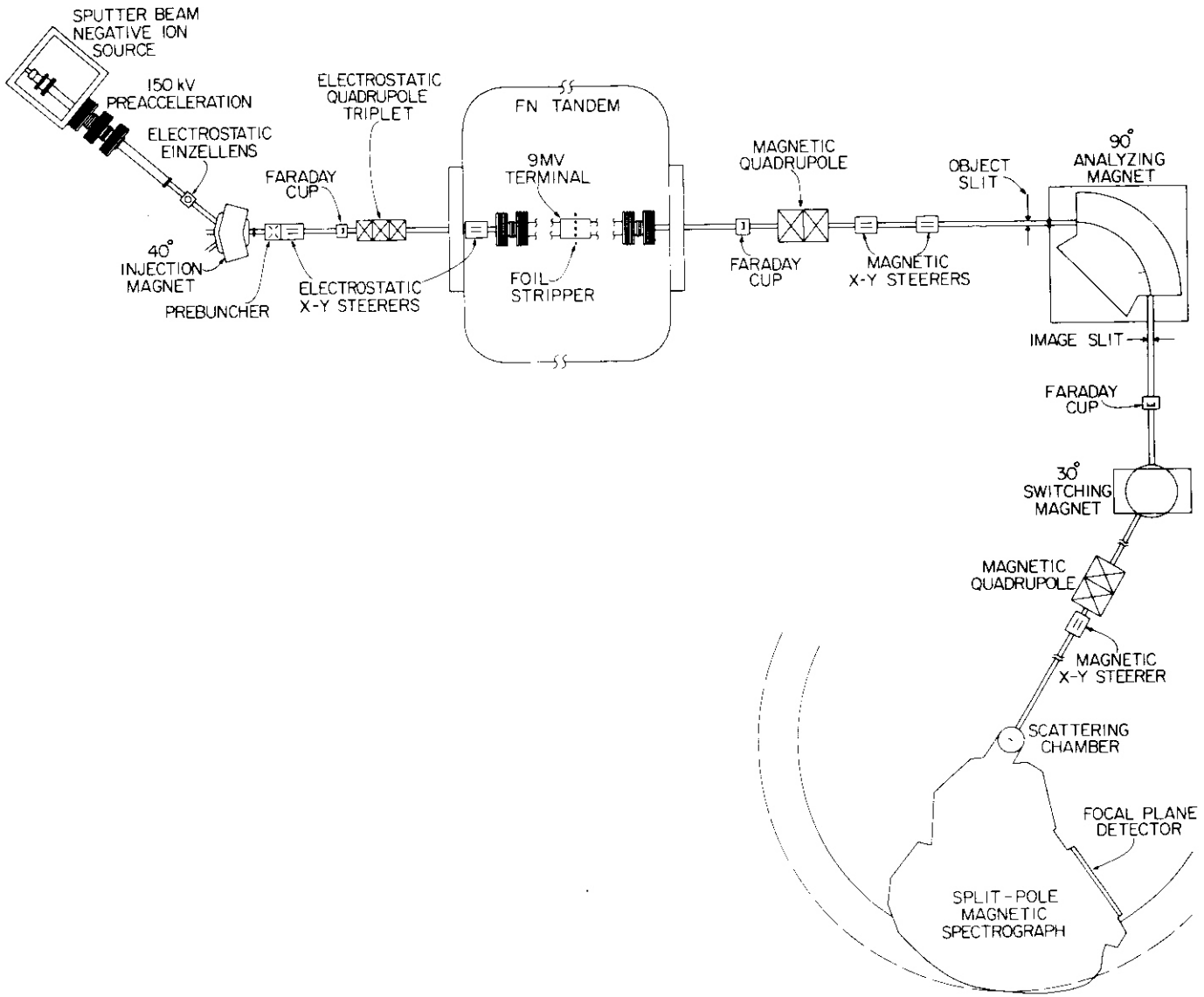

FIGURE 1. Systematic Layout of the Argonne FN Tandem Accelerator and Experimental Systems Used in the Accelerator Mass Spectrometry (AMS) Measurements.

of electrons in the carbon foil and analyzed by the large, high resolution split-pole magnetic spectrograph. In this experiment, the 11^+ charge state of ^{26}Al was used. The ^{26}Al ion particle current is detected in the special focal plane detector that measures the energy loss (ΔE) in a gas cell and the total energy (E) of the ion as well as the position and thus the magnetic rigidity ($B\rho$) of the ion. Each arriving ion is recorded as an individual event. This last combination of magnetic analysis plus the measurement of the energy loss, ΔE, and the total energy, E, of the ion allows one to identify both the mass and the Z of the ion. Thus, it is possible to separate ^{27}Al ions from ^{26}Al ions as well as ^{26}Al ions from ^{26}Mg ions. The experimental procedure is to first measure the ion current in the ^{27}Al beam in the faraday cup in the scattering chamber and then switch to the ^{26}Al particle beam and measure the count rate (particle/sec) in the focal plane detector, then switch back to the ^{27}Al beam, etc., until reproducible results and enough statistics are obtained to calculate the $^{26}Al/^{27}Al$ ratio. The high sensitivity of this method comes from the fact that we are comparing the electrical current in an ion beam of ^{27}Al, which is typically a few nanoamps (1 nA of $^{27}Al^{8+}$ ions correspond to 7.85×10^8 particle per sec), with a particle current of ^{26}Al ions where we count each ion individually. The actual formula used to calculate the $^{26}Al/^{27}Al$ ratio in this experiment is given below in equation (1).

$$\frac{^{26}Al}{^{27}Al} = \frac{Y(^{26}Al) \times Q_1 \times 1.6 \times 10^{-10}}{f_{Q_2} \times I(^{27}Al) \times R_{Q_1}} \qquad (1)$$

where $Y(^{26}Al)$ = ^{26}Al particles per sec in detector, Q_1 = ^{27}Al charge state (8^+), f_{Q_2} = ^{26}Al charge state fraction of incoming beam that is converted into the beam actually measured in the detector ($^{26}Al^{11+}$ fraction of the incoming $^{26}Al^{8+}$ beam was 0.480), $I(^{27}Al)$ = ^{27}Al beam current in nA, and R_{Q_1} = ratio of $F(^{26}Al^{8+})$ charge state fraction/$F(^{27}Al^{8+})$ charge state fraction after passing through carbon stripper foil in terminal of Tandem accelerator. (In our experiment R_{Q_1} = 1.042.)

For our experiment, equation (1) becomes (2)

$$\frac{^{26}Al}{^{27}Al} = 2.56 \times 10^{-9} \frac{Y(^{26}Al)}{I(^{27}Al)} \left(\frac{cts/sec}{nA}\right) \qquad (2)$$

In this experiment, it was possible to measure particle beam currents as low as 2×10^{-3} cts/sec per nA which corresponds to a $^{26}Al/^{27}Al$ ratio of 5×10^{-12}.

Two types of dosimetry foils were used. The first set of foils were exposed to the neutron flux from the (d,t) reaction produced by the RTNS facility at Livermore.[6,7] The foils were placed at different angles relative to the deuteron beam direction. This varied the energy of the nearly monoenergetic neutron beam at each location from 14.80 MeV at 0" to 13.64 MeV at 128° and made it possible to measure to (n,2n) cross section as a function of energy near the threshold at 13.4 MeV (lab energy) where the cross section is changing rapidly. A second set of dosimetry foils were exposed to the fast neutron flux produced by the accelerator at the University of California at Davis by bombarding a Be target with 30 MeV deutrons.[8] This facility generates a broad spectrum of neutron energies. The yield of ^{26}Al in this experiment is proportional to the integral of the product of the (n,2n) cross section times the strength of the neutron flux as a function of neutron energy. The measured ratio of $^{26}Al/^{27}Al$ is used to determine the average cross section in the 15 to 20 MeV region and to normalize the theoretical cross section to the measured value. The results of the preliminary analysis of the data are plotted in Figure 2. The data points with error bars are the results from the RTNS data taken with the (d,t) monoenergetic neutrons. They are compared with dash curve, A, which is the theoretically calculated cross section used in the present dosimetry calculation, curve "B" which is "A" minus the curve "C" which is the measured (n,2n) cross section for the production of the isomeric 0^+ state at 0.228 MeV, and "D" which is curve B normalized so that it reproduces the measured $^{26}Al/^{27}Al$ ratio obtained from the U. of C. at Davis data. Curve D agrees quite well with the individual cross section obtained from the RTNS data and both sets of data suggest that the theoretical cross sections for the total

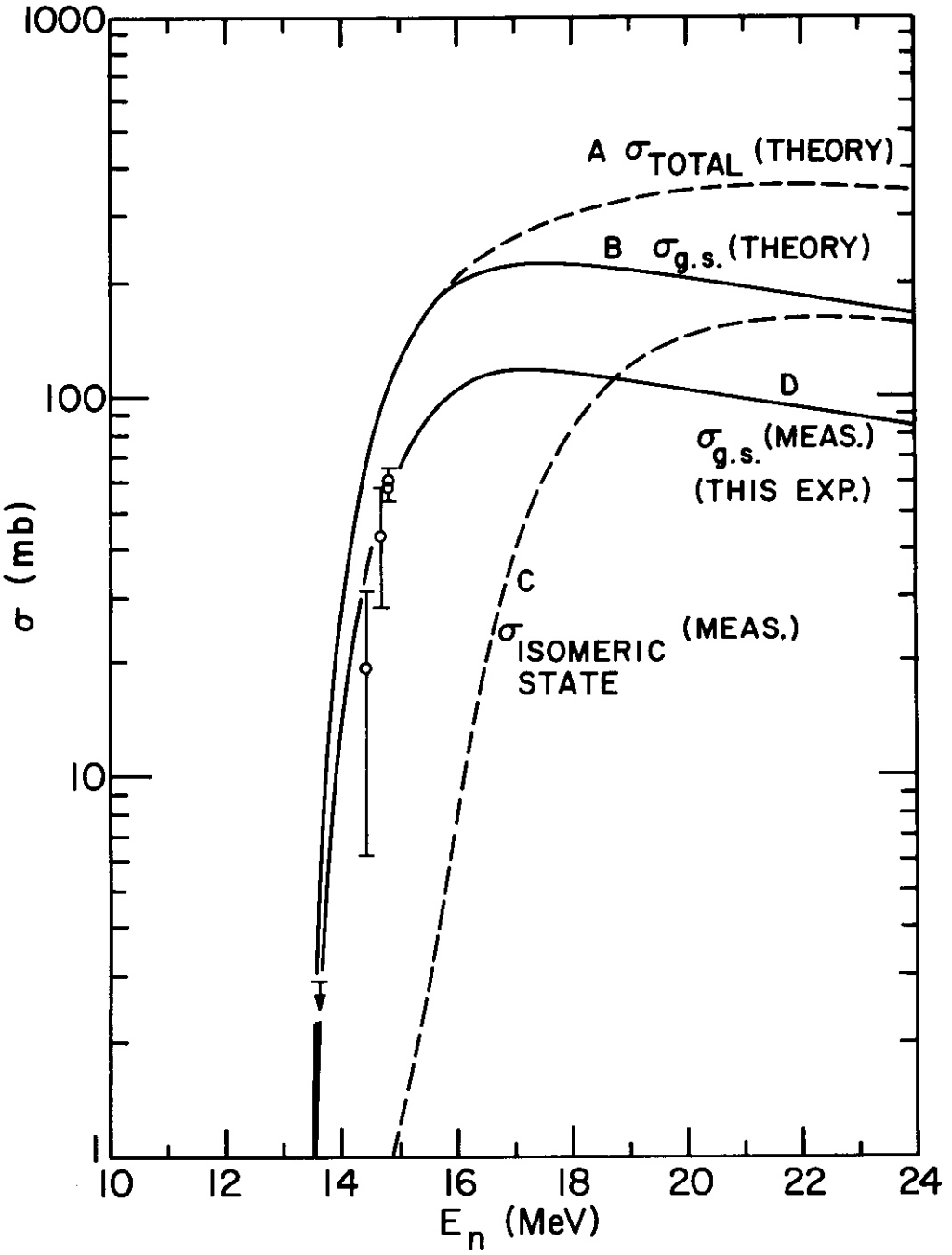

FIGURE 2. A Comparison of the Theoretical Cross Section for the $^{27}Al(n,2n)^{26}Al$ Reaction Presently Used in Damage Calculations (Curves A and B) and the Measured Results from This Work for the Production of ^{26}Al in the Ground State (Curve D), Based on the U. of C. at Davis Data and the Cross Sections at Discrete Neutron Energies (Points with Error Bars). Curve C is the Previously Measured Cross Section for the Production of the 0^+ Isomeric State.

TABLE 1

PRELIMINARY RESULTS FROM THE RTNS FOILS FOR THE $^{27}Al(n,2n)^{26}Al$ REACTION

Sample	Angle	Distance	E_n (MeV)	Neutron[a] Fluence (n/sec)	$\sigma_{g.s.}$(theory)[b] (barns)	Measured ($^{26}Al/^{27}Al$)	$\sigma_{g.s.}$(exp)[c] (barns)
A-0	0°	5 cm	14.80	1.51×10^{16}	105.0	0.909×10^{-9}	60.3 ± 3.0
c-0	0°	30 cn	14.80	3.85×10^{14}	105.0	2.29×10^{-11}	59.5 ± 8.4
C-30	30°	30 cm	14.69	3.48×10^{14}	95.0	2.10×10^{-11}	42.8 ± 17.0
C-60	60°	30 cm	14.43	3.14×10^{14}	65.0	6.0×10^{-12}	19.1 ± 12.0
I-128	128°	30 cm	13.64	4.89×10^{14}	4.7	$\leq 1.42 \times 10^{-12}$	12.9

[a]Neutron fluence determined from neutron activation measurements.

[b]$\sigma_{g.s.}$(theory) = σ_{total}(theory) - $\sigma_{isomeric\ state}$(measured).

[c]The errors quoted below are associated with the AMS measurements and do not reflect the ±7% systematic error in the Nb(n,2n) cross section used to measure the neutron fluence.

(n,2n) reaction - minus the measured value for the (n,2n) production of the isomeric state is a factor of 2 too large. The RTNS data are summarized in Table 1. The U. of C. at Davis results are summarized in Table 2. The total

TABLE 2

PRELIMINARY RESULTS FROM THE U. of C. AT DAVIS FOILS [Be(d,n) NEUTRONS] FOR THE $^{27}Al(n,2n)^{26}Al$ REACTION

Sample	Angle	Distance	$^{26}Al/^{27}Al$ (theory)	$^{26}Al/^{27}Al$ (exp)[a]	Ratio [R(exp)/R(theory)][b]
A-I-0	0°	5 cm	2.36×10^{-9}	1.07×10^{-9}	0.453
A-1-3	0°	5 cm	2.01×10^{-9}	1.23×10^{-9}	0.613
A-I-2	29.5°	5 cm	3.32×10^{-10}	1.70×10^{-10}	0.512
				Avg Ratio =	0.526

[a]There is an 8% to 12% error in the experimentally measured ratio of $^{26}Al/^{27}Al$ from the AMS part of the experiment and a 10% systematic error in the neutron flux measurements.

[b]

$$\text{Ratio } \frac{R(\text{exp})}{R(\text{theory})} = \frac{^{26}Al/^{27}Al\ (\text{exp})}{^{26}Al/^{27}Al\ (\text{theory})}$$

(n,2n) cross section will be the sum of the (n,2n) cross section measured in this experiment for the production of the 5^+ ground state in ^{26}Al plus the previously measured cross section for the production of the 0^+ isomeric state. The sum of these two measured cross sections is only 52% of the theoretical cross section in the 14 to 16 MeV neutron energy region and increases to 66% of the theoretical cross section in the 22 to 24 MeV region. The above data suggest that the (n,2n) cross section for the production of the ground state of ^{26}Al is a factor of two lower than suggested by the theoretically calculated values that are presently being used in damage calculations. They are, however, in good agreement with the results of the radioactive counting experiment described in Section 5.2.

6.0 References

1. W. Henning, W. Kutschera, M. Paul, R. K. Smither, E. J. Stephenson, and J. L. Yutema, Nucl. Inst. and Meth. 184, p. 247 (1981).

2. Evaluated Nuclear Data File - V, National Cross Section Center, Brookhaven National Laboratory (1979).

3. G. S. Mani, G. J. McCallum, and A. T. G. Ferguson, Nucl. Phys. 19, p. 535 (1960).

4. E. A. Samworth, E. K. Warburton, and G. A. P. Engelbertink, Phys. Rev. C5, 138 (1972).

5. Von R. A. Rightmire, T. P. Kohman, and H. Hintenberger, Z. Naturforsch 139, p. 847 (1958) and Phys. Rev. 113, 1069 (1959).

6. L. R. Greenwood, D. Kneff, and M. Guinan, "Flux-Spectral Definition in RTNS-II," Chapter 2, "Dosimetry and Damage Analysis," DOE/ER-0046/3, p. 20-23 (1980).

7. D. W. Kneff, B. M. Oliver, M. M. Nakata. and H. Farrar. IV. "Flux-Soectral Definition in RTNS-II," Chapter 2, "Dosimetry and Damage Analysis,"' DOE/ER-0046/3, p. 25-33 (1980).

8. O. W. Kneff, H. Farrar, IV, L. R. Greenwood, and M. Guinan, "Characterization of the Be(d,n) Neutron Field by Passive Dosimetry Techniques," Proceedings of the Symposium on Neutron Cross Sections from 10 to 50 MeV, BNL-NCS-51245, Vol. 1, p. 113 (1980).

7.0 Future Work

The new "accelerator mass spectrometry" technique will be investigated as a possible dosimetry tool. The $^{27}Al(n,2n)^{26}Al$ reaction could be quite useful for high fluence dosimetry and, in particular, for monitoring the (d,t) reaction where the threshold of the (n,2n) Al reaction at 13.4 MeV (lab) makes it sensitive only to the primary neutron flux. It may also be useful for measuring the ion temperature in the plasma. The AMS technique may also be useful for transmutation studies, other possible dosimetry reactions like $^{60}Ni(n,2n)^{59}Ni$, $^{37}Cl(n,2n)^{36}Cl$, $^{10}B(n,p)^{10}Be$, and $^{13}C(n,\alpha)^{10}Be$ may also prove to be useful.

8.0 Publications

A publication is being prepared on this work in collaboration with W. Kutschera, W. Henning, and J. Yutema of the Physics Division of Argonne National Laboratory.

NUCLEAR DATA APPLICATIONS IN RADIATION DAMAGE STUDIES

F. M. Mann (Hanford Engineering Development Laboratory)

1.0 Objective

The objective of this work is to develop and maintain a computer code system to calculate the amounts of solid and gas transmutants at various facilities used by OFE experimentalists and to-supply processed ncclear data.

2.0 Summary

Vanadium was added to the nuclear cross section library associated with the transmutation code REAC. The REAC code was modified to include non-constant irradiation levels and to decrease computer costs.

The damage energy cross sections and helium production from ENDF/B-V were processed by the NJOY code for 25 materials.

3.0 Program

Title: Irradiation Effects Analysis (AKJ)
Principal Investigator: D.G.Doran
Affi1iation: Hanford Engineering Development Laboratory

4.0 Relevant DAFS Program Plan Task/Subtask

II.A.4.5 Gas Generation Rates
II.B.l Calculation of Defect Production Cross Sections
II.C.4.1 Effects of Solid Transmutation Products on Microstructure

5.0 Accomplishments and Status

5.1 Solid and Gas Transmutation Product Code Development

A major conclusion obtained using REAC to calculate transmutations in OFE facilities is that significant amounts of vanadium are formed in stainless steel irradiated in HFIR.[1] The initial calculation neglected any vanadium burnout (vanadium was not then in the nuclear cross section library associated with REAC, but burnout was estimated to be small). Vanadium cross sections from ENDF/B-V[2] were subsequently processed and put into the library. The HFIR calculation was rerun and as expected there is little vanadium burnout.[3]

The REAC code was modified to handle irradiations involving more than one irradiation cycle. During times of no flux, significant transmutations may occur due to decay. For example, the production rate of cobalt in 316 stainless steel irradiated in FMIT is projected to be reduced by about a third relative to a steady irradiation. This modification also allows more accurate calculation of multistep reactions and decays.

In order to decrease computer costs, an improved input/output scheme has been implemented for multi-irradiation cycle runs.

5.2 Calculation of Damage Parameters

The NJOY processing code[4] was used to calculate 55 group damage energy and gas production cross sections for 23 ENDF/B-V[5] materials: ^{6}Li, ^{7}Li, ^{10}B, ^{11}B, ^{12}C, ^{14}N, ^{16}O, ^{23}Na, Mg, Al, Si, P, S, Ca, Ti, V, Cr, Mn, Fe, Co, Ni, Cu, and Nb. As ENDF/B-V does not contain He production for Y and Mo, only damage energy cross sections were calculated for these isotopes. A constant flux weighting was used in the calculations. The results are on the NMFECC system.

The conversion of NJOY to process the new ENDF/B for high energy (>20 MeV) cross sections is continuing. Processing of the LANL high energy Fe evaluation was not completed due to an inadequate description of reaction channels in the evaluation. LANL plans to reformat their data so calculations can be done.

6.0 References

1. J.F.Bates, F.A.Garner, and F.M.Mann "The Effects of Transmutation Products on Swelling in 316 Stainless Steel" in the Damage Analysis and Fundamental Studies Quarterly Progress Report, Apr-Jun 1981 DOE/ER-0046/6, US DOE, 1981.

2. F.Guenther, D.Havel, R.Howerton, F.Mann, D.Smith, A.Smith, and J.Whalen, Fast Neutron Cross Sections of Vanadium and an Evaluated Neutronic File ANL/NDM-24 Argonne National Laboratory, 1977.

3. F.A.Garner, F.M.Mann, and H.R.Brager, "The Effects of Transmutation Products on Swelling in 316 Stainless Steel" in the Damage Analysis and Fundamental Studies Quarterly Progress Report. July-Aug 1981 DOE/ER-0046/7.

4. R.E.MacFarlane, R.J.Barrett, D.W.Muir, and R.M.Boicourt, "The NJOY Nuclear Data Processing System: User's Manual" LA-8626-MS (ENDF-304) Los Alamos National Laboratory, 1978.

5. R.Kinsey (compiler), "ENDF-201, ENDF/B Summary Documentation" BNL-NCS 17541, 3rd Edition, Brookhaven National Laboratory, 1979.

7.0 Future Work

Expand the nuclear cross section library to include Ti and Mo.

Complete conversion of NJOY processing code to handle high energy evaluations.

REFLECTION OF LOW-ENERGY HELIUM ATOMS FROM TUNGSTEN SURFACES

Mark T. Robinson (Oak Ridge National Laboratory)

1.0 Objective

The purpose of this study is to construct atomistic numerical models of the development of collision cascades in solids and to apply them to studies of radiation damage production, sputtering, and plasma particle backscattering, in the context of fusion first wall materials development.

2.0 Summary

The computer program MARLOWE (Version 11.5) has been used to simulate the reflection of 8-eV to 1.5-keV helium atoms from monocrystalline, polycrystal1ine, and amorphous tungsten targets. The results are compared with recent experiments of van Gorkum and Kornelsen on <001> targets and of Seidman, et al., on <011> targets. The comparisons of calculated and measured ion ranges indicate that the electronic stopping cross section of low-energy helium atoms in tungsten is significantly greater than the traditional LSS value. The reflection coefficients calculated for the <001> surface are in fair agreement with experiment.

3.0 Program

Title: Damage Analysis and Dosimetry
Principal Investigator: M. T. Robinson
Affiliation: Oak Ridge National Laboratory

4.0 Relevant OAFS and PMI Program Plan Task/Subtask

Subtask III.B.1.3 Reflection and Backscattering: Development of Theoretical Model Descriptions

5.0 Accomplishements and Status

5.1 Introduction

The interactions of low energy ions with solid surfaces play an important role in the design and performance of limiters and divertors, as well as in other areas of fusion technology. Experimental information is very limited, mainly because most backscattered particles are electrically neutral and are thus difficult to detect. This is especially true of helium ions. Consequently, considerable reliance has been placed on computation to supply the needed information. Mashkova[1] has reviewed the earlier experimental and theoretical work in this area. New experimental information has recently become available on the interactions of very low energy helium ions with monocrystalline tungsten targets. Such data supply an opportunity to test the computational models on a system of some interest in the fusion materials program.

5.2 Experimental Background

In an experimental method developed by van Gorkum and Kornelsen,[2-4] a tungsten single crystal with a {001} surface is first implanted with a small concentration of argon or xenon atoms, which serve to trap subsequently implanted helium atoms. After the desired irradiation with helium ions, the implanted helium atoms are thermally desorbed from the specimen. The desorption curves can be interpreted to yield the total amount of trapped helium and the mean depth of penetration of the ions into the target. The technique has been used to study the channeling of 50 eV to 4 keV ^{4}He ions in the tungsten <001> direction.[5] The same method has recently been used[6] to estimate the reflection coefficients of 8 eV to 5 keV ^{4}He ions from tungsten <001> crystals as well as their mean depths of penetration into these targets. The main uncertainty in this technique is associated with the exact nature and mechanism of the trapping process.

Seidman and his coworkers[7-9] have developed a field ion microscope (FIM) technique for studying helium implanted into tungsten. The implantation is made at 60 K to prevent migration of the stopped helium particles. The target is in the form of a rod with an approximately hemispherical tip, about 30 nm in radius. The axis of the specimen is a crystallographic <011> direction. The ions are incident parallel to this axis. After the helium is implanted, the target is sectioned by pulsed field evaporation in the FIM and the particles removed are identified by an atom probe. The analysis is restricted to the central part of the specimen: only those helium atoms are counted which reside within a tube of about 3 nm radius surrounding the specimen axis. This technique has been used to estimate the penetration depth distributions of 100 eV to 1.5 keV ^{3}He and ^{4}He ions in tungsten <011> FIM tips.[7,8] It has also been used[9] to measure the reflection coefficients in the same cases. In the latter measurements, a rather large correction must be made, since only that part of the implanted helium which is desorbed as He^+ ions is detected. The balance of the helium is removed as WHe^{+3} ions which cannot be distinguished from W^{+3}. This correction is a probable source of considerable uncertainty in the results.[9,10] No such correction is needed in range determinations.

5.3 The Computational Model

The computational model is described in detail elsewhere.[11] The trajectories of the incident helium ions were constructed in the binary collision approximation, using the computer code MARLOWE (Version 11.5). The interactions of the helium atoms with the tungsten target atoms were described by the Molière potential with the Firsov screening length (10.08 pm). At incident kinetic energies above 200 eV, the maximum impact parameter in a collision was taken as p_c/a = 0.6, where a = 0.31655 nm is the lattice constant of tungsten. At incident energies *below* 100 eV, p_c/a = 0.8 was used. In the intermediate region, where both values were tested, the computed reflection coefficients and helium ion ranges were substantially the same. An inelastic energy loss proportional to the projectile velocity

was based on the nonlocal LSS model. An incident particle was considered to be stopped when its kinetic energy fell below a value E_c, except for those particles colliding near the target surfaces. These were followed below E_c until they either escaped from the crystal or turned inwards. Changing E_c from 5 eV to 2 eV produced insignificant changes in the results for incident kinetic energies greater than about 50 eV. Only below 30 eV were significant numbers of particles emitted with kinetic energies less than E_c. Results up to 100 eV are based on sets of 5000 incident particles uniformly distributed over the target surface; above 100 eV, 1000 particles were used.

Particle reflection coefficients, ion penetration depths, and other quantities were evaluated for helium ions normally incident on four different tungsten targets: <001> and <011> monocrystals, a polycrystalline target, and an amorphous one. Most calculations used a static lattice, that is, one in which there were no thermal displacements of the atoms from their ideal sites. In a few calculations, thermal displacements were included in the model using Θ_D = 300 K as the Oebye temperature of tungsten.[12] The distribution of displacements was Gaussian. The polycrystalline target was simulated by making a random isotropic rotation of the crystal at the beginning of each trajectory. An amorphous medium was simulated by performing another such rotation after each collision in which an impact parameter less than the mean atomic radius (0.4924 a for bcc crystals) was encountered.

The most uncertain part of the computational model is the inelastic energy loss. There are no experiments available on the electronic stopping of very low energy helium ions. A recent compilation[13] arrives at an electronic stopping cross section for helium in tungsten which is about 70% greater than the LSS value at 1 keV. It also depends somewhat more weakly on the particle velocity. Unfortunately, this prediction is probably not more reliable than the original LSS one at these very low energies.

5.4 Computed Reflection Coefficients and Ranges

Studies were made of the differences in behavior between ^3He and ^4He ions, but no discernible isotope effect was found. The inelastic (electronic) stopping cross section of ^3He ions in tungsten is about 15% greater than that of ^4He ions of the same kinetic energy, On the other hand, the elastic stopping cross section of ^4He is about 25% greater than that of ^3He. Since both processes contribute appreciably to the stopping in the energy range examined here, their separate isotope effects will offset each other to a large extent and only a small net isotope effect is expected. The smallness of the isotope effect found *is* in general agreement with the limited experimental data.[8,9] In the remaining calculations, therefore, only ^4He ions were studied.

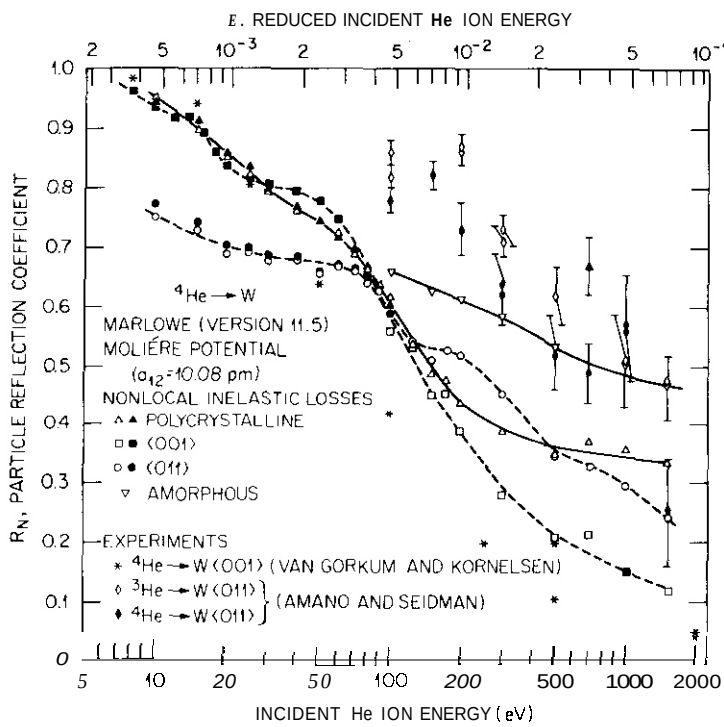

FIGURE 1. Particle Reflection Coefficients Calculated for ^4He Ions Normally Incident on Various Tungsten Surfaces, Compared with Experiments.[6,9]. The upper scale shows $\varepsilon = E/E_L$, where E_L = 21.6 keV.

Figure 1 shows the particle reflection coefficients, R_N, calculated for each static target, as well as the available experimental data.[6,9] Several aspects of the computations are worthy of mention. First, above 100 eV, the values of R_N for the amorphous target are greater than those for the polycrystalline one. Above 300 eV, the difference is some 25%, about the same as has been reported previously[14] for the reflection of low energy hydrogen ions from metals. This behavior is a result of the channeling of the incident particles along the more open directions of the crystal lattice. In the bcc structure, these are the <111>, <001>, and <011> directions in particular. Second, above 100 eV, the two monocrystals are ordered as expected: the more open <001> target has smaller values of R_N than does the <011> target. Third, below 100 eV, the order of the monocrystal targets is reversed. The origin of this behavior has not been ascertained unequivocally, but it appears to be associated with subsurface channeling.[15,16] It may be noted that the {011} planes are the densest in the bcc structure, lending support to this suggestion.

Figure 2 shows the values of the mean ^4He atom penetration depth, $\langle x \rangle$, calculated for each static target, as well as the available experimental data.[6-8] This range quantity is measured along the normal to the target surface. As expected from the foregoing discussion, the amorphous target shows substantially the smallest penetration above about 100 eV and the <001> target shows the largest. Below 100 eV, the values of $\langle x \rangle$ are roughly the same for all targets. In addition, the figure shows the mean maximum penetration of the reflected particles, $\langle x_R \rangle m$ for the <001> target only. Below 100 eV, the reflected particles sample approximately the same depths as do the trapped particles, but above this energy, they are much more closely restricted to the surface region than are the trapped ones. Finally, the figure shows the man transverse range $\langle \rho \rangle$, for the <001> target. This quantity is the average distance that the ions move perpendicular to their original direction of motion and is a measure of the lateral straggling of the implanted particles. The values for the <011> target are about twice as great as those shown for the <001> target.

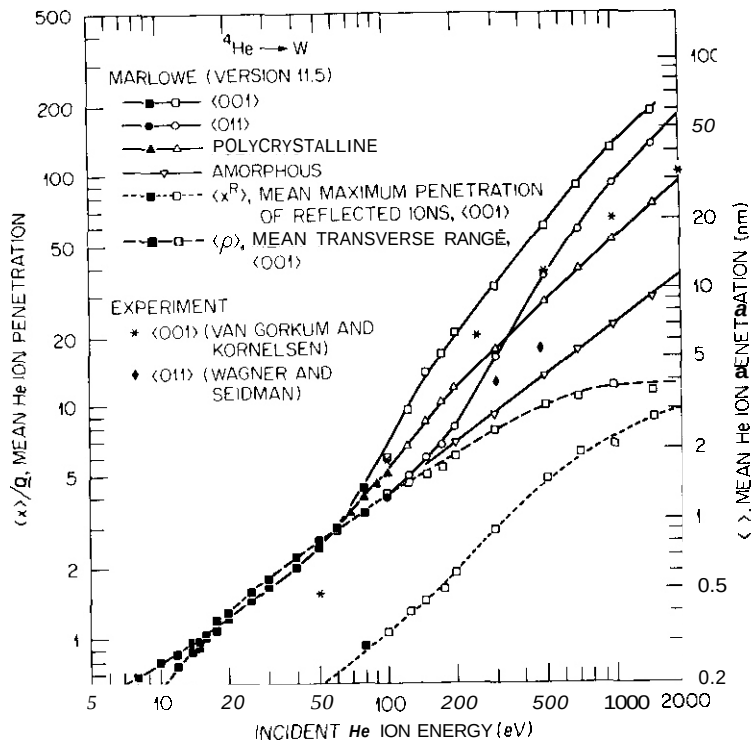

FIGURE 2. Ranges Calculated for ^{4}He Ions Normally Incident on Various Tungsten Surfaces, Compared with Experiments.[6,7] The left-hand scale is in units of the cubic lattice constant of tungsten, a = 0.316522 nm.

The penetration distributions for the static ⟨001⟩ target were bimodal at incident kinetic energies as low as 100 eV. The more deeply penetrating group consisted of well-channeled particles which lost energy almost entirely inelastically. Its population and separation from the shallower group of particles increased with increasing energy. Such well-channeled particle trajectories would be expected to be sensitive to thermal displacements of the lattice atoms. A few calculations to test this sensitivity are collected in Table I for the ⟨001⟩ target and in Table II for the ⟨011⟩ target. Thermal displacements had only a slight effect on the reflection coefficients, raising them by about the amount of the statistical uncertainty in the computed values (±0.015).

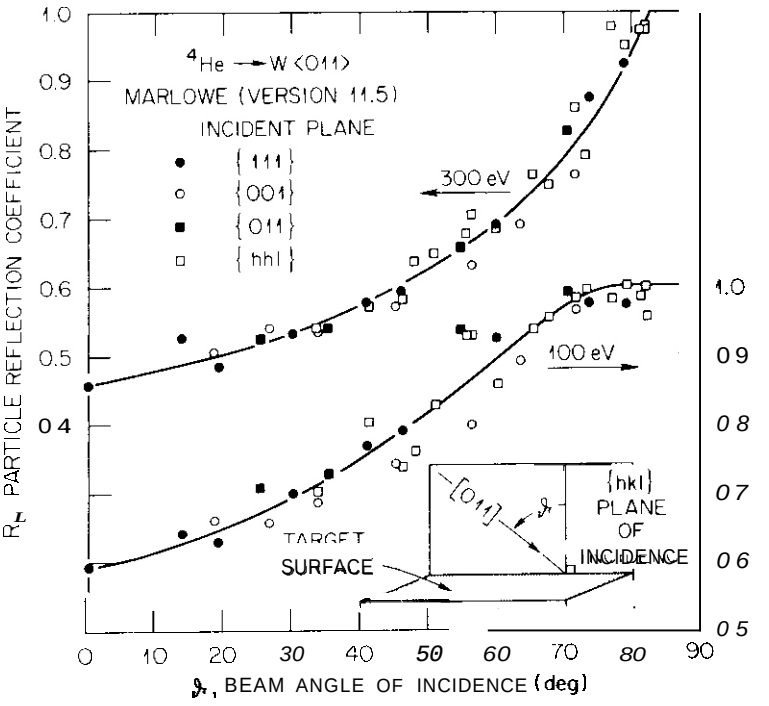

FIGURE 3. The Calculated Effect of the Angle of Incidence on the Reflection of ^{4}He Ions from Tungsten Surfaces. The ions are always incident along <011> directions. The inset shows the geometry.

complexities of backscattering from monocrystalline targets. The value of R_N depends not only on the orientation of the surface and the direction of the beam, but also on the plane in which the beam is incident. Nevertheless, the results in Fig. 3 are similar to those reported earlier[17] for low energy hydrogen and helium ions backscattered from amorphous copper targets. From this figure, it is clear that the angle of incidence alone is insufficient to account for the differences between the calculations and the experiments on <011> crystals. The penetration depths calculated for the static <001> and <011> targets are not in very good agreement with the experiments.[6-8] However, when thermal displacements are introduced, the discrepancies between the calculated and observed ranges are greatly reduced (see Tables 1 and 2). The remaining discrepancies suggest that

TABLE 1

EFFECTS OF THERMAL DISPLACEMENTS ON MEAN ^{4}He PENETRATION DEPTHS IN W <001> CRYSTALS (Θ_D = 300 K)

^{4}He Energy (eV)	<x>/a, Static	Mean Penetration Depth 300 K	Exper[6]
500	59.3±1.5	39.8±1.0	37.5
1000	128.7±2.3	79.2±1.7	63.9
1500	187.2±2.8	118.7i2.2	83.2[a]

[a]Interpolated

TABLE 2

EFFECTS OF THERMAL DISPLACEMENTS ON MEAN ^{4}He PENETRATION DEPTHS IN W <011> CRYSTALS (Θ_D = 300 K)

^{4}He Energy (eV)	<x>/a, Static	Mean Penetration Depth 60 K	Exper[8]
300	16.1±0.6	13.0k0.4	14.2±1.6
500	36.7±1.1	30.3±0.9	19.5k3.0

5.5 Comparisons with Experiment

The computed values of R/N/ for the <001> surface show generally satisfactory agreement with the experiments of van Gorkum and Kornelsen.[6] The agreement could be improved by increasing the inelastic stopping cross section. The somewhat complex dependence of R_N on the incident ion energy shows the importance of channeling even at these low energies. Indeed,

Kornelsen and van Gorkum[5] have been able to demonstrate and study the channeling of helium ions along the <001> direction of tungsten at energies above about 50 eV. Thus, the rather rapid decrease of R_N which begins near 60 eV may be attributed to channeling of the incident ions along the rather open bcc <001> direction. The decrease near 18 eV has not been identified, but is probably to be associated with subsurface channeling.[15,16]

The computed values of R_N for the <011> target agree only rather poorly with the measurements of Amano and Seidman.[9] In these experiments, however, in addition to the uncertainty in the absolute amount of implanted helium, not all of the ions were normally incident on the tip. If the incident ions slowed down without lateral straggling, the particles coming to rest in the region of the specimen which was analyzed would have entered it directly at the surface. The maximum angle of incidence included in the analysis would have been $\sin^{-1} r/R$, where r is the radius of the region analyzed and R is the radius of curvature of the FIM specimen tip. From the description of the experiment,[8] this maximum angle was about 6 degrees, approximately the divergence of the incident beam. Lateral motion of the implanted ions, however, can substantially increase the maximum angle of incidence which must be considered in the analysis, since particles striking the tip well outside of the analysis region can wander into this region. To estimate the effects of lateral straggling, the mean transverse range must be added to the radius of the analysis region. If this is done, the maximum angle of incidence is roughly 10 degrees, depending on the incident energy.

The calculated influence of the angle of incidence in the <011> experiment is shown in Fig. 3. The incident ^{4}He ions were always directed along a <011> crystal direction, onto several different low index crystal surfaces. For instance, when a (321) surface was used, there were six nonequivalent <011> directions available, at angles of incidence ranging from 19 degrees to 79 degrees. The figure was constructed from such calculations made at two energies. The scatter of the points in the figure illustrates the

the inelastic stopping cross section of helium ions in tungsten should be increased, perhaps by 50 to 75%. This conclusion is consistent with that of a recent compilation[13] and also with recent experiments on the stopping of low energy helium ions in gold,[18] where an electronic stopping cross section 50% larger than the LSS value was found.

5.6 Conclusions

The reflection coefficients calculated for the <001> target show fair agreement with the available experiments.[6] The much poorer agreement of the calculations for the <011> target is probably a result of the uncertainty in an important correction in the corresponding experiments.[9,10] The agreement of the calculated ranges with the experiments[6-8] is only fair, but suggests that the inelastic stopping cross section of low energy helium ions in tungsten is significantly larger than the traditional LSS value.

5.7 Acknowledgements

I am indebted to D. N. Seidman for permission to cite the experimental results obtained by his group in advance of publication and for several illuminating discussions. I also wish to express my appreciation to to O. S. Oen for numerous discussions of this work.

6.0 References

1. E. S. Mashkova, "Reflection of particles and energy from structural materials," Fiz. Plasmy, 5, 1385-1398 (1979) [Engl. transl.: Sov. J. Plasma Phys., 5, 777-786 (1979)].

2. A. A. van Gorkum and E. V. Kornelsen, "Attachment of mobile particles to non-saturable traps. I. A theoretical model," Rad. Effects, 42, 93-111 (1979).

3. E. V. Kornelsen and A. A. van Gorkum, "Attachment of mobile particles to non-saturable traps. II. The trapping of helium at xenon atoms in tungsten," Rad. Effects, 42, 113-124 (1979).

4. A. A. van Gorkum, "Quantitative thermal desorption spectrometry of noble gases in solids," Thesis, Delft, 1981.

5. E. V. Kornelsen and A. A. van Gorkum, "Enhanced penetration of low energy (25 eV - 5000 eV) helium along the <100> channel in tungsten," Nucl. Instr. Methods, 170, 161-170 (1980).

6. A. A. van Gorkum and E. V. Kornelsen, "The entrance probability and range of helium in W(100) for energies 8 eV to 5000 eV as measured by thermal desorption spectrometry," Rad. Effects, 52, 25-34 (1980).

7. A. Wagner and D. N. Seidman, "Range profiles of 300- and 475-eV $^4He^+$ ions and the diffusivity of ^4He in tungsten," Phys. Rev. Letters, 42, 515-518 (1979).

8. J. Amano, A. Wagner, and D. N. Seidman, "Range profiles of low-energy (100 to 1500 eV) implanted ^3He and ^4He atoms in tungsten: I. Experimental results," submitted for publication; Cornell University Materials Science Center Report COO-3158-72 (1980).

9. J. Amano and D. N. Seidman, "Direct experimental determination of the particle reflection coefficients of low-energy (100 to 1500 eV) ^3He and ^4He atoms from the (110) plane of tungsten," submitted for publication; Cornell Univ. Materials Science Center Report DOE/ER/03518-93 (1981).

10. D. N. Seidman, private communication.

11. M. T. Robinson, "Theoretical aspects of monocrystal sputtering," in Sputtering by Ion Bombardment: Physics and Applications, R. Behrisch (Ed.), (Springer-Verlag, Berlin, Heidelberg, New York, 1981) p. 73-144.

12. This value is in the range given by K. Lonsdale, "Atomic scattering factors. Temperature and other modifying factors," in International Tables for X-ray Crystallography, C. H. MacGillavry and G. D. Rieck (Eds.), (Intern. Union of Crystallography, The Kynoch Press, Birmingham, U. K., 1968), Vol. 3, p. 235.

13. J. F. Ziegler, Helium Stopping Powers and Ranges in All Elemental Matter, (Pergamon, New York, 1977).

14. O. S. Oen and M. T. Robinson, "Computer studies of the scattering of low energy hydrogen ions from polycrystalline solids," J. Nucl. Mater., 63, 210-214 (1976).

15. R. Sizmann and C. Varelas, "Surface channeling," Nucl. Instr. Methods, 132, 633-638 (1976).

16. M. Hou and M. T. Robinson, "The conditions for total reflection of low-energy atoms from crystal surfaces," Appl. Phys., 17, 371-375 (1978).

17. O. S. Oen and M. T. Robinson, "Computer studies of the reflection of light ions from solids," Nucl. Instr. Methods, 132, 647-653 (1976).

18. R. Blume, W. Eckstein, and H. Verbeek, "Electronic energy loss of H, D, and He in Au below 20 keV," Nucl. Instr. Methods, 168, 57-62 (1980).

7.0 Future Work

Exploratory calculations will be carried out to find an optimal value for the electronic (inelastic) stopping cross section of low energy helium atoms in tungsten. The exploration rmst include not only the magnitude of the cross section, but rmst also consider the extent to which it should be considered as nonlocal. The cross section finally selected will be used to repeat the calculations reported above.

8.0 Publications

None.

RADIATION DAMAGE STUDIES

G.L. Kulcinski, R.A. Dodd, and H. Attaya (University of Wisconsin-Fadison)

1.0 Objective

The objective of this work is to develop a computer program which is accurate and economical for predicting ranges and damage of ions in material. The code should also take into account the effect of nonuniformities on the ultimate range or damage distributions, and it should also be suitable for studying different aspects of radiation damage (e.g., sputtering, backscattering, etc.)

2.0 Summary

The range and damage calculations of the Monte Carlo computer program HERAD are compared with recent range and damage experimental data. The effect of the presence of nonuniformities which are developed during radiation is considered in the damage calculation. The effect of electronic stopping on the damage is also studied.

3.0 Program

Title: Radiation Damage Studies
Principal Investigators: G.L. Kulcinski, R.A. Dodd
Affiliation: University of Wisconsin-Madison

4.0 Relevant DAFS Program Task/Subtask

DAFS Subtask II.B.2.3

5.0 Accomplishments and Status

5.1 Introduction

Recent measurements of the damage produced by ion bombardment in material show that there are large differences between the measured damage profile and the calculated damage profile. In general, the measured damage profile is deeper than the calculated profile.[1,2] In this paper we try to investigate the reasons for such differences. Two effects are considered here, namely, the effect of the presence of cavities in the material, and the effect of the electronic stopping on the damage distribution.

With respect to the inclusion of cavities in the range or damage distribution calculations one important point should be underlined: the solution obtained for these quantities based on LSS[3] theory is when all atoms in motion come to rest, i.e., at infinite time. Consequently, one cannot modify this solution to take into account the non-uniformity of the target which has been developed during the irradiation. To have this effect on the distribution functions of the range and the damage one should use the forward transport formalism.[4] This means that the presence of the nonuniformity should be considered during the slowing down not after it.

An alternative approach is the Monte Carlo simulation of the ion transport. A Monte Carlo computer program "HERAD" has been written to simulate the transport of ions and knock-on atoms in a uniform or nonuniform material.[5,6] A full description of HERAD is given elsewhere.[7]

In the next section we will compare the results of HERAD with recent measurements of ranges of heavy ions in silicon. Following that, the effect of nonuniformity for the case of 14-MeV Cu ions in nickel is discussed. Finally, the effect of various electronic stopping laws for the case of 20-keV He on nickel is examined.

5.2 Comparison With Range Measurements

There have been many recent experimental studies of the range of low energy heavy ions in Si and Al because of their importance in the semi-conductor industry. We will utilize some of this later to calibrate the HERAD code. Figure 1 shows the predictions from the HERAD code for the projected range of 5, 10, 15, 30, and 60-keV antimony ions incident on Si. The results are compared to the experimental results of Oetzmann[8] et al. Also shown in the same figure the results of the BRICE[9] and the TRIM[10] codes. The excellent agreement of HERAD results with the experimental results may be attributed to the use of Born-Mayer potential for reduced energy less than ~ 0.001. The Moliere or Thomas Fermi potentials used by TRIM and BRICE, respectively, would increase the nuclear stopping for such low energies and consequently underestimate the ranges.

Next in this regard is the comparison with experimental results obtained by Combasson et al[11] for different ions with different energies incident on Si. Table 1 shows the calculated results of HERAD compared with these experimental data. The agreement with respect to the projected range and the straggling in the projected ranges is excellent and it is within the experimental errors which were ~ ± 7%.

5.3 The Effect of Non-Uniformity on the Damage Distribution (14 MeV Cu-Ni)

Whitley et al[1] found a difference of ~ 15-20% between the peak of the measured damage distribution, swelling in this case, and the calculated damage distribution by the BRICE code. Figure 2 shows the comparison between prediction from HERAD and BRICE for 14-MeV Cu ions incident on an uniform Ni target. The difference in projected range between BRICE and HERAD was only 80 A and the difference in the straggling of the projected range is only 26 A.

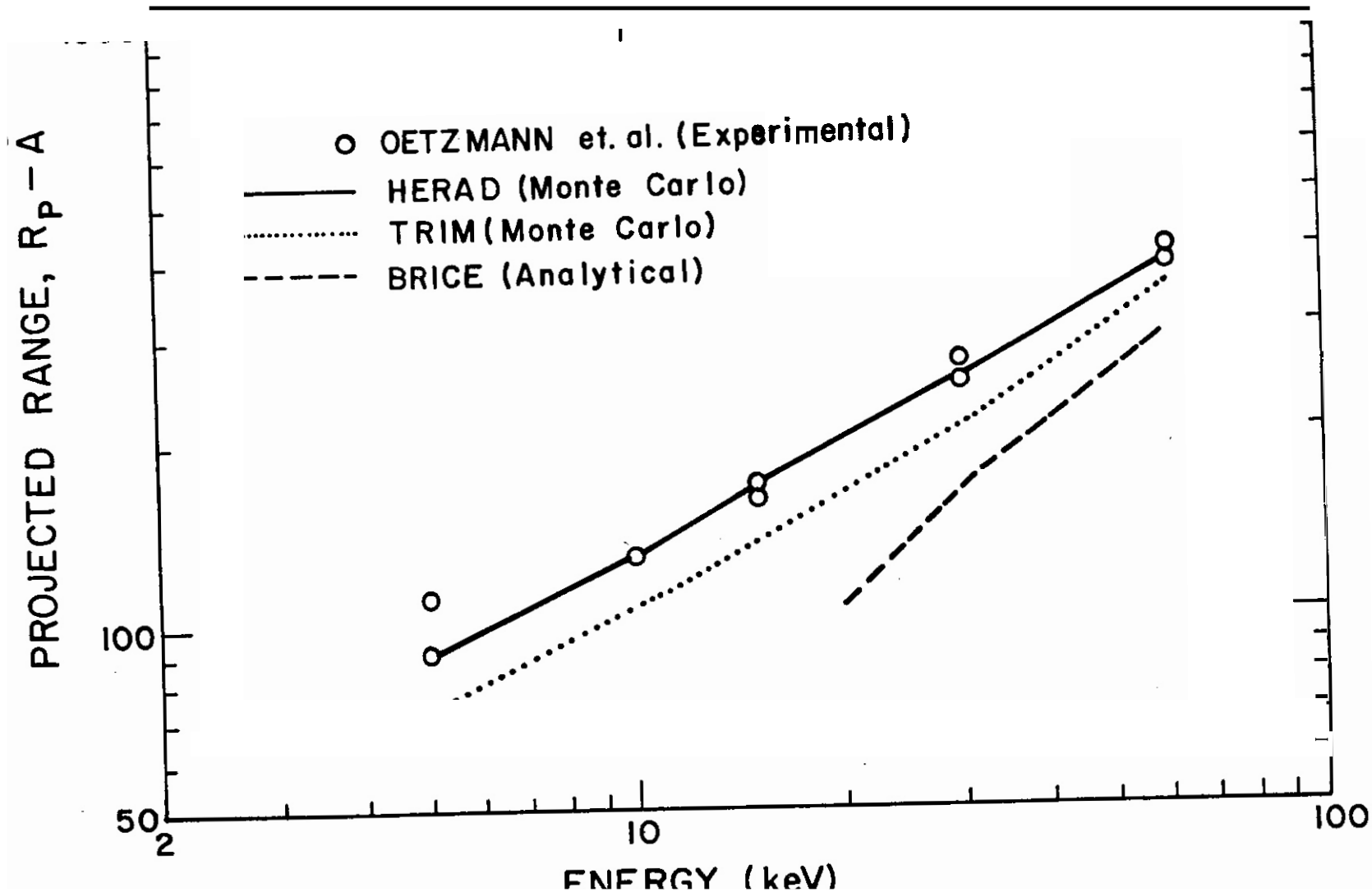

FIGURE 1. The Projected Range for 15-, 30-, and 60-keV Sb-Si

TABLE 1

COMPARISON BETWEEN HERAD RESULTS (CALC.) AND THE EXPERIMENTAL RESULTS (OBS.) OF COMBASSON ET AL[15] FOR Eu, Gd, Tb, AND Dy IONS IN SILICON

Ion	E(keV)	20	40	60	80	100	120	160	180
$_{63}Eu^{153}$									
	R_p (obs.)	159	236	318	352		496	656	684
	R_p (calc.)	162	246	322	382		514	680	755
	ΔR_p (obs.)	50	81	92	125		154	190	222
	ΔR_p (calc.)	42	64	84	108		140	175	198
$_{63}Gd^{158}$									
	R_p (obs.)	153	246	316	387		503	609	707
	R_p (calc.)	159	250	323	390		523	653	732
	ΔR_p (obs.)	48	77	97	122		166	185	203
	ΔR_p (calc.)	42	63	92	103		133	172	196
$_{65}Tb^{159}$									
	R_p (obs.)	169	251	313	367	434	501	611	685
	R_p (calc.)	163	248	317	380	451	517	633	712
	ΔR_p (obs.)	50	86	97	118	123	160	193	233
	ΔR_p (calc.)	41	65	84	102	118	139	166	188
$_{66}Dy^{164}$									
	R_p (obs.)	169	252	334	371	447	505	603	704
	R_p (calc.)	164	246	319	387	450	519	645	780
	ΔR_p (obs.)	56	81	111	115	131	171	187	211
	ΔR_p (calc.)	40	63	82	102	120	140	165	1 3

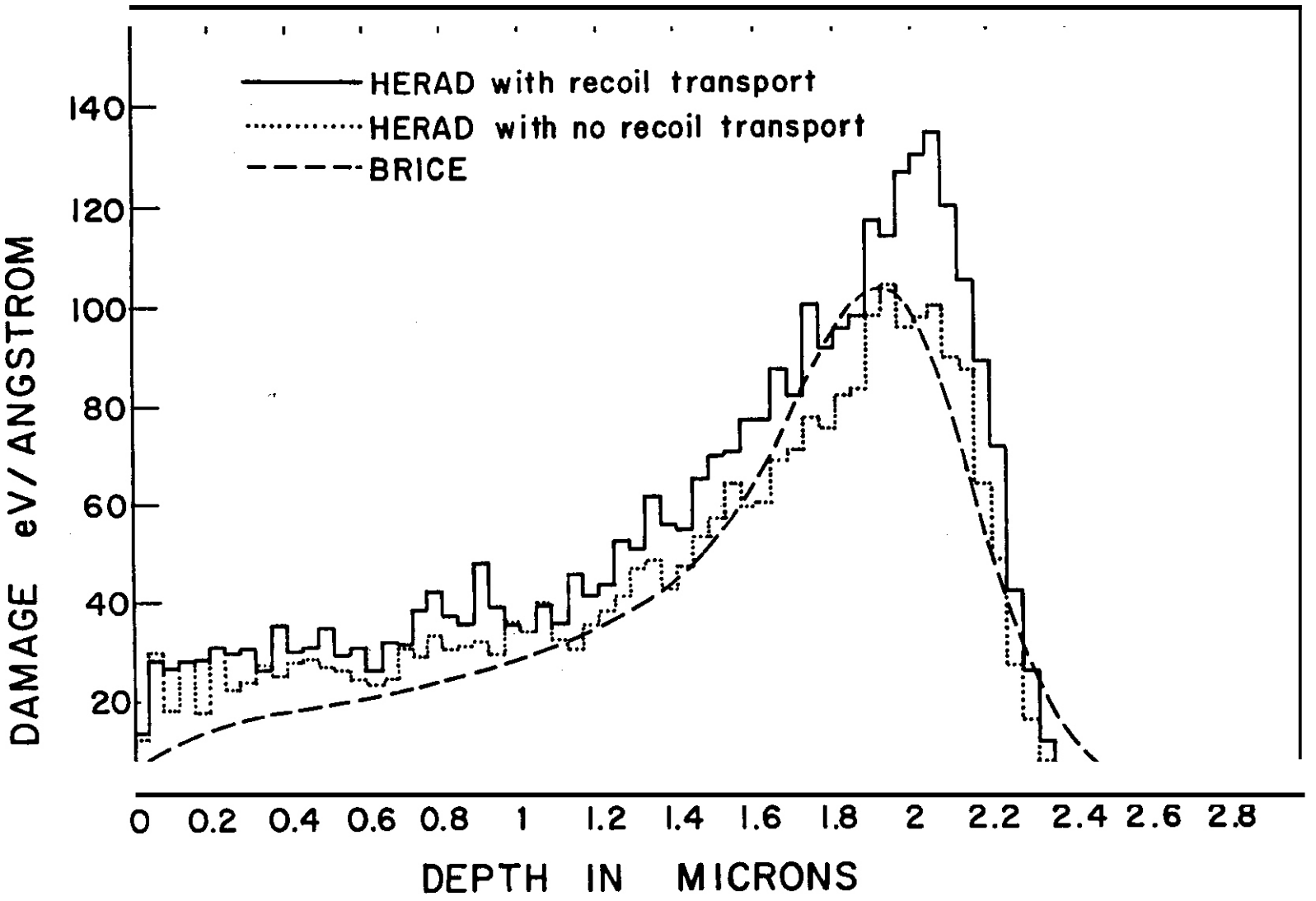

FIGURE 2. The Damage Distribution for 14-MeV Cu on Void-Free Nickel Target.

The peak of HERAD distribution is slightly deeper than that of BRICE. The dotted curve is for the damage as calculated by following only the PKAs (which is similar to Brice), where the recoil transport is included in the damage calculation. The solid curve gives the damage calculated by following all the moving atoms in the cascades.

Figure 3 shows the measured swelling profile of Whitley[1] together with calculated damage distribution by HERAD, including nonuniformities in the calculation. Also shown is the damage distribution of Brice, which is exactly the same as in Fig. 2. One can see that the calculated damage profile is deeper in the target, and the peaks of the measured and the calculated damage distributions coincide. However, at the end of the range (– 2.5 → 2.8 μ) the theoretical calculations cannot accurately predict the measured damage in this range.

5.4 Effect of Electronic Energy Loss

Fenske et al[2] have recently measured the swelling profile as a function of the implant depth for 20 keV He ions in nickel. The difference reported there between the theoretical prediction (using Brice and TRIM) of the damage profile and the measured swelling profile was as much as 50%.

The inclusion of voids was not sufficient to reduce such big difference (Fig. 4a). We have studied the effect of the electronic energy on the damage distribution in this case. The following ratios of the normal LSS electronic stopping were used 1., 0.8, 0.6, 0.4, 0.2, and 0 (i.e., with electronic stopping completely neglected). Figures 4a- 4f show the results of these calculations. The reduction of LSS electronic stopping by 20% as usually recommended appears to have very little effect on the agreement between the calculated and the measured damage profiles.

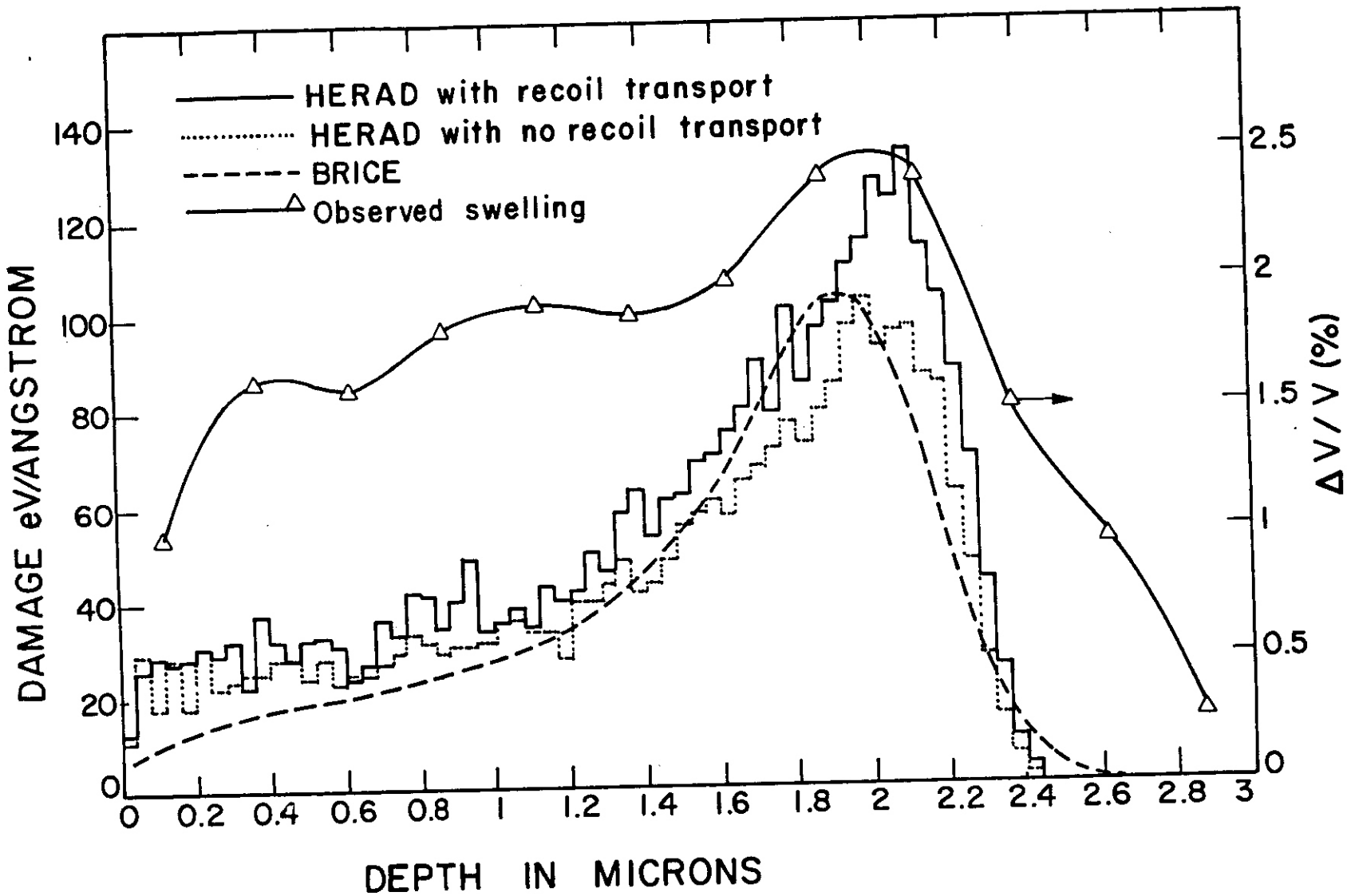

FIGURE 3 The Damage Energy for 14-MeV Cu Ions Incident on Nickel Target Containing Voids

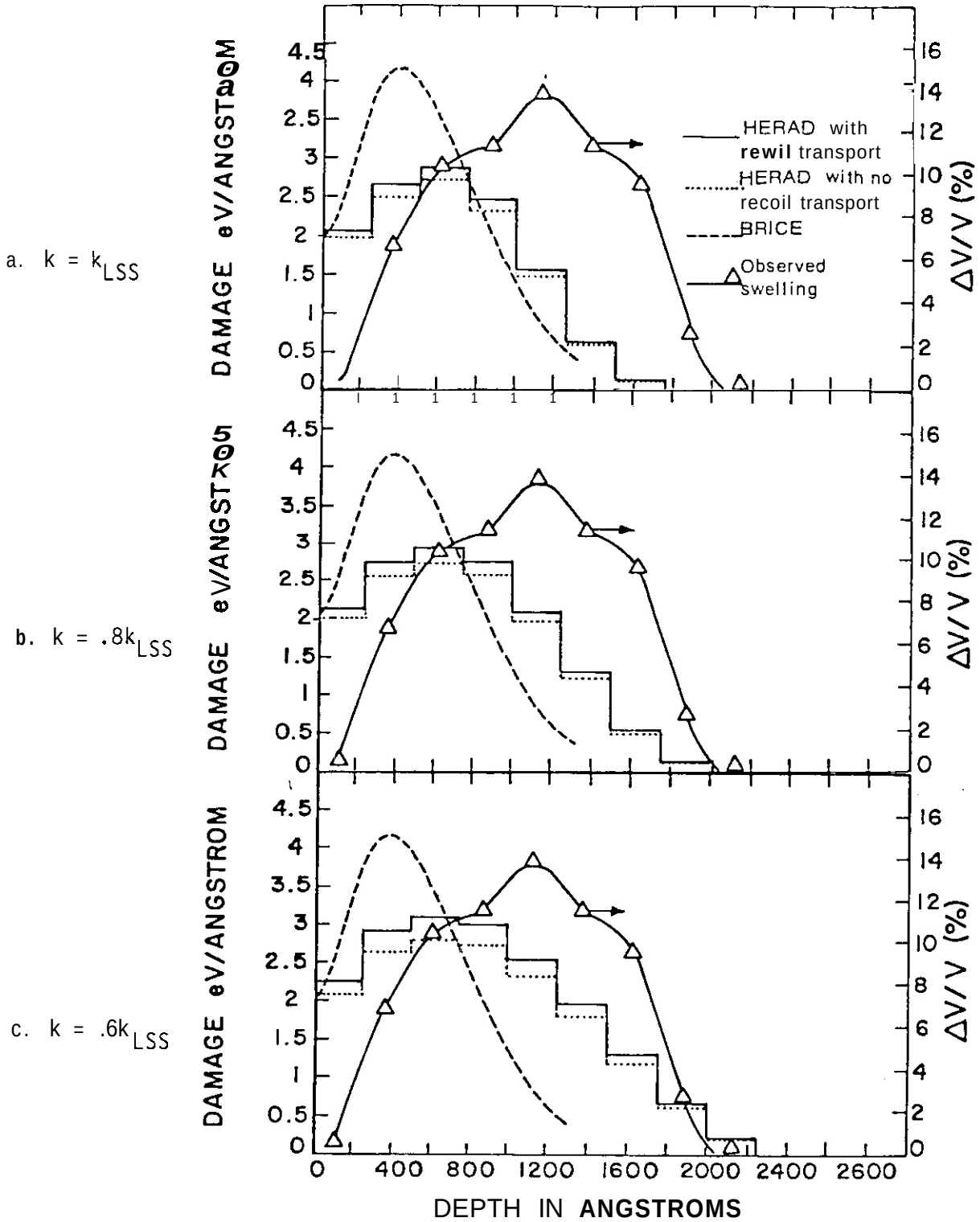

FIGURE 4. The **Swelling and Damage Profiles for** 20-keV He **Ions on** Ni, **Different Electronic Stopping Used in** HERAD.

d. $k = .4k_{LSS}$

e. $k = .2k_{LSS}$

f. $k = 0.0$

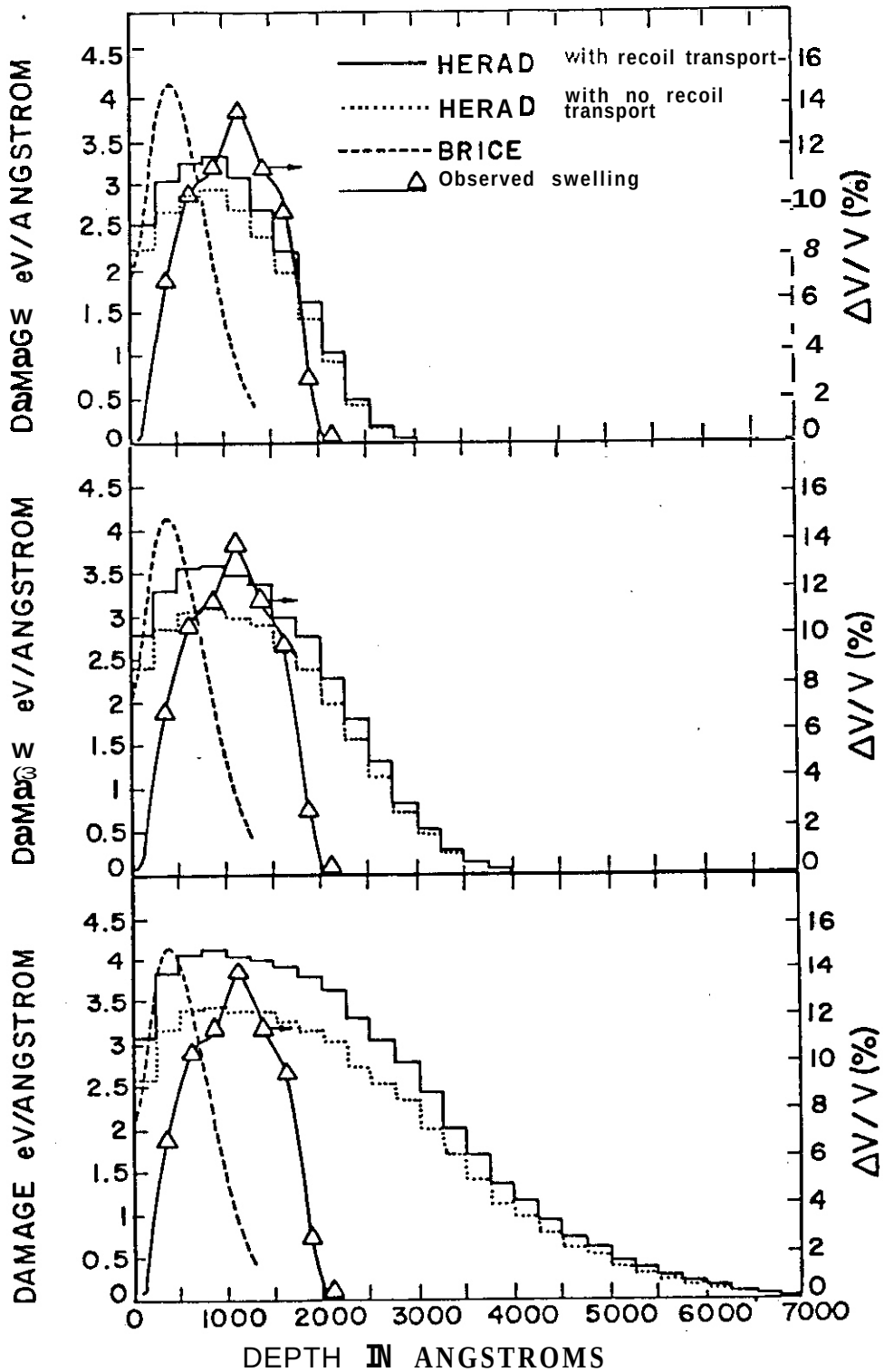

FIGURE 4. Cont'd.

Reducing the electronic stopping to 40%, or even 20%, of the "normal" value shows a much closer agreement between the calculated damage and the measured one, and perhaps the best value would be a value 30% of the "normal" number. Unfortunately, there are no experimental measurements for electronic stopping of He in Ni for energies below 30 keV.

5.5 Conclusions

The peak of the calculated damage profile using HERAO is closer to observed swelling peaks than that predicted by the Brice code regardless of whether voids were, or were not, included in the calculation. When the voids are included in the calculation the damage peak moves closer to that of the measured swelling profile. However, it was not possible to completely match the swelling profile at the end of the range of 14 MeV Cu ions on Ni. Finally, the LSS electronic stopping seems to highly overestimate the electronic stopping loss for low Z ions in metals.

6.0 References

1. J.B. Whitley, G.L. Kulcinski, H.V. Smith, Jr., and P. Wilkes, "Effect of Radiation on Structural Materials", ASTM STP 653, pp. 125-147, J.A. Sprague and D. Kramer, Eds.

2. G. Fenske, S.K. Das, and M. Kaminsky, to be published in Appl. Phys. Lett.

3. J. Lindhard, V. Nielson, M. Scharff, and P.V. Thomson, Mat. Fys. Medd. Dan. Vid. Selsk. 33, 10 (1963).

4. M.M.R. Williams, Prog. Nucl. Energy 3, 1 (1979).

5. H. Attaya and G.L. Kulcinski, Trans. ANS 34, 224 (1980).

6. H. Attaya and G.L. Kulcinski, Trans. ANS 38, 317 (1981).

7. H. Attaya, Ph.D Thesis, University of Wisconsin, 1951.

8. H. Oetzmann, A. Feuerstein, H. Grahmann, and S. Kalibtzer, Phys. Lett. 55A, 170 (1975).

9. D.K. Brice, Ion Implantation Range and Energy Deposition Codes COREL, RASE4 and DAMG2, SAND 75-0622 (1977).

10. J.B. Biersack and L.G. Haggmark, Nucl. Inst. Meth. 174, 257 (1980).

11. J.L. Combasson, B.W. Farmery, D. McMullock, G.W. Neilson, and M.W. Thompson, Rad. Eff. 36, 149 (1978).

CHAPTER 3

FUNDAMENTAL MECHANICAL BEHAVIOR

ENVIRONMENTAL EFFECTS ON FRACTURE OF FUSION REACTOR MATERIALS

R. H. Jones (Pacific Northwest Laboratory)

1.0 Objective

The purpose of this study is to identify and model stress corrosion and corrosion fatigue processes which may degrade the properties of fusion reactor materials. The purpose is not to gather engineering data but to perform exploratory experiments to identify possible degradation processes. Once the processes are identified, experiments will be directed towards characterizing the nature of the environment-material interactions in sufficient detail to impact material selection and testing performed by engineering test programs.

2.0 Summary

The known stress corrosion and corrosion fatigue fracture processes in austenitic and ferritic steels are reviewed with an emphasis on aqueous and liquid metal environments. Possible effects of irradiation are given and precautions are given for the use of austenitic and ferritic stainless steels in fusion reactor environments. Finally,,an approach to modeling the environmental effect on the local fracture toughness at the tip of a crack is given.

3.0 Program

Title: Mechanical Properties
Principal Investigator: R. H. Jones
Affiliation: Pacific Northwest Laboratory

4.0 Relevant DAFS Program Plan Task/Sub-Task

II.C.8. Effects of Helium and Displacement on Fracture
II.C.9. Effects of Hydrogen on Fracture
II.C.12. Effects of Cycling on Flow and Fracture

5.0 Accomplishments and Status

5.1 Environmental Effects on the Fracture of Austenitic Stainless Steels

Austenitic stainless steels are subject to stress corrosion cracking (SCC) and corrosion fatigue (CF) failure processes in aqueous solutions. Factors which are important in accelerating SCC in these materials include 1) surface condition from weld preparation; 2) stress (residual and applied); 3) temperature; 4) degree of sensitization; 5) grain boundary segregation of P, Si and possibly other impurities and 6) water chemical composition. Weld preparation grinding followed by welding can produce deformed and recrystallized material on the surface of material in the heat affected zone. It has been shown by Povich[1] that deformed surfaces produced by shot peening accelerated the stress corrosion cracking of 304 SS in water at 300°C. Residual and applied stresses are dependent on joint geometry, coolant pressures and several other factors and will therefore be design specific. Stresses which raise the stress intensity of a crack or flaw in contact with the environment to values between K_{Iscc} and K_{Ic} can cause sub-critical crack growth. K_{Iscc} is defined as the stress intensity below which environmentally assisted crack growth cannot be experimentally detected. The importance of the surface condition is readily apparent since deformed material may accelerate the formation of a flaw in contact with the environment. This initiation step is frequently rate limiting. Both factors 1 and 2 are important in transgranular (TGSCC) and intergranular stress corrosion cracking (IGSCC) although IGSCC is also dependent on grain boundary composition.

Sensitization of austenitic stainless steels by the precipitation of chromium carbides in the grain boundaries and the subsequent depletion of chromium in the material adjacent to the grain boundaries is the single most important consideration in causing IGSCC. The degree of sensitization is a function of the bulk carbon content and the thermal history. Welding operations which heat the material in the 500° to 700°C range for the appropriate length of time is the most common cause of sensitization. In 304 SS, bulk carbon

concentrations are restricted to an upper limit of 0.03 wt% for components in which IGSCC is a concern. However, restricting the carbon content of 316 SS is not sufficient to eliminate IGSCC in laboratory tests for intergranular corrosion.[2-5] This difference between 304 and 316 SS has recently been explained by Briant[6] by a combined molybdenum and phosphorus effect on intergranular corrosion. Briant showed that for an equal amount of grain boundary phosphorus segregation, the presence of 2 wt% molybdenum in the alloy increased the intergranular corrosion by a factor of 3. This increase is above that for phosphorus alone in which an alloy with a bulk concentration of 0.006 wt% phosphorus had about 4 times more corrosion than one with only 0.003 wt% phosphorus. Therefore, an austenitic stainless steel with 2 wt% Mo and high phosphorus could have an IGSCC rate 12 times larger than an alloy with a low phosphorus concentration. Bruemmer et al.[7] observed that the intergranular corrosion rate of nickel increased with the presence of sulfur or phosphorus at the grain boundaries. A grain boundary sulfur concentration of 0.2 monolayers resulted in an intergranular corrosion rate 7 times faster than 0.04 monolayers. A grain boundary phosphorus concentration of 0.15 monolayers had an effect similar to 0.2 monolayers of sulfur when evaluated at highly oxidizing potentials.

Grain boundary phosphorus segregation can occur by thermally activated equilibrium segregation or by radiation enhanced segregation. Brimhall et al.[8] observed radiation enhanced phosphorus segregation in 316 SS containing 300 wt% ppm phosphorus and in PE16 containing 400 wt% ppm phosphorus. A surface concentration of approximately 0.3 monolayers was observed after irradiation to 2 dpa at 600°C. At this time, there would seem to be sufficient evidence to conclude that grain boundary phosphorus segregation will occur in 316 SS and could lead to IGSCC under certain environmental conditions. Possible problems from phosphorus segregation can be minimized by bulk chemical composition and thermal history control; however, there is insufficient data on irradiation enhanced phosphorus segregation and its effect in 316 SS to specilfy a bulk composition limit.

Both TGSCC and IGSCC are strongly dependent on the water chemistry with oxygen and chloride ion concentration being two of the more important elements. Fluorides, bromides, iodides, sulfates and many other elements have been shown to enhance SCC, but there is insufficient space to present a thorough summary of all their effects. Gordon[9] has recently reviewed the effect of chloride and oxygen on SCC of austenitic stainless steels and he showed that a large data set supported an inverse relationship between the quantity of oxygen and chloride ion needed to cause IGSCC and TGSCC. For instance, the boundary between TGSCC and no SCC in 304 SS in water at 288°C occurs at concentrations exceeding 1 ppm Cl^- and 1 ppm O_2 while at 0.1 ppm Cl^-, the boundary is at about 100 ppm O_2. A similar relationship exists for IGSCC except that at 1 ppm Cl^- the boundary between the IGSCC and no SCC is at 0.05 ppm O_2.

The relationship between temperature and oxygen concentration is also important to the susceptibility of austenitic stainless steel to SCC. Since the concentration of oxygen dissolved in water is temperature dependent, the dissolved oxygen concentration of a water cooled fusion reactor will change during start-up and shut-down and refueling cycles. Ford and Povich[10] evaluated BWR start-up and shut-down cycles and concluded that 304 SS is subjected to a highly susceptible oxygen/temperature combination during these cycles. They also observed that IGSCC occurred at temperatures as low as 50°C and that at 50°C the maximum crack growth rate occurred at 2 ppm O_2. Results by Jones et al.[11] confirmed that IGSCC can occur in sensitized 304 SS at a temperature of 40°C with a crack growth rate of 5 x 10^{-6} mm/s in air-saturated water (8 ppm O_2) with 15 ppm Cl^-. In the absence of Cl^-, Jones et al.[11] have not observed IGSCC at 40°C while Ford and Povich[9] reported a crack growth rate of 10^{-6} mm/s at 50°C in the absence of Cl^-. TGSCC of austenitic stainless steels has not been reported at temperatures below 100°C and therefore the start-up/shut-down problem in BWRs can be minimized in fusion reactors by the use of low carbon 316 SS. Temperature and oxygen cycles during refueling cannot be as easily eliminated and should be evaluated before a water-cooled fusion reactor is built with 316 SS.

In summary, the following precautions are apparent regarding the use of 316 SS in a water-cooled fusion reactor:

- Use non-sensitized materials, 316L grade
- Phosphorus concentration should be minimized
- Oxygen/temperature cycle during refueling, start-up and shut-down cycle should be evaluated.

Environmental degradation of the properties of 316 SS by hydrogen from the plasma, (n, p) reactions and corrosion reactions or by lithium or lithium-lead coolants should be recognized as possibilities; however, these effects appear to be secondary to the ones listed above. For instance, 316 SS was found" to be stable in lithium for a period of 3 days at 482°C and austenitic stainless steels are not subject to hydrogen embrittlement except when the a' phase is present or at very high hydrogen fugacities. Other effects which have not been discussed include the possible effect of radiation damage on the SCC or CF of 316 SS and the difference in the sub-critical cracking behavior with static and cyclic loads. This latter point will be discussed in Section 5.3.

5.2 Environmental Effects on the Fracture of Ferritic Stainless Steels

The mechanical properties of ferritic stainless steels may be affected by water, liquid lithium or lithium-lead coolants. Stress corrosion cracking of ferritic steels in water can cause transgranular or intergranular fracture and is generally thought to involve hydrogen embrittlement. Most of the data on environmental effects on ferritic stainless steels is for steam turbine blade material and was obtained by high cycle fatigue tests in high temperature steam. Liquid metal embrittlement by lead and lead alloys has been clearly demonstrated for mild steels while the effects of Li or Li-Pb alloys on ferritic stainless steels has not been as well characterized.

Hydrogen is involved in the SCC or CF ferritic steels because of their susceptibility to hydrogen embrittlement and because hydrogen is generated by

proton reduction during the corrosion process. In a fusion reactor, hydrogen isotopes are also present in the plasma and the breeding blanket and protons are generated within the first wall by nuclear reactions. Stoltz[13] evaluated the tensile properties of HT-9 in hydrogen gas at pressures up to 5000 psi and temperatures up to 400°C and concluded that the effect of 0.1 MPa of H_2 on the ductility at 25°C is eliminated at temperatures exceeding 200°C. He also showed that the ductility decreased with increasing hydrogen pressure at 25°C. The threshold stress intensity, K_{th}, of high strength, low alloy ferritic steels has been related to the hydrogen pressure by Gerberich et al.[14] and Oriani and Josephic[15] in the following way:

$$K_{th} = C_1 - C_2 \log P_{H2}.$$

In the study by Gerberich et al.,[14] K_{th} decreased from 34 MPa $\sqrt{m}$ at a hydrogen pressure of 10^{-3} MPa to 22 MPa $\sqrt{m}$ at 0.1 MPa while in the study by Oriani and Josephic,[15] K_{th} decreased from 22 MPa $\sqrt{m}$ at 3 x 10^{-4} to 10 MPa $\sqrt{m}$ at 0.1 MPa. Stoltz's reduction of area results versus hydrogen pressure for HT-9 obeys this relationship only for hydrogen pressures exceeding 6.8 MPa. For pressures less than 6.8 MPa, there is a light decrease in ductility relative to air tests but this decrease is within the scatter in the data. There are several differences between the tests and results reported by Stoltz[13] and those by Gerberich et al.[14] and Oriani and Josephic[15] including: 1) K_{th} is measured in a static test with a precracked sample while the tensile test is a dynamic test using a smooth sample; 2) the low alloy steels had a yield strength twice that of the HT-9 and 3) hydrogen embrittlement occurred at pressures <0.1 MPa in the high strength steel with pre-cracked samples while a significant ductility loss was apparent in the HT-9 only at pressures >6.8 MPa.

The implications of these results to the susceptibility of ferritic steels to hydrogen embrittlement in fusion reactors are: 1) radiation induced hardening will increase the susceptibility at lower hydrogen pressures; 2) flaws which escape NDT examination or initiate and grow during service

will increase the susceptibility and 3) the susceptibility is a maximum at 25°C and decreases with increasing temperature. Klueh and Vitek[16] have shown that the yield strength of a 12 Cr-1 MoVW steel is doubled after irradiation to a fluence of 9 dpa. Therefore, the high strength, low alloy, steel results are probably prototypic of HT-9 after irradiation.

Segregation of impurities to the grain boundaries of ferritic steels can embrittle them by the classic temper embrittlement process or they can enhance embrittlement in hydrogen gas or aqueous solutions. Kameda and McMahon[17] have shown tht the critical local tensile stress of a Ni-Cr ferritic steel decreased with increasing Sb, Sn and P concentraion at the grain boundary with a relative potency between these elements of Sb > Sn > P. In the presence of hydrogen, the fracture stress of a steel with embrittling impurities at the grain boundary is decreased still further; however, the ratio K_{th}/K_{Ic} was 0.8, 0.7 and 0.5 for 0.2 monolayers of Sb, Sn and P at the grain boundaries, respectively. Therefore, the impurity which had the least effect on embrittlement in the absence of hydrogen had the largest effect in the presence of hydrogen. Therefore, the effects of impurity segregation on a ferritic first-wall materials must be evaluated in the presence of hydrogen and not simply by charpy impact or fracture toughness tests in air.

Impurity segregation can occur by a thermally activated, equilibrium process or by a radiation induced, nonequilibrium process. Equilibrium segregation may occur during manufacturing or fabrication processes such as hot rolling and welding or during service. The kinetics of segregation depend on bulk diffusion and the driving force for segregation. Nonequilibrium segregation may occur by a solute drag mechanism as proposed by Johnson and Lam[18] and depends on the interaction energy between a solute and a point defect, the generation rate of point defects, the bulk concentration of solute and many other parameters. The effect of irradiation on impurity segregation in HT-9 has been examined by Brimhall et al.[8] and based on these preliminary results, radiation does not enhance the segregation of phosphorus. Smidt et al.[19] evaluated the fracture resistance of HT-9 after irradiation to 10^{22} cm^{-2} at 419°C and they found that the DBTT was shifted 108°C. A DBTT shift of 45°C

which resulted after a thermal treatment of 5000 hr at 538°C was suggested as a temper embrittlement effect although no grain boundary composition measurements were made and intergranular fracture was only apparent as secondary cracks. Therefore, the present results show that HT-9 can be embrittled by irradiation but there is no evidence to suggest that impurity segregation was the cause. Lechtenberg[20] also found that HT-9 embrittled by 100 hr at 550°C failed along martensite lath boundaries with no evidence of intergranular fracture. The present knowledge about the effects of impurities in fusion reactor first-wall materials can be summarized as follows: 1) impurities at the grain boundaries of a ferritic steel can affect embrittlement with and without the presence of hydrogen; 2) there is no direct evidence of impurity segregation causing temper embrittlement or irradiation embrittlement in HT-9 in the absence of hydrogen; and 3) there is an absence of data relating grain boundary chemistry to the threshold fracture intensity of irradiated HT-9 in a hydrogen or corrosive environment.

The behavior of ferritic steels in a liquid metal environment such as Li or Li-Pb can be separated by 1) a time dependent embrittlement which is controlled by corrosion in liquid Li or 2) a time independent embrittlement such as in liquid Pb. Chopra and Smith[21] have reported that the fatigue life of HT-9 is 5 times lower in liquid lithium than in liquid sodium when tested at a strain range of 0.5% at 482°C. However, Tortorelli and DeVan[22] showed that the strength of HT-9 samples exposed to liquid lithium at 500°C for 500 hr was similar to those exposed to argon. Therefore, the time dependent embrittlement of ferritic stainless steels in liquid lithium has not been clearly shown but further evaluation is needed.

A time independent embrittlement of ferritic steels in Li-Pb coolants has not been demonstrated experimentally; however, based on the susceptibility of ferritic steels to liquid lead embrittlement there is a possibility that Li-Pb alloys may embrittle ferritic steels. The time independent embrittlement of solid metals by liquid metals, commonly called liquid metal embrittlement (LME) occurs over narrow temperature and strain rate ranges. For instance, the embrittlement of a 4145 steel by lead occurs over the temperature range

of 10°C to 400°C and the embrittlement of 2024 T4 aluminum by mercury occurs over the temperature range of ~50°C to 200°C. At temperatures outside these limits the properties are identical to those in air. Johnson et al.[23] have analyzed the temperature dependence of LME and concluded that the onset of LME is related to the rate of liquid metal transport along a crack.

Liquid metal emurittlement has a high degree of specificity in that embrittlement has been clearly demonstrated only for specific liquid-solid couples. This speciticity also occurs for compositional changes in the liquid metals such as was shown by Breyer and Johnson[24] for Pb-Sn and Pb-Sb alloys with a 4145 steel. Increasing the tin or antimony concentration in contact with 4145 steel decreased the ductility and strength and increased the temperature range over which embrittlement occurred. Therefore, it is very difficult to extrapolate embrittlement results of ferritic steels in liquid lead to their behavior in Li-Pb alloys; however, there is certainly sufficient evidence to suggest that LME may occur and should be evaluated carefully before ferritic stainless steel is used in a structural application in contact with Li-Pb coolants.

5.3 Modeling Chemical Environment Effects on Fracture

Stress corrosion and corrosion fatigue models nave emphasized dissolution controlled crack growth processes for both intergranular and transgranular fracture where the major contribution of crack tip stresses and strains is to fracture the corrosion limiting passive film. In these models, crack growth rates depend on film rupture, repassivation and anodic dissolution rates. There is little disagreement that intergranular stress corrosion cracking of sensitized stainless steel is a dissolution rate controlled process; however, the picture is not as clear for transgranular stress corrosion and corrosion fatigue. Evidence of cleavage-like fracture surfaces has been shown for austenitic stainless steels,[24] ferritic steels[25] and brasses[26] tested in corrosive environments. In ferritic steels, hydrogen embrittlement is clearly implicated, but in austenitic stainless steels and brasses,

hydrogen embrittlement has not been identified as the cause of the cleavage-like fracture surfaces. Therefore, a physical prucess other than hydrogen or anodic dissolution must be consiciered to explain these fracture surfaces. Some possible processes include corrosion generated di-vacancy hardening or enhanced creep, corrosion modifieo crack tip flow properties or surface adsorption/energy affects on fracture.

The effect of a corrosive environment on fracture or fatigue can also be expressea with fracture models by Hahn and Rosenfield,[27] Equation 1, or fatigue models by McClintock,[28] Equation 2, or Broek and Rice[29] Equation 4. These models relate K_{Ic} and da/dn to material parameters as follows:

$$K_{Ic} = C\left(\bar{\varepsilon}_f^* \, \ell_o^* \, \sigma_y \, E\right)^{1/2} \tag{1}$$

$$da/dn \; a \; \delta \; \alpha \; \frac{\Delta K^2}{2\sigma_Y E}$$

$$da/dn = \frac{\left(\Delta K - \Delta K_o\right)^2 \; C \; \Delta K^m}{(1-R) \; K_c - \Delta K} \tag{3}$$

Where

$\bar{\varepsilon}_f^*$ = critical fracture strain,
ℓ_o^* = characteristic microstructural distance,
σ_y = yield strength
K = applied stress intensity
$\Delta K = K_{max} - K_{min}$
ΔK_o = threshold stress intensity in fatigue
K_c = fracture toughness

$$R = \frac{K_{min}}{K_{max}}$$

Use of Equation 1 to evaluate the effect of a corrosive environment on subcritical flaws is not a direct measure of K_{Iscc} since K_{Ic} is the stress intensity for critical flaw growth. However, if ϵ_f^* and a_Y are defined as local properties of the material within a few μm of the crack tip, then K_{Ic} in Equation 1 can be defined as the local fracture toughness, K_{Ic}. A corrosive environment could reduce K'_{Ic} by changes in $\bar{\epsilon}_f^*$, ℓ_0^*, or σ_Y. Hydrogen uptake could decrease ϵ_f^* by a variety of embrittlement processes and increase or decrease σ_Y and ℓ_0^* by hardening or softening processes. Corrosion has been observed to reduce $\bar{\epsilon}_f^*$ during slow strain rate tests of materials and this data can be used to assess the effect of corrosion on K'_{Ic}. For instance, Mom et al.[30] observed a strain to failure of 1.5% for 304 SS tested at 123°C in 35% $MgCl_2$ as compared to a strain to failure of 50% in air. Assuming that the corrosive environment altered only $\bar{\epsilon}_f^*$ in Equation 1, the ratio between K'_{Ic} in $MgCl_2$ to that in air is:

$$\frac{K'_{Ic}}{K_{Ic}} = \sqrt{\frac{\bar{\epsilon}_f^* \ (MgCl_2)}{\epsilon_f^* \ (air)}} \approx 0.173$$

If K_{Ic} in air is 100 MPa $\sqrt{m}$ then K'_{Ic} is 17 MPa $\sqrt{m}$. This value is an upper bound on K_{Iscc} since K_{Iscc} must be less than or equal to K'_{Ic}. This calculation is only an example and unfortunately experimental values for K_{Iscc} in $MgCl_2$ are not readily available. An effort to evaluate Equations 1 through 3 would require performing constant extension rate tests, precracked fracture tests and fatigue tests with the materials and environments of interest.

The yield stress of materials tested in corrosive environments can also be altered in comparison with those measured in inert environments. This effect has been most clearly demonstrated by Kramer and Demer[31] on aluminum monocrystals which showed a decreased yield strength after a strain-electropolish cycle. A time dependent elongation was observed during anodic dissolution of copper[32] and stainless steel,[33] which were loaded to 150% to 200% of their yield strengths. Therefore, the flow stress in the region of the crack tip

can be expected to decrease as a result of crack tip dissolution. Anodic dissolution may occur as a result of film rupture or in cases when a passive film may not be stable. A decrease in the crack tip flow stress would decrease K'_{Ic} (Equation 1) while increasing da/dn (Equations 2 and 3). Therefore, stress corrosion cracking and corrosion fatigue can be related to changes in ϵ_f and σ_y. Both of these parameters can be measured with simple slow strain rate tests, but the tests must be conducted at relevant electrochemical potentials, pH's, chemical compositions (O_2, Cl, etc.) and with a notched tensile sample.

6.0 REFERENCES

1. M. J. Povich. 1978. Corrosion, 34(5):162.
2. T. M. Devine, C. L. Briant, and B. J. Drummone. 1980. Scripta Met. 14:1175.
3. D. Warren. 1959. Corrosion, 15:213t.
4. M. A. Streicher. 1964. Corrosion, 20:57t.
5. R. F. Steigerwald. 1977. Corrosion, 33:338.
6. C. L. Briant. in press.
7. S. M. Bruemmer, R. H. Jones, M. T. Thomas, and D. R. Baer. 1981. In the Proceedings of the Secono International Conference on the Environmental Degradation of Engineering Materials, September 21-23, 1981.
8. J. L. Brimhall, D. R. Baer and R. H. Jones. 1981. In the Proceedings of the Second International Conference on the Environmental Degradation of Engineering Materials, September 21-23, 1981, Paper 6C-17.
9. B. M. Gordon. 1980. Matls. Performance, p. 29.
10. F. P. Ford and M. J. Povich. 1979. Lorrosion, 35(12):569.
11. R. H. Jones, A. B. Johnson, Jr., and S. M. Bruemmer. 1981. Proceedings of the Second Internationdl Conference on Environmental Degradation of Engineering Materials.
12. G. DeVries. 1970. "The Corrosion of Metals by Molten Lithium." In the Proceedings on Corrosion by Liquid Metals, J. E. Draley and J. R. Weeks, eds., p. 251.

13. R. E. Stoltz. 1980. "Alloy Development for Irradiation Performance Quarterly Progress Report for Period Ending March 31, 1980." DOE/ER-0045/2, p. 88.

14. W. W. Gerberich, J. Garry and J. F. Lessar. 1976. "Effect of Hydrogen on Behavior of Materials," A. W. Thompson and I. M. Bernstein, eds., p. 70.

15. R. A. Oriani, and P. H. Josephic. 1974. Acta Met., 22:1065.

16. R. L. Klueh and J. M. Vitek. 1980. "Alloy Development for Irradiation Performance Quarterly Progress Report for Period Ending December 31, 1980." DOE/ER-0045/5, p. 218.

17. J. Kameda and C. J. McMahon, Jr. to be published.

18. R. A. Johnson and N. Q. Lam. 1976. Phip., Rev. B, 13, p. 4364.

19. F. A. Smidt, Jr., J. R. Hawthorne and V. Provenzano. 1981. "Alloy Development for Irradiation Performance Quarterlyi Progress Reprot for Period Ending March 31, 1981." DOE/ER-0045/2, p. 163.

20. T. A. Lechtenberg. 1980. "Alloy Development for Irradiation Performance Quarterly Progress Reprot for Period Ending December 31, 1980." DOE/ER-0045/5, p. 143.

21. Chopra and D. L. Smith. "Alloy Development for Irradiation Performance Quarterly Progress Reprot for Period Ending September 30, 1980, DOE/ER-0045/4, p. 140.

22. P. F. Tortorelli, J. H. DeVan and C. T. Lin. "Alloy Development for Irradiation Performance Quarterly Progress Report for Period Ending September 30, 1980. DOE/ER-0045/4, p. 182.

23. K. L. Johnson, N. N. Breyer and J. W. Dally. 1977. In Proceedings of Conference on Environmental Degradation of Engineering Materials, p. 91.

24. R. Liu, N. Narita, C. Alstetter, H. Birnbaum, and E. N. Pugh. 1980. Met. Trans. 11A:1563.

25. J. C. Scully. 1973. "Stress Corrosion Cracking and Hydrogen Embrittlement of Iron Base Alloys," R. W. Staehle, J. Hochmann, R. D. McCright, and J. E. Slater, eds., NACE-5, p. 946.

26. J. A. Beavers and E. N. Pugh. 1980. Met. Trans. 11A:809.

27. G. T. Hahn and A. R. Rosenfield. 1968. ASM STP-432, p. 5.

28. F. A. McClintock. 1567. "Fatigue Crack Propagation," STP-415, Philadelphia, Pennsylvania, p. 170.

29. D. Broek and R. C. Rice. 1977. "Materials and Processes in Service Performance," p. 392.

30. A. J. A. Mom, R. T. Dencher, C. J. V. D. Wekken, and W. A. Schultze. 1979. "Stress Corrosion Cracking--The Slow Strain Rate Technique." G. M. Ugianski and J. H. Payer, eds., ASTM STP-665, p. 305.

31. I. R. Kramer and L. J. Demer. 1961. Trans. AIME, 221:780.

32. R. W. Revie and H. H. Uhlig. 1974. Acta Met. 22:619.

33. M. Smialowski and J. Kustanski. 1979. Corrosion Sci. 19:1019.

7.0 FUTURE WORK

The effect of irradiation on the grain boundary segregation of impurities will be evaluated for 316 SS, PE 16 and HT-9. An exploratory experiment dill be conducted using energetic light ions to irradiate wires or foils will be conducteo. The grain boundary composition of the irradiated wires or foils will be examined by Auger Electron Spectroscopy.

Also, the hydrogen emnrittlement of 316 SS and HT-9, heat treated to produce phosphorus segregation will be examined. Tests will be conducted at cathodic potentials in aqueous solutions.

CHAPTER 4

CORRELATION METHODOLOGY

FUSION SWELLING PREDICTIONS FROM A MODEL-BASED FISSION-FUSION-FISSION INTERPOLATION - R.E. Stoller and G.R. Odette (University of California, Santa Barbara)

1.0 Objective

The purpose of this work is to develop a physically based model of cavity swelling in stainless steels which may be used to facilitate extrapolation of fission reactor swelling data to fusion conditions.

2.0 Summary

The helium/dpa (He/dpa) ratio in stainless steel under fusion conditions will be about 30 times greater than in EBR-II and about 7 times less than in HFIR. To permit the meaningful use of fission reactor swelling data, the effects of various He/dpa ratios must be understood. A rate theory model with several novel features and which explicitly considers some potential He/dpa ratio effects has been calibrated using data from both EBR-II and HFIR. The calibrated model has been used to predict swelling under fusion conditions. The results indicate that simple extrapolations of swelling data from either EBR-II or HFIR may not be valid.

3.0 Program

Title: Damage Analysis and Fundamental Studies for Fusion Reactor Materials Development

Principal Investigators: G.R. Odette and G.E. Lucas

Affiliation: University of California, Santa Barbara

4.0 Relevant OAFS Program Plan Task/Subtask

Subtask C Correlation Methodology

5.0. Accomplishments and Status

5.1 Introduction

Extrapolation of existing fission reactor data [1-3] to predict the swelling of stainless steels under fusion conditions requires considering variations in a number of environmental parameters [4]. One parameter which has been identified as potentially significant is the helium to displacement ratio (He/dpa). The He/dpa ratio for a stainless steel fusion reactor first wall is about 10 appm/dpa* while this same ratio is only about 0.35 in the fast spectrum of the Experimental Breeder Reactor-I1 (EBR-II) [5,6]. Because of the two step reaction with Ni-58, reactors with a significant thermal spectrum can generate large amounts of helium in stainless steel. For example, the He/dpa ratio in the High Flux Isotope Reactor saturates at about 70 appm/dpa [5].

Two natural engineering approaches to fission-fusion correlations might be to directly interpolate between the HFIR and EBR-II data sets to predict behavior in a fusion environment; or alternately to emphasize the relatively small macroscopic differences in gross swelling between the two data sets in some temperature/exposure regimes. However, we have chosen to make the interpolation based on a simple physical model which is calibrated to be roughly consistent with both data sets and to make a specific prediction for the fusion He/dpa ratio. As will be discussed below, the results suggest that fusion behavior may not always be bracketed by the HFIR and EBR-II data. Since the data is so limited and the model clearly oversimplified; and since all fission-fusion variable differences have not been considered, we do not claim that the results represent an accurate prediction of behavior under fusion conditions. But we do believe that the approach used represents a rational approach to such correlations.

---

*The actual He/dpa ratio can vary as much as a factor of ~40 from the first wall to the outer edge of the blanket [6].

The rate theory model which has been developed describes the evolving cavity microstructure of 316 stainless steel under irradiation. The major navel features of the model are: a non-ideal gas treatment of the helium trapped in cavities; an approximate treatment of bubble-void cavity components which can account for observed size distributions; including those which are bi-and tri-modal; an explicit treatment of the effects of various He/dpa ratios; and a helium partitioning model which accounts for helium captured by microstructural features other than the cavities. Specifically, helium can be captured by dislocations, thereby aiding bubble growth via a "pipe-diffusion" mechanism, or helium can be trapped by the sub-grain structure. Two major simplifications employed in developing the model are its neglect of microchemical evolution and the use of time independent microstructural parameters such as the dislocation density and the sub-grain size.

The model, which is an extension of some earlier work [7,8], was calibrated to obtain reasonable quantitative agreement between the model's predictions and the observed swelling of 20% CW DO-heat irradiated in E8R-II and HFIR. A detailed discussion of this data is available elsewhere [4]. The calibrated model was then used to predict the cavity swelling of this same allay under fusion conditions. The results suggest that two different regimes of cavity swelling may be important; the first being associated with a high density of uniformly distributed matrix cavities similar to HFIR irradiations and the second involving a lower density of large cavities with the largest being attached to precipitates as observed in E8R-II. The actual swelling under fusion conditions may be strongly dependent upon which path the cavity microstructure follows.

5.2 Model Description and Calibration

The following sections describe the rate theory model which has been developed and the calibration of this model to obtain agreement between the model's predictions and swelling data from irradiation of 20% CW 316 stainless steel (DO-heat) in E8R-II and HFIR.

5.2.1 Point Defect Concentrations and Sink Structure

To compute the various extended defect sink strengths and to obtain the point defect concentrations, the following assumptions are made;

1. The point defect concentrations are computed assuming a quasi-steady-state rate theory formulation [10]

2. The point defect sink structure consists of bubbles, voids, a coarse sub-grain structure, and network dislocations. Both cavity components and the sub-grains trap helium. while resolutioning is neglected. Network dislocations can also capture helium; however, this fraction of the helium is then distributed to the bubbles. Helium partitioning procedures are discussed below.

3. Bubbles, voids, and the sub-grains are treated as neutral sinks for both vacancies and interstitials while network dislocations preferentially absorb interstitials; for simplicity an effective system bias is attributed to the dislocations. The sink strength of the various extended defects are computed using a procedure similar to that described by Bullough and Hayns [11]

5.2.2 Modeling Procedures and Microstructural Parameters

In the present work, the cavity microstructure is modeled using three size classes which are initially allocated 5, 10, and 20 helium atoms per cavity respectively. The cavities are assumed to be equilibrium bubbles at time zero and the radius is computed using an equation of state developed by Brearley and MacInnes [12]. Observed void distributions are approximated by a proper choice of initial bubble densities and their associated helium content. This approach allows a crude treatment of the time dependence of void nucleation and size distributions which are the result of continuous nucleation.

Helium is continuously generated in the matrix at either a constant rate characteristic of fast, reactor or fusion irradiations or at a time

dependent rate characteristic of HFIR [5]. The helium is partitioned among the various sinks by first obtaining the matrix helium concentration from the following conservation equation:

$$\frac{dM_{He}}{dt} = G_{He} - D_{He}\,(S^{p} + S^{c} + S^{g}) \tag{1}$$

where the superscripts p, c, and g denote the sink strength of the dislocations, cavities and sub-grains respectively; G_{He} is the helium generation rate; and D_{He} is the helium diffusion coefficient.

Helium migration is assumed to proceed by a radiation enhanced self diffusion mechanism with an activation energy; $E^{m}_{He} = E^{f}_{v} + E^{m}_{v} - E^{b}_{He}$, and a pre-exponential equal to the effective vacancy supersaturation; $\phi = (D_v C_v - D_i C_i)/D_v C^{e}_{v}$, i.e. a di-vacancy mechanism. The amount of helium partitioned to a given cavity size class during a time step At is determined by its relative sink strength and if the cavities in a given size class are still bubbles, they also are allocated the relevant fraction of the helium captured by the dislocations; viz

$$\Delta N^{v}_{He} \simeq 4nr_{V}\, D_{He}\, M_{He}\, At \tag{2a}$$

$$\Delta N^{b}_{He} \simeq 4\pi r_{b} D_{He}\, M_{He}\, \left(\frac{\rho_{n+S^{b}}}{S^{c}}\right) \tag{2b}$$

where S^{b} is the bubble sink strength. As long as the number of helium atoms in a given cavity is less then N_{c}, the critical number (which will be discussed below), the stable bubble radius is found from Equation (3) using the equation of state mentioned above.

$$\dot{r} = \frac{D_v C^{e}_{v}}{r}\left(\phi - \exp\left[\frac{\Omega}{kT}\left(\frac{2\gamma}{r} - P\right)\right]\right) \tag{3}$$

A schematic plot of $\dot{r}$ is shown in Figure 1. The assumption that sufficient vacancies are available for the evolution of near steady-state or quasi-equilibrium bubbles has been found to be valid for the micro-structural and material parameters used in this study.

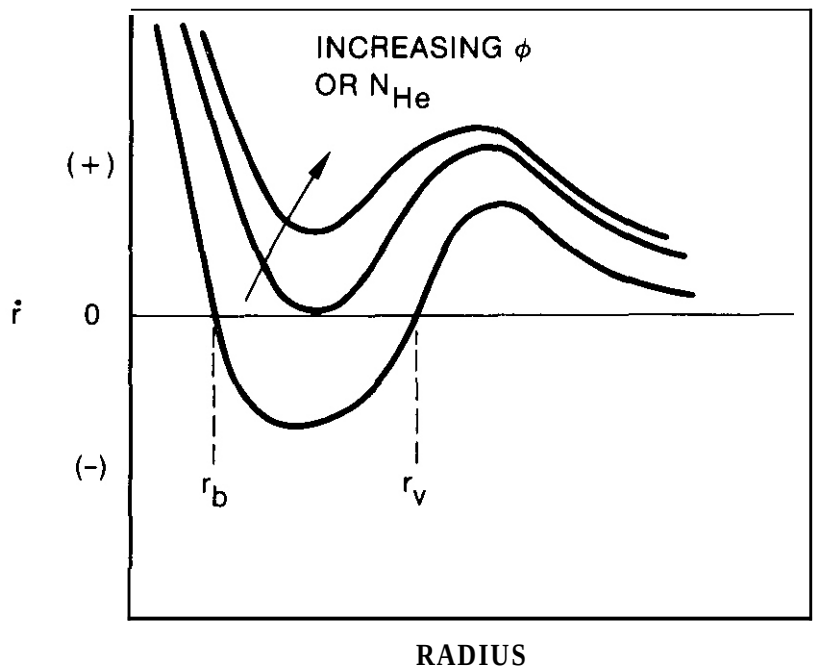

FIGURE 1. Schematic Plot of Cavity Growth Rate ($\dot{r}$).

The criterion for cavity conversion from bubble to void is also obtained from Equation (3). If the derivative in Equation (3) is set to zero, a ninth order equation for r is obtained as a function of ϕ, γ, and N_{He}. For $N_{He} < N_C$ there are two real, positive roots of the equation which are the stable bubble and critical void radii respectively. With $N_{He} < N_C$, a region of $\dot{r} < 0$ represents a barrier to void nucleation and the cavity radius is constrained to r_b. However, with increasing N_{He} or ϕ, the curve shifts upwards until $N_{He} = N_C$; at this point the cavities in such a size class are considered to have converted to voids. For $N_{He} > N_C$ there are no real, positive roots and the void radius is subsequently found by integrating Equation (3).

This idealization of the conversion of cavities from bubbles to voids neglects possible time-dependent microchemical changes which may influence

N_C; this is discussed further below. The use of reasonable initial cavity densities has yielded good agreement between observed void densities and the number density of "converted" cavities. Figure 2 is a plot of the void number density if 1, 2, or 3 size classes have converted to voids. Observed void densities of 20% cold-worked DO-heat in EBR-II and HFIR are also shown.

For the HFIR predictions all of the cavities are of the same type, either all voids or all bubbles. Note that the HFIR number densities are plotted as $Log(N_V/15)$ where 15 is approximately the square root *of* the ratio of the helium generation rate in HFIR to that in EBR-II. This scaling of cavity number densities with the square root of the helium generation rate has been observed previously [4] and was used to compute the cavity densities assumed for fusion conditions. Specifically, the fusion values were assumed to be 5.5 times the EBR-II values.

Figure 3 shows the temperature dependence of the other two major microstructural features included in the model; the network dislocation density (ρ_n) and the sub-grain size (0_g). The sub-grain structure represents the coarse distribution of micro-twins, stacking faults and deformation bands which is observed in this alloy in the 20% CW condition [9]. The values of the dislocation density used for EBR-II and HFIR in the temperature range of 400-650°C reflect the reported values of this parameter for 00-heat in the two reactors [4,13,14,15]. The value chosen in this region to simulate fusion conditions represents a linear interpolation between EBR-II and HFIR. For temperatures greater than 650°C, values were chosen which represent enhanced recovery; for less than 400°C, the estimated contribution of loops is included.

In general, the use of the simplified model may cause some difficulty in simultaneously reproducing the observed behavior in both the nucleation and steady state regimes. The values of parameters which influence the "swelling propensity" of the material (e.g. the effective system bias) may be time dependent and the use of dose independent parameters dictates that

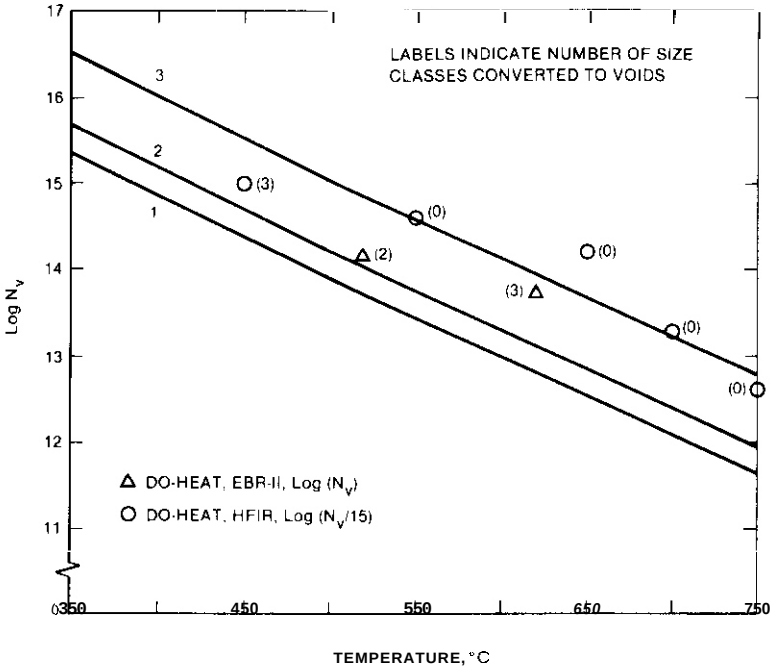

FIGURE 2. Comparison of Observed and Predicted Void Densities (N_v).

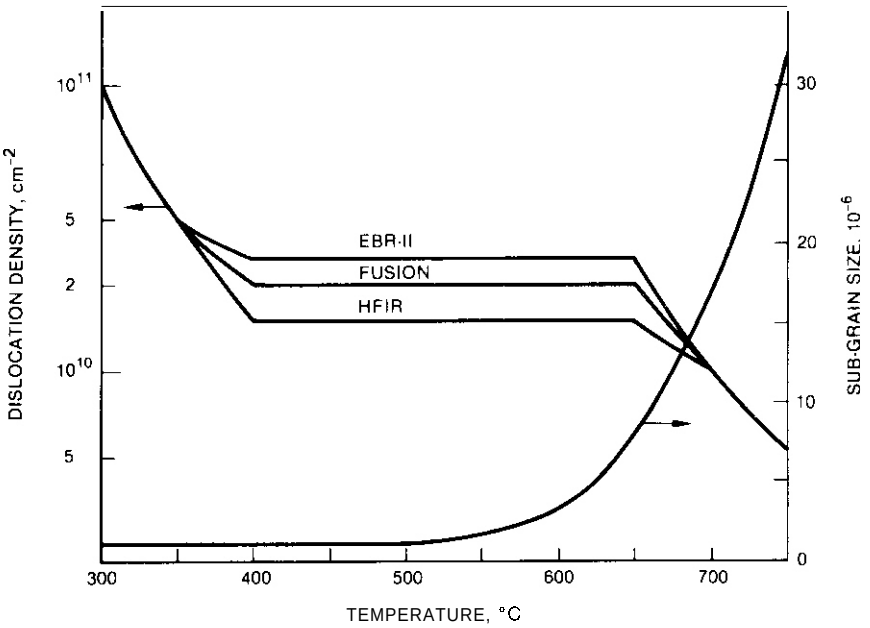

FIGURE 3. Temperature Dependence of Dislocation Density and Subgrain size.

a compromise value be chosen for these parameters. For example, the time required for significant precipitation to occur is obviously important if voids are attached to precipitates as frequently observed in EBR-II microstructures.

5.2.3 Model Calibration

The use of a relatively "standard" set of rate theory parameters permitted reasonable agreement with swelling data from the two reactors (see Table 1.) The temperature dependent surface energy was obtained from zero-creep measurements [16]. In order to obtain agreement between model predictions and swelling data in the two environments, it was necessary to enhance the "swelling propensity" in EBR-II at temperatures greater than 500°C. This requirement may be a result of the fact that in EBR-II a low density of large cavities, with the largest of these attached to precipitates appears to dominate swelling while in HFIR a higher density of more uniformly distributed matrix cavities may dominate [4]. An "effective" surface energy was used at these temperatures in EBR-II to act as a surrogate

TABLE 1. RATE THEORY PARAMETERS

Displacement Rate,	10^{-6} sec^{-1}
Vacancy Migration Energy,	1.3 eV
Vacancy Formation Energy,	1.6 eV
He-Divacancy Binding Energy,	0.5 eV
Interstitial Migration Energy,	0.5 eV
Recombination Coefficient,	$1.0 \times 10^{17} D_i$
Dislocation-Interstitial Bias,	1.03
Surface Energy (ergs/cm^2),	4050-1.75T(°C)

for those effects which lead to enhanced growth when cavities are attached to precipitates. The nominal surface energy was reduced linearly with temperature above 500°C to a minimum of 1000 ergs/cm^2 at 650°C, a value which has been used by others in similar work [17,18]

Which cavity microstructure develops may be influenced by the matrix bubble density which forms at low fluences and hence by the He/dpa ratio.

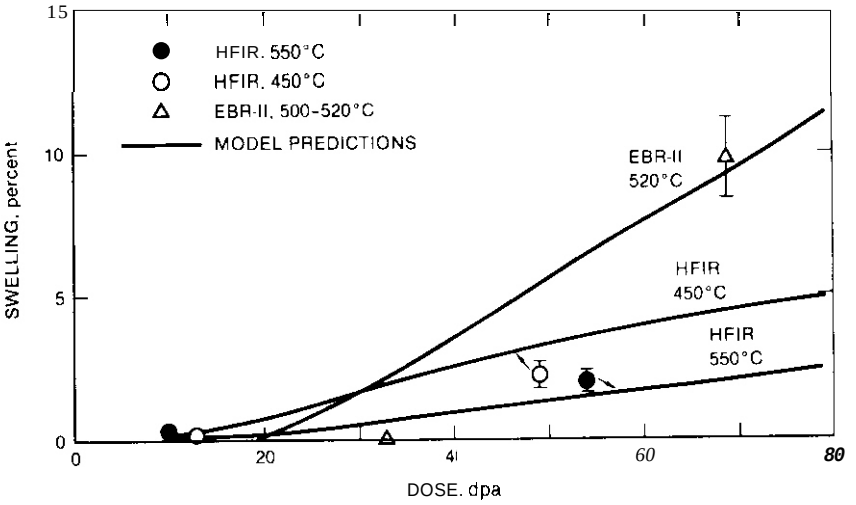

4a

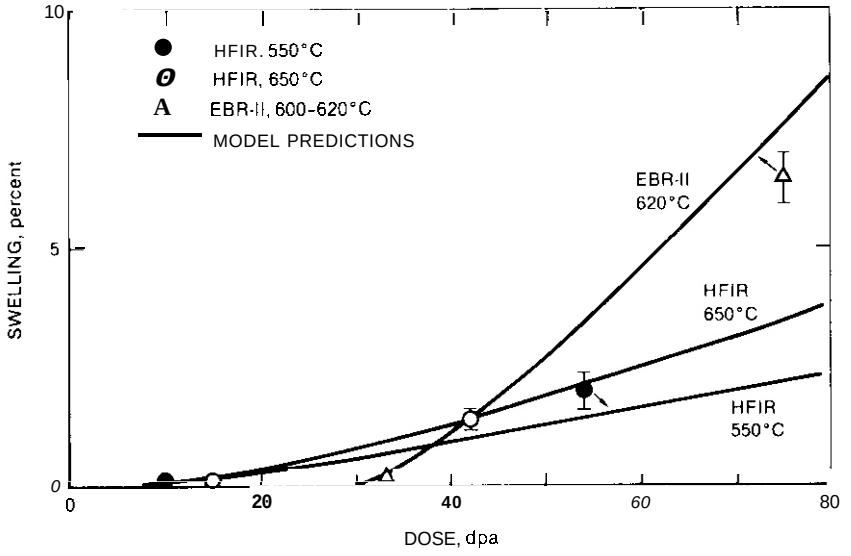

4b

FIGURE 4. Comparison Between Observed and Predicted Fluence Dependence of Swelling in EBR-II and HFIR at Two Temperatures.

The higher bubble densities in HFIR may suppress the rapid swelling of those cavities attached to precipitates by "starving" them of both He and vacancies. In addition, altering the thermal-mechanical treatment in HFIR can produce either type of cavity microstructure. Solution annealed DO-heat in HFIR has a lower cavity density than the 20% CW material and follows a path more closely resembling EBR-II microstructures [4]. These two paths of cavity evolution exacerbate the problem of extrapolating from fission to fusion since, as will be shown in the following section, the model predicts quite different swelling behavior for the two paths.

The f1uence and temperature dependence of the model's swelling prediction's are compared with data in Figures 4 and 5. Note that for temperatures greater than 450°C, all of the predicted swelling in HFIR is due to bubbles. In general, the agreement is quite good. Notably, the

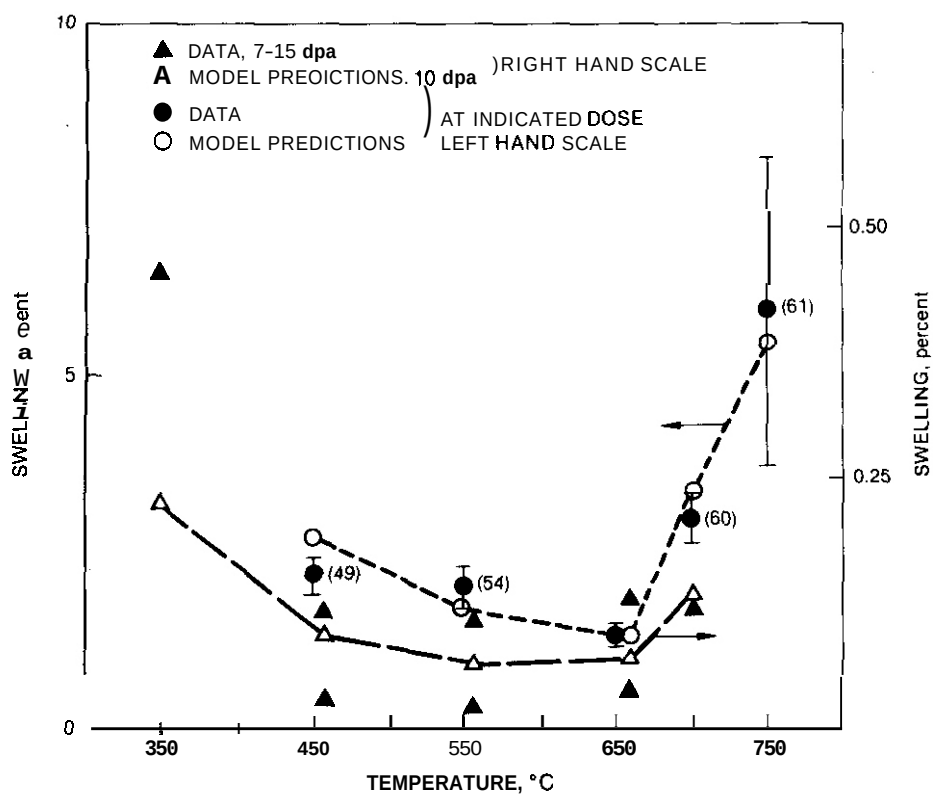

FIGURE 5. Comparison Between Observed and Predicted Temperature Dependence of Swelling in HFIR.

markedly different temperature dependence of swelling in the HFIR relative to fast reactor behavior is well reproduced. The major exception is the predicted incubation time in EBR-II at 520°C shown in Figure 4a. One possible explanation for this behavior has been discussed above, viz. the potential effects of microchemical evolution on N_C. Several other explanations could also be invoked, e.g. approximations in the helium partitioning model or the effect of the CW alloy's heterogeneity.

5.3 Model Predictions For Fusion

The dose dependence of the swelling predicted for fusion is shown in Figure 6a,b and at 500°C and 600°C. For purposes of comparison, the EBR-II and HFIR predictions at the indicated temperatures are also shown. In spite of the fact that the values of the He/dpa ratio and the cavity number densities are intermediate, the swelling predicted for fusion at 500°C is significantly greater than that observed in both fission reactors up to EO dpa. The major effects are a significantly reduced incubation dose when compared with the EBR-II predictions and an increased swelling rate when compared with the HFIR predictions. This is a consequence of the fact that while the fusion cavity densities $\alpha \sqrt{G_{He}}$, they are not high enough to suppress swelling, but manifest a reduced incubation time in the higher helium environment. At 600°C the results are similar if one assumes that the cavity evolution follows a precipitate dominated path, i.e. with the iower effective surface energy a5 used for EBR-II. However, if one assumes that the matrix cavities dominate, the fusion predictions are bracketed by the two fission reactor predictions at doses greater than 40 dpa. Below 40 dpa, the swelling predicted for fusion is slightly less than both EBR-II and HFIR for this path.

There is not sufficient data to predict which characteristic microstructure a CW steel would form in a fusion environment. However, the results for the SA steel in HFIR which had a slightly lower cavity density and large cavities on precipitates. suggest that similar behavior

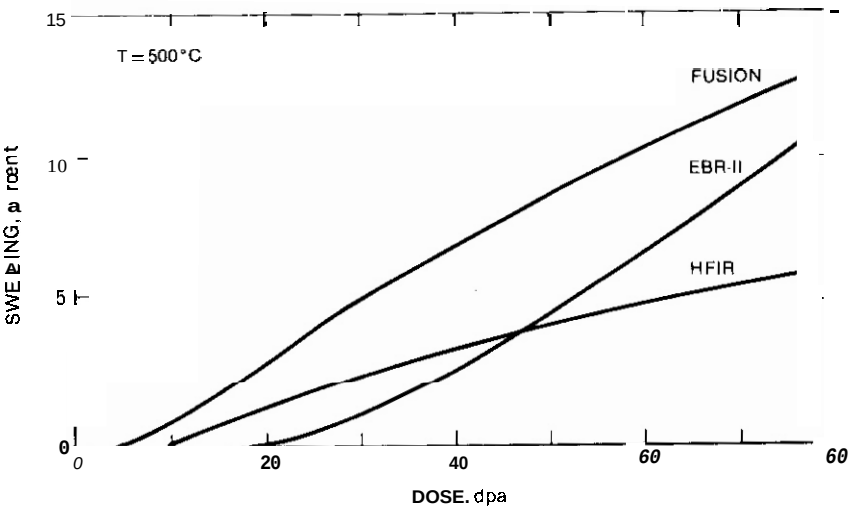

6a

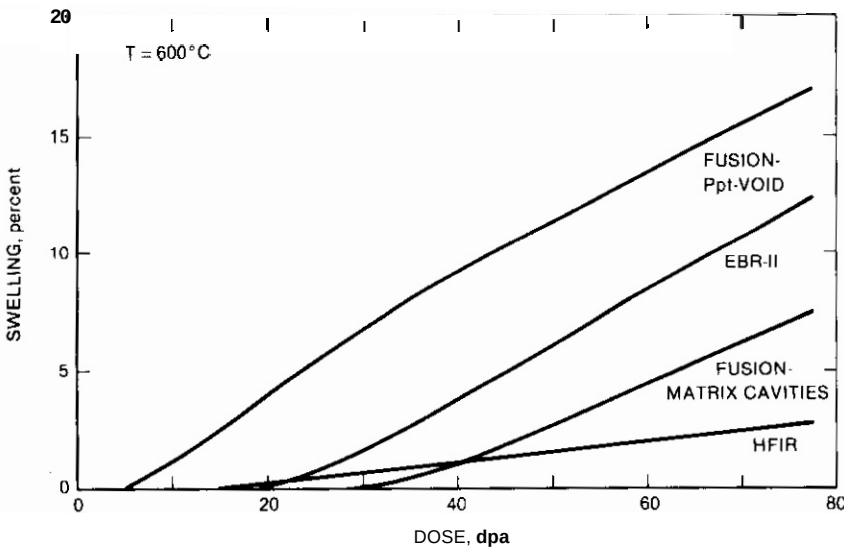

6b

FIGURE 6. Predicted Fluence Dependence of Swelling Under Fusion Conditions.

could be observed for the CW condition at a fusion He/dpa ratio; this of course assumes a cavity scaling ~ $\sqrt{G_{He}}$.

The "steady state" swelling rate and the incubation time have been normalized in Figure 7 using the results of the EBR-II and fusion predictions. The incubation time here is defined as the dose to 1% swelling and the swelling rate is the average value between 60 and 80 dpa. The normalization procedure was used in an attempt to reduce the specific parameter dependence of the results. For example. the model has also been calibrated to reproduce the swelling behavior of the higher swelling heat of steel described in Reference [3]. While the absolute swelling values are higher, when the results are normalized using this procedure the behavior is quite similar to DO-heat. As noted previously, when the fusion predictions are compared with the EBR-II results, the incubation time is more sensitive than the swelling rate. At the higher temperatures, the effect of which path the cavity microstructure follows is also seen to be more dramatic on the incubation dose than on the swelling rate.

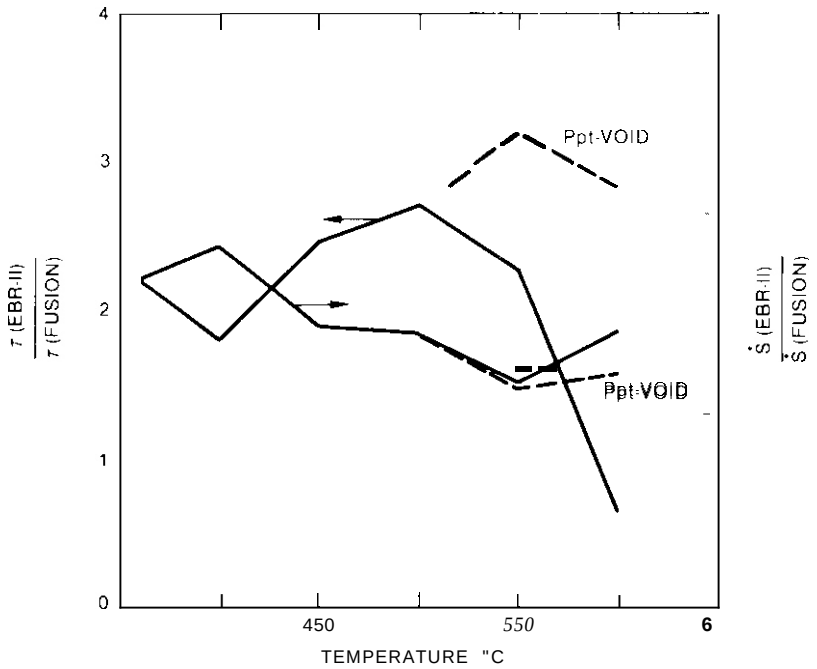

FIGURE 7. Temperature Dependence of Swelling Parameters Under Fusion Conditions as Normalized to Fast Reactor Predictions.

5.4 Conclusions

It should be noted that the results described are sensitive to certain model assumptions and the particular parameters used. for example, minor changes in parameters could lead to void swelling in HFIR. The results are also quite sensitive to the assumed $\sqrt{G_{He}}$ scaling of the cavity densities which needs to be further verified experimentally in light of the current varying interpretations of the DO-heat data [4,13,14]

Perhaps the most significant conclusion of the results of the present model calibration and of the fusion interpolation is the suggestion that cavity swelling may follow two alternate paths; one in which the cavities are distributed throughout the matrix and the other in which the cavities are attached to precipitates. Quite different swelling can be observed, depending upon which type of cavity dominates. The He/dpa ratio may strongly influence which path is followed by determining the matrix bubble density early in the irradiation. Consistent with their different He/dpa ratios the model predicts quite different swelling behavior in EBR-II and HFIR. However, although fusion's He/dpa ratio is intermediate, swelling under fusion conditions may not be bracketed by the results of irradiations in EBR-II and HFIR. If one assumes cavity-precipitate association for fusion as observed in EBR-II, the swelling for fusion is predicted to be significantly greater. If at higher temperatures a matrix cavity dominated microstructure develops under fusion conditions, swelling could be less than that observed in the two fission reactors at low fluences and intermediate at higher fluences.

6.0 References

1. Weiner, R.A. and Boltax, A., ASTM STP-725, (1980) 484.
2. Odette, G.R., J. Nuc. Mat., 85 and 86, (1979) 533.
3. Bates, J.F. and Korenko, M.K., Nucl. Tech., 48, (1980) 303.

4. Odette, G.R., Maziasz, P.J., and Spitznagel, J.A., "Fission-Fusion Correlations for Swelling and Microstructure", Proceedings of Second Topical Meeting On Fusion Reactor Materials, August 9-12, 1981, Seattle, WA.

5. Simons, R.L., ASTM STP-683, (1978) 207

6. Kulcinski, G.L., Ooran, D.G., Abdou, M.A., ASTM STP-570, (1974) 329.

7. Odette G.R. and Frei, M.W., Proc. of First Topical Meeting On the Technology of Controlled Nuclear Fusion, CONF-740402, (1974) 485.

8. Odette, G.R., and Langley, S.C., Radiation Effects and Tritium Technology For Fusion Reactors, CONF-750989, (1975) 1-395.

9. Brager, H.R. and Straalsund, J.L., J. Nuc. Mat., 47, (1973) 105.

10. Mansur, L.K., Nucl. Tech., 40, (1978) 5

11. Bullough, R. and Hayns, M.R., SM Archives, 3, (1978) 73

12. Brearley, I.R. and MacInnes, D.A., J. Nuc. Mat., 95, (1980) 239.

13. Maziasz, P.J., DAFS Quarterly Report, DOE-ER-0045/6, (1981).

14. Brager, H.R., and Garner, F.A., "Influence of the Helium Level on the Swelling and the Microstructural/Microchemical Evolution of AISI 316," Proceedings of Second Topical Meeting On Fusion Reactor Materials, August 9-12, 1981, Seattle, WA.

15. Maziasz, P.J., and Grossbeck, M.L., "Swelling, Microstructural Evolution and Helium Effects in Types 316 and (316 + Ti)", Proceedings of Second Topical Meeting On Fusion Reactor Materials, August 9-12, 1981, Seattle, WA.

16. Murr, L.E., Wong, G.I. and Horylev, R.J., Acta Met., 21, (1973) 595.

17. Brailsford, A.D. and Bullough, R., J. Nuc. Mat., 48, (1973) 87.

18. Wolfer, W.G., Mansur, L.K. and Sprague, J.A., Proc. of Int. Conf. on Radiation Effects In Breeder Reactor Structural Materials, (1977) 841.

7.0 Future Work

Additional theoretical work is needed to improve our understanding of defect partitioning and possible microchemical effects which may influence the proposed path dependence of cavity evolution. The current simplified

cavity evolution model needs to be included in a more complete treatment of microstructural and microchemical evolution.

8.0 Publications

1. Stoller, R.E. and Odette, G.R., "A Model Based Fission-Fusion Correlation of Cavity Swellina in Stainless Steel", Proceedinas of Second Topical Meeting On Fusion Reactor Materials, August 9-12, 1981, Seattle, WA.

2. Odette, G.R., Maziasz, P.J., and Spitznagel, J.A., "Fission-Fusion Correlations for Swelling and Microstructure", Ibid.

HELIUM BUBBLE FORMATION AND SWELLING IN METALS

B. B. Glasgow, A. Si-Ahmed. W. G. Wolfer (University of Wisconsin) and
F. A. Garner (Hanford Engineering Development Laboratory)

1.0 Objective

The purpose of this effort is to provide models for the influence of helium on microstructural evolution in irradiated metals; these models will then be used in the development of fission-fusion correlations.

2.0 Summary

The effect of a continuous production of helium on swelling is analyzed using an improved equation of state for gaseous helium that incorporates both a gas-kinetic as well as a static pressure for densely packed helium. In the absence of a bias, bubble swelling is characterized by two temperature regimes. At temperatures below about 550°C, bubble swelling is due to thermally assisted interstitial emission and is of a magnitude determined by the volume occupied by densely packed helium. At higher temperatures, bubbles grow by thermal vacancy emission at dislocations and their absorption at cavities. For high He/dpa ratios, bubbles remain overpressurized, and swelling is less than obtained from the equilibrium assumption. When a modest bias exists, bias-driven swelling or void growth in the low temperature regime is always larger than bubble swelling, and helim has no effect on the swelling rate.

3.0 Program

Title: Irradiation Effects Analysis (AKJ)
Principal Investigator: D. G. Doran
Affiliation: Hanford Engineering Development Laboratory

4.0 Relevant DAFS Program Plan Task/Subtask

Task II.C.2 Effects of He on Microstructure

5.0 Accomplishments and Status

5.1 Introduction

The production of heliun in structural materials by (n,α) reactions is considered to be one of the major factors which influences void formation. Many experimental and theoretical studies, reviewed recently by Farrell [1] and by Hayns,[2] have clearly shown that helium, either preinjected or continuously implanted or produced, does increase the void nucleation rate. However, this does not always imply that the terminal void nunber density at a given irradiation temperature is also increased with helim. In fact, the review in section 2 of experimental data on void number densities indicates that for He/dpa ratios of interest to fusion reactors, the terminal void number density in neutron irradiated austenitic stainless steels is independent of the helium concentration, but the time to reach it is dependent on the He production rate. As a result, swelling in excess of a few percent may not be affected by increased helium production at irradiation temperatures below about 0.5 T_m (T_m is the melting temperature). At higher temperatures, however, helium bubbles are expected to form and thereby extend the temperature range of swelling.

This high-temperature swelling by helium bubbles can be easily computed provided the bubble density, the gas law, and the surface energy γ are known, and provided all the heliun can be assumed to reside in the bubbles. Furthermore, the most important assumption is, of course, that the bubbles are in thermodynamic equilibrium, i.e., $2\gamma/r = p$, where r is the bubble radius and p the gas pressure. Strictly speaking, the equilibriun assunption is never completely satisfied, particularly when the He/dpa ratio is large. The reason is that gas-driven swelling requires an overpressure, i.e., $p > 2\gamma/r$, for a finite bubble growth rate. As a result, the equilibrium assumption leads to the maximun possible bubble swelling when bias-driven growth is negligible.

The purpose of the present paper is to evaluate the effect of helium on swelling without adopting the equilibrium assunption and to compare it with bias-driven swelling and swelling by equilibriun bubbles. Important features of the

present swelling model are an improved equation of state for helium and several new contributions to the driving force for gas-driven swelling. The latter consist of the static pressure of densely packed He atoms, and the possibility for interstitial generation by over-pressurized bubbles. The model is applied to type 316 stainless steel irradiated in either HFIR or EBR-II after the termial void number density has been reached.

5.2 Terminal Void Number Densities

The evolution of the void number density in neutron-irradiated AISI 316 has been found to depend on a number of variables.[3] In general, however, it follows for isothermal irradiation two major regimes, transient and saturation, followed by a minor stage of void coalescence at high values of swelling. Most variables exert their strongest influence on the transient regime where the void nucleation takes place. These variables are temperature, displacement rate, cold-work level, prior thermal history, He/dpa ratio, and applied stress. The cold-work level is perhaps the dominant determinant for the duration of the transient regime.

The saturation regime, defined by a dose-independent void number density, has been found to be much less sensitive to these variables than originally anticipated with the exception of temperature and displacement rate. It is important to note that the action of these two variables on void number densities is very often coupled in fission reactor irradiations. For instance, the very high γ-heating rates in HFIR required to obtain the highest irradiation temperatures are obtained at the core positions of peak displacement rate. In EBR-II, on the other hand, the highest and lowest irradiation temperatures are usually obtained at the top and bottom of the core where the displacement rates are the lowest. Only in special test assemblies can other flux-temperature combinations be achieved. As a result, great care is required when cmparisons are made between data from various fission reactors. When this is done, the following findings emerge.

Figure 1(a) shows the void number densities developed in a particular heat of

AISI 316 [4] during HFIR irradiation. Note that the displacement rate at 380°C is roughly one-third of that at 680°C. There are two temperatures, 380°C and around 575°C, where void number densities for different fluences can be compared. It is seen that the void nunber densities have not increased beyond their values observed at the low fluence of 1×10^{26} n/m^2 (E >0.1 MeV). This means that void nucleation is over before about 300 appm of helium has accumulated. Since the He/dpa ratio increases in HFIR substantially after a fluence of 1×10^{26} n/m^2, the large He/dpa ratios quoted for HFIR at higher fluence are of little consequence to void nucleation in this material.

In Figure 1(b), the void number densities in a DFR [6] breeder fuel pin cladding are added to the HFIR data. It is seen that the DFR data are comparable to the HFIR data, in spite of the lower heliun concentration produced in the DFR. Figure 1(c) shows additional DFR data fran two fuel pins with lower dose. It is seen that the void number densities from different fuel pins are reproducible, and that the approach to the terminal void number densities at low He/dpa ratios is slowest at higher temperatures where nucleation is most difficult.

This build-up of the void number density towards saturation is further illustrated in Figure 1(d). The two data sets added are for the N-lot heat irradiated at 500°C in EBR-II. Due to the lower He/dpa ratio in EBR-II the void number densities have not yet reached the saturation levels already attained in comparable HFIR irradiations. The intermediate void number densities in each fluence subset of data also increase with increasing stress. [6-7]

5.3 Equation of State for Helium Gas

The helim density in small gas bubbles is sufficiently high so that neither the ideal nor the van der Waals gas law is an appropriate equation of state. Therefore, Wolfer [8] has recently developed a gas law which can be written in the form

$$z(y_0,T) = p_k/(N_{He}kT) \qquad (1)$$

where p_k is the kinetic gas pressure, N_{He} the number of heliun atoms per

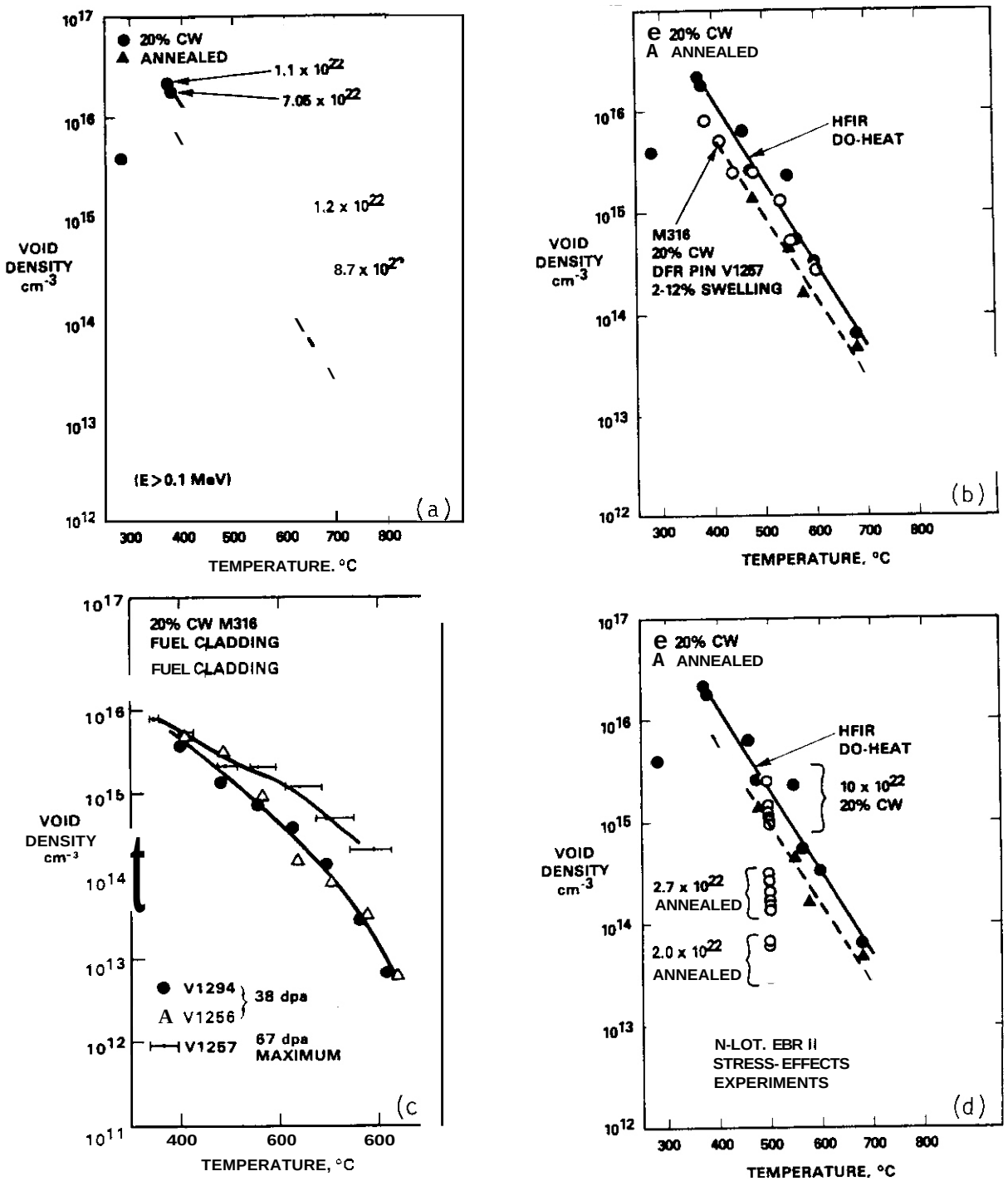

FIGURE 1. Void Number Densities in Stainless Steels.

cavity volune, k is the Boltzmann constant, and T the absolute temperature. Furthermore

$$y_o = \frac{\pi}{6} N_{He} d_o^3 \tag{2}$$

is the "hard-sphere" packing fraction with d_o = 0.2637 nm as the "diameter" of the hard-core potential of helium. Equation (1) as obtained earlier [8] has been compared more recently with the empirical gas law of Mills, Liebenberg, and Bronson [9] developed from their data in the temperature range from 75 to 300°K. This comparison makes it necessary to slightly modify the earlier theoretical gas law in addition to correcting an error. These changes mainly affect the compressibility factor z for temperatures below 400°K and packing fractions y_o >0.7. The newly revised compressibility factor z is shown in Figure 2 together with the empirical results of Mills et al. [9] at 200°K; the agreement between the empirical and theoretical correlations is excellent. When the hard-sphere packing fraction becomes of the order of one or larger, the densely packed helium acts more like a compressible medium than a gas. As a result, a static pressure p_s exists even at 0°K. Baskes and Holbrook [10] have obtained this static pressure from computer simulations of helium-vacancy clusters in copper. From their work it is found that

$$p_s \cong 30400(y_o - 1) \text{ MPa}$$

for y_o >1 and p_s = 0 for y_o <1.

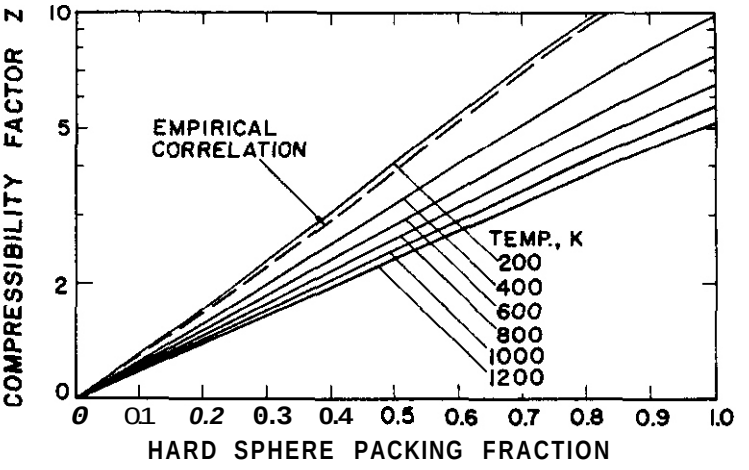

FIGURE 2. Compressibility Factor for Gaseous Helium.

The static pressure builds up rapidly as y_o exceeds one, whereas the kinetic gas pressure p_k rises much less. Accordingly, we have made the assunption that the total helium pressure for $y_o > 1$ is equal to the sun of p_s and p_k, where p_k is obtained from Equation (1) for $y_o = 1$. For packing fractions $y_o < 1$, only the kinetic pressure p_k contributes to the total pressure. This particular matching avoids a discontinuity in pressure at $y_o = 1$.

5.4 Bubble and Void Growth

After the terminal void nunber density N_v has been reached, the swelling rate S can be evaluated with the equation

$$S = \Omega N_v 4\pi r\{D_v(\Delta C_v + \overline{C}_v - C_v^o) - D_i(\Delta C_i + \overline{C}_i - C_i^o)\}. \tag{3}$$

Here, Ω is the atomic volume, D_v and D_i are the diffusion coefficients for vacancy and interstitial migration, and ΔC_v and ΔC_i are the corresponding concentrations as produced by displacement damage. The concentrations of vacancies and interstitials in thermodynamic equilibrium with voids of radius r are given by

$$C_v^o = C_v^{eq}\exp(-p_o\Omega/kT),\ C_i^o = C_i^{eq}\exp(p_o\Omega/kT), \tag{4}$$

where

$$p_o = P - 2\gamma/r \tag{5}$$

is the net pressure in the void and C_v^{eq} and C_i^{eq} are the equilibriun concentrations in an ideal and stress-free crystal. Although C_i^{eq} is very small, C_i^o may be substantial for very large overpressures p_o in the voids. The equilibrim concentrations in the real crystal are give by

$$\overline{C}_v = C_v^{eq}\exp(\sigma_H\Omega/kT),\ \overline{C}_i = C_i^{eq}(-\sigma_H\Omega/kT). \tag{6}$$

Since the hydrostatic stress σ_H is no larger than the yield stress, the exponential in Equation (6) is never large enough to give $\overline{C}_i$ a substantial value in contrast to C_i^o; hence, we may assume that $\overline{C}_i \cong 0$.

5.5 Results

Swelling was computed by numerical integration of Equation (3), assuning a dose-independent void density given by

$$\log N_v = 26.94 - 7.54 \times 10^{-3} * T(°K) \tag{7}$$

which represents the terminal values given in Figure 1.

The dislocation density at saturation is assuned to be equal to 6×10^{14} m^{-2} according to experimental observations,[7] and the displacement rate is 10^{-6} dpa/sec. Furthermore, it is assumed that the heliun concentration increases linearly with dose at a specified rate. Other materials parameters are those given in Reference (11), and the net bias for void growth is varied with temperature according to theoretical results as $B_o * 873/T$ where $B_o = 0.2$ is the net bias at 773°K.[12]

In addition to computing the swelling with Equation (3), bubble swelling is evaluated under the assumption that $2\gamma/r = p$ and that all heliun atoms are contained in cavities. This results in a swelling depending only on the heliun concentration C_{He} [atoms m^{-3}] but not the dose, and it is given by

$$S = [3/4\pi N_v)]^{1/2}(zC_{He}kT/2\gamma)^{3/2}. \tag{8}$$

Note that $C_{He} = N_{He}S$. The surface energy in Equations (8) and (5) is taken to be temperature dependent, $\gamma = 1 + 0.00173(773 - T)[J/m^2]$, with the temperature coefficient as measured for 304 stainless steel.[13]

Figures 3, 4, and 5 show canputed swelling values for helium contents of 100, 1000, and 10,000 appm. Curves a are obtained from Equation (8), whereas curves b and c are numerical integrations of Equation (3) for a He/dpa ratio of 70 and for a net bias of zero and 0.2, respectively. Comparing the curves a and b, we find that Equation (8) overpredicts the bubble swelling by a factor of 3 to 4 at high temperatures. This is due to the fact that a finite bubble swelling rate requires an overpressure, i.e., a positive value of p_o, as a driving

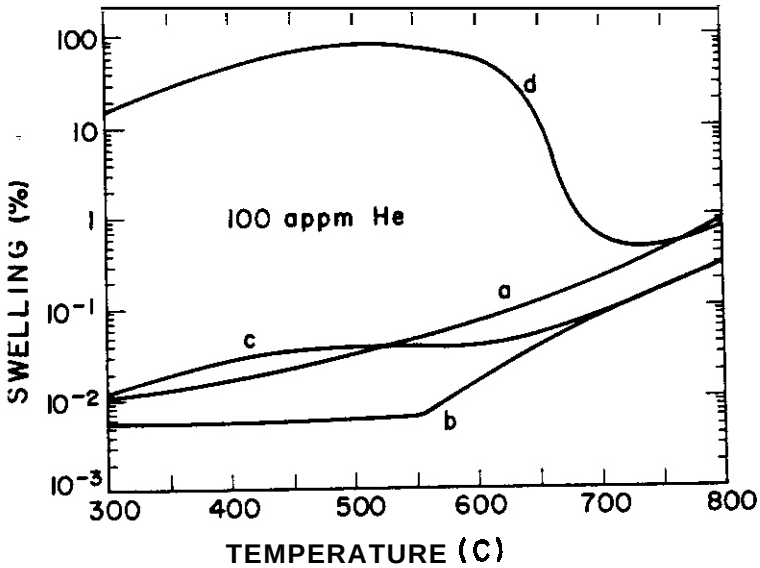

FIGURE 3. Swelling for He/dpa Ratios of 70 (a,b,c) and 1 (d) After 100-appm He is Produced; (a) for Equilibriun Bubble Swelling; (b) Dynamic Bubble Swelling Without Bias; (c,d) Dynamic Bubble Swelling With Bias

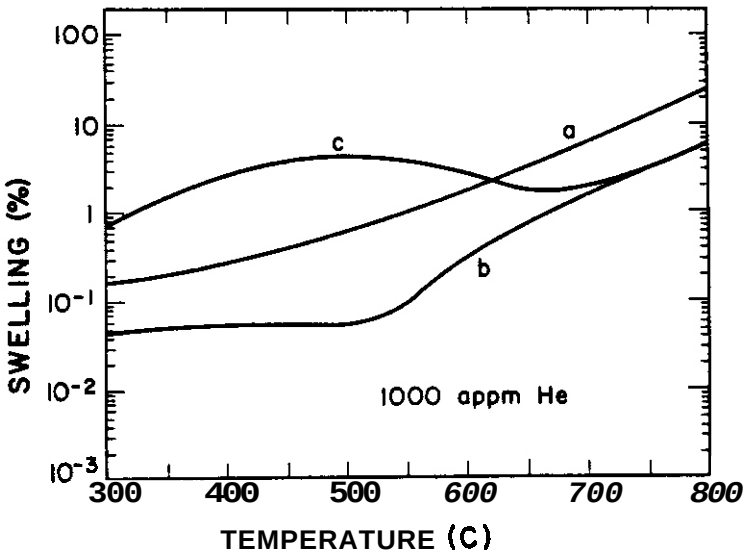

FIGURE 4. SWelling for He/dpa Ratio of 70 After 1000-appm He is Produced

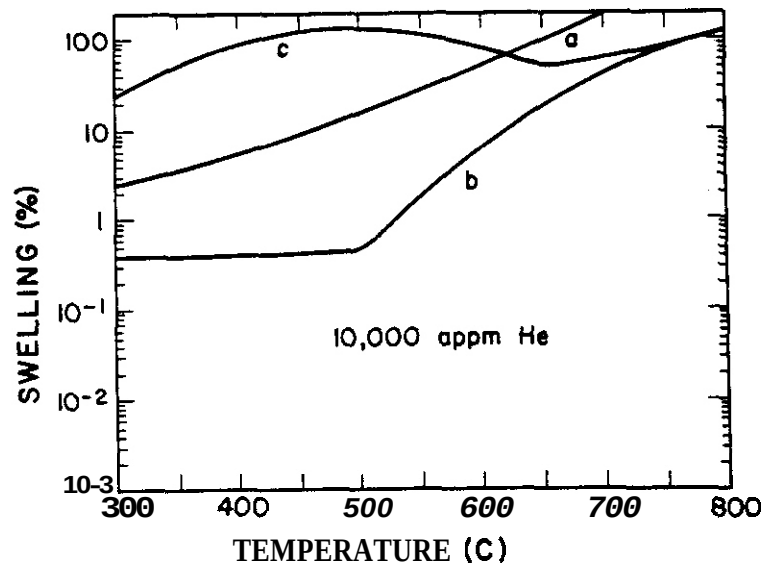

FIGURE 5. Swelling for He/dpa Ratio of 70 After 10,000-appm He is Produced.

force for swelling. The higher the He/dpa ratio, the greater is the over-pressure and the difference between the equilibrium bubble size and the dynamically growing bubble size. To confirm this, curve d in Figure 3 gives the swelling for a He/dpa ratio of one, being an upper value for breeder reactor irradiations. At temperatures greater than 750°C, bias-driven void growth is negligible, and swelling is entirely gas-driven. It is seen that for the low values of He/dpa in breeder reactors, the assumption of equilibrium bubble swelling is indeed appropriate at high temperatures. Note that the displacement damage for case d in Figure 3 is 100 dpa, whereas for case a it is only about 1.4 dpa.

The difference between equilibrium and *the* dynamic bubble swelling depends also on the surface energy. For example, if the surface energy is assumed to be $\gamma = 3[J/m^2]$, this difference becomes very small even for the He/dpa ratio of 70. This is mainly due to the reduction in the equilibriun bubble swelling, since $S \sim \gamma^{-3/2}$.

At temperatures below 550°C, the dynamic bubble swelling without bias (curves b) becomes nearly independent of temperature. This is explained by the fact that

the bubble growth by vacancy absorption, being proportional to $D_v (\overline{C}_v - C_v^o) \lesssim D_v \overline{C}_v$, becomes negligible no matter how large the overpressure p_o *is.* In fact, the helium packing fraction y_o becomes larger than one, resulting in a dramatic increase of the heliun pressure from the kinetic to the static pressure regime. As a result, the interstitial emission term in Equation (3) is activated, **i.e.,** the bubble grows by the thermally assisted generation of Frenkel pairs with retention of the vacancy and thereby relieves the static helium pressure. This mechanism is analogous to the spontaneous Frenkel pair formation discovered by Bisson and Wilson [14] in computer simulation studies. They found that (at 0°K) a cluster of five heliun interstitial atoms in a fcc metal will spontaneously create a Frenkel pair and then occupy the vacancy.

The relief of the static helium pressure by themally-assisted Frenkel pair creation keeps the helium to vacancy ratio in these over-pressurized bubbles close to one. Swelling produced by this densely packed heliun is then simply given by $S \cong 0.6\ C_{He}\Omega$ where the factor 0.6 is based on the results of Baskes and Holbrook.[10]

With a net bias of $B_o = 0.2$, void swelling remains in excess of bubble swelling for temperatures below 600 to 650°C. Even if the net bias is reduced to 0.02, bubble swelling still remains negligible compared to void swelling below about 600"C.

5.6 Discussion and Conclusions

Although helim accelerates the void nucleation rate at all temperatures it does not contribute to the bias-driven growth of voids below irradiation temperatures of about 600°C and for displacement rates of 10^{-6} dpa/sec. *It is* often argued that higher helium production may create a higher void number density, and thereby alter void swelling. The present review of void number densities in AISI 316 irradiated in fission reactors suggests, however, that differences in void nunber densities for irradiations carried out at the same temperature and dose rate will not persist indefinitely. Similar observations have been made with regard to the dislocation density.[7] Consequently, one

must expect that the steady-state swelling rate is nearly independent of the heliwn production rate at low temperatures. Since small void nuclei, even if present at low doses, do not produce large swelling values, early termination of the void nucleation by higher helium generation rates may not result in drastically different swelling behavior, particularly when microchemical evolution is a major variable for the transient regime.[3]

It is possible to produce a higher void number density than the saturation value by helium preinjection or dual-ion bombardment. Experiments demonstrating this have been reported by Agarwal et al.[15] These experiments were carried out at a dose rate of 3 x 10^{-3} dpa and at a correspondingly higher irradiation temperature of 700°C. In spite of the likelihood for bubble growth at this temperature, the void number densities produced for different He/dpa ratios show the tendency for converging to a saturation value both from higher and lower values. Unfortunately, the irradiations were not carried out to sufficiently large displacement doses to achieve canplete saturation in all cases.

6.0 References

1. K. Farrell, Rad. Eff., 53 (1980) 175.

2. M. R. Hayns, "Theory of Void Swelling: Effects on Continuous Gas Generation," to be published in The Fusion Reactor, J. Gittus and J. R. Wier (Eds.).

3. H. R. Brager and F. A. Garner, "Comparison of the Swelling of the Microstructural/Microchemical Evolution of AISI 316 Irradiated in EBR-II and HFIR," Proceedings Second Topical Meeting of Fusion Reactor Materials, August 9-12, 1981, Seattle, WA, (in press).

4. P. J. Maziasz and M. L. Grossbeck; ADIP Quarterly Progress Report, DOE/ER-0045/5, 43.

5. C. Brown, J. K. Butler and E. J. Fulton, Proceedings of Symposium on Irradiation Behavior of Metallic Materials for Fast Reactor Components, June 5-14, 1979, Ajaccio, Corsica.

6. H. R. Brager, F. A. Garner and G. L. Guthrie, J. Nucl. Mat., 66, (1977) 301.

7. H. R. Brager, F. A. Garner, J. E. Flinn, and W. G. Wolfer, Proceedings International Conference on Radiation Effects in Breeder Reactor Structural Materials, June 19-23, 1977, Scottsdale, AZ, M. L. Bleiberg and J. W. Bennett (Eds.), 727.

8. W. G. Wolfer, Effects of Radiation on Materials, ASTM STP 725 (1980), 201.

9. R. L. Mills, D. H. Liebenberg, and J. C. Bronson, Phys. Rev. B21 (1980), 5137.

10. M. I. Baskes and J. H. Holbrook, Phys. Rev. B17 (1978), 422.

11. W. G. Wolfer, J. Nucl. Mat., 90 (1980), 175.

12. W. G. Wolfer, Proceedings International Conference on Fundamental Aspects of Radiation Damage in Metals, Gatlinburg, TN (1975), 812.

13. L. E. Murr, G. I. Wong, and R. J. Horyley, Acta Met., 21, (1973), 595.

14. C. L. Bisson and W. D. Wilson, Proceedings Conference on Tritium Technology in Fission, Fusion, and Isotopic Applications, Dayton, OH (1980).

15. S. C. Agarwal, G. Ayrault, D. I. Potter, A. Taylor, and F. V. Nolfi, J. Nucl. Mat., 85 and 86 (1979), 653.

THE RADIATION-INDUCED EVOLUTION OF AISI 316 (DO-HEAT) IN HFIR AND EBR-II

H. R. Brager and F. A. Garner (Hanford Engineering Development Laboratory)

1.0 Objective

The objectives of this effort are to examine the microstructural/microchemical evolution of AISI 316 irradiated at conditions of both low and high helium/dpa ratio and to determine the effect of helim and other transmutants on void swelling and phase development.

2.0 Sumnary

Additional data on the microstructural and microchemical evolution of the DO-heat of AISI 316 irradiated in EBR-II are consistent with other data presented in an earlier report. It appears that a late-term microchemical evolution occurs after 33 dpa at 500 to 600 °C, approaching saturation near 70 dpa.

Examination of a HFIR-irradiated specimen at 42 dpa shows that the dislocation density and phase evolution are consistent with that of comparable EBR-II-irradiated material but that the void densities are higher. Microchemical analyses show that a Comparable evolution that has not saturated at 42 dpa is in progress during HFIR irradiation and it is expected that the swelling rate will increase at higher fluence. Measurements of the vanadim and manganese concentrations have been performed and agree reasonably well with calculated values. Details of the precipitate formation and void morphology characteristics indicate that the temperature is ∿100 °C higher than the reported nominal temperature of 550°C.

3.0 Program

Title: Irradiation Effects Analysis (AKJ)
Principal Investigator: O. G. Doran
Affiliation: Hanford Engineering Development Laboratory

4.0 Relevant DAFS Program Task/Subtask

Task II.C.2 Effects of He on Microstructure
Task II.C.4 Effect of Solid Transmutants on Microstructure

5.0 Accomplishments and Status

5.1 Introduction

In an earlier report it was shown that the microstructural and microchemical evolution of the DO-heat of 20% cold-worked AISI 316 in EBR-II was not very different from that in HFIR, with the major difference residing in the void number density but not the swelling.[1] The magnitude of the difference in void density is sensitive to the temperature assignments for the HFIR data, and these have not yet been definitively determined. It was also shown that the acceleration of swelling in EBR-II between 33 and 70 dpa appears to be related to late-tern changes in the microchemical evolution and evidence was presented to show that the microchemical evolution is not completed in EBR-II at 500 to 600°C until fluences well in excess of 33 dpa are attained. The HFIR data are at relatively low fluences compared to the ∿75 dpa level attained in EBR-II and therefore the expected additional acceleration of the swelling rate has .yet to occur. The annealed DO-heat, however, has already attained at these fluences a steady-state swelling rate which is comparable to that of the cold-worked material in EBR-II. It is expected from experience gained in fast reactor irradiations that solution-annealed and cold-worked AISI 316 will swell at the same steady-state swelling rate but with different incubation fluences.

In this report some additional data are presented on the EBR-II irradiated specimens and new data are provided on one HFIR irradiated specimen.

5.2 Experimental Detai 1s

The techniques employed to examine the specimens irradiated in EBR-II have been presented previously.[1] New techniques were employed, however, in preparing

and examining the DO-heat specimen from HFIR, designated D2-4, which was irradiated to 42 dpa at a reported nominal temperature of 550°C.[2] This specimen was later examined by ion microprobe analysis, the details of which will be described in a separate section.

The as-received specimen provided by P. J. Maziasz of ORNL was about one-fourth the volume of the usual TEM disk. It had a thickness of 0.38 mm which is comparable to that employed in most EBR-II irradiation studies but had a diameter of only 1.5 mm instead of the usual 3.0 mm. Nevertheless, the specimen was quite radioactive by EBR-II standards (~10 R/hour at one inch), particularly when oneconsiders that this material was removed from HFIR over six years ago.

This high level of activity has discouraged examination of the composition of the alloy matrix, and previous studies relied only on examination of extracted precipitates. In order for the specimen activity not to saturate the detector of the EDX system, three procedures can be used: decrease the specimen volume, increase the distance between the specimen and the detector, and increase the current density of incident electrons to increase the X-ray signal generated at the specimen.

The specimen was reduced in volune by first mechanically thinning the disk from 0.38 mm to about 0.10 mm thickness, and then electrolytically-thinning in a holder adapted far small diameter material using the usual electrapolishing equipment, electrolyte and thinning conditions.

At this point the activity of the specimen was still causing the detector in its normal position to exhibit excessive dead-time. The detector was withdrawn 18 mm further from the specimen than its normal distance of ~30 mm. Even at this position, the dead-time of the X-ray detection system with the electron beam off was ~70%. The beam current was increased to a value greater than normally used by increasing the size of the condenser lens aperature and the first condenser lens current. The dead-time with the electron beam penetrating the specimen now had increased to 75%, a level considered acceptable for the examination of this specimen. In increasing the electron current density to

improve the signal-to-noise ratio, the effective diameter of the electron probe increased from the usual 5 to 10 nm to perhaps 30 nm, thereby decreasing the spatial resolution of the examination. The distance between EDX measurements on the specimen were therefore maintained at 50 to 100 nm so that the widened beam probe would still provide spatially relevant results.

Extraction and analysis of precipitates was also performed in the standard manner.

5.3 Experimental Results

5.3.1 Specimens Irradiated in EBR-II

In Reference 1 near-precipitate concentration profiles of Cr, Fe, Ni, Mo and Si were shown for DO-heat specimens irradiated in EBR-II at 500°C to 33 and 69 dpa. These illustrated the initiation of nickel segregation into precipitates (M_6C at 33 dpa) and the cessation of segregation at higher fluence (G-phase at 69 dpa). Figures 1 through 3 show three typical profiles obtained for material irradiated at 620°C to 74 dpa. These show that at this fluence and temperature the nominal nickel level in the matrix of 13 weight % has been reduced substantially to ~9 weight %. There does not appear to be a large amount of active segregation in progress; the steep profile near the precipitate boundary reflects the tendency to average the compositions of the precipitate and matrix.

5.3.2 Specimen D2-4 Irradiated in HFIR

This specimen was first examined by transmission electron microscopy. As shown in Figures 4(a) and (b) there is a very narrow size distribution of cavities at 4×10^{15} cm^{-3} with a mean size of about 200 Å. These cavities do not have the well-defined faceted structure typical of EBR-II irradiated material but are much more rounded. The cavities are fairly homogeneously distributed but also appear to be correlated with twin boundaries, subgrain boundaries and other features. The cavity volune in a measured representative area was 1.7%. Given

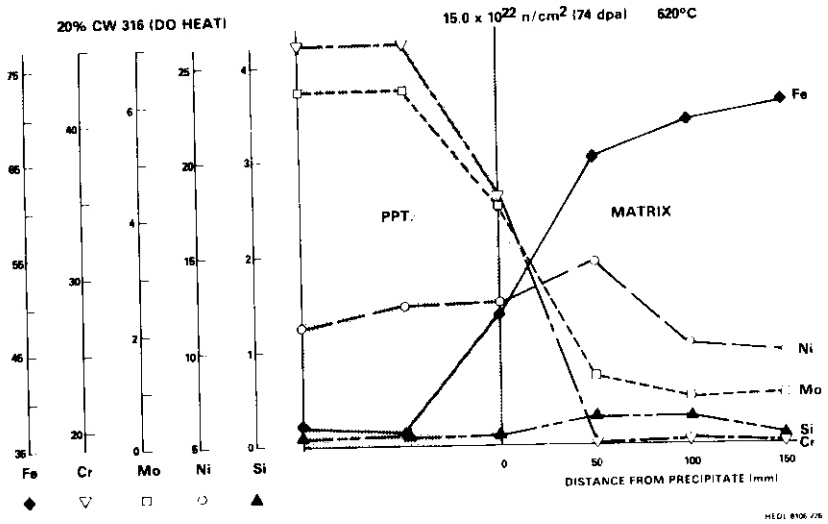

FIGURE 1. Near-Precipitate Composition Profiles Measured for $M_{23}C_6$ in 20% Cold-Worked 00-Heat Specimen Irradiated at 620°C to 75 dpa in EBR-II.

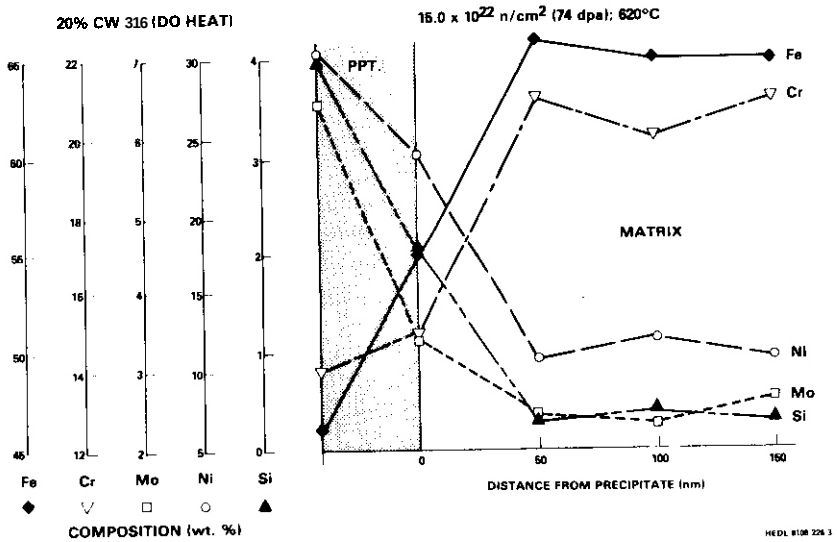

FIGURE 2. Near-Precipitate Composition Profiles Measured for Laves in 20% Cold-Worked DO-Heat Specimen Irradiated at 620°C to 75 dpa in EBR-II.

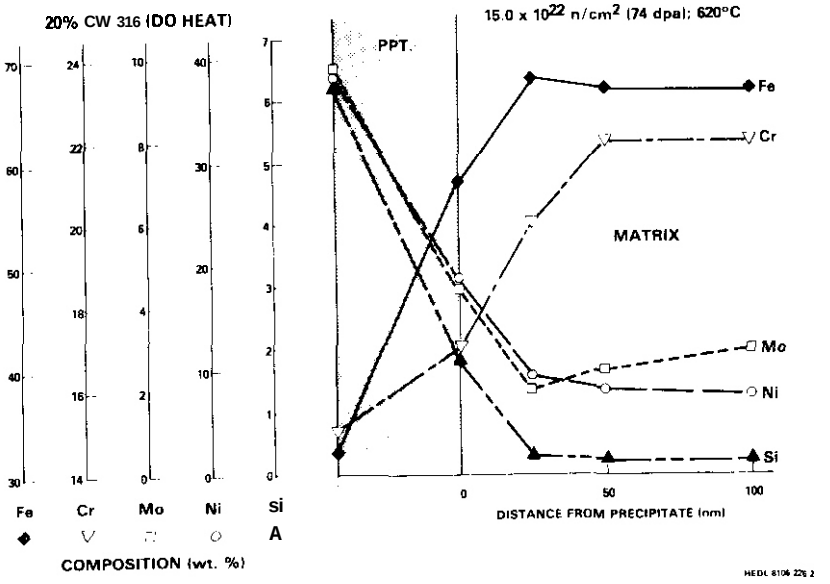

FIGURE 3. Near-Precipitate Composition Profiles Measured for Another Laves Precipitate in 20% Cold-Worked DO-Heat Specimen Irradiated at 620°C to 75 dpa in EBR-II.

the heterogeneity of the voids from one area to another in this specimen, these measurements agree reasonably well with those of Maziasz (200 Å, 2.4 x 10^{15} cm^{-3}, 1.4%).(2)

There has been some speculation that the dislocation density might be lower in HFIR-irradiated specimens. The dislocation density was determined for one area that was thought to **be** typical of this specimen and found to **be** 3 **x** 10^{10} cm^{-2}. The densities reported earlier for the specimens irradiated in EBR-II are 2 x 10^{10} cm/cm^3 (33 dpa) and 3 x 10^{10} (69 dpa) at 500 to 510°C, and 1.2 x 10^{10} (33 dpa) and 2.0 x 10^{10} (75 dpa) at 600 and 620°C. It does not appear that the dislocation density has relaxed more in the HFIR-irradiated specimens than for those irradiated in EBR-II. These values are slightly less than the saturation densities of 6 ±3 x 10^{10} cm/cm^3 typically observed in austenitic steels irradiated in fast reactors at temperatures from 400-600°C.

Ten of the precipitates that were located on the foil edge were examined and identified by X-ray and diffraction analysis to be five different phases.

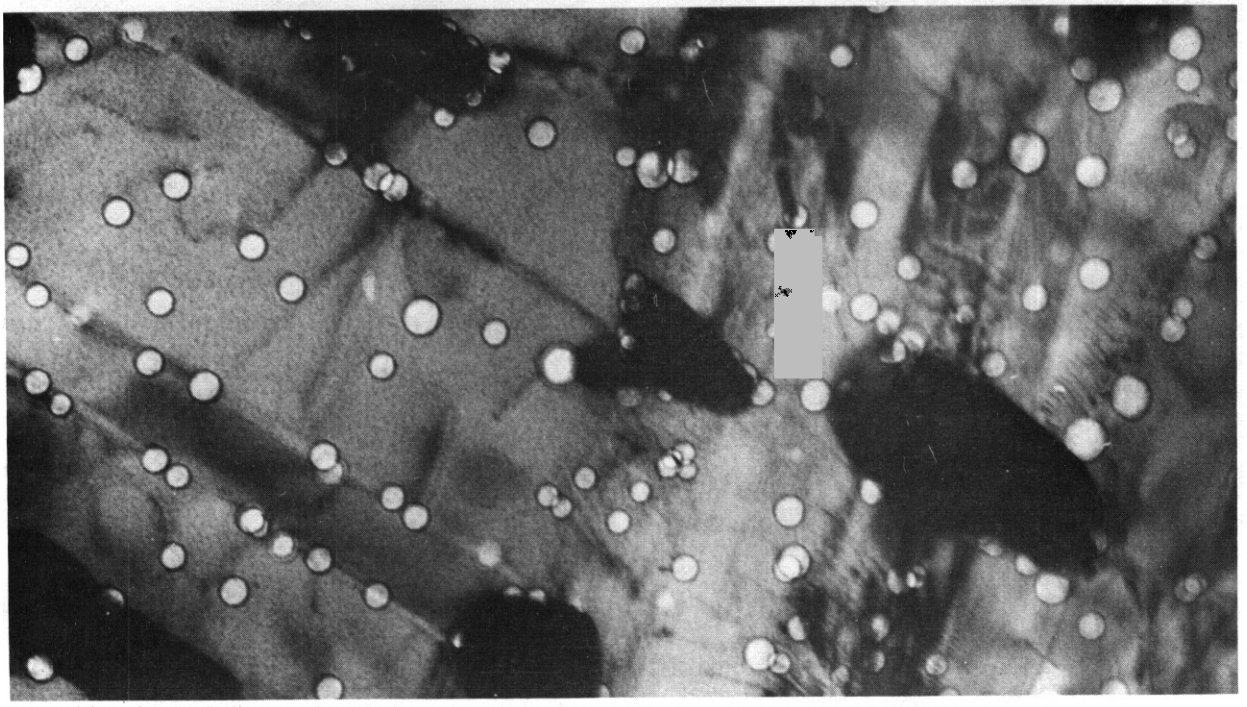

(a)

(b)

FIGURE 4. Typical Void Microstructures Observed in 20% Cold-Worked DO-Heat Specimen Irradiated at 550°C (Nominal) to 42 dpa in HFIR.

There were M_6C (30 weight % Fe, 25% Cr, 20% Ni, 15% Mo, 6% Si and 1% V), $M_{23}C_6$ (50% Cr, 20% Mo, 10% Fe, 10% Ni, 5% Si and 1% V), Laves (40% Fe, 30% Mo, 15% Cr, 5% Ni, 5% Si), Sigma (40% Cr, 40% Fe, 10% Mo, 2% Ni, 1.5% Si) and Chi (50% Fe, 25% Cr, 15% Mo, 3% Ni, 1.5% Si). The Sigma and Chi phases, which are normally formed at temperatures higher than 650°C, accounted for 7 of the 10 particles.

There were ten concentration profiles measured near precipitate surfaces. Three showed definite gradients in nickel toward the precipitate, one showed a minor gradient, and six exhibited no detectable gradient. Two of the profiles which exhibit gradients in nickel at the Laves phase are shown in Figures 5(a) and (b). Note that in Figure 5(a) the matrix nickel level far from the precipitate approaches that of the original nickel content.

X-ray analysis was performed on twenty-two precipitate particles extracted using the standard electrolyte for carbides (HCl and methanol). The particles were then grouped into three classes based on their composition range. In the first class four particles were identified by diffraction to be M_6C in structure and to have a composition of 30% Cr, 20% Ni, 20% Mo, 10% Fe, 7% Si and 2.5% V. Sixteen particles fell in the second class and were tentatively identified as Laves (35% Fe, 30% Mo, 20% Cr, 5% Ni, 4% Si and 1% V). The third class contained two as yet unidentified precipitates (30% Fe, 25% Mo, 20% Cr, 10% Ni, 6% Si and 2% V).

The major conclusions drawn from the extraction replica analysis was that particles of a particular phase have a consistently narrow range of composition and that the identity and relative number of precipitates found by extraction can differ from that found in random sampling of precipitates near the foil edge.

With one exception the phases identified in this study correspond to those identified by Maziasz.[5] Whereas he found sigma, M_6C (η-silicide), $M_{23}C_6$ and Laves, the Chi phase was also identified in this study.

In another set of X-ray analyses conducted on this specimen the matrix compositions were measured at approximately sixty different positions. Figure 6 shows

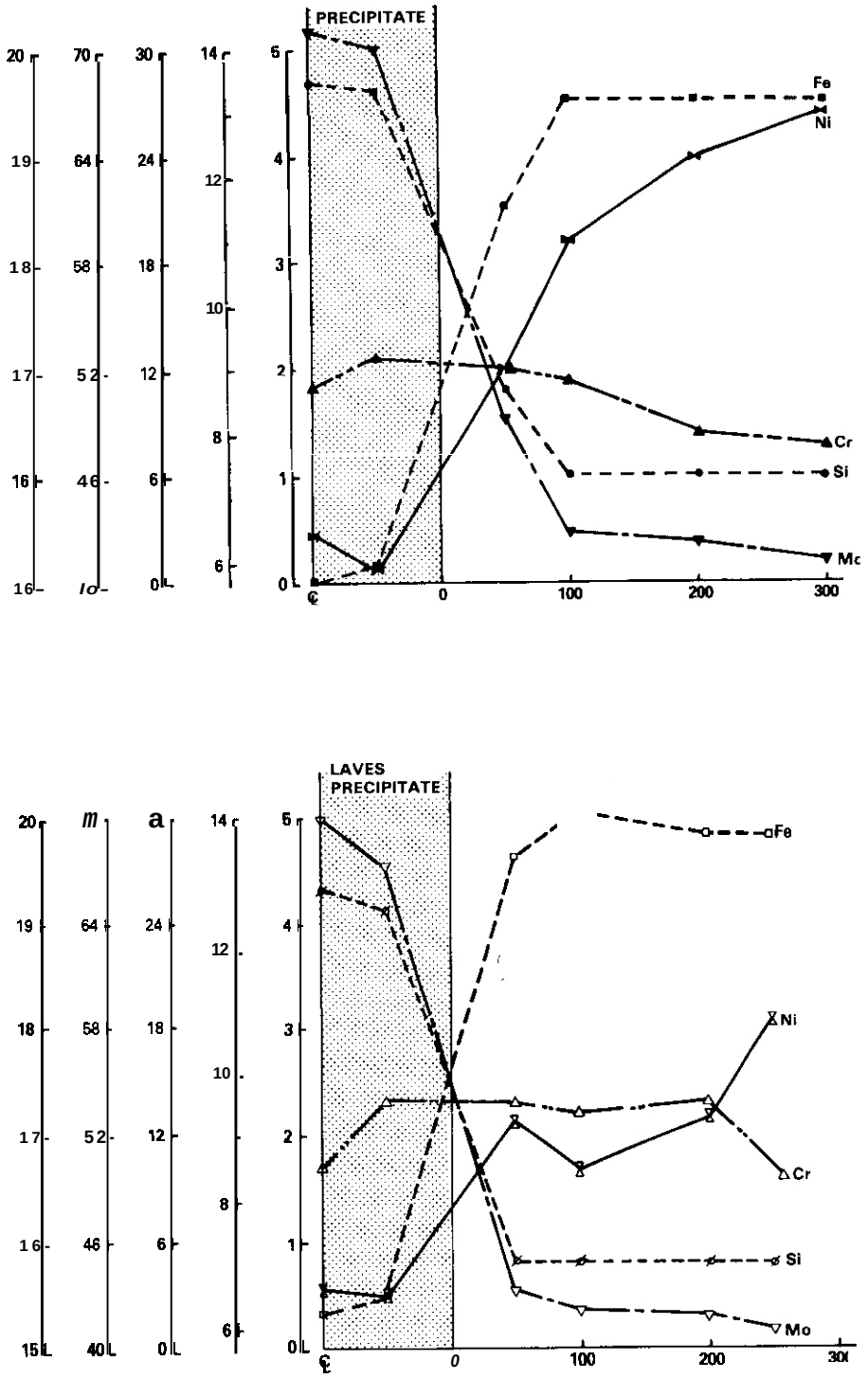

FIGURE 5. Near-Precipitate Composition Profiles Measured for Laves in the HFIR-Irradiated Specimen Shown in Figure 4.

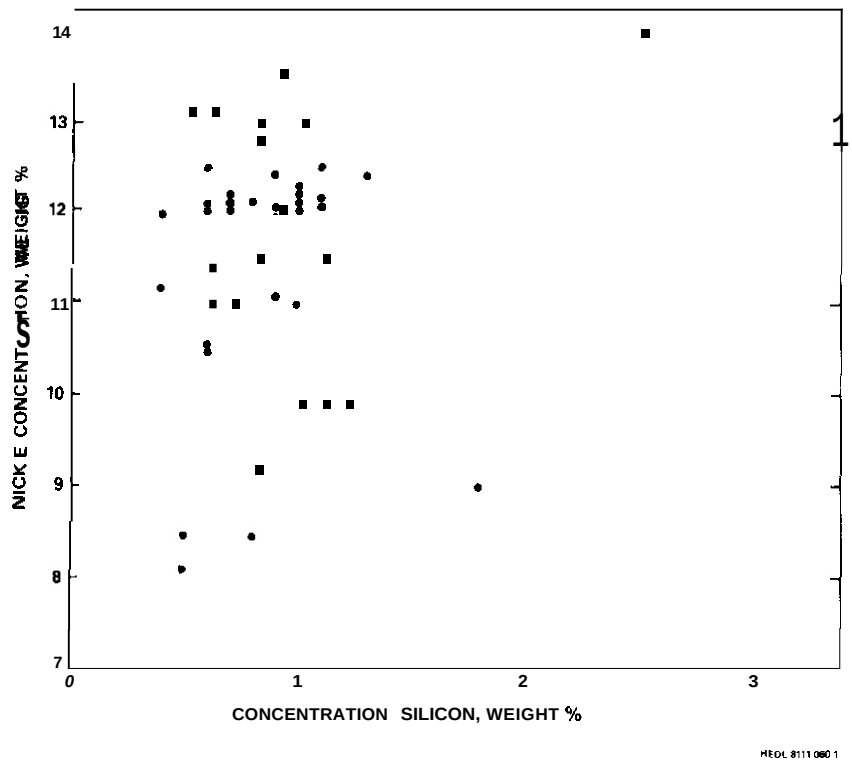

FIGURE 6. Nickel and Silicon Levels Measured at Various Points in the Matrix of the HFIR-Irradiated Specimen.

the nickel and silicon levels measured at each position. Note that there is heterogeneity of both nickel and silicon distributions. The centroid of the data lie very close to 11.5 to 12% nickel and 0.8% silicon. This indicates that very little nickel and silicon have yet been removed from the matrix. The original levels were 13 and 0.8%. This localized reduction of nickel content has previously been identified as signalling the onset of microchemical instability.

It was previously reported that significant amounts of vanadium form and that manganese tends to burn-out in HFIR-irradiated 316.[3-4] The vanadium is easily discernible in precipitates using X-ray analysis and appears to be concentrating in them at levels significantly above that produced in the bulk alloy. Typical values obtained by EDX analysis of ~10 to 50 square micron areas of the sample are 0.2 to 0.4 weight % compared to an initial chemical analysis value of 0.1 appm. Manganese concentrations cannot be as easily determined for two reasons. The X-ray peaks of iron and chromium are superimposed with the characteristic

Mn X-rays requiring that they be determined by nunerical analysis. In specimens of this high level of radioactivity, quantitative analysis of the manganese is very difficult, however.[6] This is due to the fact that the predominant X-ray produced by the natural decay of the radioactive isotopes is the ^{55}Fe (2.7 year half-life) which produces characteristic manganese X-rays. The magnitude of the superimposed X-ray signal from manganese K_α plus that of chromium K_β produced by the electron beam are, for HFIR irradiated steels, less than the ^{55}Fe decay γ-rays. Attempts to subtract the large manganese X-ray contribution from the ^{55}Fe using a "hole-count" measurement frequently result in a small but negative value for the manganese.

In an attempt to measure the bulk levels of both vanadiun and manganese another specimen, *D2-6,* was first examined by ion microprobe. This specimen was irradiated in HFIR at 460°C to 54 dpa, but was found to be contaminated with aluminum and unacceptable as a microprobe specimen. After attempting to remove the aluminun by ion milling the manganese and vanadium concentrations were found to be 1.33% and 0.61% respectively. The procedure was repeated using the LIZ-4 specimen, irradiated to 42 dpa, where the manganese and vanadium concentrations were found to be 1.30% and 1.06% respectively. The calculated vanadiun concentration at this fluence lies just above 0.4%. The source of the discrepancy may be preferential sputtering of the vanadium-rich precipitates. For the core centerline position of PTP in HFIR it is expected that ~40% of the manganese will burn out by 42 dpa leaving 1.14 weight % sane variation is expected at positions away from the core centerline. This specimen was not at the centerline but the measured value of 1.3% is reasonably close to the calculated value.

5.4 Discussion

As shown in Figures 7 and 8, there are currently two interpretations on how to extrapolate the HFIR data to higher fluence in the range 500 to 600°C. One of these approaches assumes that cold-worked AISI 316 has the same steady-state swelling rate in both HFIR and EBR-II.[1] Noting that the steady-state swelling rates for annealed and cold-worked steel in EBR-II are comparable, it is assumed

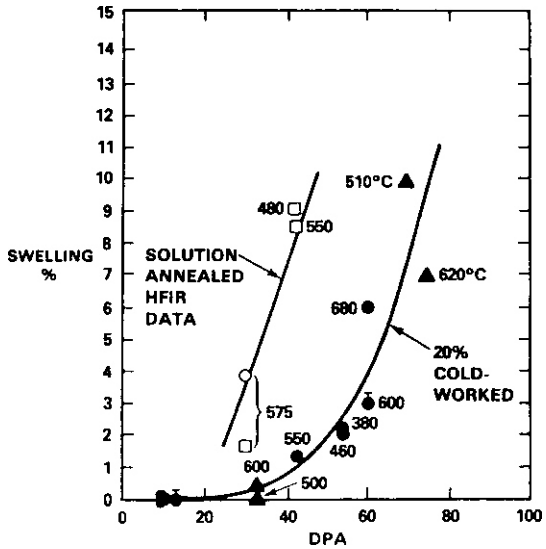

- HFIR DATA ON ANNEALED STEEL EXHIBITS SLOPE SIMILAR TO COMPOSITE EBR II/HFIR DATA
- BOTH CURVES COMPARABLE TO BREEDER-INDUCED SWELLING RATES AT 500-600°C

FIGURE 7. Comparison of Annealed and Cold-Worked DO-Heat in HFIR With That of Cold-Worked DO-Heat in EBR-II. All temperatures used are the nominal irradiation temperatures quoted for the original experiments.

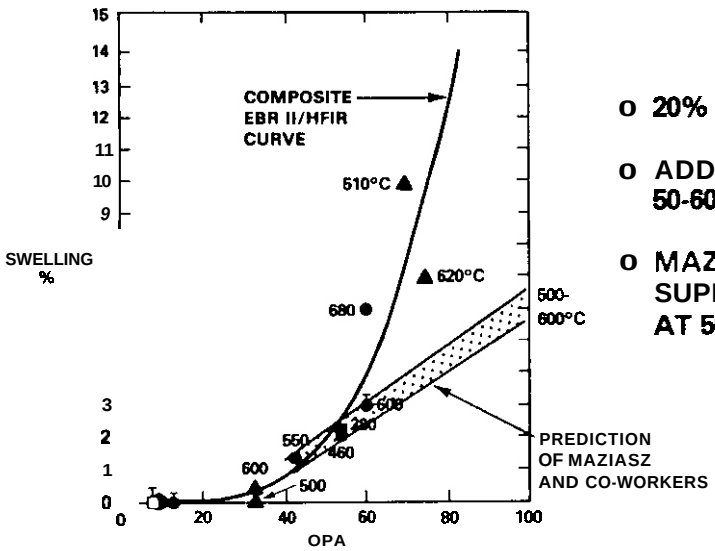

- 20% CW 316 DATA ONLY
- ADDITIONAL CURVATURE ABOVE 50-60 dpa?
- MAZIASZ AND CO-WORKERS PREDICT SUPPRESSION OF SWELLING RATE AT 500-600°C

FIGURE 8. Comparison of Composite Swelling Curve for 20% Cold-Worked DO-Heat With Predictions Based on HFIR Data Only and Rate Theory Principles.

that they will be comparable in HFIR also. As can be seen in Figure 7, the HFIR data on annealed steel suggest a swelling rate which not only is comparable to the composite HFIR/EBR-II data curve on 20% cold-worked DO-heat but is also comparable to the steady-state swelling rate observed in other U. S. breeder steels.

The alternate approach is to assume that the higher void densities induced by HFIR irradiation will lead to earlier swelling but lower steady-state swelling rates.[7] In effect it is assmed in this approach that no additional curvature occurs in the swelling curve beyond the last data point.

The major differences between these two approaches can be summarized in three statements.

(a) The fast reactor data base has shown that the steady-state swelling regime of this steel generally lies beyond 5% swelling. The second approach does not incorporate this insight.

(b) The first approach stipulates that the microchemical evolution of the matrix and precipitate phases is one of the dominant determinants of swelling, while thesecond approach asserts the dominance of helium over that of the microchemical evolution.

(c) The first approach assumes that large amounts of helium will not change the phase evolution very much and this assumption has been confinned by experimental studies in the range 500 to 600°C. It also assumes that distributing the voidage over a larger number density will not affect the swelling rate. The second approach takes the opposite stance. It should be noted that the void number densities in annealed HFIR-irradiated steel are Comparable to those in the cold-worked steel and yet the HFIR-induced swelling rate of the annealed steel is not depressed by the larger void nunber density but rather is similar to that observed in EBR-II irradiated steels.

The dislocation density produced in HFIR is comparable to that produced in EBR-II. The presence of gradients in elemental composition at precipitates (Laves, in particular) which have been shown to be enriched in nickel and silicon during irradiation in EBR-II supports the contention that the microchemical evolution is still in progress, as does the large range of nickel and silicon concentrations found in the matrix and the nickel and silicon enrichments of the M_6C phase. The precipitate phases found in HFIR-irradiated 00-heat are the same as those found in EBR-II irradiated specimens. All of the above suggest that the swelling rate of the cold-worked DO-heat will continue to increase at higher fluence to values comparable to that of the annealed steel in HFIR and the cold-worked steel in EBR-II.

In order to resolve these differences, the direct approach would be to generate more high fluence data on the limited amount of DO-heat steel which is available or to continue irradiations to higher fluences with the better characterized and more abundant specimens of the MFE heat of steel. Neither of these solutions appears to be feasible in the near future, however. It is therefore necessary to examine the data derived from DO-heat and from dual ion beam studies to gain insight on the role of helim on swelling behavior.

The data presented in this report would indicate that the cold-worked specimen irradiated at a nominal temperature of 550°C in HFIR was actually 100°C or more higher in temperature, a conclusion drawn from the presence of high temperature intermetallic phases and the distribution and rounded shape of the voids.

5.5 Conclusions

Additional data on the microstructural and microchemical evolution of the 00-heat of AISI 316 irradiated in EBR-II are consistent with other data in an earlier report. It appears that a late-term microchemical evolution occurs after 33 dpa at 500 to 600°C and appears to approach saturation near 70 dpa.

Examination of a HFIR-irradiated specimen at 42 dpa shows that the dislocation and phase evolution are consistent with that of comparable EBR-11-irradiated

material but that the void densities are higher. Microchemical analysis shows that a comparable evolution is in progress during HFIR irradiation and it is expected that the swelling rate will increase at higher fluence. Measurements of the vanadiun and manganese concentrations have been performed and agree reasonably well with calculated values. Details of the phase and void characterisitics indicate that the temperature is ~100°C higher than the reported nominal temperature of 550°C.

6.0 References

1. H. R. Brager and F. A. Garner, "Comparison of the Swelling and the Microstructural/Microchemical Evolution of AISI 316 Irradiated in EBR-II and HFIR," DAFS Quarterly Progress Report, DOE/ER-0046/6, (in press).

2. P. J. Maziasz and W. F. Wiffen, "Swellina and Microstructural Chanqes in Type 316 Stainless Steel Irradiated Under Simulated CTR Conditions;" ORNL/TM-5396, May 1976.

3. J. F. Bates, F. A. Garner and F. M. Mann, "The Effects of Solid Transmutation Products on Swelling in 316 Stainless Steel," DAFS Quarterly Proqress Report, DOE/ER-0046/6, (in press).

4. F. A. Garner, F. M. Mann and H. R. Brager, "Measurement and Calculation of Solid Transmutants Formed in AISI 316," this report.

5. P. J. Maziasz, J. Nucl. Mat., 85 and 86, 1979, 713-717.

6. L. E. Thomas, "EDX Microanalysis of Neutron-Irradiated Alloys," Proc. of Symposium on Advanced Techniques for Characterization of Irradiated Metals, Las Vegas, NV, February 1980, (in press).

7. P. J. Maziasz and M. L. Grossbeck, "Swelling, Microstructural Development and Helim Effects in Type 316 Stainless Steel Irradiated in HFIR and EBR-II," Proc. Second Topical Meetinq on Fusion Reactor Materials, Seattle, WA, August 9-12, 1981.

7.0 Future Work

The results of dual ion beam studies and related breeder studies will be examined, along with a review of the relevance to this study of microstructurally-deterministic rate theory approaches.

MIGRATION AND TRAPPING OF HELIUM BY CAVITIES AND DISLOCATIONS IN DUAL-ION IRRADIATED STAINLESS STEELS

J. A. Spitznagel, Susan Wood and W. J. Choyke (Westinghouse Research and Development Center)

1.0 Objective

The objective of this work is to assess the phenomenology and mechanisms of microstructural evolution in materials exposed to simultaneous helium injection and creation of atomic displacement damage by a second ion beam.

2.0 Summary

Dual-ion experiments have been conducted on specimens of 304 SS and 316 SS to estimate the fraction of implanted helium associated with cavities, dislocations or in submicroscopic bubbles. The results suggest that approximately 99 percent of the helium is in visible cavities near the peak swelling temperature. Numerical calculations of helium partitioning based on cavity and dislocation sink strengths for vacancies are shown to overestimate the number of gas atoms associated with dislocations and to reduce the maximum possible equilibrium bubble size by a factor of two.

3.0 Program

Title: Irradiation Response of Materials
Principal Investigators: S. Wood, J. A. Spitznagel and W. J. Choyke
Affiliation: Westinghouse Research and Development Center

4.0 Relevant DAFS Program Plan Task/Subtask

Subtask II.C.1.2 Modeling and Analyses of the Effects of Material Parameters on Microstructure

II.C.Z.I Helium Mobility, Distribution and Bubble Nucleation

5.0 Accomplishments and Status

5.1 Introduction

Much emphasis has been placed on the high helium and hydrogen concentrations expected in fusion reactor first wall and blanket structural materials. It is the distribution (or redistribution) of such nuclear transmutation products, however, that will determine their effects on mechanical properties.

Unfortunately, little is known about helium mobility and trapping at various microstructural "sinks." This is mainly due to experimental limitations. At present helium partitioning must be inferred from TEM observations of bubbles, measurements of helium release rates from surfaces, elastic and anelastic mechanical measurements, theory, etc.

Dual ion beam experiments, where helium can be implanted and the atomic displacement rate controlled by a second ion beam, are very useful for developing and testing such indirect approaches. In this report we outline a scheme to estimate helium partitioning between cavities and dislocations in dual ion bombarded 304 SS and 316 SS.

5.1.1 Experimental Details

Chemical compositions, thermomechanical processing history and results of extensive ion irradiation experiments on these samples have been reported previously.[1-2] Other experimental details have been described by us elsewhere.[2]

For the 316 SS samples calculated atomic displacement rates of ~2 x 10^{-4} dpa/s to 6 x 10^{-4} dpa/s and helium (appm) to dpa ratios of ~12-85 have been used. For the 304 SS, data obtained with atomic displacement rates of ~2 x 10^{-5} to 2 x 10^{-4} and helium (appm) to dpa ratios of ~11 to 475 are reported. Since a serious concern in estimating helium partitioning

is the amount remaining in submicroscopic form, e.g. less than ~2 nm diameter bubbles, care has been taken to try to use foil preparation and electron imaging conditions which maximize the possibility of detecting small bubbles. Data on cavity size distributions and dislocation densities have been encoded and analyzed using a data management code.

5.1.2 Numerical Analysis and Helium Partitioning Algorithms

A computer code has been developed which permits rapid retrieval of data satisfying a specified range of experimental parameters. Calculations of helium partitioning to cavities and dislocations have been performed for selected experimental conditions by adding various models to the code.

Helium is essentially insoluble in solid metals,[5] is readily trapped by vacancies,[6] and probably migrates as a divacancy-rare gas complex in an f.c.c. lattice.6 We will thus assume that the helium flux to a microstructural sink is proportional to the flux of vacancies to that sink. Under continuous helium implantation, populations of growing bubbles, cavities and dislocations (as well as grain boundaries and precipitate surfaces) will compete for the helium. To a first approximation, the partitioning of helium to these sinks should be related to the sink strength for vacancies.7

In this study we consider two possibilities: (1) All of the helium is trapped in visible cavities and (2) some fraction of the implanted helium is trapped at dislocations with the remainder trapped at visible cavities. In the latter case we make no distinction between network or loop components, i.e. the trapping is proportional to the total dislocation line length per unit volume. For this approximation we have assumed that no helium remains in the matrix and have ignored the direct contributions of precipitate surfaces and grain boundaries since their contributions to the overall vacancy sink strength are small. Indirect effects on helium partitioning from heterogeneous nucleation of bubbles on acicular precip-

itates and accelerated growth of cavities attached to such precipitates can be important. However, such effects will be discussed in a future paper. Dislocations are treated as unsaturable helium sinks (i.e. no "solubility limit"). This precludes bubble precipitation on dislocations, for example. Sticking coefficients of unity are assumed for both cavities and dislocations precluding thermal or kinetic resolution of gas atoms. Time (fluence) dependent partitioning to account for the evolving sink structure is treated in a quasi-empirical fashion. Finally, the total number of helium atoms in a slice Ax is always conserved except for those added by implantation.

Defining Q^{-1} as the fraction of helium partitioned to cavities (based on the cavity sink strength for vacancies[7]):

$$Q^{-1} = \frac{\sum_i 2\pi D_i N_i}{\sum_i 2\pi D_i N_i + \rho_D} \tag{1}$$

where D_i = diameter of a cavity in size class i,
N_i = number of cavities in size class i,
ρ_D = dislocation density.

The amount of helium to be distributed to the cavities (for a constant implantation rate, k_g and implant time At) is

$$[He]_c = k_g \cdot \Delta t \cdot Q^{-1} \quad . \tag{2}$$

The amount of helium partitioned to dislocations is

$$[He]_d = k_g \cdot \Delta t[1 - Q^{-1}] \quad . \tag{3}$$

If all the helium is assumed bound in cavities then clearly $Q^{-1} = 1$.

The idea that equilibrium gas bubbles should grow slowly, with vacancy

emission balanced by the influx of helium and vacancies until a critical size is reached[3] is central to our method of assigning helium atoms to cavities of different sizes. The validity of this model which has been described elsewhere.[4] Observations of stable bimodal cavity populations, selective growth of bubbles above a certain size under irradiation following preimplantation of helium, and theoretical calculations of conditions necessary for bias-driven cavity growth strongly support the model. We use the concept in the following way: (1) The Van der Waals equation of state is used to calculate the number of helium atoms in successive size classes up to a maximum possible equilibrium bubble diameter, D_c (determined by the number of available gas atoms), and (2) it is assumed that cavities with diameters $D > D_c$ contain *at least* as many gas atoms as when they passed through size class D_c.

After determining the amount of helium partitioned to the cavities, the Van der Waals equation of state and surface energy constraint ($P = 2\gamma/r$) is used to distribute the gas atoms in spherical equilibrium bubbles, beginning with the smallest size class. The choice of an appropriate equation of state and surface energy values for small bubbles has been discussed at length elsewhere.[8] Existing high pressure data suggests that Van der Waals equation is suitable even at extreme densities.

Figure 1(b) demonstrates the effect of using different values of Van der Waals' constant on the maximum possible equilibrium bubble diameter for the size distribution in Fig. 1(a) assuming all of the helium is in visible cavities. The limiting size class D_c increases linearly with the exclusion volume (b) but the effect is small. The Van der Waals equation with $b = 16.4 \times 10^{-24}$ $cm^3/atom$, consistent with Bridgeman's data[9] has been used in this investigation.

Values of surface energy appropriate for small cavities in a solid are difficult to define. For the purpose of this study, values of γ extrapolated from zero creep measurements on 304 SS[10] have been used giving a

temperature dependent surface energy

$$\gamma = 4250-2.0T(°C),\ mJ/m^2 \tag{4}$$

No corrections for cavity size or shape, gas adsorption or solute segregation effects have been attempted here. Figure 1(c) shows the effect of varying the surface energy on the maximum equilibrium bubble size for the distribution shown in Fig. 1(a). All of the helium is assumed bound in visible cavities. The abscissa reflects the effect of partitioning different (total) amounts of helium to the cavities. The implanted concentration C_{He} corresponds to C_{He} = 1. The effect of changing γ by a factor of ~5 is surprisingly small. Wood et al.[11] have discussed the probable reasons.

5.2 Results and Discussion

5.2.1 Dose Dependence

The sink structure and hence the capture efficiency of cavities and dislocations for vacancies and helium can change rapidly with fluence. Deductions of helium partitioning from "snap-shots" of the microstructure do not explicitly treat this continuous evolution. Approximations are possible, however, if the partitioning is calculated for specimens bombarded to different fluences under identical conditions. An example is shown in Table 1.

The effect of increasing fluence near the peak swelling temperature of ~600°C is to broaden the cavity size distribution. Nucleation of cavities has continued in the fluence range 0.26 to 2.7 dpa. It is not clear whether nucleation has continued up to 31 dpa; even though there are many small bubbles present, the cavity number density has decreased by a factor of two - probably reflecting the onset of coalescence. The dislocation density has increased from a value of ~1 x 10^9 cm/cm^3 in the unirradiated material to a saturation value of ~8 x 10^{10}. Surprisingly,

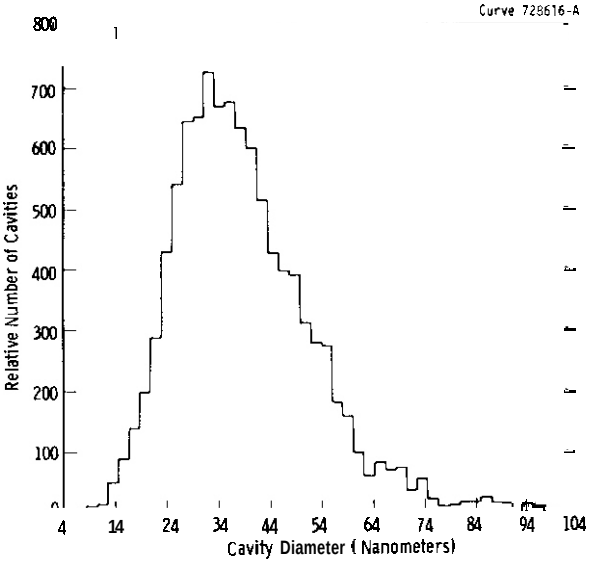

FIGURE la. Experimental Cavity Size Distribution for 304 SS Following Dual-Ion Bombardment at 600°C to 6-dpa and 782-appm Helium.

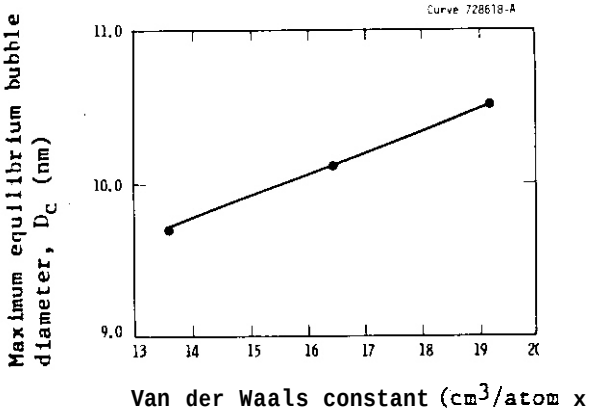

FIGURE lb. Maximum Equilibruum Bubble Diameter for the Distribution Shown in Figure la for Various Choices of Van der Waals Constant.

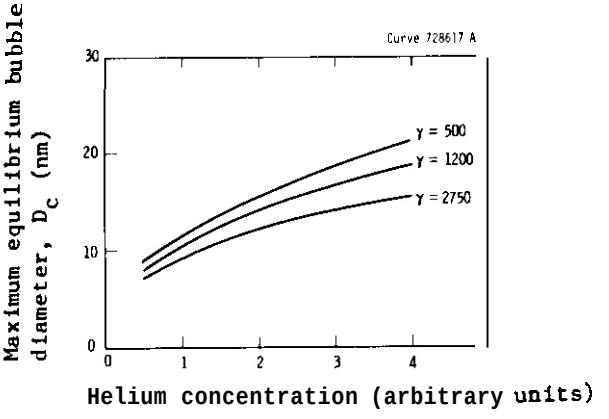

FIGURE lc. Effect of Surface Energy (mJ/m^2) and Helium Concentration on the Calculated Maximum Equilibrium Bubble Diameter for the Distribution in Figure la.

TABLE 1

EFFECT OF FLUENCE ON THE FRACTION OF IMPLANTED HELIUM (Q^{-1}) NUMERICALLY PARTITIONED TO CAVITIES FOR 304 SS DUAL-ION BOMBARDED AT 600°C AND 2 x 10^{-4} dpa/s

dpa	appm He	Cavities/cm^3	Dislocation Density cm/cm^3	Q^{-1}
0.26	49	3.1 x 10^{15}	2.3 x 10^{10}	0.49
2.7	522	7.3 x 10^{15}	8.2 x 10^{10}	0.37
31.4	5314	3.4 x 10^{15}	8 x 10^{10}	-0.5

even in the midst of such rapid changes in microstructure, the fraction of helium distributed to the cavities (Q^{-1}) on the basis of Eq. (1) is relatively constant. This is a consequence of the high cavity nucleation and growth rates which apparently counterbalance the increasing dislocation sink strength.

At higher irradiation temperatures and lower helium injection rates - conditions less favorable for cavity nucleation - the model suggests that >90 percent of the implanted helium may be associated with dislocations.

For example, Fig. 2 shows the fraction of helium numerically partitioned to dislocations in 316 SS as a function of measured dislocation density. Although the model predicts that 40-100 percent of the implanted helium should be associated with dislocations we will present evidence that suggests this is an overestimate.

5.2.2 Helium in Submicroscopic Form

A question which arises immediately in this method of assigning helium to sinks is: What fraction of the implanted gas atom concentration remains in submicroscopic form either in the matrix or in association with dislocations? An answer can be obtained from an approach making use of the critical cavity size concept.

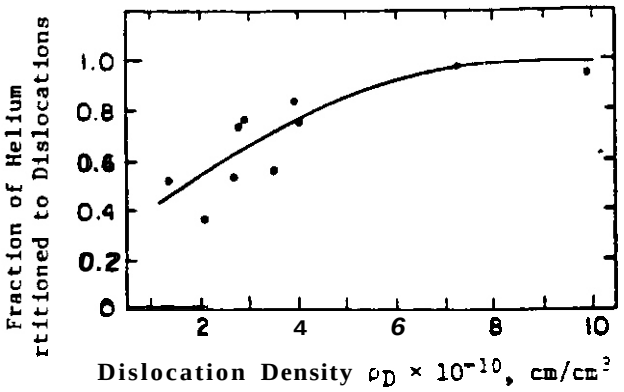

FIGURE 2. Fraction of Implanted Helium Atoms Numerically Partitioned to Dislocations $(1 - Q^{-1})$ as a Function of the Measured Dislocation Density for Dual-Ion Bombarded 316 SS in the Solution-Annealed, 20% Cold-Rolled or Aged (800°C) Condition. 600°C $T_{IRR} \leq$ 750°C; ϕt~3-12 dpa.

Figure 3a shows a cavity size distribution resulting from dual ion bombardment at 700°C to produce a population of bubbles followed by an additional bombardment with the 28 MeV Si^{+6} beam alone at 550°C. The cavity sizes produced at 700°C are larger than the critical cavity size (calculated) at 550°C. Thus a relatively coarse population of voids has been established, which contains only ~3 percent of the helium implanted at 700°C according to the partitioning algorithms. Figure 3(b) shows the result of annealing an identical control specimen at 600°C for 168 h. The preexisting distribution of voids (and dislocations) are essentially unchanged but a new population of small bubbles has appeared. The small bubble distribution contains only ~0.09 percent of the implanted helium. Sites adjacent to existing large cavities *not associated* with dislocations are where the tiny bubbles are found. Thus the amount of helium (numerically) partitioned to the dislocations on the basis of their relative sink strength for vacancies is clearly an overestimate since it is well known that bubbles grow on dislocations under these conditions.

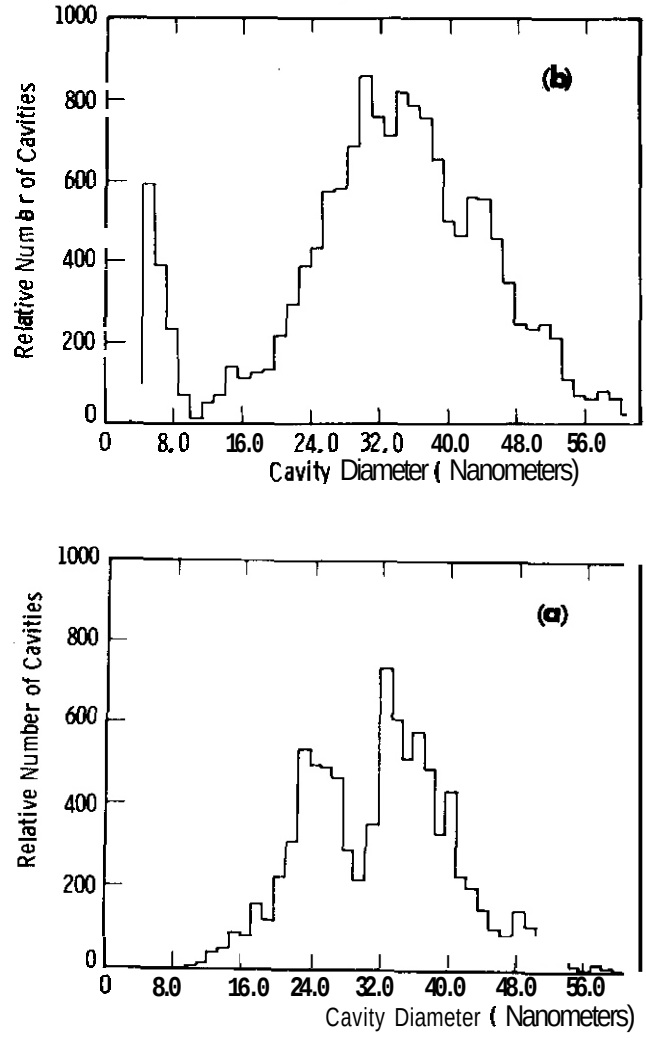

FIGURE 3. Cavity Size Distribution for 304 SS Dual-Ion Bombarded to 1.1-dpa and 117-appm He at 700 C Followed by Bombardment Without Helium to 3.3 dpa at 550 C; Then Annealed at 600 C-168 h.

5.2.3 Effects of Helium Partitioning on the Critical Cavity Size

As far as cavity growth is concerned, helium partitioning is only important for cavities smaller than or equal to the critical size.[3] The maximum equilibrium bubble size is a very good upper bound estimate of the critical cavity size,[12] and is affected by distributing part of the helium to the dislocations as shown in Fig. 4. Coupling the helium partitioning to the sink strength for vacancies reduces D_c by a factor of ~2. Theoretical estimates of D_c[12] fall between the two curves in Fig. 4 and offer no firm

support for either set of values. However, experimental observations of well separated bimodal cavity distributions with the lower gaussian terminating at D_c suggest that the $Q^{-1} = 1$ curve is the better estimate of the critical cavity size.

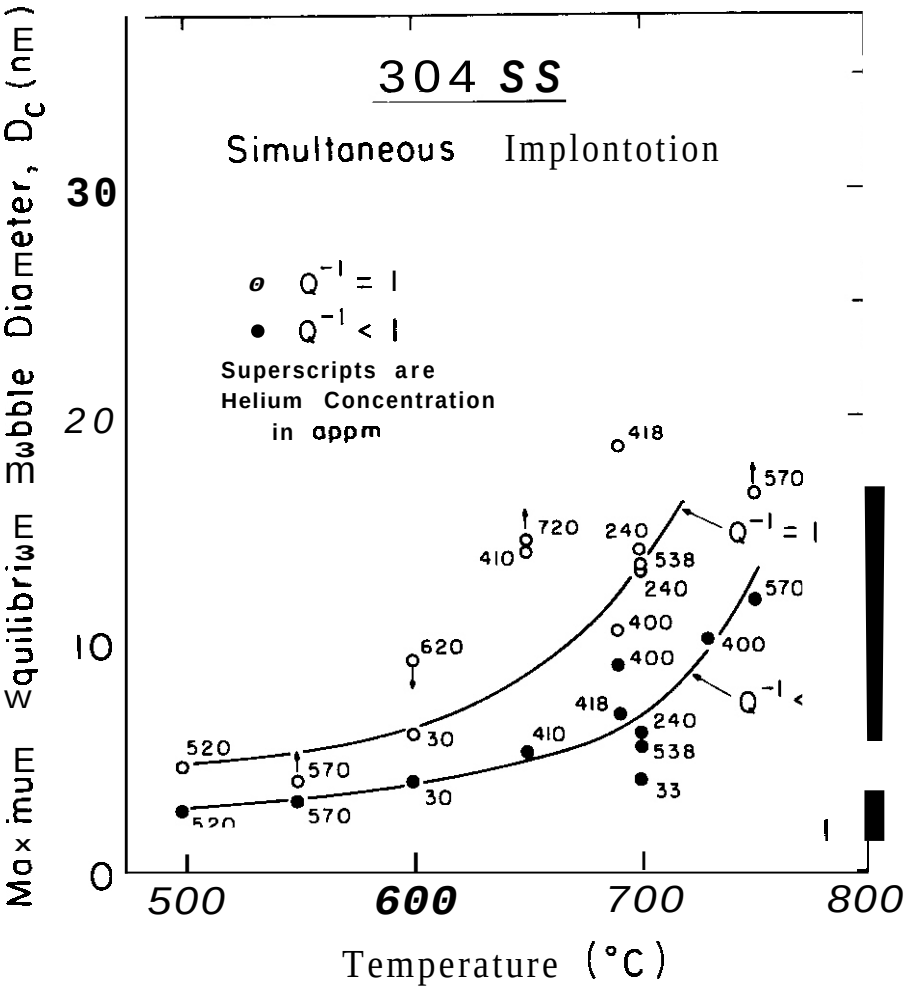

FIGURE 4. Comparison of Calculated Maximum Equilibrium Bubble Sizes Calculated from Dual-Ion Data Assuming All Helium Partitioned to Cavities ($Q^{-1} = 1$) or a Portion to Dislocation ($Q^{-1} < 1$).

5.2.4 Extension of the Method

Despite limitations in deducing helium trapping at various microstructural

sinks, imposed by the lack of detailed theoretical models and assumptions in the present work, many useful insights can be gained using the approach outlined here. The method is clearly applicable to fission reactor and high energy ex-reactor neutron studies, as well. The principal advantage of the dual-ion technique, however, is its ability to critically test assumptions in the partitioning schemes. Such an approach also offers the possibility of estimating helium migration distances and perhaps, rates of migration which are critical parameters in modeling alloy behavior under projected fusion reactor first wall and blanket conditions.

5.4 Conclusions

(1) Partitioning of helium to cavities and dislocations calculated on the basis of their relative sink strengths for vacancies overestimates the number of gas atoms associated with dislocations.

(2) The maximum possible equilibrium bubble size (which approximates the critical cavity size) is reduced by a factor of two for such partitioning.

(3) Dual ion beam bombardment coupled with post-irradiation annealing are most useful for testing models of helium redistribution for projected fusion reactor first wall and blanket conditions.

6.0 References

1. Choyke, W. J., McGruer, J. N., Townsend, J. R., Spitznagel, J. A. Doyle, N. J., and Venskytis, F. J., J. Nucl. Mater. 85 and 86 (1979) 647.
2. Wood, Susan, Spitznagel, J. A., Choyke, W. J., Doyle, N. J., McGruer, J. N., and Townsend, J. R., 10th ASTM International Symposium on Effects of Radiation on Materials, ASTM STP 725 (1981) 455.
3. Hayns, M. R., AERE-R8806, *May* 1977, Harwell.
4. Hayns, M. R. and Wood, M. H., J. Nucl. Mater. 87 (1979) 97.
5. Blackburn, R., Metallurgical Reviews 11 (1966) 159.

6. Melius, C. F., Wilson, W. D., and Bisson, C. L., Rad. Effects 53 (1980) 111.

7. Hayns, M. R. and Mansur, L. K., Ibid. Ref. 2, p. 213.

8. Cost, J. R. and Chen, K. Y., J. Nucl. Mater. 67 (1977) 265.

9. Bridgeman, P. W., Physics of High Pressures (1949) 114.

10. Murr. L. E., Wong, G. I., and Horylev, R. J., Acta Met. 21 (1973) 595.

11. Wood, S., Spitznagel, J. A., and Choyke, W. J., Damage Analysis and Fundamental Studies, Quarterly Progress Report DOE/ER-0046/5, U.S. Dept. of Energy, Office of Fusion Energy (1981).

12. Townsend, J. R., University of Pittsburgh, unpublished research (1981)

7.0 Future Work

No additional effort is planned.

8.0 Publications

This paper will be published in the Proceedings of the Second Topical Meeting on Fusion Reactor Materials, August 9-12, 1981 in Seattle, WA.

BUBBLE GROWTH KINETICS ASSOCIATED WITH IRRADIATED AND POST-IRRADIATION ANNEALED METALS

M. L. Sattler, J. L. Bennetch, W. A. Jesser (University of Virginia)

1.0 Objective

The objective of this work is to assess the role of gas pressure and grain boundaries in helium bubble growth.

2.0 Summary

During in-situ observations of the irradiation of CVD Ni films with He ions, it was found that growth rate of bubbles on the grain boundary increased up to 4.5 times that of bubbles growing in the grain interior. Neighboring bubbles on a grain boundary were dynamically seen shrinking and growing in volume exchange patterns when the He-irradiated Ni was annealed. The annealing of He irradiated 316 stainless steel specimens showed that bubbles grew in underpressurized states as well as in overpressurized states; the overpressurized bubbles were found to grow more rapidly than underpressurized bubbles. Changes in diameter, bubble surface area, and swelling were found to be non-constant with annealing time.

3.0 Program

Title: Simulating the CTR Environment in the HVEM
Principal Investigators: W. A. Jesser and R. A. Johnson
Affiliation: University of Virginia

4.0 Relevant DAFS Program Plan Task/Subtask

Subtask 11.C.2.1 Mobility, Distribution and Bubble Nucleation

5.0 Accomplishments and Status

5.1 Introduction

Factors that influence bubble growth kinetics can be classified into two categories, migration and coalescence or accumulation of vacancies. The first type relies on mechanisms such as surface diffusion, volume diffusion, or vapor transport. Mechanisms for the latter case also include ledge nucleation processes. Because theoretical approaches have found that growth rate drops rapidly with increasing bubble size, a logarithmic plot of bubble size vs. time can help in the assessment of possible rate controlling mechanisms. This is summarized by P. Goodhew and S. Tyler.[1] Experimental work by D. Braski, H. Schroeder, and H. Ullmaier[2] and by I. Smith and B. Russell[3] have shown a logarithmic dependence of the mean bubble radius on time with constant slope n. Their work is used for comparison.

In the present work, the dependence of radius on time has been recorded for the case of in-situ irradiation of thin foils, rather than on bulk materials which have been pre-injected and subsequently annealed. Post-irradiation annealing experiments were also performed on thinned foils where, in one case, the annealing was observed dynamically. It is the aim of this study to determine the effect of gas pressure and of grain boundaries on bubble growth.

5.2 Experimental Results

5.2.1 Experimental Procedure

Nickel samples of either the carbonyl-grown chemical vapor deposited (CVD) type or the physical vapor deposited (PVD) type were irradiated in an HVEM linked to an 80 kV He ion accelerator. The CVD Ni had been electropolished to a thickness of 150 nm; the PVD Ni was also 150 nm thick. Microstructure in both types of Ni samples consisted of very small grain sizes prior to irradiation: 600 nm grains surrounded by 30 nm grains in the CVD Ni, and

220 nm grains in the PVD Ni. The Ni films were irradiated at fluxes from 5.6×10^{14} ions/cm^2-sec to 7.5×10^{14} ions/cm^2-sec to doses of 1.0×10^{18} ions/cm^2 and 1.4×10^{18} ions/cm^2 at a temperature estimated to be 550° C. In-situ recordings were made by video camera or by EM plates taken at appropriate time intervals.

Samples of 316 stainless steel (SS) were also irradiated with 80 kV He-ions after initial annealing and electropolishing steps were taken. The 1 hour pre-irradiation anneal at 1000" C resulted in a dislocation-free, large grain microstructure; electropolishing gave a 100 nm thickness. Doses ranged from 1.0×10^{17} ions/cm^2 to 1.0×10^{18} ions/cm^2 at a constant flux of 3×10^{14} ions/cm^2-sec and at an irradiation temperature of 300" C.

After irradiation, the 316 SS was annealed in a quartz wire-wound heater in 10^{-7} torr vacuum. The temperature was constant at 900" C for times ranging between 10 minutes and 30 minutes. Data was gathered after the anneal. The PVD Ni was annealed in a Philips 400 TEM heating assembly at 600" C for 80 minutes. During this annealing step micrographs were taken at convenient time intervals.

5.2.2 Irradiation Kinetics

Table I gives the results of the in-situ CVD Ni irradiation as they were recorded on HVEM plates.

In less than two minutes of irradiation, the CVD Ni grains grew to an average 810 nm size and all of the small 30 nm grains disappeared. Continued irradiation increased the grain size slowly to a maximum of 2300 nm.

During the irradiation bubbles initially appeared on the grain boundaries, but their growth was irregular. In HVEM micrographs taken at timed intervals, bubbles on the grain boundaries were seen to grow to an average of 110 nm, decrease to 88 nm, and then increase to 130 nm. Bubbles in the grain interi-

TABLE I

MICROSTRUCTURAL PARAMETERS FOR HELIUM-IRRADIATED NICKEL

Dose ($x10^{17}$ ions/cm^2)	Time of Irr. (min)	Cavity Diameter (nm) D_{gb}	D_{int}	D_{tot}	$Density_{tot}$ ($x10^{13}/cm^3$)	$Swelling_{tot}$ (%)	Grain Size (μm)
.9	2	88	50	81	7.8	4.7	.81
3.6	8	110	54	89	9.9	11.2	1.2
9.0	20	88	68	75	15	9.4	2.3
14.0	30	130	82	100	12	22.8	1.7

or, however, only increased in size from 50 nm to 82 nm. Plotting grain interior bubble radius versus time, the solution is linear (correlation of 99.5%) with a slope of 1.2 nm/min. The graph for grain boundary bubble radius with time did not yield a good correlation for either a linear plot or a logarithmic plot. The irregular growth of bubbles on the grain boundary is emphasized by the calculation of growth rate for bubbles on each type of site. Bubbles on the grain boundary exhibit a negative growth during a certain time interval. However, the rates before and after this interval show that the growth rates for bubbles on the grain boundary are 2.5 to 4.5 times that of bubbles in the grain interior.

The interpretation of the measured bubbles termed to be in the grain boundary or in the grain interior is complicated by the fact that the grain boundary moved during the irradiation, thereby leaving large grain boundary bubbles behind to subsequently be counted as grain interior bubbles. Micrographs showing a row of bubbles in the grain interior close to a row of slightly smaller bubbles in the grain boundary were typical. The area between these two rows of bubbles appeared denuded of any visible bubbles. It should be noted that the area on the other side of the grain boundary was not denuded.

The number density of the bubbles as measured with irradiation time followed a typical pattern of increasing slowly to an apparent saturation level and remaining approximately constant. This saturation level was found to be approximately 1.5 x $10^{14}/cm^3$.

Swelling data was calculated by summing over each range of volumes and multiplying by the total average number density. Volumes of bubbles with radii greater than the foil thickness were found by assuming a cylindrical shape for these bubbles. Using the above method, the swelling was found to increase from 4.7% at two minutes (2.5 dpa) to 22.8% at 30 minutes (38 dpa). This increase was not linear, however. Histograms show a spike of bubbles grouping around the mean bubble radius that tended to blunt and spread out as time of irradiation continued. The greater amount of very large bubbles could explain the tremendous swelling increase at longer times.

Two calculations to estimate bubble pressure were made: N_{imp} is the estimated number of helium atoms implanted during the irradiation per bubble as found using the EOEP-1 computer program of I. Manning and G. Mueller[4]; N_{eq} is the equilibrium number of helium atoms per bubble as found using a modified van der Waals equation[5] by inserting a temperature dependent b[6]. N_{imp}/N_{eq} should equal unity for equilibrium bubbles. This ratio will be an overestimate, though, since all the deposited helium is assumed to go to bubbles and not to other sinks. For the CVD Ni, N_{imp}/N_{eq} ratios show all bubbles to be overpressurized with ranges from 15 at 2.5 dpa to 93 at 38 dpa.

5.2.3 Post-Irradiation Annealing Kinetics

Table II gives the results for the post-irradiation annealing of 316 stainless steel.

In the 316 SS specimens, the average bubble size increased and the average number density of bubbles decreased after the annealing of both irradiated specimens. In the specimen subjected to a dose of 1×10^{17} ions/cm^2, bubbles grew from an average of 1.2 nm to an average of 7.9 nm after a 30 minute anneal. The sample with a dose of 1×10^{18} ions/cm^2 increased in its average bubble size from 1.7 nm to 4.0 nm after a 10 minute anneal. The microstructure for each irradiated sample prior to annealing was similar. However, after the anneal, the specimen with the lower dose contained no bubbles great-

TABLE II

MICROSTRUCTURAL PARAMETERS FOR HELIUM IRRADIATED TYPE 316 SS

Dose (ions/cm^2)	T_{irrad} (°C)	T_{anneal} and t (°C and min)	D (nm)	ρ (x10^{17}/cm^3)	$\frac{\Delta S}{V}$ (x10^4 cm^2/cm^3)	$\frac{\Delta V}{V}$ (%)
	300	---	1.2	15.4	7.0	.14
	300	900, 30	7.9	.13	1.6	.32
10^{18}	300	---	1.7	18.0	16.0	.46
10^{18}	300	900, 10	4.0	.60	5.8	3.9

er than 15 nm while the specimen with the higher dose contained bubbles greater than 1000 nm in diameter.

Histograms of number versus size for these two cases show spikes around the average for the prior-to-annealing cases and blunted spikes after they are annealed. The sample with the 1 x 10^{18} ions/cm^2 dose seems to have a small peak at 190 nm in addition to the blunted spike mentioned earlier.

Measurements of swelling show that annealing after irradiation increases the swelling twofold in the low-dose specimen and almost tenfold in the high-dose specimen. Similarly, total bubble surface area per unit volume does not remain constant upon post-irradiation annealing, but instead decreases. These numbers are recorded in Table II.

Examination of the N_{imp}/N_{eq} ratio shows that the sample with the lower dose was not overpressurized before the anneal but that the sample with the higher dose was overpressurized. In both cases, the anneal resulted in a lower helium to vacancy ratio and also apparently caused underpressurization. These results can be found in Table III.

Post-irradiation annealing of PVD Ni shows an increase in the average bubble size from 5.8 nm after 7 minutes of annealing to 7.2 nm after 80 minutes of annealing for grain boundary sites and correspondingly from 5.0 nm to 9.5 nm for grain interior sites.

TABLE III

RATIO OF IMPLANTED HELIUM TO HELIUM IN EQUILIBRIUM BUBBLES FOR TYPE 316 STAINLESS STEEL

Dose (ions/cm^2)	N_{imp}/N_{eq}	He/vac
10^{17} before annealing	1.31	3.2
10^{17} after annealing	.083	1.5
10^{18} before annealing	4.03	9.8
10^{18} after annealing	.040	1.2

The growth of grain interior bubbles showed a typical slow increase with time. However, the growth of grain boundary bubbles varied significantly. For bubbles grouped close together on the boundary, it was found that they would shrink and grow by as much as 2 nm during a ten minute time interval. This is illustrated by the following graph (Figure 1) of radius versus time for four grain boundary bubbles. Note that the maximum size of a bubble before it starts to shrink is about 10 nm. Total volumes for these bubbles increases to an apparent saturation level. The sum of the volumes of bubbles 1 and 2 is approximately constant for the saturation section of the total volume curve and the same holds approximately true for bubbles 3 and 4.

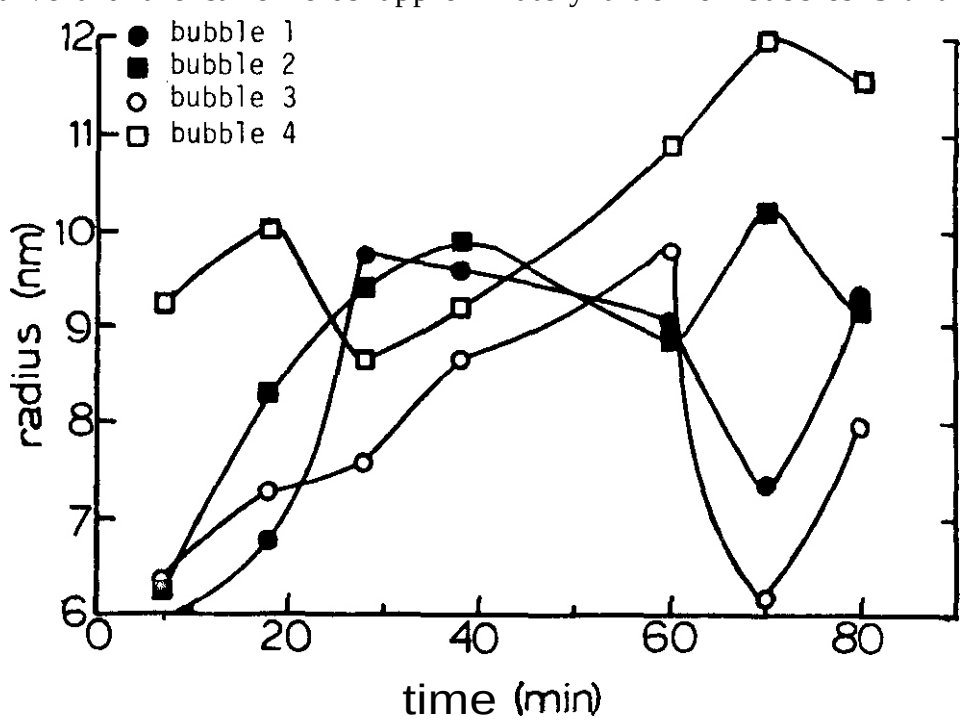

FIGURE 1. Bubble Radius Versus Irradiation Time for Grain Boundary Bubbles in Nickel Under Continuous Observation.

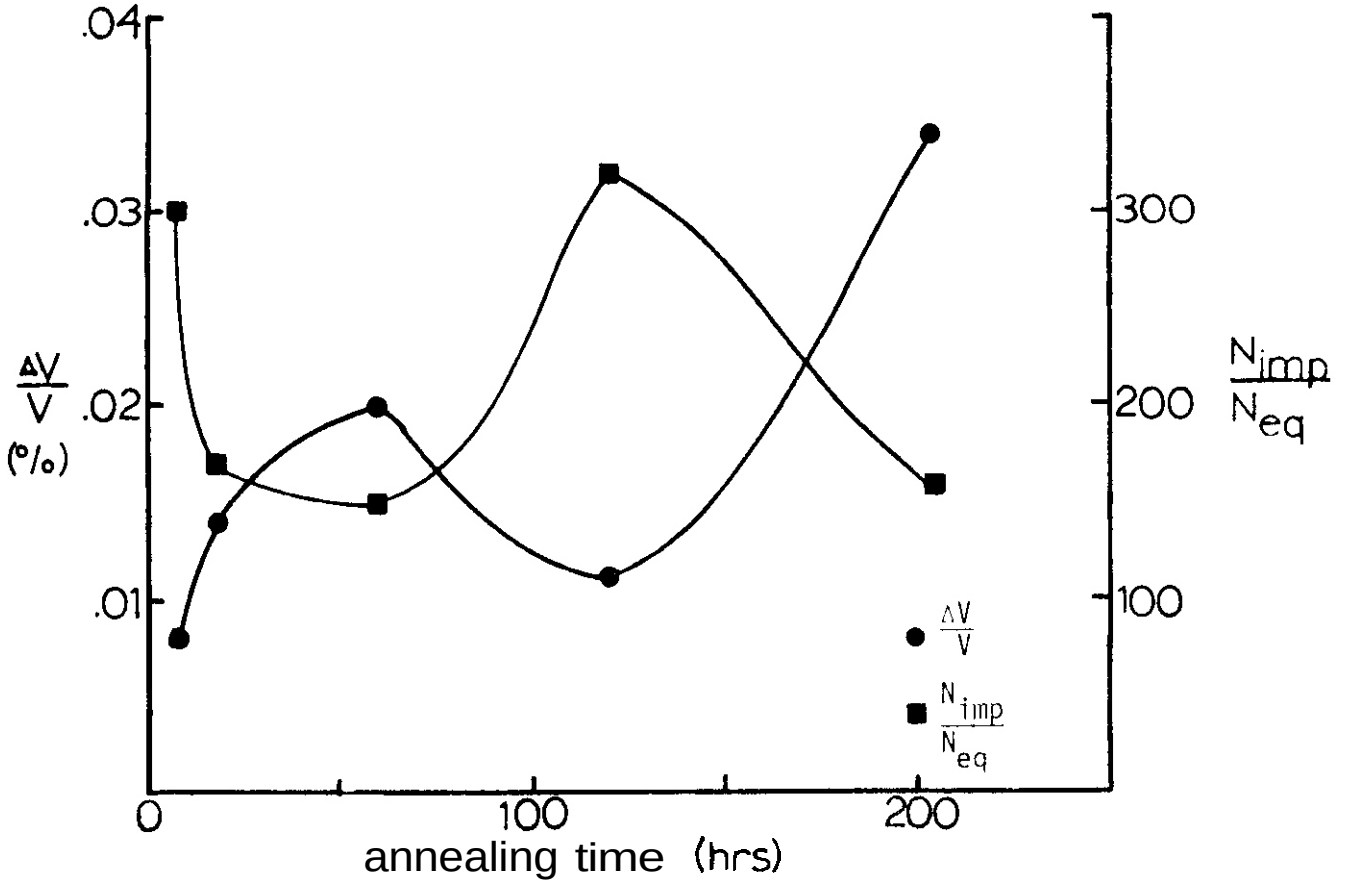

FIGURE 2. Swelling and Ratio of Implanted Heliun to Heliun in Equilibrium Bubbles Versus Annealing Time for Type 316 Stainless Steel as Calculated From Data of Braski et al. (2)

5.3 Discussion

In-situ observations of bubble growth in helium-irradiated CVD Ni have shown that the total swelling decreases at one time during the irradiation. It is also during this time interval that the average grain boundary bubble size decreases and the average grain size is maximized. This was explained by the movement of the grain boundary such that it abandons its large bubbles although this process was not dynamically observed. It is possible that the denuded zone that appeared behind the migrating grain boundary served to decrease the total possible density and thus helped in decreasing the swelling. Total density measurements could not just be summed and averaged over the grain boundary density and the grain interior density but rather included this denuded zone. The other component of swelling, total average diameter, was summed from grain boundary and grain interior diameter numbers.

The large increase in swelling for the next time interval was a result of the tremendous growth in grain boundary bubbles after migration of the grain boundary. Histograms showed large numbers (12%) of bubbles greater than 200 nm (the edge of the blunted spike) during the final time interval compared to 0% at 2 minutes, 6% at 8 minutes, and 6.8% at 20 minutes. Rapid growth of bubbles in contact with the boundary was previous observed by W. Beere.[7]

In order to compare the CVD Ni results with grain boundary work done by D. Braski, et al.[2], the data was fit to the equation $r \propto t^n$. It was found in the present work that for grain interior bubbles, n = 1; there was no good fit for grain boundary bubbles. D. Braski, et al. obtained slope values of n = 1/6 for grain boundary bubble growth and of n = 1/4 for the grain interior bubble growth. These authors had previously stated, however, that the bubbles in the grain boundary initially grew much faster than those in the grain interior. The higher slope of n = 1 obtained in the irradiated sample compared to the annealed pre-injected sample could be a result of the continuous amount of helium being supplied to the sample.

Because cavities have been observed to nucleate and grow in CVO Ni upon heating without prior irradiation or pre-injection of helium gas,[8] a thinned sample of CVD Ni was annealed at 600" C for 90 minutes. No voids were observed.

The grain boundary also played a fundamental role in bubble growth during annealing of He-irradiated PVO *Ni* samples. Apparently the helium atoms and/or vacancies associated with the bubbles at the grain boundary were mobile enough at 600" C to interact with the grain boundary and to cause shrinkage or growth of the bubbles. There also appeared to be some sort of critical bubble size to which each bubble grew before shrinking.

Total swelling was found to be nonconstant in the annealing of pre-irradiated 316 SS; it increased upon annealing. Also total bubble surface area and bubble diameter was not constant upon annealing. Comparison of this data is easily made with the annealing data of He pre-injected 316 SS of D. Braski, et al.[2] This comparison is shown in Figure 2. Volume changes increase, decrease, and increase again with annealing time, ranging from .08% at 8 hrs. to .3% at 210 hrs. Calculation of N_{imp}/N_{eq} ratios for the data of 0. Braski et al. show the bubbles to be highly overpressurized, even though these values vary as greatly as the swelling did with time. For example, at 8 hrs., the ratio is 300, at 60 hrs. it has decreased to 149 and at 120 hrs., it has increased again to 320. Another comparison can be made with the post-irradiation annealing data of a neutron-irradiated Al-Li alloy by I. Smith and B. Russell.[3] (They observed the non-constancy of D, D^2 and D^3 in the curves for $D \alpha t^n$, since n varied from 0.02 to 0.97 depending upon annealing temperatures.) Calculation of the N_{imp}/N_{eq} ratio shows their bubbles to be underpressurized, but constant, ranging from 1.5×10^{-4} to 4.5×10^{-4} depending on the annealing temperature.

The present work of annealing pre-irradiated 316 SS shows the growth of bubbles from either an underpressurized condition or an overpressurized condition. While this seems to match results from I. Smith and B. Russell (underpressurized) and from D. Braski, et al. (overpressurized), data from J.

Mancuso and C. Y. Li[9] does not seem to follow these observations. Upon annealing of samples with a pre-injection of H, equilibrium bubbles were not seen to grow. Only those bubbles which were overpressurized grew. The present results for helium seem to imply that bubble overpressure is not necessary for bubble growth.

5.4 Conclusions

1. The grain boundary, interacting with He atoms and/or vacancies, causes bubbles on it to grow during He-ion irradiation of thin Ni films at a rate up to 4.5 times that of bubbles in the grain interior.

2. For the relation $r \propto t^n$, n = 1 for bubbles growing in the grain interior during irradiation; n is undetermined for bubbles growing on the grain boundary.

3. The interaction of He atoms and/or vacancies with the grain boundary can cause neighboring cavities along its length to grow and shrink when the He-irradiated sample is annealed.

4. Diameter, total bubble surface area, and volume change were found to vary when 316 SS is annealed after He-ion irradiation.

5. Bubble overpressurization is not a necessary condition for bubble growth upon annealing.

6.0 References

1. P. J. Goodhew and S. K. Tyler, "Helium bubble behaviour in b.c.c. metals below 0.65 T_m", Proc. R. Soc. Lond. A **377**, 151-184 (1981).
2. D. N. Braski, H. Schroeder, and H. Ullmaier, "The effect of tensile stress on the growth of helium bubbles in an austenitic stainless steel", J. Nucl. Mat. 83, 265-277 (1979).

3. I. O. Smith and B. Russell, "The behaviour of radiation-induced gas in irradiated aluminum-lithium alloys", J. Nucl. Mat. 35, 137-157 (1970).

4. I. Manning and G. P. Mueller, "Depth distribution of energy deposition by ion bombardment", Comp. Phys. Comm. 7, 85-94 (1974).

5. J. R. Cost and K. Y. Chen, "The number of gas atoms per bubble of inert gases at high pressures", J. Nucl. Mat. 95, 239 (1980).

6. N. V. Tsederberg, V. N. Popov, and N. A. Morozova, Thermodynamic and Thermophysical Properties of Helium, U.S. Dept. of Commerce, Springfield, Va. p.18 (1971).

7. W. Beere, "An in-situ observation of the grain boundary/bubble interaction", Scripta Met. 9, 999-1001 (1975).

8. J. T. Houston and K. Farrell, "Swelling of carbonyl nickel", Metallography 4, 157-164 (1971).

9. J. F. Mancuso and C. Y. Li, "The growth of grain boundary cavities under applied stress and internal pressure", Met. Trans. A 10A, 1719-1722 (1979).

SINGLE- AND DUAL-ION IRRADIATIONS OF FERRITIC ALLOYS AND TYPE 316 STAINLESS STEEL

G. Ayrault (Argonne National Laboratory)

1.0 Objective

The objective of this work is to determine the microstructural evolution, during irradiation, of first wall materials with special emphasis on the effects of helium production, displacement damage rates, and temperature.

2.0 Summary

A series of ferritic alloy and Type 316 stainless steel samples were single- and dual-ion irradiated. The ferritics were unmodified and Ni-modified HT9 and 9Cr-1Mo alloys; samples were single- and dual-ion irradiated to a single dose level (25 dpa) in the temperature range 350-600°C. The primary purpose was to isolate the irradiation induced microstructural changes that result from helim injection and from Ni-modification, by comparing single- and dual-ion irradiated samples of the same alloy and unmodified and Ni-modified samples irradiated under the same conditions. For 316 SS, the emphasis in this series of irradiations *was* on the influence of helium injection schedule and prior thermomechanical treatment on microstructure development.

3.0 Program

Title: Effects of Irradiation on Fusion Reactor Materials
Principal Investigator: A. P. L. Turner
Affiliation: Argonne National Laboratory

4.0 Relevant DAFS Progam Plan Task/Subtask

Subtask II.C.2.1 Mobility, Distribution and Bubble Nucleation

%.0 Accomplishments and Status

5.1 Introduction

A major question in the irradiation response of candidate magnetic fusion reactor (MFR) structural materials is the influence of concurrent displacement damage and helium production. Dual-ion irradiation, using heavy-ions for damage production and helium ions to simulate gas production by transmutation events, provides a means of investigating such events in the absence of a high energy neutron source.

In continuation of our work on irradiation microstructural development in Type 316 SS and ferritic alloys, we have recently performed a series of irradiations on these alloys. This report describes those irradiations. In all cases, 3.0 MeV $^{58}Ni^{+}$ ions were used for damage production, and a degraded 0.83 MeV $^{3}He^{+}$ beam was used for helium injection (preinjection or simultaneous).

5.2 Variation of Helium Injection Schedule in Type 316 SS

In mixed-spectrum reactor irradiations of nickel-bearing alloys, helium is generated by a two-step process:

$$^{58}Ni(n,\gamma)^{59}Ni$$

and

$$^{59}Ni(n,\alpha)^{56}Fe \ .$$

At the start of an irradiation, no helium is generated, because there is no ^{59}Ni; helium generation increases with dose, as the ^{59}Ni level increases. In contrast, rapid helium generation will commence at the onset of irradiation in an MFR. Helium is likely to affect loop and cavity nucleation, so at low doses one would expect differences between the irradiation microstructures produced by mixed-spectrum reactor irradiation and MFR irradiation. However it is not clear whether these differences will persist at higher doses. With dual-ion irradiation, the (simulated) helium production schedule can be chosen arbitrarily. In the irradiations described here we have chosen simple schedules to investigate the influence of helium on the microstructure at low

dose (5 dpa) and the persistence of any low-dose differences at higher dose (25 dpa).

All irradiations were performed at 625°C, which is near the peak swelling temperature for the 3×10^{-3} dpa • s^{-1} damage dose rate employed. The material irradiated was 316 SS from the MFE heat (15893). Irradiations were performed on samples with three different preirradiation thermomechanical treatments: solution annealed (0.5 h at 1050°C), solution annealed and aged (1 h at 1050°C, 10 h at 800°C) and 20% cold-worked. Four irradiations were performed, each on samples with all three thermomechanical histories:

(1) single-ion irradiation to 5 dpa,
(2) dual-ion irradiation to 5 dpa with 15 appm He/dpa,
(3) dual-ion irradiation to 25 dpa with 15 appm He/dpa,
(4) single-ion irradiation to 5 dpa followed by 20 dpa dual-ion irradiation with 18.8 appm He/dpa, giving the same final helium concentration as (3).

Comparison of (1) and (2) will give insight into helium effects at low dose. Comparison of (3) and (4) will show whether microstructural differences between (1) and (2) persist at higher dose.

Helium preinjection is commonly used in both reactor- and ion-irradiations to compensate for the lack of helium generation during the nucleation stage. In a companion experiment to the one described above, we have hot-preinjected (15 appm ^{3}He at 650°C) and cold-preinjected (15 appm ^{3}He at room temperature) MFE 316 SS samples, and single-ion irradiated them to 25 dpa at 625°C. Solution-annealed, solution-annealed and aged, and 20% cold-worked samples were included. Comparison of these samples with one-another and with (3) and (4) above will aid in elucidating the role of helium in the nucleation stage, and in judging the validity of helium preinjection as a simulation technique.

5.3 Irradiation of Unmodified and Ni-Modified Ferritic Alloys

Nickel concentrations in the ferritic alloys of interest for MFR applications are usually low. This makes in-reactor testing of helium effects problematical, because helium generation by the two-step nickel transmutation

reaction is significantly slower in these alloys than is expected in MFR service. For this reason current reactor irradiations in the ADIP program are being performed both on unmodified ($\lesssim$ 0.5 wt. % Ni) and Ni-modified (with ~ 1 to 2 wt. % additional Ni) ferritic alloys. The Ni additions are specifically aimed at increasing the helium generation rates (in HFIR) to levels expected in MFR service.

However isolation of helium effects from the results of Ni-modified alloy irradiations may be difficult because the additional nickel may alter the irradiation performance of the alloys via mechanisms other than helium generation. With the dual-ion irradiation technique, the (simulated) helium generation is independent of metallurgical variables, and isolation of the Ni and He effects should be possible; the irradiations described here are designed to isolate the two effects.

The ferritic alloys, in the form of 0.010 in sheet, were received from M. L. Grossbeck. They were heat treated at ANL to give tempered martensite structures, using schedules supplied by R. L. Klueh. Additional information about these alloys can be found in [I-31.

The alloys and irradiation conditions are listed in Table 1. In this first series of experiments we concentrated on temperature dependence, and spanned a broad range (350-600°C), at a single damage dose (25 dpa). For the HT-9, HT9 + 2Ni and 9Cr-1Mo + 2Ni alloys we performed both single- and dual-ion irradiations over the entire temperature range; comparison of the two irradiation conditions (single- versus dual-ion) should effectively isolate the helium effects in these alloys. For HT9 we can also isolate the influence of nickel additions (by comparing HT9 with HT9 + 2Ni) over the entire temperature range and under both single- and dual-ion irradiation. The 9Cr-1Mo alloy was dual-ion irradiated over the entire temperature range, but was single ion irradiated only at 440°C. Thus for the 9Cr-1Mo system we can assess the influence of nickel additions over the entire temperature range in dual-ion irradiated samples, and at a single temperature for single-ion irradiation.

TABLE 1

IRRADIATION CONDITIONS FOR FERRITIC ALLOYS

Material	Heat	Temperature: Dual-Ion Irradiation (25 dpa, 15 appm He/dpa)	Temperature: Single-Ion Irradiation (25 dpa)
HT9	XAA-3587	350,410,470,530, 600°C	350,410,440,470,530, 600°C
HT9+2Ni	XAA-3589	350,410,470,530,600°C	350,410,440,470,530 ,600°C
9Cr-1Mo	XAA-3590	350,410,470,530, 600°C	440°C
9Cr-1Mo+2Ni	XAA-3591	350,410,470,530,600°C	350,410,440,470,530 ,600°C
HT9+2Ni adjusted	XAA-3592		440°C
9Cr-1Mo+2Ni adjusted	XAA-3593		440°C

6.0 References

1. M. L. Grossbeck, V. K. Sikka, T. K. Roche and R. L. Klueh, ADIP Quarterly Progress Report for Period Ending Dec. 31, 1979, DOE/ER-0045/1, p. 100.

2. R. L. Klueh and J. M. Vitek, ADIP Quarterly Progress Report for Period Ending June 30, 1980, DOE/ER-0045/3, p. 294.

3. M. L. Grossbeck and J. W. Woods, ibid. p. 30

7.0 Future Work

TEM inspection of the 316 SS helium schedule samples is now under way; this work is being performed by A. Kohyama, a visiting scientist at ANL under the US-Japan Fusion Cooperation Program. Inspection of the ferritic samples will begin in the near future.

FURTHER EXAMINATION OF SWELLING OF "PURE" AISI 316 IRRADIATED IN ORR

H. R. Brager and F. A. Garner (Hanford Engineering Development Laboratory)

1.0 Objective

The objective of this effort is to examine the interactive roles of helium, cold-work and pre- and postirradiation aging on cavity development in a quarternary alloy, Fe-17Cr-16.7Ni-2.5Mo (alloy P-7).

2.0 Summary

Examination of additional specimens of Fe-17Cr-16.7Ni-2.5Mi corroborate the previously reported result that cold working of this "pure" 316 alloy has no influence on suppressing void formation. The new data show that the differences in density determined by microscopy are probably related to problems in imaging small voids in thick foils.

In addition, the apparent suppression of swelling in this alloy by pre-injection of 40 appm helium appears to be an illusion. Both density change and aging studies indicate that swelling exists in the preinjected specimens in the form of unresolvable voids.

3.0 Program

Title: Irradiation Effects Analysis (AKJ)
Principal Investigator: D. G. Doran
Affiliation: Hanford Engineering Development Laboratory

4.0 Relevant DAFS Program Plan Task/Subtask

Task II.C.l Effects of Materials Parameters on Microstructure
Task II.C.2 Effects of Helium on Microstructure
Task II.C.17 Microstructural Characterization

5.0 Accomplishments and Status

5.1 Introduction

In two earlier reports it was shown that cold working of the quaternary alloy P-7 did not substantially affect its swelling in ORR and that the effect of preinjected helium could be stronger than that of the helium generated by transmutation.[1,2] The P-7 alloy, frequently referred to as "pure" 316 stainless, has the composition Fe-17Cr-16.7Ni-2.5Mo. This alloy was irradiated at several temperatures in each of the following conditions: annealed, 20% cold-worked, annealed plus He implanted, 20% cold-worked plus He implanted, and various annealed and aged plus implanted conditions.[3] The implanted specimens contained a range of helium concentrations injected at ambient temperature. All the specimens chosen for examination were irradiated to 3 to 5 dpa. Additional data are now available on some of the specimens whose microstructures were reported in References 1 and 2.

5.2 The Effect of Cold-Work on Swelling of the P-7 Alloy

The swelling of this alloy at 550°C was previously reported to be very insensitive to cold-working. Whereas swelling in one area of the annealed specimen was 0.08%, it was 0.03% in one area of the 20% cold-worked specimen. However, density change measurements of these specimens indicated more swelling, 0.15% and 0.22%, respectively. It did appear, however, that cold working had increased the void density by roughly a factor of two. There was concern that the smaller voids in the cold-worked material would not be as easily resolvable, and therefore would lead to an underestimate of the void volume. It was also thought that the areas chosen may not have been representative since the swelling indicated by density change measurement was larger than that derived from microscopy measurements.

To address these concerns, microscopy was performed on a number of areas in each of the annealed and cold-worked specimens irradiated at 550°C. As shown in Table 1 the void development at this fluence appears to be somewhat variable. Micrographs of the examined material, however, illustrate a surprising consistency and homogeniety in any one void micrograph, Figure 1. In addition, the void densities are shown to decrease with increasing foil thickness, Figure 2, for both annealed and cold-worked specimens. The increase in the size of voids which are resolvable in thick foils appears to dominate over any nonuniformity in the void formation. Note that the range of swelling in each of the annealed and cold-worked specimens overlaps, supporting the conclusion that, while apparently nonuniform on a microscopic level, the macroscopic swelling is essentially unaffected by cold working. The result contrasts with the very large effect that cold-work has on swelling in austenitic steels such as AISI 316. The insensitivity of swelling to cold-work in the P-7 alloy has been explained as due to the absence of carbon and possibly other minor solute elements.[1,4]

TABLE 1

VOID FORMATION IN Fe-17Cr-16.7Ni-2.5Mo SPECIMENS
(550°C IRRADIATION TEMPERATURE; 3 TO 5 dpa)

Specimen Identification	(*)	Foil Thickness, Å	Void Density, cm^{-3}	Mean Diameter, Å	Swelling, %
Annealed	(a)	2000	0.7×10^{15}	114	0.08
	(b)	600	5.2×10^{15}	66	0.10
	(c)	350	3.1×10^{15}	109	0.31
20% Cold-Worked	(d)	2000	0.9×10^{15}	90	0.04
	(e)	1600	1.3×10^{15}	70	0.02
	(f)	590	3.3×10^{15}	79	0.10
	(g)	510	4.3×10^{15}	62	0.11
	(h)	440	2.5×10^{15}	59	0.03

(*) Letter identifies micrograph in Figure 1 corresponding to area used to obtain void data.

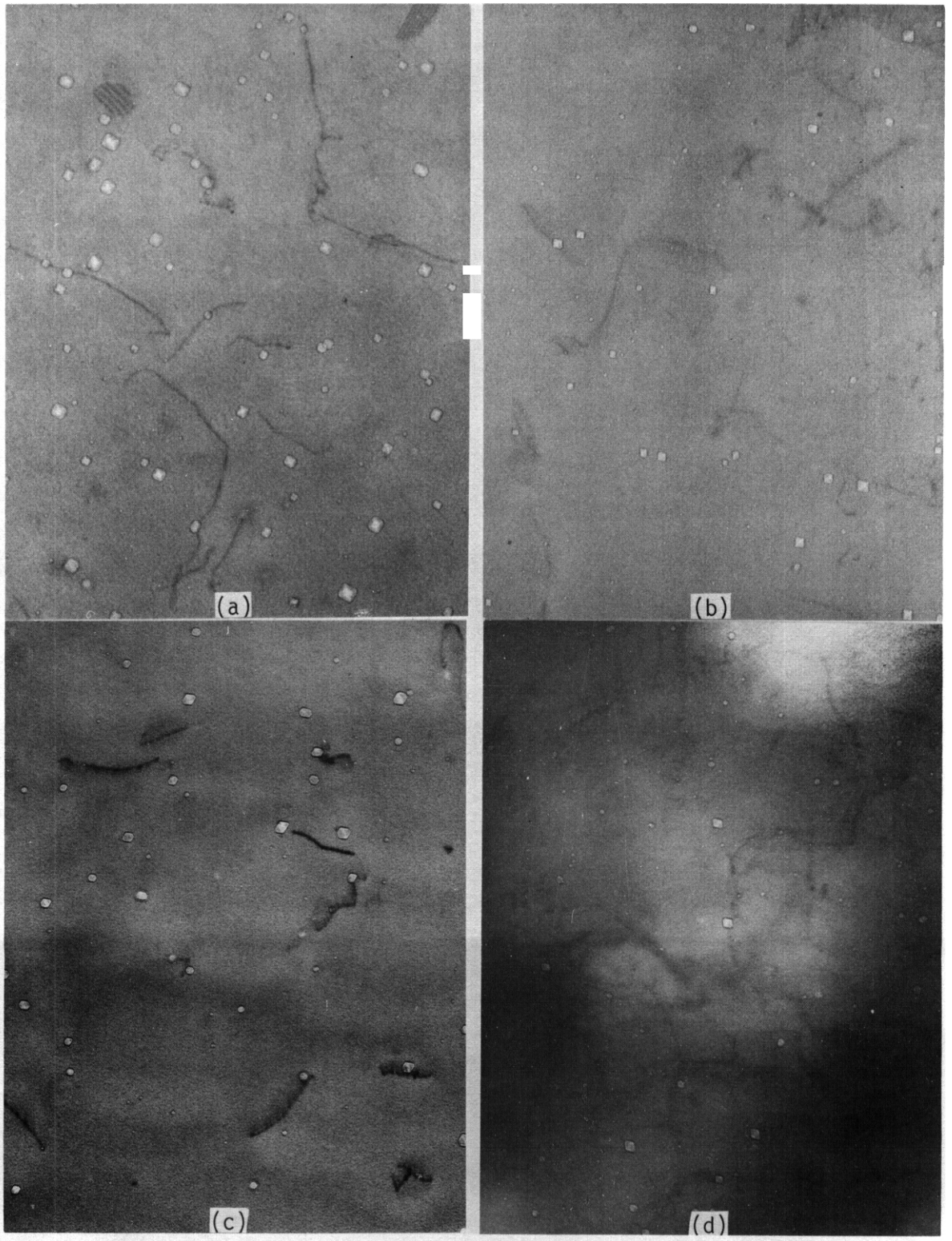

FIGURE 1. Void Microstructure in Annealed and 20% Cold-Worked Fe-17Cr-16.7Ni-2.5Mo Irradiated in ORR at 550°C to 3 to 5 dpa. (Micrographs Shown in the Same Order as Indicated in Table 1.)

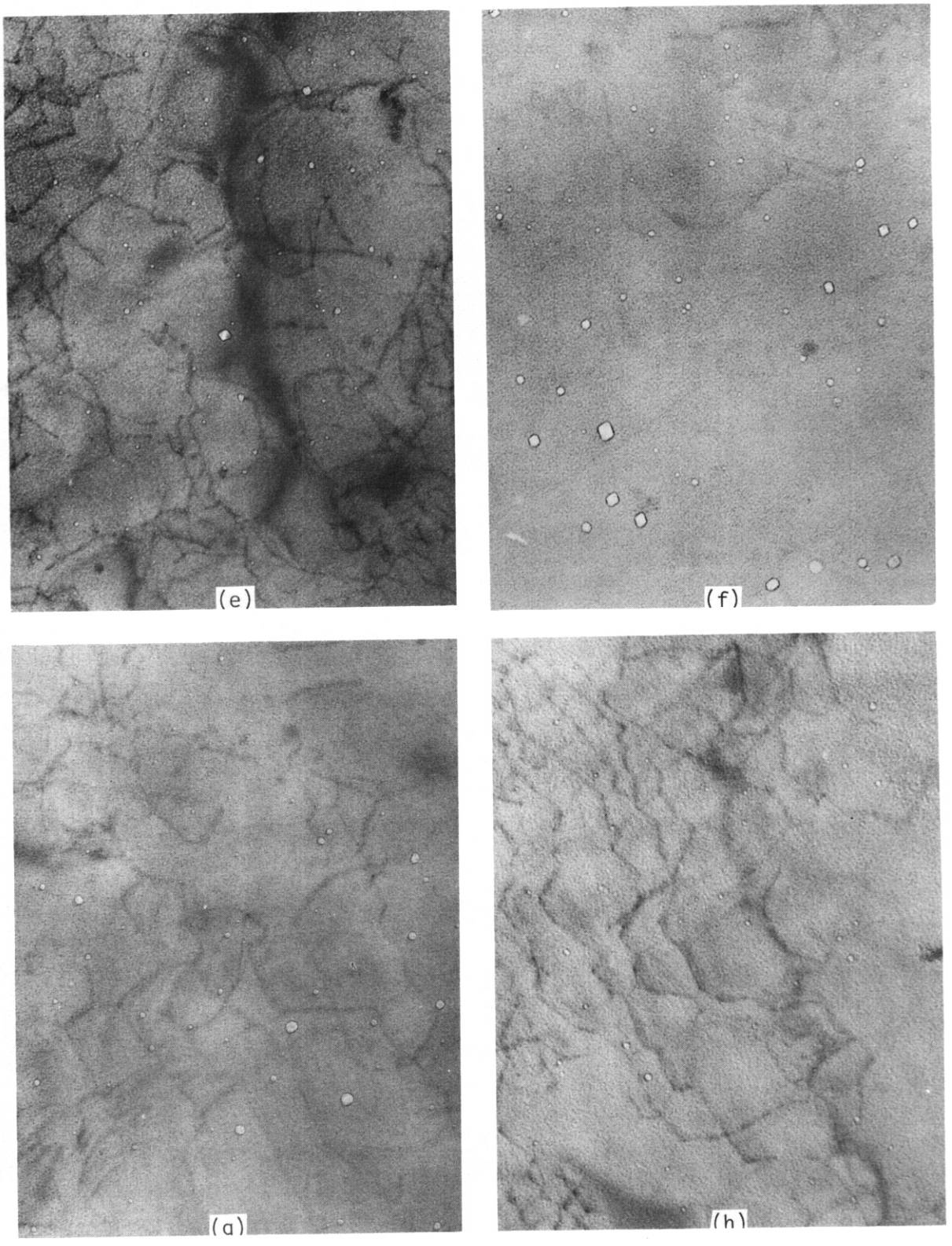

FIGURE 1. (Cont'd.)

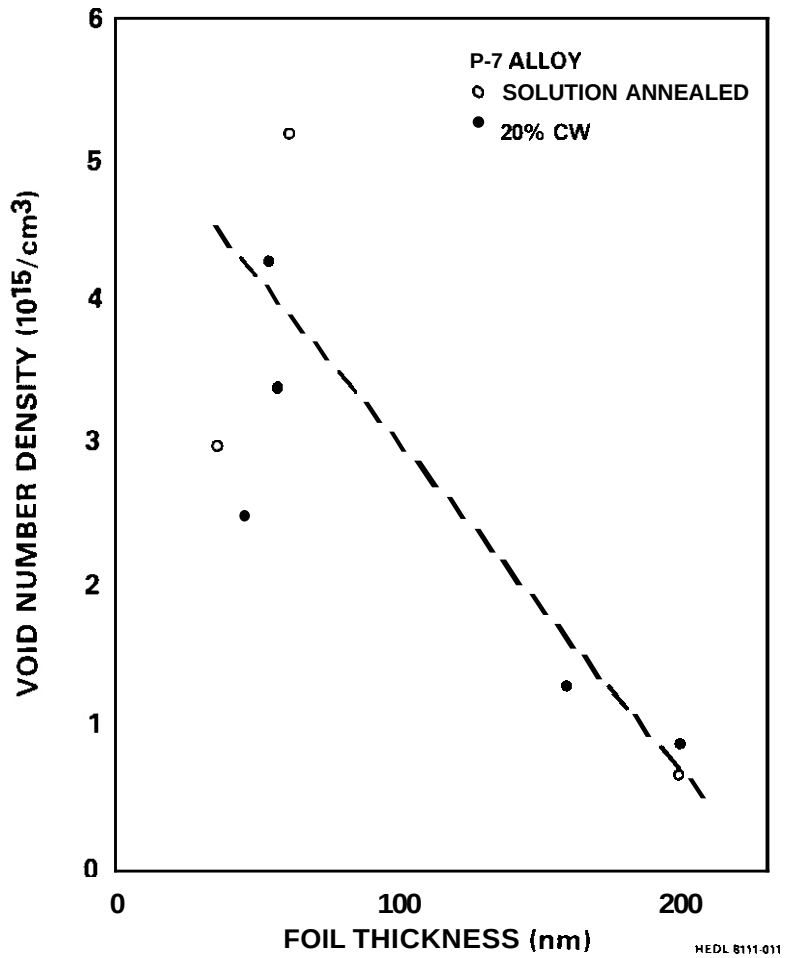

FIGURE 2. Effect of Foil Thickness on Number Density of Visible Voids.

5.3 Examination of Specimens with Preimplanted Helium

Two other specimens irradiated at 550°C exhibited no resolvable voids although density change measurements showed swelling comparable to that of the uninjected specimens discussed in the previous section. These specimens were (1) annealed plus ∿40 appm He and (2) annealed plus ∿40 appm He followed by aging at 750°C for one hour. It appeared that pre-injection either completely suppressed the swelling or distributed it in such small cavities that they were unresolvable (≤3 nm).

Further examination has not revealed any resolvable cavities. Therefore, one of four other identical specimens which had been implanted with ~35 appm He and aged 1 hour at 700°C was aged after irradiation at 900°C for ¼ hour under argon and examined by electron microscopy. Preliminary results indicate a high density (mid-10^{15} cm^{-3}) of cavities with sizes of about 5 nm; most likely these were produced by coarsening of small unresolvable cavities.

6.0 Conclusions

Examination of additional specimens of Fe-17Cr-16.7Ni-2.5Mo corroborate the previously reported result that cold-working of this "pure" 316 alloy has no influence on suppressing void formation. The new data show that the differences in density determined by microscopy are probably related to problems in imaging small voids in thick foils.

In addition, the apparent suppression of swelling in this alloy by pre-injection of 40 appm helium appears to be an illusion. Both density change and aging studies indicate that swelling exists in the preinjected specimens in the form of unresolvable voids.

7.0 References

1. H. R. Brager and F. A. Garner, "Influence of Cold-Work on Swelling of Pure AISI 316 Irradiated in ORR," DAFS Quarterly Report, DOE/ER-0046/6, p. 148.

2. H. R. Brager, F. A. Garner and R. L. Gaines, "The Influence of Pre-injected Helium on Void Nucleation in Fe-17Cr-16.7Ni-2.5Mo," ibid., p. 144.

3. H. R. Brager and F. A. Garner, "ORR Irradiation of the MFE-II Experiment," DAFS Quarterly Progress Report, DOE/ER-0046/5, p. 233.

4. F. A. Garner and W. G. Wolfer, "The Influence of Dislocation Density and Radiation on Carbon Activity and Phase Development in AISI 316," DAFS Quarterly Progress Report, DOE/ER-0046/4, p. 88.

8.0 Future Work

Additional microscopy will proceed on the three other specimens that will be aged after irradiation and are identical to the one reported here that was aged ¼ hour at 900°C. Activities to determine the size distribution of cavities by a non-microscopy technique (probably positron annihilation) will be pursued.

9.0 Publications

Some of the results of this study have been included with those of other studies in a paper entitled, "The Role of Cold-Work in the Temporary Suppression of Void Swelling," F. A. Garner, H. R. Brager and W. G. Wolfer. This paper was presented at the International Conference on Neutron Irradiation Effects, Argonne, Illinois, November 9-13, 1981.

THE EFFECT OF APPLIED STRESS ON PRECIPITATE STABILITY IN IRRADIATED AISI 316

K. C. Russell (Massachusetts Institute of Technology) and F. A. Garner (Hanford Engineering Development Laboratory)

1.0 Objective

The primary objective of this work is to understand the effect of an externally applied stress state on the formation and evolution of precipitate phases under fusion reactor first wall conditions. A second objective is to use this understanding to develop stress-affected dimensional change correlations.

2.0 Sunmary

The effect of applied stress on precipitation has been analyzed by two equivalent methods. Each component of an applied stress interacts only with the corresponding component of the transformation strain required to form the precipitate. Depending on the transformation strains, a particular state of applied stress may either stabilize, destabilize, or have no effect on a particular phase.

Shear stresses can alter precipitation as effectively as hydrostatic stresses. Applied stresses may increase or decrease the incubation rate of a particular phase by several orders of magnitude. An applied stress may change the solubility of a particular phase or crystallographic variant of a phase sufficiently to yield preferred coarsening. Interaction energies arising from changes in elastic constants induced by precipitate formation are usually much smaller than those arising from transformation strains.

It appears that the acceleration of swelling of AISI 316 by applied stress at high temperature is accomplished by the action of hydrostatic stress components on precipitation and not by the action of deviatoric components. This conclusion means that the current stress-affected swelling correlation need not be changed.

3.0 Program

Title: Irradiation Effects Anlaysis (AKJ)
Principal Investigator: D. G. Doran
Affiliation: Hanford Engineering Development Laboratory

4.0 Relevant DAFS Program Plan Task/Subtask

Task II.C.2.1 Effects of Material Parameters on Microstructure
Task II.C.2.5 Modeling

5.0 Accomplishments and Status

5.1 Introduction

Numerous experimental studies have shown that an applied stress may have a major influence on precipitation processes in solid state phase transformations.[1-2] The stress state may hinder, assist or have no effect on the fornation and evolution of a particular phase. The direction and magnitude of the effect of the stress is dependent on a number of factors including: state of stress, magnitude of stress(es), crystal structure and composition of the phase being formed, crystal structure and composition of matrix in which the phase is formed, nature of precipitate/matrix interface (coherent vs. incoherent), temperature and presence or absence of irradiation.

There exists a well-developed body of theory for describing the effects of stress on phase stability. The basic tenets of the theory for stress effects in a uniform system were laid down by Gibbs.[3] Subsequently, Eshelby[4] produced a theory for the strain energies of ellipsoidal particles embedded in matrices of much larger dimensions. The Eshelby treatment may be extended in at least an approximate manner to a wide range of precipitation problems in either irradiation or purely thermal environments.

Stress effects on phase stability are of major interest in fission and fusion

reactor environments. In both types of reactor, some components must operate under stress. In the fission environment, the stress state in fuel cladding may reasonably be approximated as that of a pressurized tube. The stress state in such a tube is essentially that of biaxial tension, with one principal stress equal to twice the other, and the third (through the tube thickness) close to zero. Pressurized tubes are also the major mode of in-reactor testing of potential fusion reactor materials. Unfortunately, the time-independent biaxial stress state in a pressurized tube is not a good approximation of the complex, pulsed stress states expected to exist in a fusion reactor first wall. Accordingly, it is important to be able to relate effects observed in breeder-irradiated pressurized tubes to those expected in the fusion reactor first wall; and furthermore to predict what new phase stability effects might occur in the fusion environment.

It was recently suggested [5-6] that the shear components of the stress state in a pressurized tube might be responsible for the high temperature (>550°C) acceleration of stress-enhanced swelling observed in AISI 316.[7] It was shown that the intermetallic phases formed in this alloy during irradiation were involved in the swelling process and were accelerated by stress. If this possibility is substantiated, this would require a change in the correlation developed in the breeder program which describes stress-affected swelling. This correlation currently assunes that only the hydrostatic components of stress are involved in precipitate formation. The correlation also recognizes the operation of other microstructural mechanisms which dominate the response below 550°C and which appear to respond only to the hydrostatic stress.[6-7]

In order to address the possibility of the influence of nonhydrostatic components, this paper first uses the formalism of Eshelby to determine the effect of a general state of stress on particle thermodynamics. These thermodynamic effects may be of first order, resulting from differences in nuclear volune or crystal structure of the matrix and precipitate phases, or second order, resulting from changes in the elastic moduli. Typical strain energies are then calculated for some special cases. The effect of these strain energies on nucleation and growth processes are then calculated. The results of the

calculations are then applied to various phases that develop in irradiated AISI 316 stainless steel.

5.2 Theory for Coherent Particles

Eshelby [4] has presented a general analysis of the strain energy associated with a coherent ellipsoidal particle of arbitrary misfit and which lies within a much larger volume of matrix phase. Both particle and matrix are treated as being isotropic continua having uniform but possibly different elastic constants.

Tractable solutions may be obtained under such conditions for many strain energy problems of interest. The calculation may be extended to anisotropic solids, but at considerable cost in computational complexity. Calculations for non-ellipsoidal particles are usually intractable. However, many particle shapes may be approximated reasonably well by ellipsoids, e.g., a cuboid by a sphere, or a lath by a highly elongated triaxial ellipsoid.

Eshelby's calculation of the thermodynamics of a phase transformation is based on the following series of imaginary operations:

(a) Cut out the region which is to transform and remove it from the matrix.

(b) Allow the transformation to take place, unconstrained by the matrix. These "stress-free'' transformation strains are designated ε^T_{ij}.

(c) Apply surface forces to restore the region to its original form, and place it back into the hole in the matrix, rejoining the material across the cut.

(d) Apply a layer of body forces at the precipitate/matrix interface so as to just balance the forces applied in (c).

At the completion of the above four steps, the matrix and particle are in a state of mechanical equilibriun.

The strain energy associated with the transformation may then be calculated from the forces involved in steps c and d. In the simple case of a dilational

transformation, which involves only linear strains of $\varepsilon_{11}^T = \varepsilon_{22}^T = \varepsilon_{33}^T$, the strain energy per unit volume of precipitate is given by

$$\Delta G_\varepsilon = \frac{2\mu(1+\nu)(\varepsilon_{11}^T)^2}{(1-\nu)} \tag{1}$$

where μ = shear modulus and ν = Poisson's ratio.

This strain energy is independent of the sign of ε_{11}^T and may be shown to be independent of the shape of the particle and unaffected by the presence of other particles of the same kind.

In the present context we are primarily interested in the energy of interaction between an applied stress and the transformation strains of the particle. This interaction energy (per unit volume of particle) is given by Eshelby as

$$\Delta G_{int} = -\sum_{ij} \sigma_{ij}^e \varepsilon_{ij}^T \quad , \tag{2}$$

where σ_{ij}^e are the components of the externally-applied field, and ε_{ij}^T are the components of the stress-free transformation strains calculated in step (b).

The summation gives a seris of products of stresses and strains of the same indices ($\varepsilon_{11}^e \varepsilon_{11}^T$ t $\sigma_{12}^e \varepsilon_{12}^T$ . . .) but does not involve dissimilar cross terms such as $\sigma_{11}^e \varepsilon_{12}^T$. Thus, each component of the applied stress interacts with the corresponding transformation strain canponent and no others.

In the case of the dilational transformation considered earlier where $\varepsilon_{11}^T = \varepsilon_{22}^T = \varepsilon_{33}^T$,

$$\Delta G_{int} = \sigma_{11}^e \varepsilon_{11}^T + \sigma_{22}^e \varepsilon_{22}^T + \sigma_{33}^e \varepsilon_{33}^T \tag{3}$$

Eshelby also developed expressions for the strain and interaction energies when the particle has a different elastic constant than does the matrix. Evaluation of these expressions involves extensive computations which must be performed on a case by case basis. However, simple and useful equations

have been derived for the composite elastic constant of a matrix with a small volume fraction of spherical particles of different elastic constants. The effective bulk and shear moduli (K_e, μ_e) are given in terms of those in the matrix (K,μ) and of the particle (K', u') by

$$K_e = D(1 - AV) \tag{4}$$

$$\mu_e = \mu(1 - BV) \tag{5}$$

where V = volume fraction of particle and

$$A = \frac{(K - K')(4\mu + 3K)}{K(4\mu + 3K')} \tag{6}$$

$$B = \frac{\mu' - \mu}{(\mu - \mu')\ \beta - \mu} \tag{7}$$

$$\beta = \frac{2\ (4 - 5v)}{15\ (1 - \nu)} \tag{8}$$

For isotropic solids v = 1/3 and

$$K = \frac{E}{3(1 - 2\nu)}\ , \tag{9}$$

$$\mu = \frac{E}{2(1 + \nu)}\ . \tag{10}$$

For a very soft particle (such as a void), $K' = \mu' = 0$, $A = 3$ and $B = 15/8$. For a very hard particle in a soft matrix $K' >> K$, $\mu' >> \mu$ and $A = -3/2$, $B = -15/7$. This leads to the very simple result that a dispersion of very soft particles will reduce the bulk and shear moduli of a composite material by about twice its volune fraction, whereas a dispersion of a very hard particle will stiffen the moduli by a comparable amount.

It must be emphasized that equations 4-10 apply only *to* isotropic solids and

will apply only in an approximate manner to real anisotropic alloys such as austenitic stainless steels.

5.3 Incoherent Particles

The Eshelby treatment assunes complete coherency between matrix and particle, which occurs in only a minority of cases. At the other extreme the particle and matrix structures and/or lattice spacings are so different that no shear stresses may be transmitted across the interface. Accordingly, any transformation shear strains within the particle must relax with time and the interior can only be stressed by hydrostatic components. Diffusion of vacancies to or from the particle will then eventually eliminate the hydrostatic stresses. However, relief of these stresses will give an external volume change of

$$\Delta^T = V\,(\varepsilon^T_{11} + \varepsilon^T_{22} + \varepsilon^T_{33}) \qquad (11)$$

where V = volume of the particle phase.

Most particles are semi-coherent, a state midway between the complete matching characteristic of full coherency and the very poor matching of incoherent particles. Part of the shear strains may be relaxed at such an interface, and not interact with the external shear stresses. Such situations would have to be considered on a case by case basis. Therefore, incoherent particles will not support shear stresses except for times shorter than those needed for internal rearrangement of matter. This implies a shear modulus of zero. Under such slow loading conditions, in calculations of μ_{eff} for a matrix with incoherent particles, μ' should be taken as zero. Incoherent particles can support normal stresses, so K' is that of the particle phase as measured in bulk specimens.

5.4 Application to Diffusional Transformations

Eshelby's treatment is strictly applicable only when a particular region of the matrix transforms, leaving the remainder unaffected except for elastic

strains. Martensite is an example of such a transformation. Transformations of interest in nuclear materials are almost, if not entirely, of the diffusional type, where formation of a precipitate particle will change the composition, and therefore both the lattice spacing and elastic constants of the matrix. A simple analysis based on the LeChatelier principle will now be developed to deal with such situations.

Suppose that in a unit volume of matrix phase a volune V of precipitate phase is formed. The formation of the phase leads to some external strains ε_{ij} in the unit cube of material. The difference between the free energy of precipitate formation in a matrix subject to a set of external stresses $[\sigma^e_{ij}]$ and in the absence of such stresses is the work done by the applied stresses against the external strains

$$\Delta G_{int} = -\frac{1}{V} \sum_{ij} \sigma^e_{ij} \varepsilon_{ij} \tag{12}$$

per unit volume of precipitate.

Equation (12) is very similar to equation (2) from Eshelby. Strains which tend to relieve the external stresses give a negative interaction energy, whereas strains which oppose the applied stress give the opposite result. The factor $\frac{1}{V}$ appears in equation (12) and not in equation (2) since ΔG_{int} is defined per unit volume of precipitate. In fact the external strains (ε_{ij}) will be $\frac{1}{V}$ times the transformation strains. For example

$$V\ (\ \varepsilon^T_{11} + \varepsilon^T_{22} + \varepsilon^T_{33}\ ) = \varepsilon_{11} + \varepsilon_{22} + \varepsilon_{33}\ . \tag{13}$$

Equation (12) is convenient to use because it requires knowledge of only applied stresses and the external strains, which in many cases will consist only of a uniform expansion. In the latter case

$$\Delta G_{int} = \frac{P\Delta}{V}\ , \tag{14}$$

where $P = \frac{1}{3}(\sigma^e_{11} + \sigma^e_{22} + \sigma^e_{33})$ and $\Delta = (\varepsilon_{11} + \varepsilon_{22} + \varepsilon_{33})$.

In the case of transformations with a shear component, in the absence of an applied stress and in a cubic matrix, the particles would tend to distribute themselves at random about various habit planes and lead to no external shear strains. All equivalent habit planes are equally favorable, however, in the absence of an applied stress. An applied shear stress would cause the particles to favor a particular habit plane and thereby give an external shear, say ε_{12}. Then

$$\Delta G_{int} = -\frac{2\,\sigma^e_{12}\,\varepsilon_{12}}{V} \tag{15}$$

5.5 Changes in Elastic Constants

Altered elastic constants may give a ΔG_{int} even in the absence of any external shape or volume change ($\varepsilon_{ij} = 0$). The changed elastic constant may occur only in the precipitate (as with martensite) or in both the matrix and precipitate, as will tend to happen with diffusional transformations. It was shown earlier that formation of x% of a precipitate phase with elastic constants very different from those of the matrix phase would change the overall elastic constants by the order of x%. In addition, the elastic constants of phases may be approximately proportional to the concentrations of certain solutes.[8] Thus, if x% of a certain solute drained from the matrix to form x% of a precipitate phase, the elastic constants of the matrix may be changed by about x%. Thus, formation of a precipitate particle may change the overall elastic constant by two different mechanisms. The two changes may be of approximately equal magnitude, and may tend to either cancel or reinforce one another.

We now consider the interaction energy due to this second order elastic constant effect for two cases where all $\varepsilon^T_{ij} = 0$. In the first case, the external stresses are first assmed to be purely hydrostatic. Then, the strain energy of a unit volune of solid before forming the particle is given by $P^2/2K$ and that after by $P^2/2K_e$, where K and K_e are bulk moduli of the solid before and after precipitation. The difference in strain energy per volume of precipitate is given by

$$\Delta G_{int} = \frac{P^2}{2}\left(\frac{1}{K_e} - \frac{1}{K}\right) \cong \frac{P^2}{2K^2}\left(K - K_e\right) \tag{16}$$

In the case where the external stress is a single pair of shears, say σ_{12} and σ_{21},

$$\Delta G_{int} = \frac{\sigma_{12}^2}{\mu^2}\left(\mu - \mu_e\right) \tag{17}$$

5.6 Application of the Theory to Phase Transformations

We may now consider the probable magnitudes of the various interaction energies defined above and their effect on nucleation and growth processes of phase transformations.

For comparison with strain energies, the free energy changes associated with nucleation of intragranular precipitates (ΔG_{chem}) are on the order of -10^9 J/m^3. The surface energy/volume ratio of a 100 Å diameter particle is the order of 10^8 J/m^3, and of a 1μm particle is 10^6 J/m^3.

Let us for comparison take elastic constants similar to those of austenitic stainless steels.

$$E = 2 \times 10^{11} \text{ MPa } (30 \times 10^6 \text{ psi})$$

$$K = 1.5 \times 10^{11} \text{ MPa } (15 \times 10^6 \text{ psi})$$

$$M = 8 \times 10^{10} \text{ MPa } (12 \times 10^6 \text{ psi})$$

To estimate the maximun plausible ΔG_{int} we assume $\varepsilon_{11} = \varepsilon_{22} = \varepsilon_{33} = .03$ and $\sigma_{11} = \sigma_{22} = \sigma_{33} = 200$ MPa (30,000 psi). Then, $\Delta G_{int} = 6 \times 10^7$ J. The values chosen are an upper limit in that at elevated temperatures 200 MPa is fairly high stress for application of austenitic steels. Furthennore, full coherency is hard tomaintainabove a few percent mismatch in lattice constants. Values

of $\Delta G_{int} \lesssim 10^7$ J/mole are more likely. Assuning a 3% shear strain and 200 MPa shear stress would also give a similar value of ΔG_{int}. In either case, ΔG_{int} is substantially less than that of the chemical free energy change ΔG_{chem}, but important nucleation and growth effects are possible, as will be seen presently.

Let us now consider the effect of a change in elastic moluli. We take equation (16), assume that as a reasonable upper limit that $(K - K_e)/K \cong V$, as discussed earlier, and P = 200 MPa. Then $\Delta G_{int} = 3 \times 10^5$ J/M^3. A similar ΔG_{int} would arise from similar shear stresses and similar changes in μ.

Thus, ΔG_{int} for modulus changes is some four orders of magnitude smaller than ΔG_{chem}, and is likely to be important only when very subtle free energy differences are crucial. However, very few transformations occur entirely without strain and the first order ΔG_{int} from even a very small strain would usually be greater than that from the maximum modulus effect. The dominance of first order effects is of considerable computational assistance in that moduli of precipitate phases are often only very approximately known and the variations of moduli with composition are very seldom known.

The rate equation for steady state precipitate nucleation is

$$J = A \exp(-\Delta G^*/kt) \tag{18}$$

where J = nucleation rate in particles/m^3-sec,
A = pre-exponential factor,
ΔG^* = activation energy for nucleation,

and
$$\Delta G^* = \frac{16\pi\gamma^3 f(\Theta)}{3(\Delta G_{chem} + \Delta G_{\varepsilon} + \Delta G_{int})^2} \tag{19}$$

kt = Boltzmann factor,
γ = particle/matrix interfacial energy,
$f(\Theta)$ = catalytic factor, to account for effects of heterogeneities, and

ΔG_ε = strain energy associated with nucleus formation in the absence of external stress.

To study the effect of ΔG_{int} on the nucleation rate, we take the derivative of J.

$$\frac{\partial \ln J}{\partial G_{int}} = \left(\frac{\Delta G^*}{kt}\right)\left(\frac{2}{\Delta G_{chem} + \Delta G_\varepsilon + \Delta G_{int}}\right) \tag{20}$$

In general ΔG_{chem} is considerably greater in magnitude than either ΔG_ε or ΔG_{int}, and as shown earlier is typically the order of -10^9 J/m^3. Nucleation typically occurs when $\Delta G^*/kt \lesssim 60$. Using these values and a ΔG_{int} of $\pm 10^7$ J/m^3 we find

$$\Delta \ln J = \pm 1$$

Thus, the energies available by interaction of transformation strains with an external stress may easily double or halve the nucleation rate. This change may be effected equally well by normal or shear stresses, depending on the transformation strain. The ΔG_{chem} associated with nucleation at heterogeneities may be as much as an order of magnitude smaller than that for intragranular precipitation. In this case, ΔG_{int} could give several orders of magnitude change in the nucleation rate. Such an effect is of obvious importance.

An externally applied stress will in general also affect the solubility of a precipitate particle. If responding to the applied stress decreases the size of the particle, more solute will be forced into the matrix and the solubility will increase. If responding to the applied stress gives an increase in particle size, solute will tend to be absorbed from the matrix and the solubility will decrease.

At equilibrium, the solute solubility and ΔG_{int} will be related by

$$\Delta G_{int} - \frac{RT}{\Omega} \text{ en } C'/C_e \tag{21}$$

where C_e and C' are solubilities of the solute in unstressed and stressed systems, respectively, and Ω is the molar volume.

Taking $\pm 10^7$ J/m^3 as typical of ΔG_{int}, we find that an external pressure will change the solubility of the order of 1%. Such a change in solubility is comparable to the increase due to the surface energy of a 1000 Å diameter particle. Coarsening of a system of particles of various sizes is driven by the differences between the solubilities of particles of various sizes. Stress gives similar differences in solubilities and as such could have a substantial effect on coarsening kinetics. Specifically, in a system of particles with several orientational variants, the variant alinged most favorably with respect to the applied stresses would tend to survive; those unfavorably aligned would tend to dissolve.[7]

5.7 Application to Phase Development in Austenitic Stainless Steel

Table 1 lists the various phases which appear in type 316 stainless steel, in both the unirradiated and irradiated conditions, and summarizes some crystallographic and microstructural data.[9] The matrix γ phase and the precipitate γ' phase have the same crystal structure and nearly the same lattice parameter. Accordingly the two phases should and, in fact, do maintain full coherency in a cube-on-cube orientation. At the other extreme the ZrO phase as a much larger lattice parameter than does γ, and the two phases would be expected to be largely incoherent. The globular morphology and absence of an observed orientation relationship between ZrO and the matrix suggest a very low level of coherency. The carbides and the G, n, σ, χ and Laves phases all lie between the two extremes with regard to coherency.

The effects of stress on the stability of the various phases in AISI 316 are best calculated from observed external volume and shape changes. A calculation based on matrix and precipitate lattice constants arid on transformation strains would be very uncertain, due to uncertainties in the degree of coherency and in partial molar volumes.

Table 1

SUMMARY OF CRYSTALLOGRAPHIC DATA OF PRECIPITATE PHASES IN 316 STAINLESS STEELS (9)

PHASES	CRYSTAL STRUCTURE	LATTICE PARAMETER (nm)	SOLUTE ATOMS PER UNIT CELL	TYPICAL MORPHOLOGY	ORIENTATION TO γ-MATRIX
γ	Cubic, A1, Fm3M	a_o = 0.36	4	Matrix	—
γ'	Cubic, $L1_2$, Fm3m	a_o = 0.35	4	Small Sphere	Cube-on-Cube
G	Cubic, A1, Fm3m	a_o = 1.12	116	Small Rod	Random
Fe_2P*	Hex., C_{22}, P_{321}	a_o = 0.604 c_o = 0.36	6	Thin Lath	$(1\bar{2}\bar{1}0)ppt//(011)_\gamma$ $(0001)ppt//(001)_\gamma$
η	Cubic, $E9_3$, Fd3m	a_o = 1.08	96	Rhombohedral	Cube-on-Cube or Twin
Laves	Hex., C14, $P6_3/mmc$	a_o = 0.47 c_o = 0.77	12	Faulted Lath	Many Variants
$M_{23}C_6$	Cubic, $D8_4$, Fm3m	a_o = 1.06	92	Rhombohedra1 Platelet	Cube-on-Cube or Twin
MC*	Cubic, B1, Fm3m	a_o = 0.433	4	Small Sphere	Cube-on-Cube
σ	Tet., $D8_b$, P4/mnm	a_o = 0.88 c_o = 0.46	30	Various	Many Variants
X	Cubic, A12, $I\bar{4}3m$	a_o = 0.89	58	Various	Many Variants
TiN*	Cubic, 61, Fm3m	a_o = 0.425	4	Large Cuboid	
$Zr_4C_2S_2$*	Hex., $P6_3/mmc$	a_o = 0.34 c_o = 1.21		Globular	
ZrO*	Cubic, B1, Fm3m	a_o = 0.46	4	Globular	

* These phases are not major phases in AISI 316 but are found occasionally.

AISI 316 stainless steel has been observed to shrink slightly during precipitation of the various carbide phases.[10] Accordingly an applied stress state with a compressive hydrostatic component should enhance carbide formation and a tensile hydrostatic component should retard formation.

The cubic carbides $M_{23}C_6$ and MC would form without shear strain, and hence should not be affected by an applied shear stress, independent of the degree of particle/matrix coherency. The large difference in lattice constants of MC and y suggest that MC might be sensitive to hydrostatic stresses. Since MC-forming elements such as titaniun are quite insoluble, however, it is doubtful that stress would affect the kinetics of MC precipitation appreciably.

Very little external volume change is observed during the formation of γ' in AISI 316. This implies that ΔG_{int} is small and hydrostatic stresses would exert very little effect on its nucleation. Shear stresses would also have no effect since both y and γ' are cubic.

"Voidless-swelling" or dilation has been observed during the formation of intermetallic phases such as σ, χ and Laves.[5] Accordingly, a stress state with a tensile hydrostatic component would favor their formation. Assuning that 0.5% external volume expansion occurs for 5% of Laves volume, then $\Delta^T \simeq 10\%$ or $\varepsilon_{11}^T \simeq 3\%$. For a 200 MPa tensile stress in a pressurized tube this yields a $\Delta G_{int} \simeq -4 \times 10^{-7}$ J/m^3, which can lead to substantial increases in nucleation rate of Laves precipitates. If nucleation in absence of stress is difficult (as indicated by the long times required for its formation) the 200 MPa could easily reduce the time required for formation of the Laves phase by a factor of two or more. On the other hand, compressive stresses would retard the nucleation of Laves phase. However, it is not expected that either tensile or compressive stresses would change the total amount of phase eventually formed.

All of the phases discussed above possess cubic crystal structures with the exception of σ and Laves. Therefore the cubic phases should not be affected

by the application of a purely deviatoric (shear) state of stress. Since the Laves phase is hexagonal and the σ is tetragonal, the possibility exists that their formation may be influenced by shear strains. The σ phase is known to be incoherent. The effect of shear stresses on the formation of Laves is harder to determine. If the phase is coherent or exhibits well-defined crystal habit planes it will respond to shear components. Laves is known not only to have a crystal structure sufficiently different from the matrix to probably preclude coherency, but it also forms with no regular orientation relationship with the matrix. It also forms with a globular morphology. Both of these latter points indicate that Laves is most likely incoherent with the matrix. Laves fornation therefore would not be affected by shear stresses.

5.8 Application of Results to Stress-Affected Swelling Correlation

The acceleration of swelling of AISI 316 with stress appears to be composed of two separate mechanisms.[5] The response below 550°C is independent of temperature while the phases that form in this temperature regime are not. These phases are cubic however (such as γ' and G-phase), and it does not appear that they would be sensitive to stress. Above 550°C the phases that form are primarily Laves, σ and χ. It is known that the fornation of these phases lead to a volume expansion of the lattice (as much as 3%) but they appear to be incoherent with the matrix. It is therefore expected that these phases will nucleate earlier with applied tensile stress but will ignore the shear components of stress inherent in the walls of pressurized tubes. Since these phases concentrate nickel and silicon it is expected that their earlier formation with stress will lead to a shorter incubation period for void swelling.[6] The present stress-affected swelling correlation involves only the hydrostatic stress to change the incubation period. Therefore, no change is required in this correlation.

5.9 Conclusions

The effect of applied stress on particle stability has been calculated by two methods with equivalent results. It has been shown that stress alters precipitate

stability primarily due to shape and volume changes rather than due to changes in elastic moduli. Shear stresses were shown to be as effective in altering particle stability as are normal hydrostatic stresses, providing shear stresses can be maintained at the precipitate/matrix interface. For some precipitates applied stresses can increase or decrease nucleation rates by as much as several orders of magnitude. Stress can also affect precipitate solubility enough to give preferred coarsening of particles with a favorable orientation with respect to the applied stresses.

Application of these principles to the phases formed in irradiated AISI 316 leads to the conclusion that stress-affected swelling due *to* enhanced precipitation rates will occur above 550°C but will not be influenced by the presence of shear components of stress.

6.0 References

1. T. Tanaka, A. Sato and T. Mori, Acta Met., 26, 579 (1978).
2. G. Saulhoff, Acta Met., 29, 637 (1981).
3. J. W. Gibbs, The Scientific Papers of J. W. Gibbs, Volume I, Longmans, Green and Company, New York, 1906.
4. J. D. Eshelby, Proc. Royal Soc., A241, 376 (1957).
5. F. A Garner, "Extrapolation of Stress-Affected Swelling Models Into Compressive and Cyclic Stress States," DAFS Quarterly Progress Report, DOE/ER-0046/5, p. 198.
6. F. A. Garner. "The Microchemical Evolution of Irradiated Stainless Steels," HEDL-SA-2159; Proc. of AIME Symposium on Irradiation Phase Stability, October 5-9, 1980, Pittsburgh, PA (in press).
7. F. A. Garner, E. R. Gilbert and O. L. Porter, "Stress-Enhanced Swelling of Metals During Irradiation," Effects of Radiation on Materials, ASTM STP 725, p. 680.
8. J. F. Bates, J. Nucl. Mat., 89, 201 (1980).
9. E. H. Lee, P. J. Maziasz and A. F. Rowcliffe, see Reference 6 (in press).

10. F. A. Garner, W. V. Cummings, J. F. Bates and E. R. Gilbert, Densification-Induced Strains in 20% Cold-Worked 316 Stainless Steel During Neutron Irradiation, HEDL-TME-78-9, Hanford Engineering Development Laboratory, June 1978.

7.0 Future Work

The results of this effort and that of Reference 5 will be used to produce a recommended stress-affected correlation for the Fusion Materials Handbook.

8.0 Publications

None.

MEASUREMENT AND CALCULATION OF SOLID TRANSMUTANTS FORMED IN AISI 316

F.A.Garner, F.M.Mann and H.R.Brager (Hanford Engineering Development Laboratory)

1.0 Objective

The purpose of this effort is to identify potentially significant transmutation products and to quantify their generation rates in various facilities used to provide data for fission-fusion correlations.

2.0 Summary

A reassessment of the amount of two transmutation products produced in HFIR irradiations of AISI 316 has shown that the inclusion of all competing reactions leads to changes in the predicted concentrations. The vanadium level is reduced somewhat but not enough to dismiss it as a potential determinant of alloy behavior. The copper level is increased substantially but not enough to influence the swelling of AISI 316.

Measurements of the vanadium concentration in AISI 316 irradiated in the HFIR reactor have been performed by two methods and confirm the presence of this element. The manganese level has also been shown by ion microprobe analysis to be decreasing due to exposure in HFIR.

3.0 Program

Title: Irradiation Effects Analysis (AKJ)
Principal Investigator: D.G.Doran
Affiliation: Hanford Engineering Development Laboratory

4.0 Relevant DAFS Program Plan Task/Subtask

Subtask II.C.4 Effects of Solid Transmutants on Microstructure
Subtask II.C.10 Effects of Solid Transmutation Products on Fracture Behavior

5.0 Accomplishments and Status

5.1 Introduction

In two earlier reports it was shown that differences in identity and amount of solid transmutants generated in various reactor systems could have a significant effect on the development of fission-fusion correlations.[1-2] A search has therefore been initiated to identify those areas wherein the effects of solid transmutants might be important.

It was recognized that in some cases the influence of transmutants might be very subtle, arising primarily from trace amounts of elements formed by transmutation. A possible example may be the void shrinkage observed in molybdenum by Evans.[3] Void growth proceeded in molybdenum and the molybdenum alloy designated TZM during irradiation in the Dounreay Fast Reactor but was later followed by void shrinkage. Evans calculated that a dose of 17 dpa produced 400 appm of long-lived ^{99}Tc and that this concentration was sufficient to segregate to and cover the void surfaces with between half and one monolayer of technetium. Since molybdenum is also a component of 316 stainless steel the possibility arises that perhaps the low level of technetium produced may play a subtle role in some facet of the irradiation response of 316 SS.

Other changes in behavior may arise from the larger (and measurable) levels of transmutants produced in some materials in thermal or fusion reactors; both types of reactors produce more transmutants than do fast reactors. Examples are the large changes in manganese and vanadium produced in AISI 316 by HFIR and expected to be produced in fusion reactors.[1]

This report presents interim results of a continuing study on various transmutant elements that may be important in the development of fission-fusion correlations.

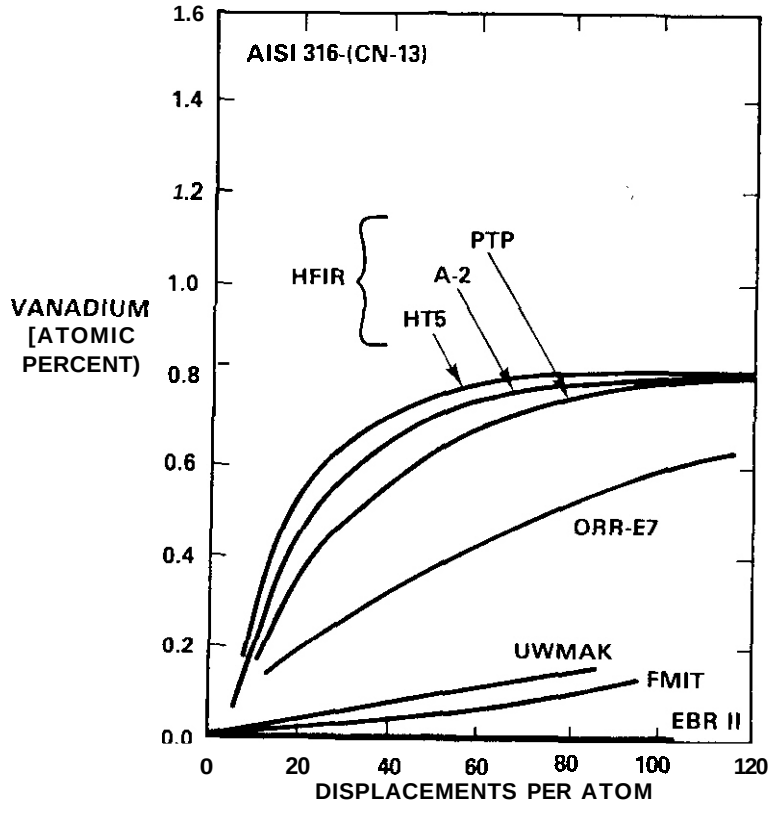

FIGURE 1. Predicted Vanadium Concentration in AISI 316 as a Function of Exposure for Various Reactors. (1) Vanadium burn-out reactions are not included. HT-5, A2 and PTP refer to different positions in HFIR.

5.2 Vanadium

In an earlier report it was noted that the ^{50}Cr in AISI 316 would be quickly transmuted in the HFIR reactor to ^{51}V via decay from ^{51}Cr. As shown in Figure 1, the calculation predicted a maximum level of 0.8% of vanadium. However, this calculation did not include any burn-out of vanadium, but the effect was estimated to be small.[1,4] The reaction $^{51}V(N,\gamma)^{52}V \rightarrow {}^{52}Cr$ ($t_{\frac{1}{2}}$ = 3.8 m) leads to a loss of vanadium to a stable chromium isotope. The REAC library has now been modified to include vanadium cross sections.[4] Figure 2 shows that the vanadiun concentration peaks at about 0.5% at 60 dpa in the PTP core centerline position of HFIR rather than rising to a level of 0.8%. The actual saturation level may change somewhat as a function of posi-

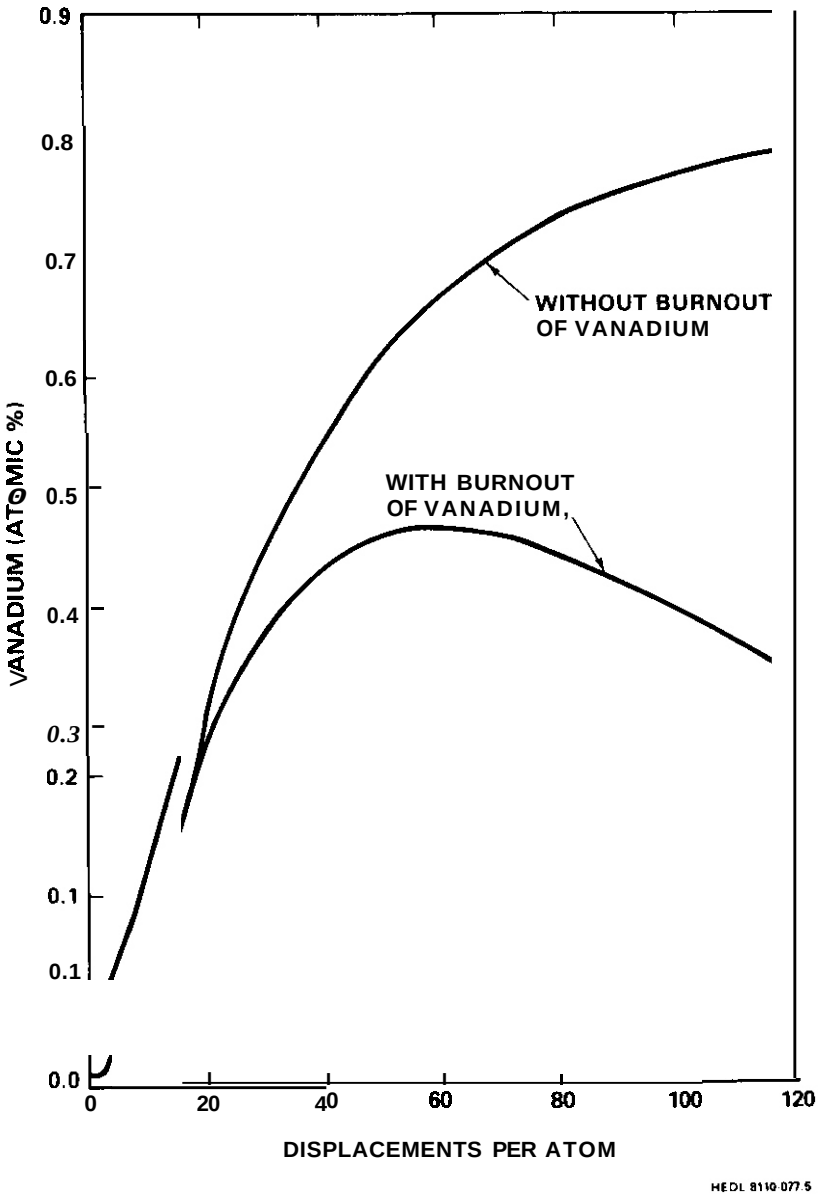

FIGURE 2. Comparison of Predictions of Vanadium Concentration Produced in AISI 316 During Irradiation in the PTP Position of HFIR with and Without Burnout of Vanadium.

tion in the core. (Note dependence on HFIR core position in Figure 1.) While the revised peak leve of vanadiun is lower than originally estimated,, it is still a rather large amount and is comparable to or larger than the levels of other strong Mc-carbide-forming elements (Ti,NB) added to modify the properties of various austenitic steels.

Figure 1 shows that vanadium builds up slowly in fission neutron spectra. Vanadium burnout in fusion spectra was also considered and found to be insignificant. The (n,2n) reaction of ^{51}V leads to long-lived ^{50}V and the (n,p) reaction leads to ^{51}Cr which quickly decays back to ^{51}V.

Since the actual level of vanadium formed is a function of reactor position and neutron spectrum it was decided to measure the concentration of vanadim in a HFIR-irradiated AISI 316 specimen by two methods, energy-dispersive x-ray analysis and ion microprobe. The specimen had been irradiated to 42 dpa in HFIR and its microstructure is described in another report.(5) Based on Figure 2 and assuming a core center position during the irradiation, one would expect 0.4% vanadium. The actual core position during the irradiation has not yet been identified by these authors.

The x-ray analysis technique showed the local vanadium concentrations to be very heterogeneous, with area-averaged values ranging from 0.2 to 0.4%, but with precipitate concentrations reaching several percent.(5) The ion microprobe measurements indicated much higher area-averaged levels (21%) and it is suspected that the sputtering process used in this technique may be selectively eroding the vanadium-rich precipitates compared to the matrix, leading to an overestimate of the vanadium concentration.

5.3 Manganese

Figure 3 shows the predicted levels of manganese in AISI 316 during irradiation in various reactors. The specimen described above would be expected to decline from its original value of 1.90 to 1.14% manganese at 42 dpa, based

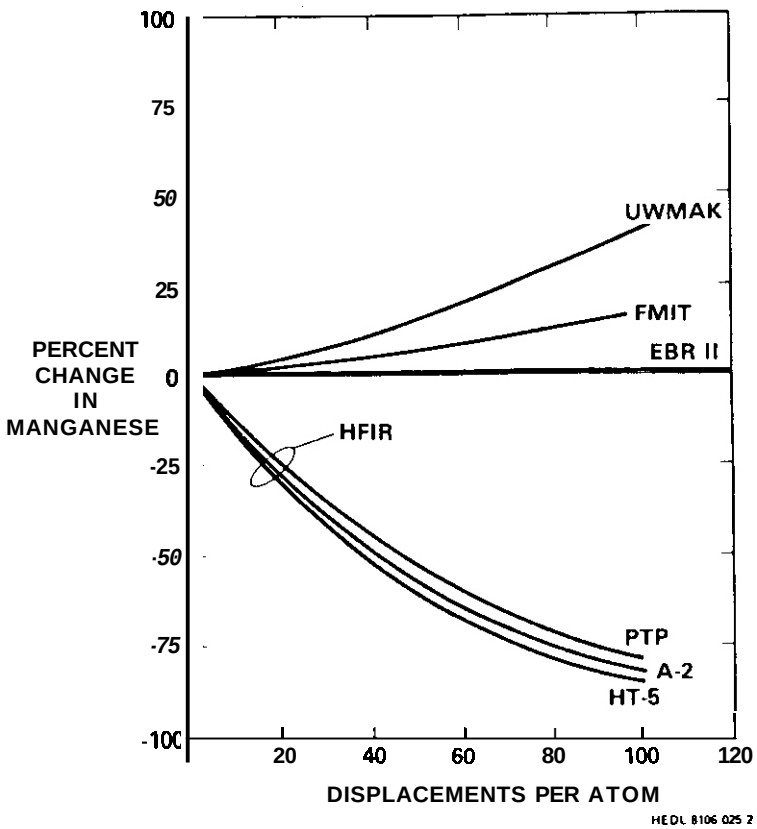

FIGURE 3. Predicted Changes in Manganese Concentration in AISI 316 in Various Reactors.[1]

on the assumption of a core-centerline irradiation in the PTP region of the HFIR core. The value measured by ion microprobe analysis was 1.3%. The manganese level cannot be reliably measured in highly radioactive iron bearing specimens by the x-ray analysis technique.[5]

5.4 Copper

In an earlier paper it was shown that during HFIR irradiation to 60 dpa the initially low concentration of copper in AISI 316 would be increased six-fold.[1] The additional copper was formed by the $^{64}Ni(n,\gamma)^{65}Ni \rightarrow {}^{65}Cu$ ($t_{1/2}$ = 2.6 hr) reaction. Since ^{64}Ni exists naturally at only 1.08% atomic abundance in unirradiated nickel it was thought that there would be no consequences of

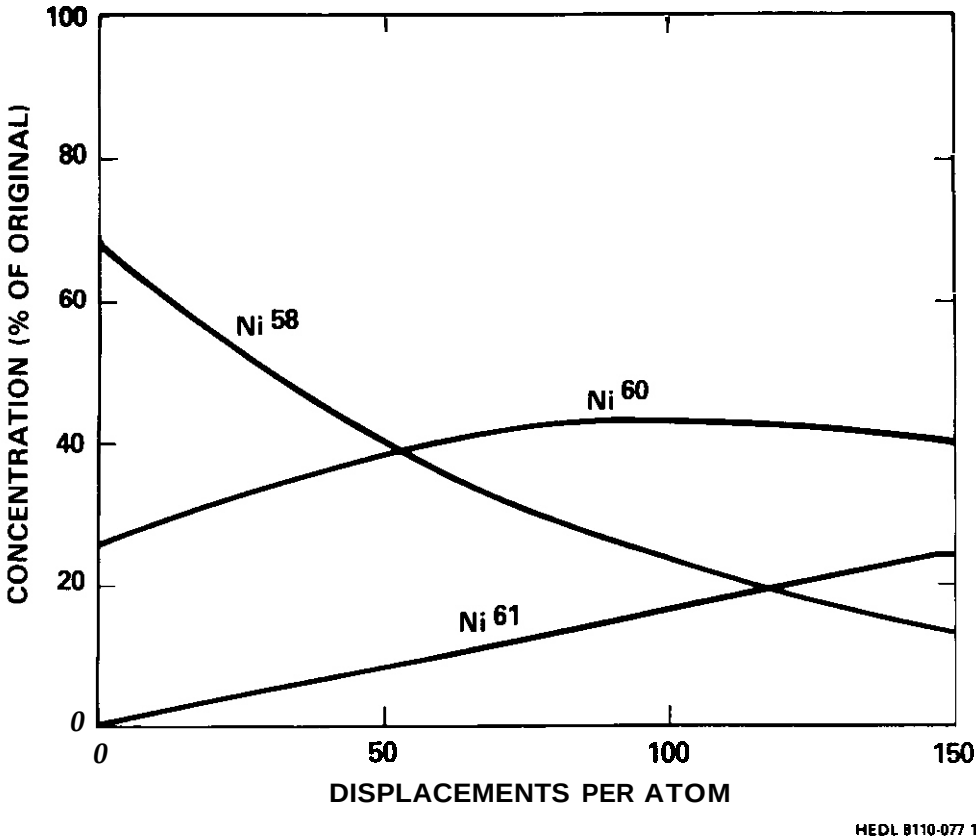

FIGURE 4. Predicted Time Histories of ^{58}Ni, ^{60}Ni, and ^{61}Ni in Rure Nickel Irradiated in the PTP Position of HFIR.

the limited copper increase. A reassessment of the nickel transmutation sequence has shown that considerably more copper is produced than originally estimated. In effect the ^{64}Ni concentration increases throughout the radiation by way of transmutation from lower isotopes of nickel.

Figures 4-6 show the time history of the various isotopes of nickel.

The most abundant Ni isotope (^{58}Ni) is steadily reduced as it transforms to ^{59}Ni. While some of ^{59}Ni quickly transmutes to ^{56}Fe and helium atoms, the majority of it is converted very quickly to stable ^{60}Ni (normally 26% abundance), which in turn is slowly converted to ^{62}Ni, normally at 3.6%

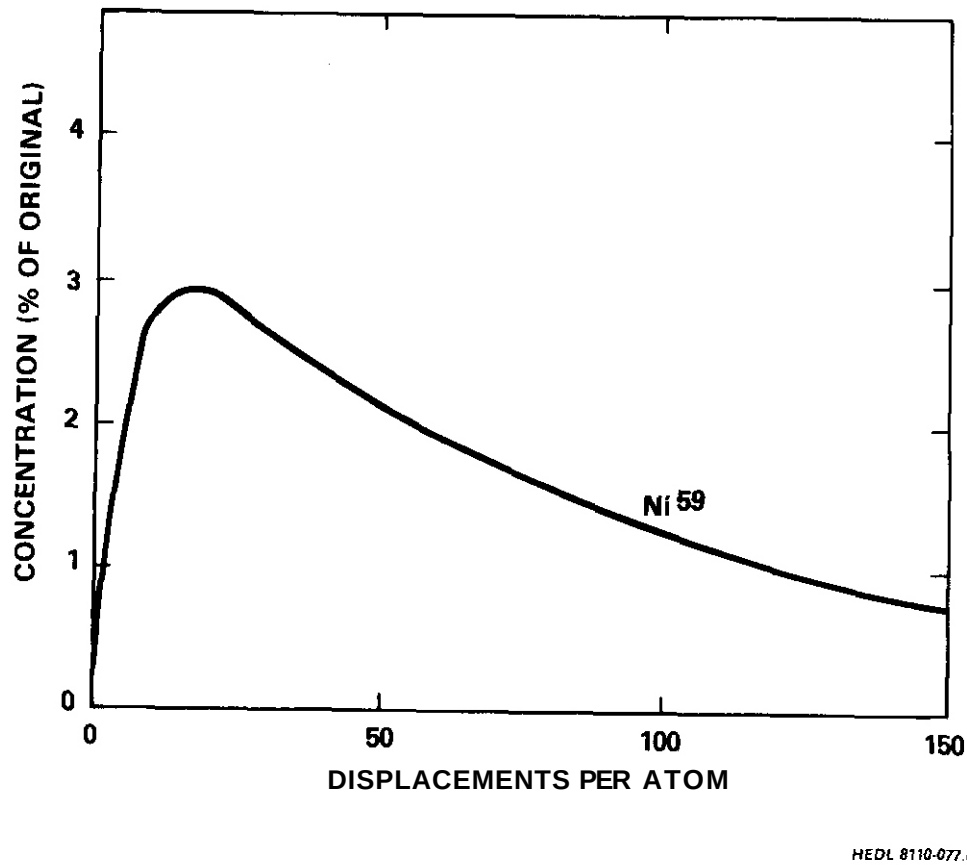

FIGURE 5. Predicted Time History of ^{59}Ni in Pure Nickel Irradiated in the PTP Position of HFIR.

abundance. This isotope has a very large thermal cross section however and is quickly converted to ^{63}Ni, which also has a very large thermal cross section. Therefore ^{64}Ni is constantly being generated, leading to a continously increasing rate of copper formation. In effect the nickel transmutation chain operates with three low-resistance shunts at ^{59}Ni, ^{61}Ni, and ^{63}Ni. (The calculation of isotopic composition for these isotopes is complicated by the fact that one-group cross sections can be generated by the REAC code only for isotopes in its library. For isotopes not in its library (particularly non-naturally occurring isotopes) the one-group cross sections were estimated from the 2200 meter cross section by multiplying with the average ratio of the one-group to 2200 meter cross sections of ^{58}Ni, ^{62}Ni, and ^{64}Ni.

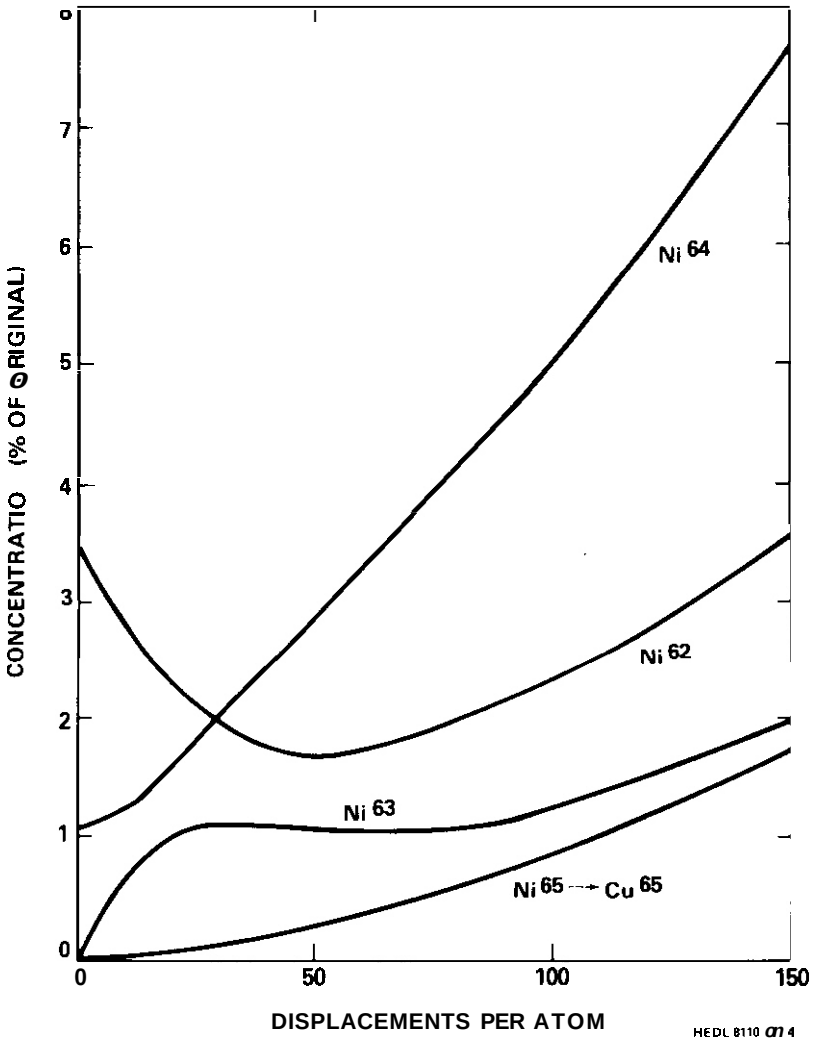

FIGURE 6. Predicted Time Histories of ^{62}Ni, ^{63}Ni, ^{64}Ni, and ^{65}Cu in Pure Nickel Irradiated in the PTP Position of HFIR. Due to the short half life of ^{65}Ni its concentration at any moment is too low to show.

In AISI 316 at 60 dpa the total copper formed in the core centerline PTP position of HFIR is calculated to be 0.03 atomic percent, at 100 dpa the level would be 0.12%. Figure 7 shows that copper-modified AISI 316 alloys irradiated in EBR-II have not shown a sensitivity of void swelling to copper concentration at such low levels.[6] It appears that the slight sensitivity of density change to copper content is not due to an effect on void volume

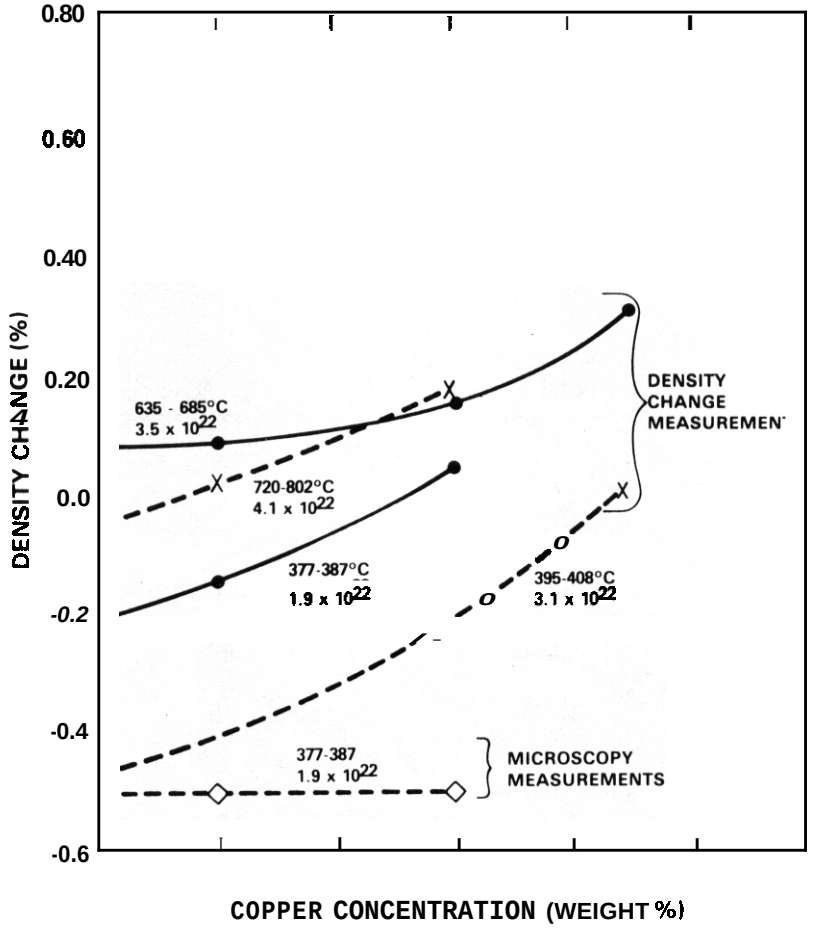

FIGURE 7. Dependence on Copper Content and Temperature of Density Change of Annealed AISI 316 Irradiated in EBR-II.(6)

but rather is due to an effect on alloy matrix density. As shown in Figures 7 and 8 the measured void volume and its distribution is completely unaffected by copper content, at least at ∿380°C.

5.5 Conclusion

The vanadium generated in AISI 316 during HFIR irradiation will not reach the previously calculated level of 0.8% but will peak at ∿0.5% at 60 dpa and decline slowly thereafter. The vanadium buildup occurs quickly, reaching

VOID FORMATION
COPPER VARIATION

TYPE 316 STAINLESS STEEL

0.01% Cu

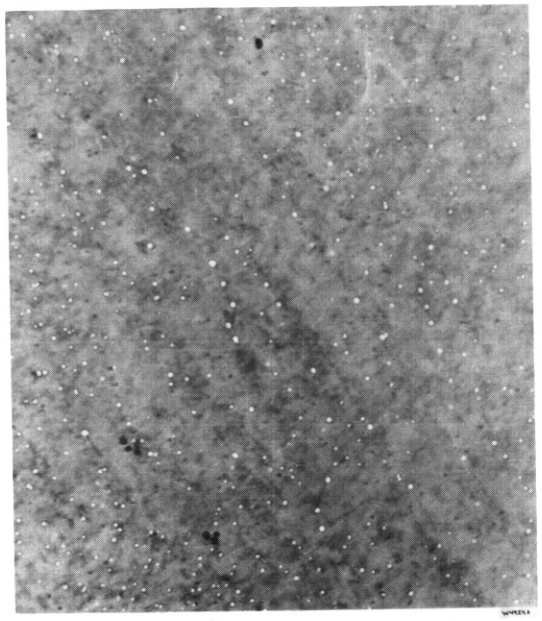

$\Phi = 1.8 \times 10^{22}$

T~730°F

$\frac{\Delta V}{V} \sim 0.5\%$

0.11% Cu

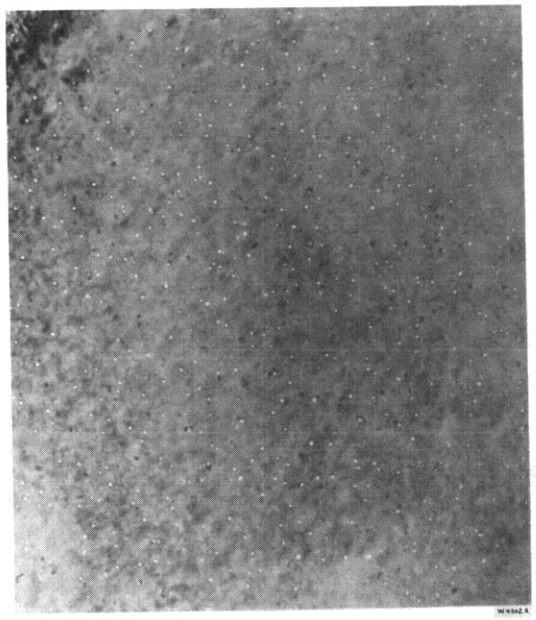

$\Phi = 1.8 \times 10^{22}$

T~760°F

$\frac{\Delta V}{V} \sim 0.5\%$

2.94% Cu

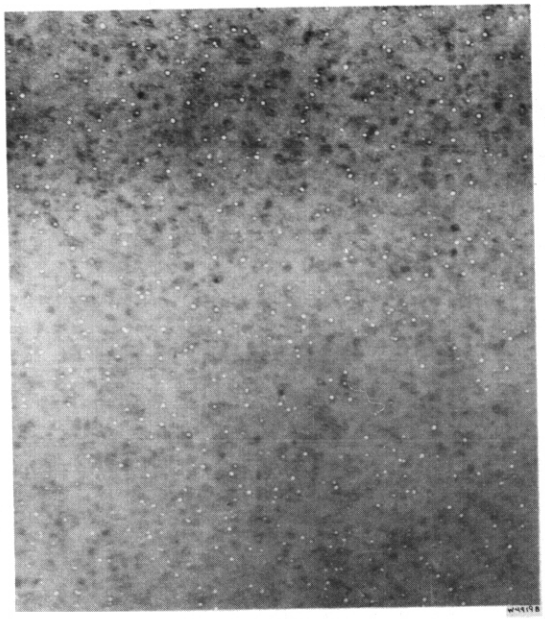

$\Phi = 1.8 \times 10^{22}$

T~730°F

$\frac{\Delta V}{V} \sim 0.6\%$

FIGURE 8. Void Formation in Copper-Modified AISI 316 Alloys in the Annealed Condition

levels (0.3% at 20 dpa) which will be significant in the microstructural evolution of the steel. The magnitude of these calculations appear to be consistent with measured values of vanadium in HFIR-irradiated AISI 316 steel. The measured value of manganese is also consistent with the predicted value. The buildup of copper is larger than anticipated but should not affect microstructural evolution significantly.

6.0 References

1. J. F. Bates. F. A. Garner., and F. M. Mann. "The Effects of Solid Transmutation Products on Swelling in 316 Stainless Steel," DAFS Quarterly Progress Report, DOE/ER-0046/6, April-June 1981, p. 190.

2. F. A. Garner and F. M. Mann, "The Inclusion of Transmutant Effects in Development of Fission-Fusion Correlations," DAFS Quarterly Progress Report, DOE/ER-0046/6, April-June 1981, p. 205.

3. J. H. Evans, J. Nucl. Mat., 88, (1980) p. 31-41.

4. F. M. Mann, "Solid and Gas Transmutation Production Code Development," this report.

5. H. R. Brager and F. A. Garner, "The Radiation-Induced Evolution of AISI 316 (DO-heat) in HFIR and EBR-II," this report.

6. J. F. Bates, in Properties of Reactor Structural Alloys After Neutron or Particle Irradiation, ASTM STP 570, (1975), p. 369-386.

7.0 Future Work

This effort will continue as more data become available.

8.0 Publications

Reference 1 was recently presented at the Second Topical Meeting on Fusion Reactor Materials, Seattle, WA, August 9-12, 1981, and will be included in the proceedings of the conference.

A MODEL FOR THE EVOLUTION OF NETWORK DISLOCATION DENSITY IN IRRADIATED METALS

W. G. Wolfer (University of Wisconsin) and F. A. Garner (Hanford Engineering Development Laboratory)

1.0 Objective

The object of this effort is to provide models of radiation-induced microstructure that can be used in the development of fission-fusion correlations.

2.0 Sunmary

A model has been developed to explain the relative insensitivity of network dislocation density in irradiated metals at high fluence to starting microstructure, temperature, stress and displacement rate. The model also explains how the rate of approach to saturation can be sensitive to flux and temperature while the saturation level itself is not dependent on temperature.

3.0 Program

Title: Irradiation Effects Analysis (AKJ)
Principal Investigator: D. G. Doran
Affiliation: Hanford Engineering Development Laboratory

4.0 Relevant DAFS Program Plan Task/Subtask

Task II.C.l Effects of Materials Parameters on Microstructure
Task II.C.6 Effects of Rate and Cascades on Microstructure

5.0 Accomplishments and Status

5.1 Introduction

It has been shown that the saturation network dislocation density that evolves

at high fluence in irradiated stainless steel is remarkably insensitive to temperature, displacement rate, stress, helium content or starting microstructure.[1] The major features of this evolution can be described as being the result of the competitive action of two primary mechanisms in a material where there are no additional losses of dislocation line length to surfaces or substantial losses to grain boundaries. These two primary mechanisms are generation of line length by loop growth and interaction with other components of the network, and recovery processes involving annihilation of line length.

5.2 Description of Recovery Processes

Both thermally-activated and radiation-induced climb of edge dislocations leads to encounters of dislocations, some of which result in annihilation of line length and recovery. The rate of annihilation of the network dislocation density ρ is commonly assumed to be proportrional to ρ^2 in recovery models for thermal creep. The ρ^2 dependence is based on the simple argument that the chance encounter of two edge dislocations with opposite Burgers vectors on the same glide plane is proportional to ρ^2. This assunption is only appropriate when the motion of edge dislocations by climb and glide is completely random.

On the other hand, in the absence of large creep deformations, the motions of adjacent edge dislocations are actually correlated during radiation-induced recovery. Consider, for example, the simple model of an edge dislocation structure shown in Figure la. Numerous edge dislocations can be paired up into dislocation dipoles, i.e., closest pairs of parallel edge dislocations with opposite Burgers vectors on parallel glide planes. As a result of radiation-induced climb, a pair may either increase or decrease the distance $h(t)$ between the parallel glide planes. When $h(t)$ increases, the members of the pair become partners in other dipole configurations until eventually they pair up in such a way that the corresponding values of the glide plane separation $h(t)$ decrease with time. As a result, the members of approaching pairs eventually interact primarily with each other, and the orientation of the dipole remains at an angle

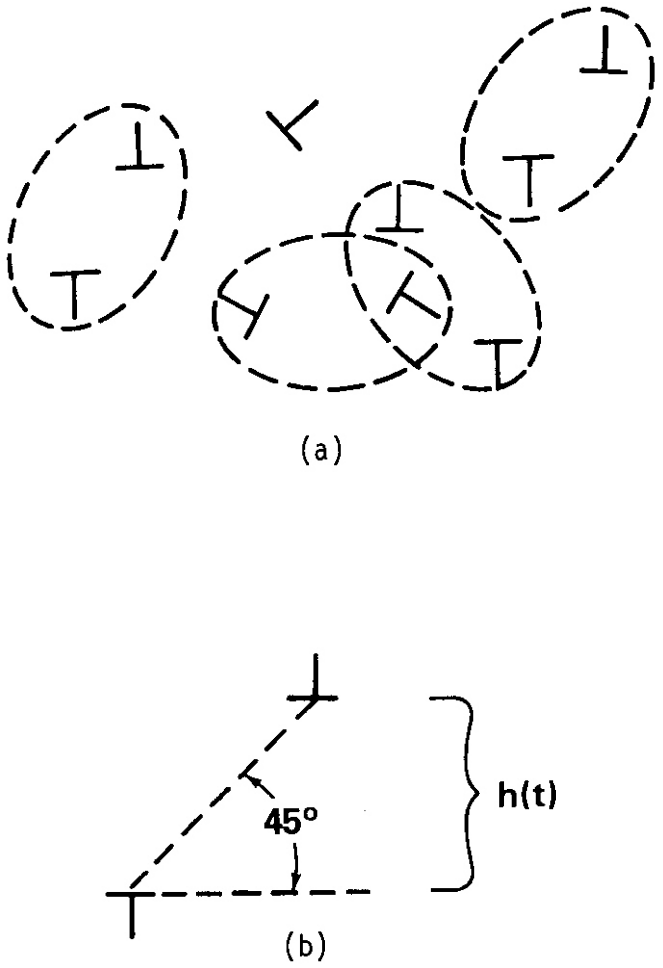

FIGURE 1. Schematic Representation of Correlated Movement of Dislocation Pairs (Dipoles).

of 45° to the glide plane as h(t) decreases further. Subsequent motion by climb and glide is then completely correlated.

This argunent can be made more general by stating that the configuration of continuously climbing dislocations is determined by their mutual interaction, and that the network will always adjust by glide to minimize the total elastic interaction energy of the network. Again, glide and climb motions are correlated.

In order to arrive at the rate of annihilation of network dislocations consider

the dislocation array shown in Figure lb. The number of adjacent dislocations able to form dipoles is obviously $\rho/2$. On the average the time required for the two dislocations to climb to a common glide plane is equal to

$$\tau = h_0/2V \quad ,$$

where h_0 is the initial dipole separation distance and V the dislocation climb velocity. Consequently, the rate of annihilation is $\rho/2\tau$ or $\rho V/h_0$. On the average, we may assume that $\pi h_0^2 = 1/\rho$, so that the annihilation rate is equal to $\sqrt{\pi}\, V\, \rho^{3/2}$.

5.3 Description of Generation Processes

The generation of network dislocations by the formation, growth, coalescence, and unfaulting of Frank loops is a complicated process. However, several facts can be utilized to simplify matters for this derivation.

First, detailed computer solutions by many authors,[2-6] have shown that formation of an interstitial loop occurs very quickly, requiring only a few seconds of irradiation. Furthermore, both coalescence and unfaulting of loops are relatively fast processes in comparison to that of loop growth. As a result, the generation of network dislocations occurs at a rate dictated by the lifetime τ_e of an interstitial loop, defined as the period from its formation to its coalescence with other components of the network. If R(t) is the radius of a loop, its growth rate can be calculated by differentiating the expression describing the growth rate of loop area and is given by

$$dR/dt = b^2[Z_i^1 D_i C_i - Z_v^1 D_v C_v + Z_v^1 D_v C_v^1] \quad , \qquad (1)$$

where b is the Burgers vector, Z_i^1 and Z_v^1 the loop bias factors, D_i and D_v the diffusion coefficients, and C_i and C_v the concentrations for interstitials and vacancies, respectively. C_v^1 is the vacancy concentration in thermodynamic equilibriun with the loop.

If equation (1) is written in the abbreviated fashion

$$\frac{dR}{dt} = b^2 \Phi \ , \tag{2}$$

then Φ is a function which depends on displacement rate, stress, temperature, and the total sink density according to conventional rate theory. After the first generation of loops has been formed, it is no longer dependent on the individual loop radii. Hence equation (2) can be integrated to obtain the loop lifetime as

$$\tau_l = \overline{R_{max}} \ / \ b^2 \Phi \ , \tag{3}$$

where $\overline{R_{max}}$ is the average maximum loop radius in a quasi-stationary population.

Brager, Garner and Guthrie have [7-8] shown that $\overline{R_{max}}$ is proportional to $\rho^{-\frac{1}{2}}$ in well-developed microstructures at high fluence. Therefore the generation rate of dislocations is proportional to $1/\tau_l$ or $b^2\Phi\rho^{\#}$.

5.4 The Evolution of Network Dislocation Density

Assuming no other losses the rate of change of dislocation density is

$$\frac{d\rho}{dt} = B\rho^{\frac{1}{2}} - A\,\rho^{3/2} \ , \tag{4}$$

where

$$B \sim b^2\Phi$$

and

$$A \sim V = b^2[Z_i^d D_i C_i - Z_v^d D_v C_v + Z_v^d D_v C_v^d] + V_{th} \tag{5}$$

Apart from the different bias factors for edge dislocations, Z_i^d and Z_v^d, and the different thermal vacancy concentration C_v^d in equilibrium with the edge dislocation, the radiation-induced contribution to the climb velocity V is very similar to the average loop growth rate $b^2\Phi$.

In fact, the loop bias factors as well as C_v^1 differ from the corresponding values for edge dislocations only for small loop radii (less than 50 Å).[9] Therefore, B is essentially proportional to the loop growth rate in equation (2).

The second term in this equation, V_{th}, represents the thermally-induced climb rate which determines the rate of recovery in the absence of radiation. Since thermal recovery is significant only at room temperatures above 650°C for typical fast reactor irradiation[1] it can be neglected at lower irradiation temperatures.

At higher displacement rates the temperature at which V_{th} becomes important increases as the microstructural densities undergo an upward shift in temperature.

Therefore, there is some relatively high temperature (dependent on displacement rate) below which the ratio B/A becomes a constant independent of the various sink densities. The strong temperature dependence of both A and B cancels, yielding a temperature-independent value of B/A. The saturation dislocation density, defined by $d\rho/dt = 0$ is

$$\rho_S = B/A \ . \tag{6}$$

This means that below the temperature where V_{th} is important the saturation density is not only independent of temperature and the details of the temperature-dependent microstructure but also independent of the starting microstructure. Since stress also makes no substantial changes in terms of equations (1) and (5), this means that the saturation density should also be essentially independent of stress. It has been shown however that the application of stress to irradiated metals speeds up the early evolution toward the saturation state.[7-9]

The solution to equation (4) is given by

$$\rho(t)/\rho_S = \frac{1 - e^{-x} + \sqrt{\rho_c/\rho_s}\,(1 + e^{-x})}{1 + e^{-x} + \sqrt{\rho_o/\rho_s}\,(1 - e^{-x})} \ , \tag{7}$$

where ρ_o is the initial dislocation density and

$$x = A\sqrt{\rho_s}\, t$$
$$= \sqrt{\pi\rho_s}\, Vt \qquad (8)$$

Since A and V are dependent on temperature, the approach to the saturation level ρ_s is also dependent on temperature.

Using a saturation dislocation density of $6 \times 10^{10} cm^{-2}$,[1,8] an initial dislocation density of $4 \times 10^{8}\ cm^{-2}$ for annealed 316 and $7 \times 10^{11}\ cm^{-2}$ for 20% CW 316, the fluence-dependent dislocation densities according to equation (7) are as shown in Figure 2. The relationship between fluence and the variable x was chosen such that the dislocation density for annealed 316 reaches the value of $2 \times 10^{10}\ cm^{-2}$ at $2 \times 10^{22}\ n/cm^2$, as reported for AISI 316 irradiated in EBR-II at 500°C.[9] This fluence value corresponds to x = 1.2, so that

$$x = \frac{10^{-22}}{0.6}\,\phi t \qquad (9)$$

where the fluence is given in units of n/cm^2 (E >0.1 MeV).

The dislocation climb velocity V was also computed according to rate theory for a displacement rate of 1.0×10^{-6} dpa/s. The results are shown in Figure 3. At low temperature, recombination of point defects results in a reduced climb velocity. Since the dislocation bias decreases slightly with temperature, the climb velocity also decreases at high temperatures.

It is seen from Figure 3 that the climb velocity is proportional to the bias difference between dislocations in different configurations. Dislocation climb occurs even in the absence of voids as a result of these bias differences. Assuming that 1% difference in bias is a typical value, it is possible to compute independently according to equation (8) the relationship between the fluence and the variable x. At 500°C, the climb velocity is computed to be

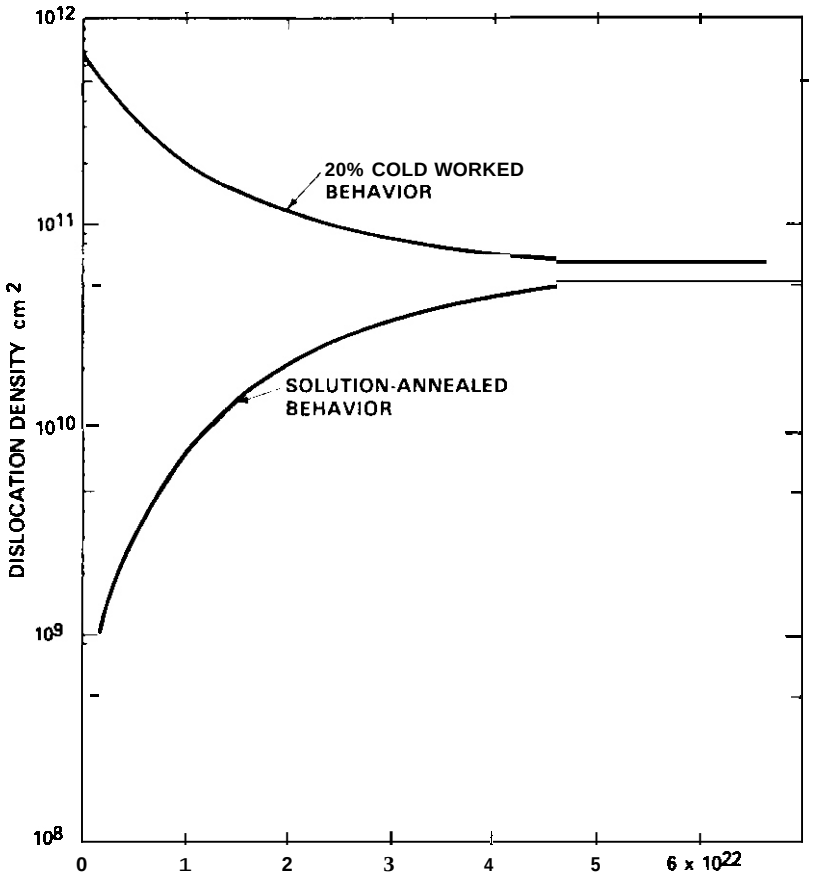

FIGURE 2. Predictions of the Evolution of Dislocation Density in AISI 316 at 500°C for Starting Densities of 7 x 10^{11} cm/cm^3 and 4 x 10^8 cm/cm^3, Chosen to Represent Cold-Worked and Annealed Conditions.

V = 100 Å/dpa, or for a displacement rate of 1.0 x 10^{-6} dpa/s, V = 10^{-12} cm/s. Hence

$$x = \sqrt{\pi\rho_s}\ Vt = \sqrt{\pi\rho_s}\ \frac{V}{\phi}\ \phi t$$
$$= 1.737 \times 10^{-22}\ \phi t \qquad (10)$$

assuning a neutron flux of 2.5 x 10^{15} n/cm^{2}s. The numerical factors in equations (9) and (10) are equal within 10%.

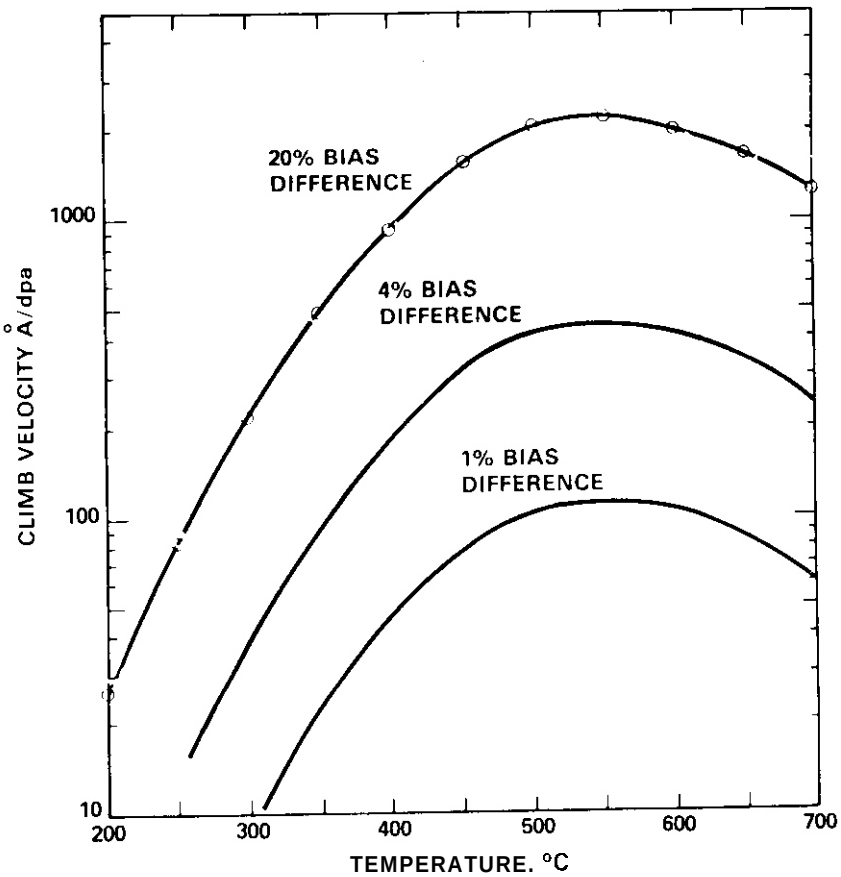

FIGURE 3. Calculation of Dislocation Climb Velocity V at 500°C for Several Values of Bias Difference Between Dislocations in Different Configurations. The displacement rate was assmed to be 10^{-6} dpa/sec.

5.4 Conclusions

It appears that it is possible to explain how the rate of approach to the saturation density of network dislocations is dependent on temperature but the eventual saturation level is not. The model developed to explain this apparent contradiction also predicts an independence of saturation level on starting microstructure, stress and displacement rate below temperatures where thermal emission of vacancies from dislocations becomes an important factor in their climb rate.

6.0 References

1. F. A. Garner, "Saturation Density of Network Dislocations in Irradiated Metals," this report.

2. M. R. Hayns, J. Nucl. Mat., 56, p. 267 (1975).

3. R. A. Johnson, J. Nucl. Mat., 75, p. 77 (1978).

4. N. M. Ghoniem and D. D. Cho, Phys. Stat. Sol. [A], 54, p. 171 (1979).

5. B. O. Hall, J. Nucl. Mat., 91, p. 63 (1980).

6. N. M. Ghoniem and S. Sharafat, J. Nucl. Mat., 92, p. 121 (1980).

7. H. R. Brager, F. A. Garner and G. L. Guthrie, J. Nucl. Mat., 66, p. 301 (1977).

8. H. R. Brager, F. A. Garner, E. R. Gilbert, J. E. Flinn and W. G. Wolfer, in Radiation Effects in Breeder Reactor Structural Materials, M. L. Bleiberg and J. W. Bennett (Eds.), The Metallurgical Society of AIME, (1977) p.727.

9. F. A. Garner, W. G. Wolfer and H. R. Brager, in Effects of Radiation on Structural Materials, ASTM STP 683, J. A. Sprague and D. Kramer (Eds.), ASTM, p. 207 (1979).

7.0 Future Work

This effort will continue in an attempt to rationalize the independence of saturation density on helium content.

8.0 Publications

It is anticipated that this report will form the basis of a paper to be submitted to the ASTM Symposium on Effects of Radiation on Structural Materials, to be held in Scottsdale, AZ, in June 1982.

THE MICROSTRUCTURAL ORIGINS OF YIELD STRENGTH CHANGES IN AISI 316 DURING FISSION OR FUSION IRRADIATION

F. A. Garner, M. L. Hamilton, N. F. Panayotou and G. D. Johnson (Hanford Engineering Development Laboratory)

1.0 Objective

The objectives of this effort are to develop a microstructurally-based correlation for yield strength of AISI 316 irradiated in fast reactors, identify the strengthening contributions of each microstructural component, and using microstructural comparisons with fusion simulation experiments predict the yield strength of AISI 316 in projected fusion devices.

2.0 Summary

The changes in yield strength of AISI 316 irradiated in fast reactors have been successfully modeled in terms of concurrent changes in microstructural components. Two new insights involving the strength contributions of voids and Frank loops have been incorporated into the hardening models. Both the radiation-induced microstructure and the yield strength exhibit transients which are then followed by saturation at a level dependent on the irradiation temperature. Extrapolation to anticipated fusion behavior based on microstructural comparisons leads to the conclusion that the primary influence of transmutational differences in non-pulsed environments is to alter the transient behavior and not the saturation level of yield strength.

3.0 Program

Title: Irradiation Effects Analysis (AKJ)
Principal Investigator: D. G. Doran
Affiliation: Hanford Engineering Development Laboratory

4.0 Relevant DAFS Program Plan Task/Subtask

Subtask II.C.2 Effects of He on Microstructure
Subtask II.C.4 Effects of Solid Transmutants on Microstructure
Subtask II.C.14 Models of Flow and Fracture Under Irradiation

5.0 Accomplishments and Status

5.1 Introduction

AISI 316 stainless steel is the major structural alloy employed in the fast reactor programs of the United States, Britain and France. It may also be chosen for service in first generation fusion devices. In the absence of data developed in fusion neutron spectra, the design of such devices requires that the data developed in fission reactors be extrapolated to the spectral and operational environment projected to be characteristic of fusion devices.

If the consequences of differences in environmental variables such as neutron flux and stress state are discounted there are still substantial differences in the displacive and transmutational characteristics of the neutron spectra of fusion devices and those of various fission reactors. To a first approximation it appears that the differences in atomic displacement characteristics of neutrons can be factored into a low temperature fission-fusion correlation by expressing the exposure dose in damage energy units (eV/atom). This was recently demonstrated for AISI 316 irradiated at room temperature with T(d,n), Be (d,n) and fission (thermal reactor) neutrons.[1] The changes in yield strength and total elongation, as well as in the density of radiation-induced defect clusters that cause these changes, were all found to correlate with damage energy.

In reactor environments operating at realistic power-generating temperatures, however, the microstructural alterations are quite different and much more extensive than that observed at room temperature. There is also a substantial radiation-induced and temperature-sensitive elemental redistribution that

occurs. There is concern that in the fission and fusion environments that differences in both the identity and generation rates of gaseous [2] and solid [3] transmutants will lead to differences in the microstructural [4] and microchemical [5] evolution. This possibility can be partially addressed by comparing the microscopic response of the steel to irradiation in two fission reactors with different transmutational characteristics. A recent effort of this type concerned the microstructural and microchemical evolution of this steel in EBR-II (Experimental Breeder Reactor II) and HFIR (High Flux Isotope Reactor).[6] Transmutation rates of all important elements of AISI 316 in EBR-II are very much smaller than those in either HFIR or projected fusion devices.[3]

In this report the microstructural origins of yield strength changes are examined and projections of anticipated behavior in fusion spectra are made on the basis of conclusions drawn from dual ion irradiations and EBR-II/HFIR comparisons. Yield strength is the easiest mechanical property measurement to model since the microstructural interactions involve primarily the mechanical rather than the chemical aspects of the various microstructural components. More importantly, changes in yield strength are determined primarily by the radiation-induced intragranular microstructure while other parameters, such as total elongation, are probably influenced to a greater degree by the microstructure produced both in and between grains during ex-reactor deformation.

5.2 Modeling of Yield Strength Changes

The modeling effort requires knowledge of the relevant microstructural components, their densities and sizes, and their individual action with respect to determination of the yield strength. Previous attempts on austenitic alloys have been made to determine the contribution of each microstructural component to the hardening or softening observed for a given set of irradiation conditions.[7-10] These efforts were hampered by incomplete microstructural descriptions and some ambiguity concerning the nature of the hardening model for each component.

Recent developments now allow a potentially more successful microstructural description of yield strength. Breeder reactor programs have yielded not only detailed strength data as a function of neutron exposure, temperature and starting condition,[11-16] but have also provided insight on the nature of the microstructural/microchemical evolution of this alloy. The central insight is that all microstructural components evolve toward saturation
observation is that all microstructural components evolve toward saturation
It has been shown that the yield strength also saturates at a level which is dependent on irradiation temperature (Figure 1) but not cold-work level (Figure 2). Although there is some variation in the strength of various heats of unirradiated AISI 316, Blackburn and coworkers[17] have shown that the radiation-induced strength changes reported for breeder-irradiated heats of annealed AISI 316 are independent of heat identity and depend only on temperature.

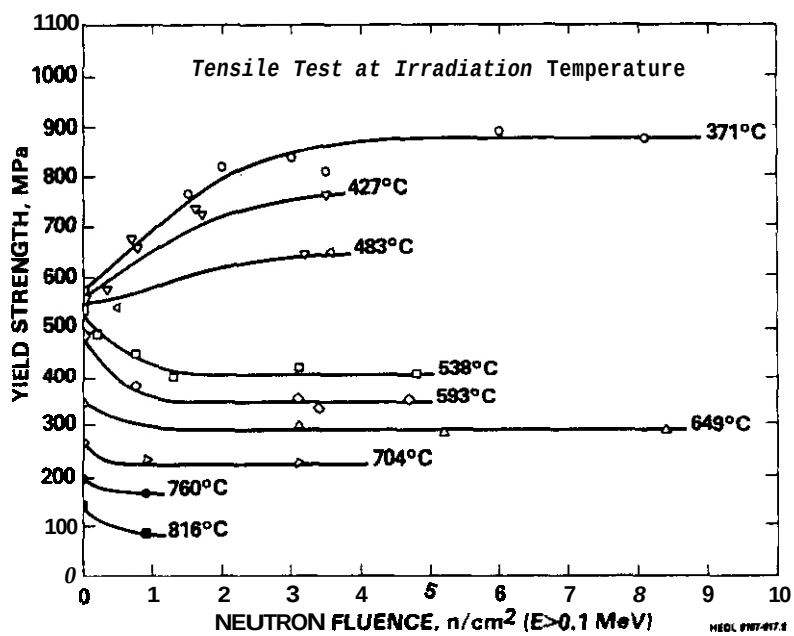

FIGURE 1. Yield Strength of 20% Cold-Worked AISI 316 After Irradiation in EBR-II.

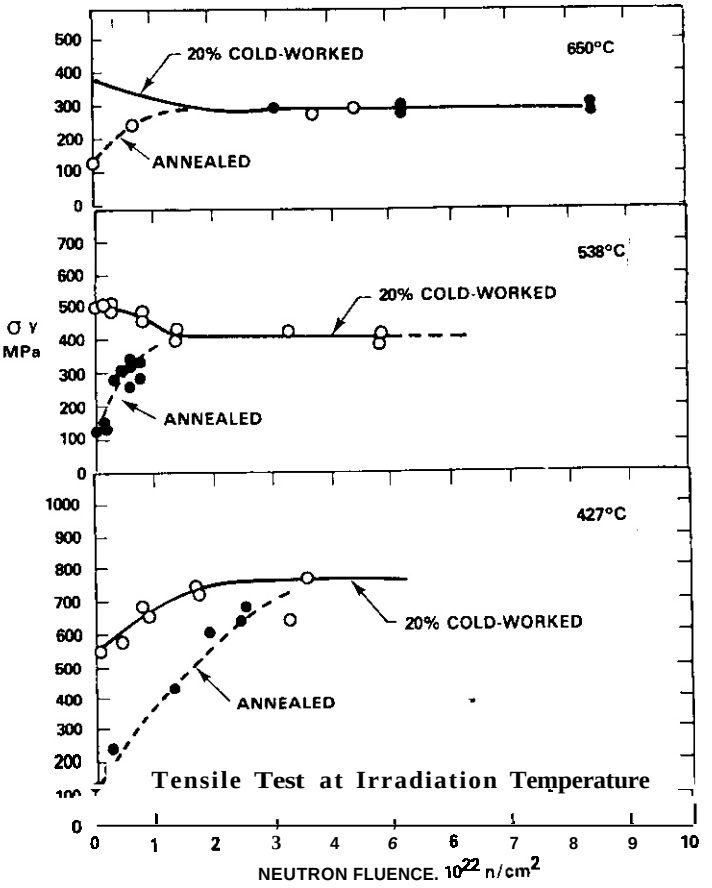

FIGURE 2. Yield Strength of Irradiated AISI 316 at Temperatures of 427, 538 and 650°C.

The path-independence of the saturation strength allows a better assessment to be made of the relative contribution of each microstructural component, since some components such as voids and precipitates are temporarily suppressed by cold-working.[5] This allows the unobscured determination of the strengthening contributions due to dislocations and loops.

It is traditional to describe irradiation hardening with models that invoke the interaction of various defects with moving dislocations.[18] Barriers which resist the motion of dislocations have been classified as either long range (LR) or short range (SR). Long range forces are due to the interaction of moving dislocations with the dislocation network of the material. Obstacles

lying in the slip plane of the moving dislocation produce short range forces when the dislocation is in close proximity to the obstacles. The increase in the shear stress, $\Delta\tau$, is given by:

$$\Delta\tau = \Delta\tau_{LR} + \Delta\tau_{SR} \tag{1}$$

The long range term is given as

$$\Delta\tau_{LR} = \alpha G b \sqrt{\rho_d}, \tag{2}$$

where ρ_d is the dislocation density, G the shear modulus, b the Burgers vector and α ranges from 0.15 to 0.30.[19] The short range contribution of an obstacle is

$$\Delta\tau_i = \frac{G b \sqrt{N_i d_i}}{\beta_i} \tag{3}$$

and

$$\Delta\tau_{SR} = [\Sigma\Delta\tau_i^2]^{\frac{1}{2}}, \tag{4}$$

where N_i is the number of defects of a given type and diameter d_i per unit volume and β_i is a constant for each type of defect. The β values for loops range from 2 to 4,[18-20] while those for voids[21] and precipitates[22] are about 1.0. However, as will be shown later, it does not appear that Frank loops at these temperatures should be treated as short range obstacles.

Finally, in calculating the flow or yield stress, it is necessary to convert from shear stress to uniaxial stress, namely $\Delta\sigma_Y = \sqrt{3}\,\Delta\tau$ based on the Von Mises criterion. Thus, the strength of the irradiated steel, σ_i is

$$\sigma_i = \sigma_o + \Delta\sigma_{cw} + \Delta\sigma_i, \tag{5}$$

where $\sigma_o + \Delta\sigma_{cw}$ is the intrinsic strength plus cold work strengthening of the unirradiated steel. σ_o is assumed not to change during irradiation.

The microstructural data required to generate yield stress predictions using equations 1-5 were presented earlier.[11] With only minor modifications, these same data were employed using the values $\beta_{FL} = 3$, $\beta_V = 1$ and $\beta_P = 1$.* The value of $a = 0.2$ was determined from the room temperature strength data (Figure 3) and the knowledge that the dislocation density of this heat of steel in the 20% cold-worked condition is approximately 3×10^{11} cm/cm^3.[4] Since there are no discernible precipitates in this steel at room temperature and none that develop on the short time frame of tensile tests at elevated temperatures, it is reasonable to assume that the softening that occurs is due to the temperature dependence of the shear modulus and the relaxation of dislocation densities. Therefore, the data of Figure 3 were also used to generate the initial dislocation density ρ_d^{cw} of the cold-worked steel after relaxation at temperature and prior to significant irradiation.

$$\rho_d^{cw} = \left[\frac{\tau_{cw} - \tau_{sa}}{0.2Gb}\right]^2 \qquad (6)$$

The preirradiation dislocation density of the solution-annealed (sa) steel was assumed to be 10^8 cm/cm^3 at all temperatures.

5.3 Results of Calculations

In a previous report, it was shown that the major features of the evolution in strength of AISI 316 could be described using the above models.[11] However, the microstructurally-based correlation based on equation (4) tended to underpredict the observed behavior at most temperatures. In reviewing the assumptions employed in the treatment of Fleischer[20] for Frank loops it was determined that at 300-600°C, Frank loops cannot be considered as short range obstacles. The Fleischer model was normalized to data derived from low temperature irradiation, leading to low dislocation densities and high densities of very small loops. At temperatures relevant to fast reactors, Frank loops are two-dimensional in nature and relatively large, with diameters on the order of the dislocation spacing; they also contain a large fraction of the total dislocation line length.

*FL = Frank Loops, v = voids, p = precipitates

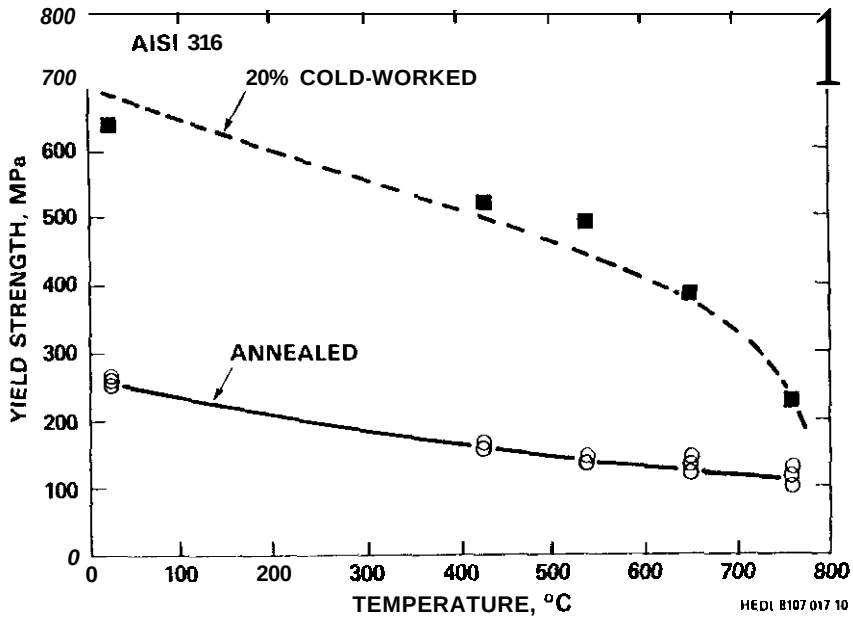

FIGURE 3. Yield Strength of Unirradiated AISI 316.

Assuming for the moment that equation 3 is still valid and β_{FL} = 3.0, the Frank loop contribution to hardening was treated as a long range contribution; the loop contribution was included in equation 2 and not 4. Figure 4 shows a comparison of the microstructurally-based predictions with the available data.

5.4 Discussion

It can be seen in Figure 4 that the relaxation of dislocation density of cold-worked steels during irradiation leads to a softening contribution to yield strength, particularly evident at temperatures above 2550°C. The presence of voids, Frank loops and radiation-stable precipitates leads to a hardening contribution which obscures the softening, particularly at lower temperatures where the densities of these defects are the largest. Since these components are sensitive to displacement rate, it is expected that the saturation strength will vary with neutron flux and spectra.[11]

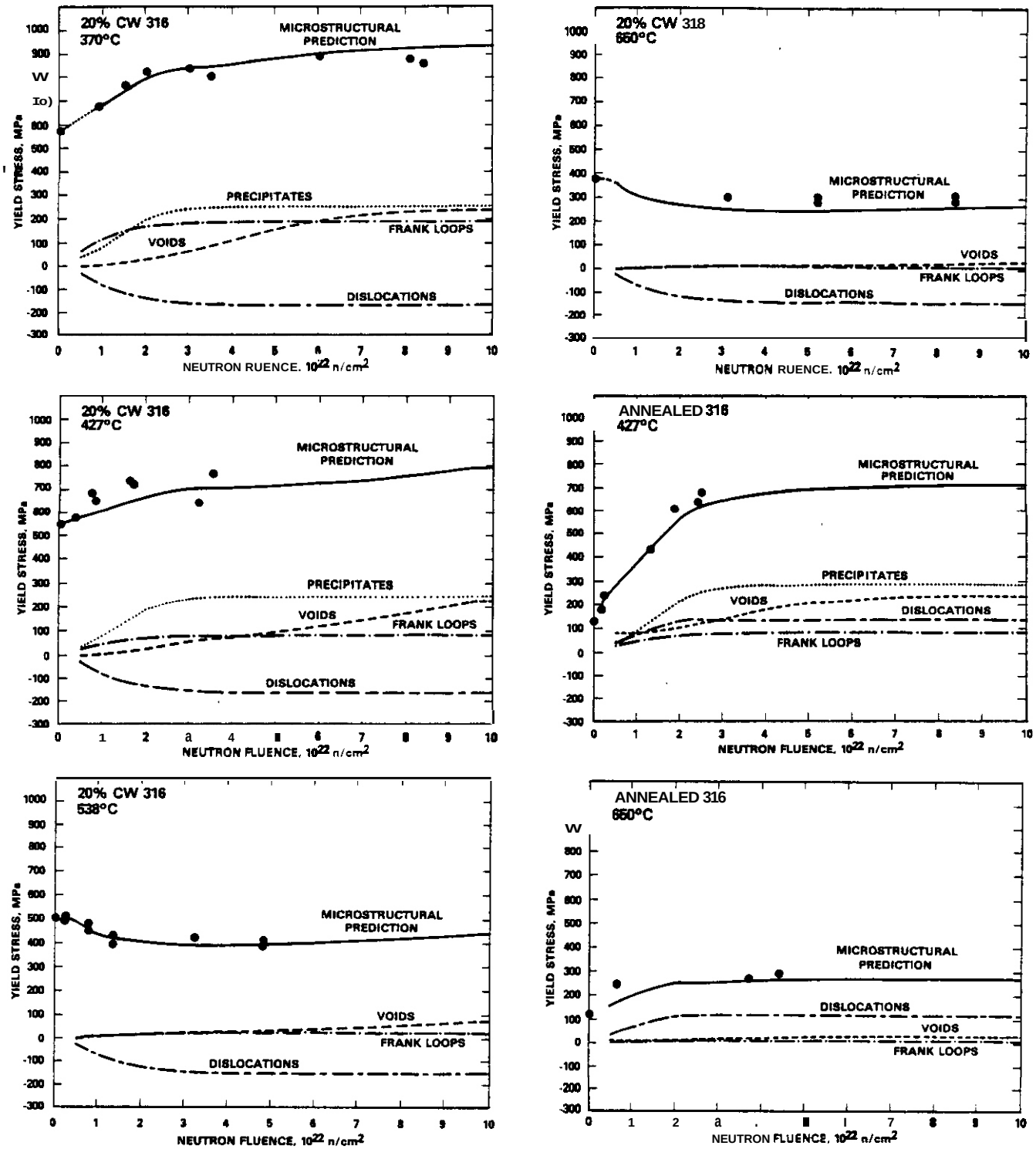

FIGURE 4. Comparison of Microstructurally-Based Predictions with Yield Stress Measurements of AISI 316. The separate strenqthening contributions of each microstructural component (11) are shown.

If Frank loops are not short range obstacles, why was the short range formulation of equation 3 employed for loops in this study? Actually, the apparent success of the "wrong" model was fortuitous since the total line length of Frank loops is $\rho_{FL} = N_{FL}(\pi d_{FL})$. Therefore,

$$\frac{\sqrt{N_{FL}\, d_{FL}}}{\beta_{FL}} = \frac{\sqrt{\pi\, N_{FL}\, d_{FL}}}{3\sqrt{\pi}} = 0.19\sqrt{\rho_{FL}} \qquad (7)$$

and the short and long range formulations are identical; the value of 0.19 agrees with the value of $\alpha = 0.2$ determined earlier. Since the predictions agree with the data at high temperatures where dislocations provide the major hardening contribution, it appears that the assumption is valid that the intrinsic yield stress σ_0 is largely unaffected by radiation-induced segregation. The major effect of the microchemical evolution on yield strength thus lies in the formation of radiation-stable precipitates which function as obstacles.

The data of Figure 1 are from steel that had not developed large void swelling at the fluences attained. Although the strength saturates at all temperatures, it is expected that a late-term softening will occur as the voids change the shear modulus of the steel, particularly at low temperatures. Several researchers[23-24] have shown that the modulus of irradiated stainless steels is decreased with swelling $\Delta V/V_0$, according to the relationship $G' = G(1-2\,\Delta V/V_0)$. Decreases in modulus of 20% have been observed for 10% swelling.[24]

5.5 Projection to Fusion Environments

In principle, it should be possible to predict strength changes in fusion environments by studying the response of fusion-induced microstructure to anticipated changes in transmutants. The available neutron data fall into two classes: direct comparisons of irradiation response in two reactors with different spectra and studies in one reactor involving variations in concentration of expected transmutants. In a recent comparative study of AISI 316 it was shown that the microchemical and microstructural evolution

at 500-620°C was remarkably insensitive at 40-70 dpa to more than two orders of magnitude difference in helium generation rates found in the EBR-II and HFIR reactors.[6] This study was complicated by the burn-out of manganese and the formation of ~0.8% vanadiun at relatively moderate doses in HFIR.[3] Neither of these elements suffer measurable changes at comparable doses in EBR-II. Breeder reactor studies have also shown a sensitivity of void swelling to manganese content [3] and also to carbide-forming elements similar to vanadium.[5] Both of these elements are projected to increase slowly in fusion irradiation of AISI 316, with possible late-term consequences in phase stability and yield strength.

In another study it has been shown that large helium generation rates in AISI 316 irradiated in HFIR lead to earlier void nucleation at all temperatures in the range 300-700°C, but not to void densities which are substantially different at saturation than those that develop in breeder reactors.[25] Therefore, the effect of helium is concentrated in the transient regime.

Dual ion irradiation experiments to date have concentrated only on the gaseous transmutants. The development of Frank loops and their subsequent conversion to dislocations have been shown to be sensitive to the helium level.[26-29] At high fluences, however, the dislocation density has been found to be remarkably insensitive to helium concentration or the mode of implantation.[28-29] It also appears that large levels of helium can alter the early phase evolution, particularly in accelerated simulation experiments.[26-27] There are no supporting neutron data.

Since the steady-state swelling rate is insensitive to helium content[6] and the saturation dislocation density is also unaffected it appears that the primary effect of helium is in the transient regime, particularly the contributions of voids and Frank loops. Unless solid transmutants change the precipitation behavior or matrix strength, no effect is anticipated in the saturation regime. This conclusion may not be valid for pulsed reactor systems due to the flux sensitivity of voids, Frank loops and radiation-stable precipitates.[5]

6.0 Conclusions

Yield strength changes in AISI 316 during breeder reactor irradiation can be described in terms of microstructurally-based models. Microchemical changes are of importance only in that they lead to extensive precipitation. The saturation observed in yield strength is a reflection of the saturation of microstructural densities, but it is expected that a second-order softening will eventually occur as accumulated voidage decreases the shear modulus. While voids and precipitates can be considered as short range obstacles, large Frank loops cannot and therefore should be treated as additional dislocation line length.

The projection of these insights to the anticipated response of AISI 316 in fusion devices yields the conclusion that, under steady-stare irradiation, the strength behavior at a given displacement rate will differ from fast reactor behavior primarily in the transient and not the saturation regime.

7.0 References

1. R. R. Vandervoort, E. L. Raymond and C. J. Echer, Radiation Effects, 45, 1980, pp. 191-198.

2. G. L. Kulcinski, D. G. Doran and M. A. Abdou, "Comparison of Displacement Rates in Current Fission and Future Fission Reactors", ASTM-STP-570, p. 239, February 1976.

3. J. F. Bates, F. A. Garner and F. M. Mann, "The Effects of Transmutation Products on Swelling in the 316 Stainless Steel'', this conference.

4. H. R. Brager, F. A. Garner, E. R. Gilbert. J. E. Flinn and W. G. Wolfer. in Radiation Effects In Breeder Reactor Structural Materials, M. L. Bleiberg and J. W. Bennett (eds.), AIME, 1977, pp. 727-755.

5. F. A. Garner. "The Microchemical Evolution of Irradiated Stainless Steels", Proc. Symp. on Irradiation-Phase Stability, October 5-9, 1980, Pittsburgh, PA (in press).

6. H. R. Brager and F. A. Garner, "Comparison of the Swelling and the Microstructural/Microchemical Evolution of AISI 316 Irradiated in EBR-II and HFIR", this conference.

7. J. J. Holmes, R. E. Robbins, J. L. Brimhall and B. Mastel, Acta Met., 16, 1968, p. 955.

8. J. R. Matthews, Contemp. Phys., 18, 1977, p. 571.

9. G. R. Odette and D. Frey, J. Nucl. Mat., 85 & 86, 1979, p. 817.

10. M. Bŏcek and K. Ehrlich, J. Nucl. Mat., 58, 1975, pp. 247-256.

11. G. D. Johnson, F. A. Garner, H. R. Brager and R. L. Fish, "A Microstructural Interpretation of the Fluence and Temperature Dependence of the Mechanical Properties of Irradiated AISI 316", ASTM-STP-725, p. 393, March 1981.

12. J. J. Holmes and J. L. Straalsund, "Effects of Fast Reactor Exposure on the Mechanical Properties of Stainless Steels", Ref. 4, pp. 53-63.

13. J. M. Dupouy, J. Erler and R. Huillery, Ref. 4, pp. 83-93.

14. K. Q. Bagley, J. W. Barnaby and A. S. Fraser, BNES Conference on Irradiation Embrittlement and Creep on Fuel Cladding and Core Components, 1972, pp. 143-153.

15. R. L. Fish, N. S. Cannon and G. L. Wire, ASTM-STP-683, pp. 450-465.

16. R. L. Fish and J. J. Holmes, J. Nucl. Mat., 46, 1973, p. 113.

17. L. D. Blackburn, D. L. Greenslade and A. L. Ward, "Mechanical Properties of Type 316 Stainless Steel Materials After Irradiation at 515°C and 585°C", HEDL-TME 81-4, April 1981.

18. A. L. Bement, Jr., Proceedings, 2nd International Conference on the Strength of Metals and Alloys, ASM, 1970, pp. 693-728.

19. J. D. Embury, in Strengthening Methods in Crystals, A. Kelly and R. B. Nicholson (eds.), J. Wiley & Sons, New York, 1971, Chapter 6.

20. R. L. Fleischer, Acta Met., 10, 1962, p. 835.

21. P. Coulomb, Acta Met., 7, 1959, p. 556.

22. E. Orowan, "Internal Stresses in Metals and Alloys", Inst. of Met., London, 1948, p. 451.

23. J. L. Straalsund and C. K. Day, Nuclear Technology, 20, October 1973, p. 27.

24. M. Marlowe and W. K. Appleby, Trans. Am. Nucl. Soc., 16, 1973, p. 95.

25. B. B. Glasgow, A. Si-Ahmed, W. G. Wolfer and F. A. Garner, "Helium Bubble Formation and Swelling in Metals", this conference.

26. K. Farrell, Radiation Effects, 53, 1980, pp. 175-194.

27. E. A. Kenik, J. Nucl. Mat., 85 & 86, 1979, pp. 659-663.

28. W. J. Choyke, et al, J. Nucl. Mat., 85 & 86, 1979, pp. 647-651.

29. S. C. Agarwal, G. Ayrault, D. I. Potter, A. Taylor and F. V. Nolfi, J. Nucl. Mat., 85 & 86, 1979, pp. 653-657.

8.0 Publication

An abbreviated version of this report has been submitted to J. Nucl. Mater., which will publish a special issue on the Proceedings of the Second Topical Meeting on Fusion Reactor Materials, Seattle, WA, August 9-12, 1981. About 75% of this work was recently published in another report: G. D. Johnson, F. A. Garner, H. R. Brager and R. L. Fish, "A Microstructural Interpretation of the Fluence and Temperature Dependence of the Mechanical Properties of Irradiated AISI 316", Effects of Radiation Materials: Tenth Conference, ASTM-STP-725, David Kramer, H. R. Brager and J. S. Perrin (eds.), ASTM, 1981, pp. 393-412.

7.0 Future Work

The possible consequences of void-related softening of the shear modulus will be investigated further. The impact of temperature reassessments in HFIR irradiation experiments on the helium-affected yield strength models will also be determined. The appropriate choice of hardening models for Frank loops will also be studied for both AISI 316 in breeder reactors and copper alloys in RTNS-II.

COMPOSITIONAL DEPENDENCE OF RADIATION-INDUCED CHANGES IN DIMENSIONAL AND PHYSICAL PROPERTIES OF Fe-Cr-Ni AUSTENITIC ALLOYS

W. G. Wolfer (University of Wisconsin) and F. A. Garner (Hanford Engineering Development Laboratory)

1.0 Objectives

The purpose of this study is to investigate the potential causes of the compositional dependence of swelling and irradiation creep and their connections to various fundamental physical properties of Fe-Cr-Ni alloys.

2.0 Sumnary

The compositional dependence of void swelling in irradiated Fe-Ni-Cr alloys has been shown to possibly arise from corresponding dependencies of the lattice parameter and shear modulus. Both of these parameters are invoked in theoretical descriptions of void nucleation and both change with increasing nickel content. Nickel segregates to void embroys in these alloys, increasing the nickel level at their surfaces, and leading to changes in their interstitial capture efficiency. This leads to changes in the void nucleation rate and the duration of the transient regime of swelling. Other secondary effects of nickel content on the dislocation bias and the matrix vacancy diffusion are currently under investigation.

3.0 Program

Title: Irradiation Effects Analysis
Principal Investigator: D. G. Doran
Affiliation: Hanford Engineering Development Laboratory

4.0 Relevant Program Plan Task/Subtask

II.C.l Effects of Material Parameters on Microstructure

5.0 Accomplishments and Status

5.1 Introduction

A correlation between swelling and the nickel concentration in Fe-Ni-Cr alloys has been experimentally established by Johnston and co-workers,[1] and subsequently confirmed by other researchers. The onset of swelling in austenitic stainless steels has also been correlated with radiation-induced changes in the nickel level of the alloy matrix.[2] The selection of candidate alloys in the ADIP program is partly based on these empirical correlations between swelling and nickel content. In spite of its importance, however, no completely satisfactory explanation has yet been given for the marked dependence of swelling on nickel content.

5.2 Review of Proposed Models of the Compositional Dependence of Swelling

Watkins, et al.[3] have proposed that in fcc Fe-Ni-Cr alloys, the iron atoms may exist in two states, an antiferromagnetic and a ferromagnetic one. These are postulated to differ in their atomic volumes and their contributions to the elastic moduli of the alloy. With increasing nickel conte'nt, the ratio of antiferromagnetic to ferromagnetic iron atoms decreases with a corresponding increase in the lattice parameter and a decrease in the elastic shear modulus. They speculate that the increase of the average atomic volume may imply a greater recombination of self-interstitials and vacancies.

According to recent results by Wolfer and Si-Ahmed,[4] the recombination rate at reactor irradiation temperature is simply proportional to the lattice parameter. Figure 1 shows the lattice parameter[5] of Fe-Ni-Cr-phase alloys at room temperature. It is seen that the variation is no more than about 2%. Such a small variation in the recombination rate would be insufficient to account for the much larger variation observed in the swelling as a function of nickel content.

Bates[6] has recently measured the variation of the shear modulus with nickel composition. These data are in general agreement with the more extensive and earlier measurements by Masunoto, et al,[7] shown in Figure 2. Bates suggested that the arrival ratio (α/β) of interstitials and vacancies at void embryos decreases with increasing shear modulus. Therefore, in this treatment the void nucleation rate increases with the shear modulus.

This suggestion was based on a model proposed by Wolfer and Ashkin[8] for the capture efficiency for interstitials at a bare void. In this latter derivation, the image interaction of an interstitial with the void surface was not included. When this important interaction was included later by Wolfer and Yoo,[9] it was found that the arrival rate ratio (α/β) increases with increasing shear modulus. This would imply that the void nucleation rate increases sharply as the shear modulus drops to its minimum value for a binary Fe-Ni alloy with 40% nickel. In contrast, the data show that swelling is at a minimum for this alloy composition.

It should further be noted that Bates did not consider the fact that the bias of the dislocations also increases with the shear modulus, and that it is the net bias or bias difference between dislocations and voids which is the driving force for both void nucleation and growth.

In any case, the homogeneous nucleation of bare voids was shown to occur with such low probability[9,10] that it cannot be invoked in any explanation of the composition dependence of swelling. In order for void nucleation to proceed at a rate commensurate with experimental findings, segregation to void embryos must precede their growth. As shown by Si-Ahmed, Wolfer and Mansur,[10,11] this requires that segregation results in a slight compositional change around the void embryo such that the shear modulus increases locally by a few percent and/or that the lattice parameter increases by a few tenths of a percent. Such minor changes are well within the range of the compositional variation of the shear modulus, Figure 2, and the lattice parameter, Figure 1. Segregation of nickel to the surface of voids has been observed previously.[12]

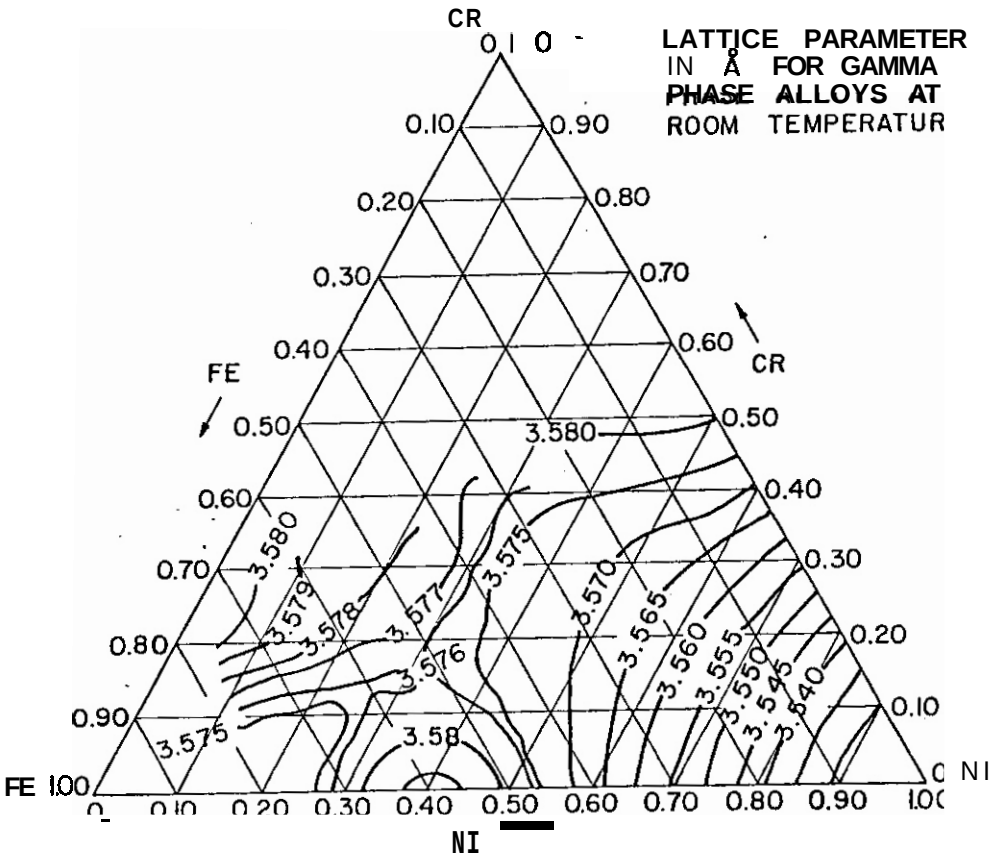

FIGURE 1. Compositional Dependence of Lattice Parameter Measured for Fe-Ni-Cr Alloys at Room Temperature. (5)

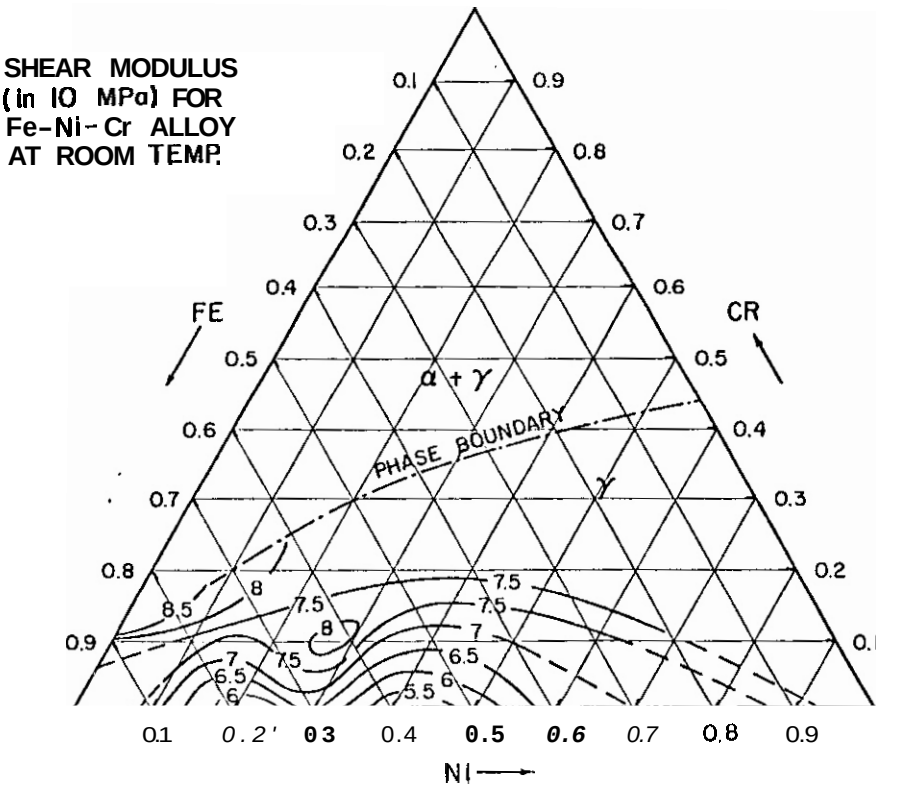

FIGURE 2. Compositional Dependence of Shear Modulus Measured for Fe-Ni-Cr Alloys at Room Temperature. (7)

The pronounced effect of segregation to void embryos is illustrated in Figures 3 and 4. Figure 3 shows the void nucleation rate as a function of the increase in lattice parameter around the void, assuming that radiation-induced segregation produces a region with a thickness of 10% (curve b) or 20% (curve a) of the void radius. The shear moduli of both the shell and matrix are assumed to be consistent and identical for the results of Figure 3. On the other hand, if the lattice parameter is constant everywhere but the shear modulus increases around the void embroys due to segregation, a similar increase in found in the void nucleation rate. This is shown in Figure 4, where $(1-g) = (\mu_s - \mu_m)/\mu_m$ with μ_s and μ_m being the shear moduli in the void shell region and the matrix, respectively.

An explanation using some of these ideas about the void shell was recently advanced by Hishinuma and coworkers[13] to explain the results of an irradiation study conducted in a high voltage microscope. They observed nickel enrichment around void embryos in low nickel alloys, as well as a strain field indicating a lattice parameter mismatch of about 0.0005 nm which represents a difference of 0.14%. Hishinuma assuned that the nickel enrichment would produce a lattice parameter reduction based on the general trend for high nickel alloys. It is seen from Figure 2, however, that the lattice parameter can in fact increase with increasing nickel in the composition range of 25% to 40%. It is therefore possible that nickel enrichment around void embryos produces a positive lattice parameter mismatch when the original nickel composition is below 40%. This contributes to the reduction of the interstitial capture efficiency (or bias) of a void embryo. However, this reduction is counteracted by the decrease in shear modulus which accompanies the nickel enrichment. By itself, the lowering of the shear modulus around a void increases the interstitial bias of a void.

With the presently available data for the lattice parameter and the shear modulus, it is not possible to judge which of these two compensating effects is the dominant one. The data shown in Figures 1 and 2 are for room temperature and not for the elevated temperatures at which irradiations are carried out.

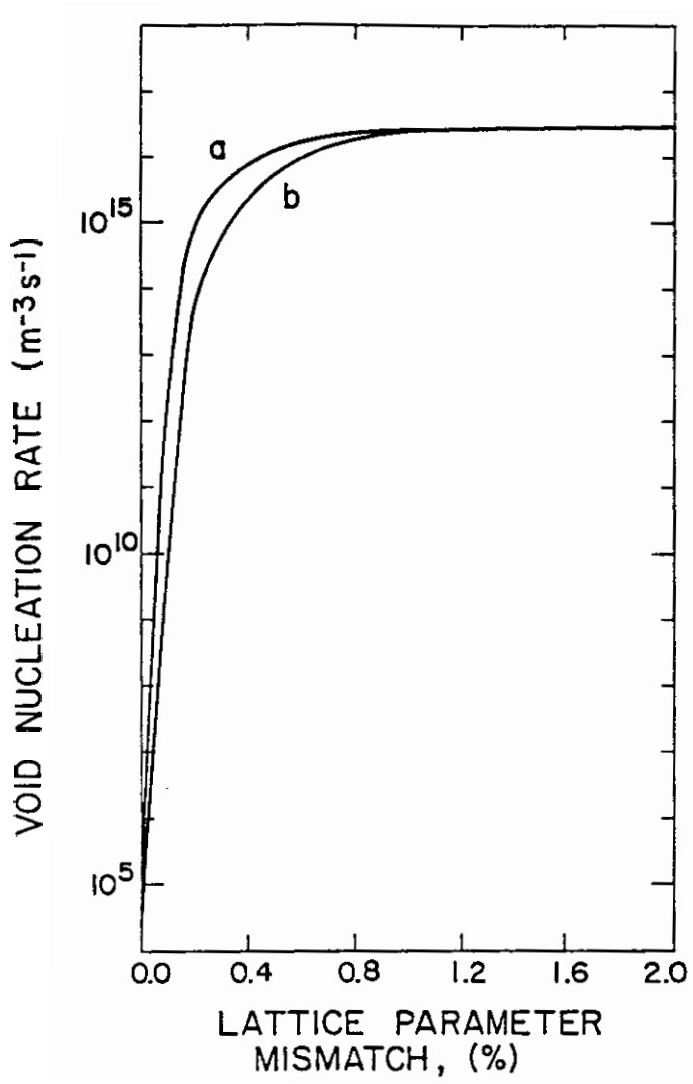

FIGURE 3 Calculated Effect of Lattice Parameter Mismatch (between the matrix and the segregated shell surrounding the void) on the Void Nucleation Rate at 500°C for Shell Thicknesses of 10 and 20% (b and a) of the Void Radius.(10)

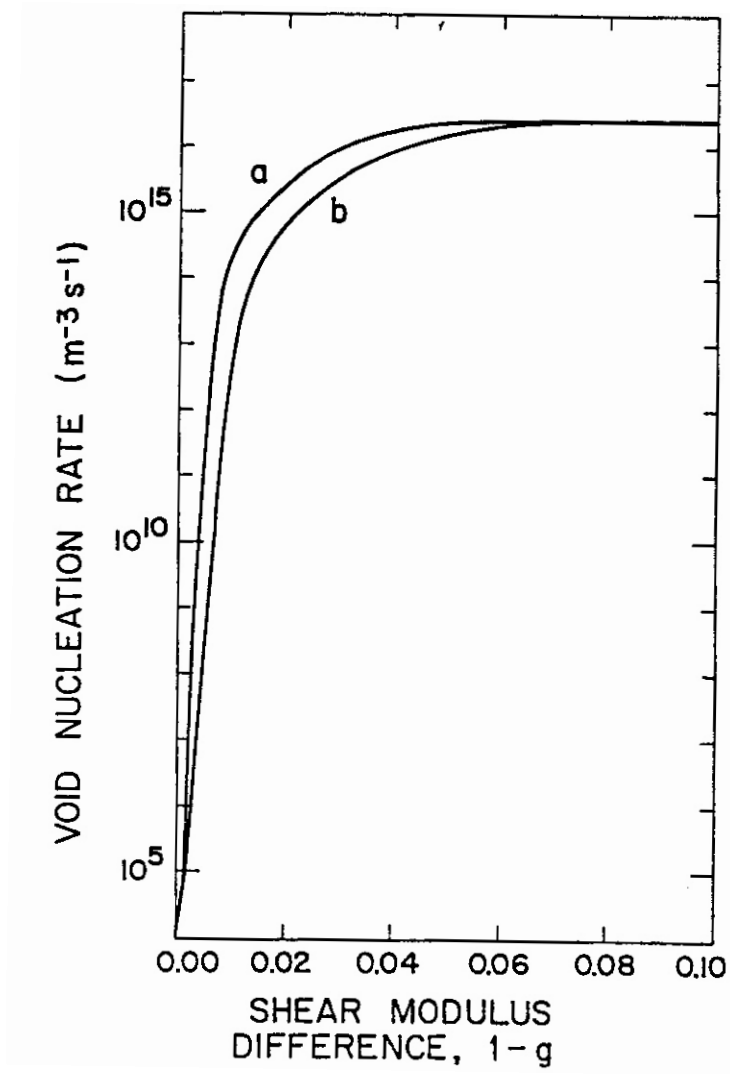

FIGURE 4. Calculated Effects of Shear Modulus Difference (between the matrix and the segregated shell surrounding the void) on the Void Nucleation Rate at 500°C for Shell Thicknesses of 10 and 20% (b and a) of the Void Radius.(10)

Considering the anomalous thermal expansion coefficients in the Invar region around 30% to 50% nickel as well as the ferromagnetic contributions to the elastic constants at low temperatures, the elevated temperature properties cannot be expected to be exactly the same as those at room temperature. Nevertheless, the anomalous variation of lattice parameter and elastic shear modulus in the vicinity of 40% nickel is expected to be present at higher temperatures.

In summary, nickel enrichment at an embryo's surface by radiation-induced segregation will result in local changes of lattice parameter and elastic properties of sufficient magnitude to affect the bias of void embryos. Because of the lack of complete data, it is not possible at the present time to clearly establish the full connection between segregation, reduction in the interstitial bias of small voids, and the compositional dependence of swelling in the Fe-Cr-Ni alloy series. However, there exists already a substantial body of corroborating evidence to warrant further investigations.(2)

So far, we have explored the potential of segregation on the bias of small voids. An implication is that the void nucleation rate rather than the steady-state swelling rate is a strong function of the nickel composition. This would imply that increasing nickel content would extend the transient regime of swelling but not the steady-state regime. This behavior has been experimentally demonstrated as shown in Figure 5.

5.3 Other Compositional Effects

Segregation can result in bias modifications at dislocations as well. However, since the long-range stress field of an edge dislocation cannot be significantly altered by segregation around the core, its relative impact on the dislocation bias is certainly less than on the void bias. Furthermore, whereas a void is stationary, a climbing dislocation moves away from segregated nickel atoms. This will further reduce the average effect of segregation on the dislocation bias. Other segregation effects on the bias of both voids and dislocations

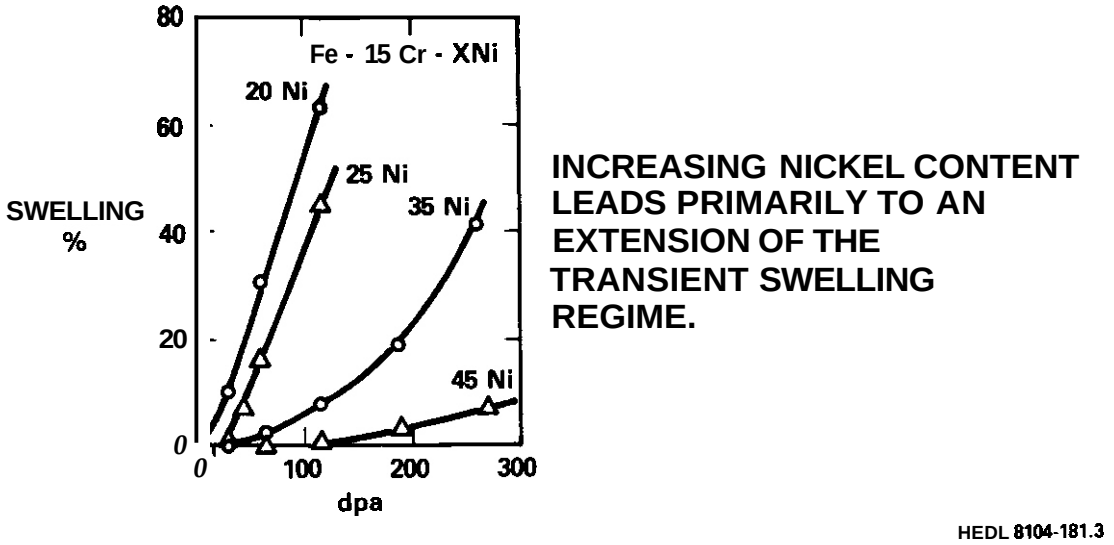

FIGURE 5. Influence of Nickel Content on Swelling Behavior on Fe-15Cr-XNi Alloys at 675°C When Bombarded with 5 MeV N_i + Ions.(15)

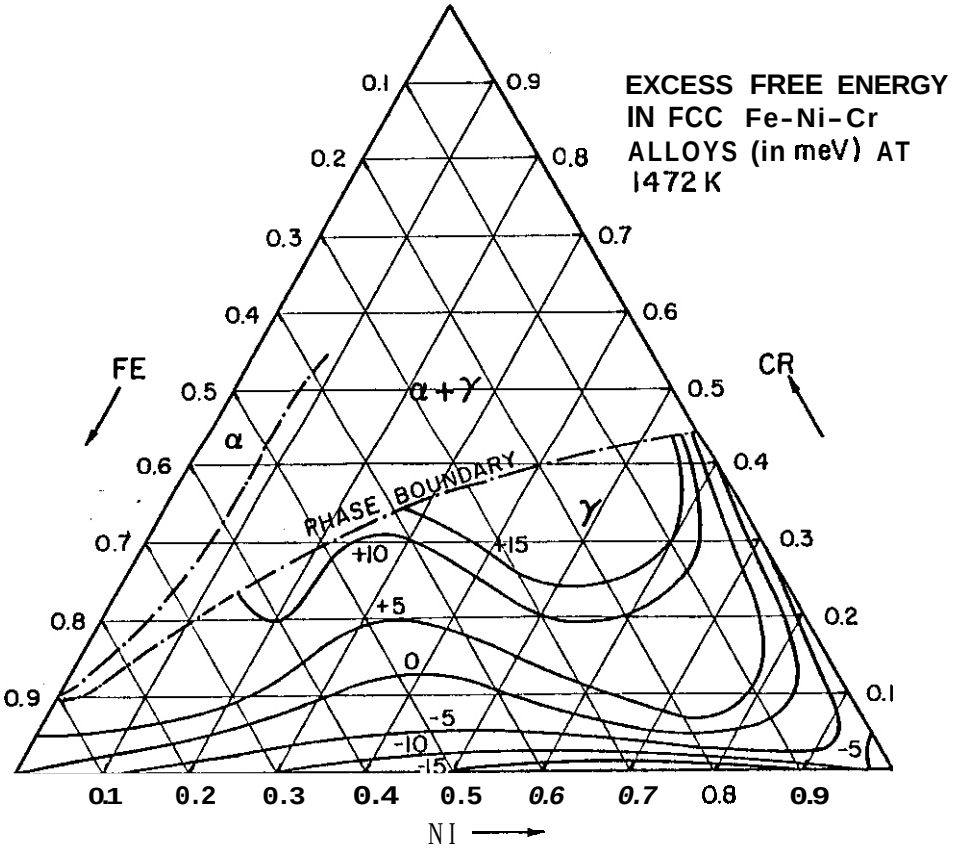

FIGURE 6. Compositional Dependence of Excess Free Energy at 1472°K in Fe-Cr-Ni Alloys. (14)

arise from changes in the vacancy mobility and the vacancy formation energy. The latter is related to the excess free energy of the alloy. As shown in Figure 6, the excess free energy is also a function of the composition for the Fe-Cr-Ni alloys.[14]

5.4 Conclusions

The compositional dependence of void swelling in irradiated Fe-Ni-Cr alloys has been shown to possibly arise from corresponding dependencies of the lattice parameter and shear modulus. Both of these parameters change with increasing nickel content. Voids in these alloys segregate nickel at their surface, leading *to* changes in the interstitial capture efficiency and therefore the void nucleation rate and transient regime of swelling. Other secondary effect! of nickel content on the dislocation bias and vacancy diffusion are currently under investigation.

6.0 References

1. W. G. Johnston., T. Lauritzen. J. H. Rosolowski and A. M. Turkalo, "Properties of Reactor Structural Alloys After Neutron or Particle Irradiation", ASTM-STP-570, 1975, p. 525.

2. F. A. Garner, "The Microchemical Evolution of Irradiated Stainless Steels" Proceedings of the AIME Symposium on Irradiation Phase Stability, October 5-9, 1980, Pittsburgh, PA (in press).

3. J. S. Watkins, J. Standring, A. D. Miodownik and J. H. Gittus, Proc. International Conference on Radiation Behavior of Claddina and Structural Materials for Fast Breeder Reactors; Ajaccio Corsica, 1979.

4. W. G. Wolfer and A. Si-Ahmed, J. Nucl. Mat., 99, (1981), p. 117

5. W. R. Rees, B. D. Burns and A. T. Cook; J. Iron Steel Institute, 162 (1949), p. 325.

6. J. F. Bates, J. Nucl. Materials, 87 (1979), p. 409.

7. H. Masunoto, H. Saito, T. Kono and Y. Sugai; Science Rep. Research Inst. Tohoku Univ., Series A, Vol. 8 (1956), p. 471.

8. W. G. Wolfer and M. Ashkin, J. Appl. Phys., 47 (1976), p. 791.

9. W. G. Wolfer and M. Yoo; International Conference on Radiation Effects and Tritium Technology for Fusion Reactors, Gatlinburg, TN, 1975, CONF-750889, 1976, Vol. 4, p. 458.

10. A. Si-Ahmed and W. G. Wolfer, to be published in J. Nucl. Materials.

11. W. G. Wolfer and L. K. Mansur, J. Nucl. Materials, 91 (1980), p. 265.

12. H. R. Brager and F. A. Garner, Analysis of Radiation-Induced Microchemical Evolution in 300 Series Stainless Steels, Proceedings of AIME Symposium on "Advanced Techniques for the Characterization of Irradiated Materials", January 1980 (in press).

13. A. Hishinuma, K. Katano and K. Shiraishi; to be published in J. Nucl. Materials.

14. W. Slough, P. J. Spencer and O. Kubaschewski; J. Chem. Thermodynamics, 2 (1970), p. 117.

15. J. F. Bates and W. G. Johnston, "Effects of Alloy Composition on Void Swelling in Radiation Effects in Breeder Reactor Structural Materials", M. L. Bleiberg and J. W. Bennett (Eds.), AIME, 1977, p. 625.

7.0 Future Work

A review will be presented of the possible ways in which compositional changes could affect either defect diffusion or biases of various microstructural components.

8.0 Publications

None.

DISTRIBUTION

uc-20 (119)

UC-20c (77)

DOE-HQ/Office of Reactor Research and Technology
NE-530
Washington, DC 20545

PB Hemmig, Safety & Physics

DOE-HQ/Office of Fusion Energy (2)
Washington, OC 20545

JF Clark
JF Decker, G-256, ER-54

DOE-RL/Office of Asst Manager For Projects and Facilities Management

GM Chenevert, FMITPO

DOE-RL/Office of Asst Manager for Advanced Reactor Programs

AR DeGrazia, Physical Scientist, Technology Development

Argonne National Laboratory (5)
9700 South Cass Avenue
Argonne, IL 60439

LR Greenwood
APL Turner
A. Taylor
H. Wiedersich
RE Nygren

Battelle Memorial Institute (3)
Pacific Northwest Laboratory
P.O. Box 999
Richland, WA 99352

JL Brimhall
DA Dingee
TD Chikalla

Brookhaven National Laboratory
Associated Universities
Upton, Long Island, NY 11973

Chairman, Nuclear Energy Dept

Columbia University
Plasma Physics Laboratory
New York, NY 10027

RA Gross

General Atomic Company (2)
P.O. Box 81608
San Diego, CA 92138

GR Hopkins
JR Gilleland

INESCO
11011 Torreyana Rd
San Diego, CA 92121

RO Stevenson

Lawrence Livermore Laboratory (2)
P.O. Box 808
Livermore, CA 94550

MW Guinan
CM Logan

Los Alamos National Laboratory (2)
P.O. Box 1663
Los Alamos, NM 87544

DJ Dudziak
CR Emigh

Massachusetts Institute of Technology (4)
77 Massachusetts Avenue
Cambridge, MA 02139

L. Lidsky
I- W Chen, Rm 13-5118
NJ Grant
DB Montgomery, Bldg. NW 21

DISTRIBUTION (Cont'd)

McDonnell-Douglas Astronautics
P.O. Box 516
St. Louis, MO 63166

O. Kummer

Mound Laboratory
P.O. Box 32
Miamisburg, OH 45342

Manager, Tech Appl & Development

National Bureau of Standards
Gaithersburg, MO 20760

CO Bowman

Naval Research Laboratory (3)
Washington, OC 20375

I. Manning, Code 6672
JA Sprague
LE Steele, Code 6390

North Carolina State University
Department of Nuclear Engineering
Raleigh, NC 26707

JR Beeler, Jr

Oak Ridge National Laboratory (7)
P.O. Box X
Oak Ridge, TN 37830

Director, Thermonuclear Div,
(Bldg 9201-2)
FG Perey
M. Roberts, Bldg 9204-1
J. Sheffield
JO Stiegler
C. Weisbin
FW Wiffen

Princeton University (2)
Plasma Physics Laboratory
Forrestal Campus
P.O. Box 451
Princeton, NJ 08544

K. Wakefield
H. Furth

Rockwell International
8900 DeSoto Ave
Canoga Park, CA 91304

O. Kramer

Sandia Laboratories (2)
P.O. Box 5800
Albuquerque, NM 87185

FL Vook, Org 5100

Sandia Laboratories
Livermore, CA 94550

WD Wilson

University of California
Los Angeles, CA 90024

RW Conn

University of Michigan
Nuclear Engineering
Ann Arbor, MI 48109

T. Kammash

University of Missouri
Mechanical & Aerospace Engineering
1006 Engineering Bldg
Columbia, MO 65211

M. Jolles

DISTRIBUTION (Cont'd)

University of Virginia
Charlottesville, VA 22901

WA Jesser

University of Wisconsin
1500 W. Johnson Drive
Madison, WI 53706

WG Wolfer

Westinqhouse
Advanced Reactors Division
P.O. Box 158
Madison, PA 15663

A. Boltax

Westinghouse
Research and Development Center (2)
1310 Beulah Road
Pittsburgh, PA 15235

S. Wood
JA Spitznagel

Commission for the European Communities
200, Rue de la Loi
B-1049 Brussels, Belgium

J. Oarvas

(ECN)
Energieonderzoek Centrum Nederland
Westerdionweg 3
NL-1755 ZG Petten, NH, The Netherlands

B. Van Der Schaaf

(EIR)
Swiss Federal Institute
For Reactor Research
CH-5303 Wuerenlingen, Switzerland

WV Green

EURATOM
Joint Research Center Ispra
Materials Science Division
I-21020 Ispra, Varese, Italy

P. Schiller

University of Tokyo
Faculty of Engineering
Bunkyo-ku,
Tokyb 113, Japan

Taijiro Uchida

Hahn-Meitner Institute
fur Kernforschung
Glienickerstrasse 100
D-1000 Berlin,
Federal Republic of Germany

H. Wollenberger

Japan Atomic Energy Research Institute
Physical Metallurgy Laboratory
Division of Nuclear Fuel Research
Fukoku Seimei Bldg
2-2, Uchisaiwai-cho 2-chome, Chiyoda-ki,
Tokyo 100, Japan

K. Shiraishi

(KFA-IFF)
Kernforschungsanlaqe Jüiich GmbH
Postfach 1913
D-517 Julich,
Federal Republic of Germany

H. Ullmaier

(KFK-IMF II)
Kernforschungsaniage Karlsruhe
Institut fur Reaktorbauelemente
Postfach 3640
0-7500 Karlsruhe 1,
Federal Republic of Germany

K. Ehrlich

DISTRIBUTION (Cont'd)

National Research Council
Montreal Road
Ottawa, Canada

EV Kornelson

(SCK/CEN)
Studiecentrum voor Kernenergie
Centre d'Etude de l'Énergie Nucléaire
Boeretang 200
B-2400 Mol, Belgium

J. Nihoul

(UKAEA-Harwell)
United Kingdom Atomic Energy Authority
Atomic Energy Research Establishment
Metallurgy Division
Building 388
Oxfordshire, OX11 ORA, UK

DR Harries

HEDL (38)

HR Brager	W/A-64	NF Panayotou	W/A-65
WL Bunch	W/B-47	EF Parker	W/E-17
LL Carter	W/B-47	RW Powell	W/A-64
DG Doran (5)	W/A-57	RJ Puigh	W/A-58
EA Evans	W/C-23	FH Ruddy	W/C-39
FA Garner	W/A-57	FA Schmittroth	W/A-4
DS Gelles	W/A-64	WF Sheely	W/C-62
R. Gold	W/C-39	RL Simons	W/A-57
HL Heinisch	W/A-57	AL Trego	W/E-15
DL Johnson	W/A-4	GL Wire	W/A-58
GD Johnson	W/A-65	HH Yoshikawa	W/C-44
NE Kenny	W/C-115	Central Files (5)	W/C-110
FM Mann	W/A-4	Publ Services (2)	W/C-115
WN McElroy	W/C-39	Doc Management	W/C-125
EK Opperman	W/A-58		